Depositional patterns, diagenetic evolution, physical properties and quantitative seismic analysis of the early Miocene Yadana carbonate gas reservoir (Offshore Myanmar)

Thomas Teillet

To cite this version:

Thomas Teillet. Depositional patterns, diagenetic evolution, physical properties and quantitative seismic analysis of the early Miocene Yadana carbonate gas reservoir (Offshore Myanmar). Applied geology. Aix Marseille Univ., CEREGE, 2019. English. NNT : . tel-02368235

HAL Id: tel-02368235
https://theses.hal.science/tel-02368235v1

Submitted on 18 Nov 2019

Depositional model
Diagenetic evolution
Physical properties
Quantitative seismic analysis

of Early Miocene Carbonate gas reservoir of Yadana, Offshore Myanmar

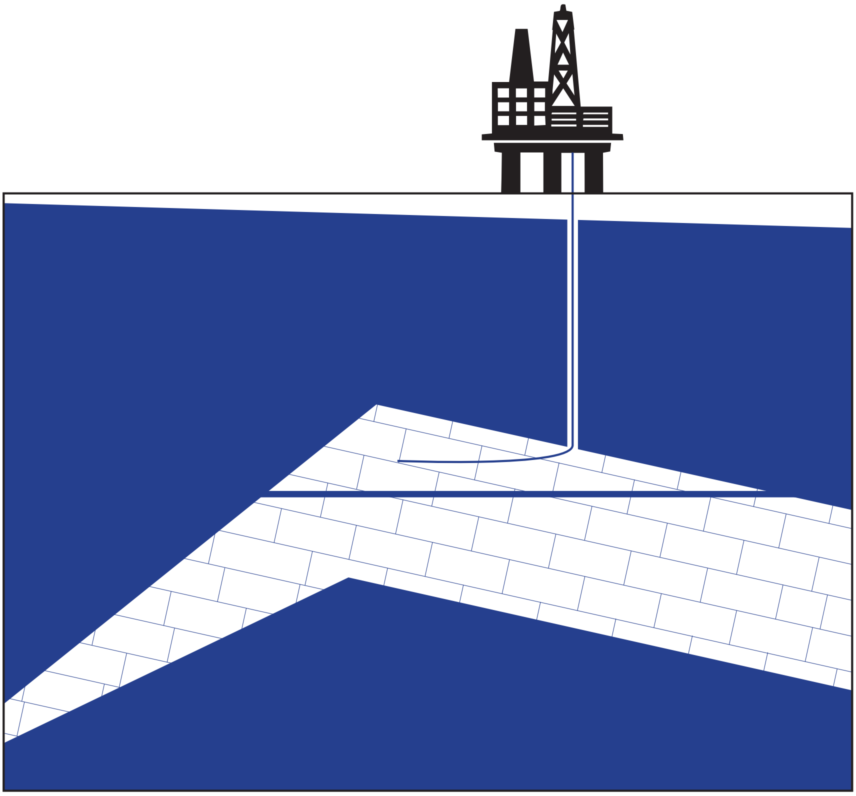

Thomas Teillet

— PhD Thesis

Thèse de doctorat

Présentée pour obtenir le grade universitaire de
docteur des Universités d'Aix-Marseille.
SPÉCIALITÉ: Géosciences de l'environnement
ÉCOLE DOCTORALE : ED251 Sciences de l'environnement

Thomas TEILLET

Depositional patterns, diagenetic evolution, physical properties and quantitative seismic analysis of the early Miocene Yadana carbonate gas reservoir (Offshore Myanmar)

Soutenue le 08/11/2019 devant le jury :

Rapporteur : Michele Morsilli (Univ. Ferrara, Italie) — Professeur associé
Rapporteur : Anneleen Foubert (Univ. Fribourg, Suisse) — Professeur
Examinateur : Jérôme Fortin (ENS Paris) – Chargé de recherche
Examinateur : Pierre Rochette (CEREGE) — Professeur
Directeur : François Fournier (CEREGE) — Maitre de conférences
Directeur : Jean Borgomano : (CEREGE) — Professeur
Invité : Lucien Montaggioni (CEREGE) — Professeur émérite
Invité : Georg Warrlich (SHELL)
Invité : Emmanuelle Poli (TOTAL)

Key words: carbonates, depositional models, diagenesis, acoustic properties, seismic inversion

Bold ideas, unjustified anticipation, and speculative thought, are our only means for interpreting nature: our only organon, our only instrument, for grasping her. And we must hazard them to win our prize. Those among us who are unwilling to expose their ideas to the hazard of refutation do not take part in the scientific game.

Karl Popper — Logic of scientific discovery — 1934

La connaissance est une navigation dans un océan d'incertitudes à travers des archipels de certitudes — Edgar Morin — 1999

Knowledge is navigation in an ocean of uncertainties through archipelagos of certainties.
Edgar Morin — 1999

Remerciements

Tous mes remerciements aux membres du jury pour avoir accepté de considérer avec attention ce travail de thèse.

Tous mes remerciements à François Fournier et Jean Borgomano pour avoir fait de moi un chercheur et un géologue. Merci à tous les membres de l'équipe RRH du laboratoire du CEREGE. Merci à Lucien Montaggioni, Luanxiao Zhao, Marcelle BouDagher-Fadel, Juan-C Braga d'avoir contribué scientifiquement à la réalisation de ce travail.

Tous mes remerciements à Matthieu Pellerin et Fei Hong de la R&D Carbonates de TOTAL pour l'initiation de ce projet. Merci également au sein de TOTAL à Franck Gisquet, Caroline Planteblat, Fanny Bastide, Robert Boichard, Audrey Neau et tant d'autres…

Merci à Quentin Villeneuve, Jean Cochard, Irène Aubert, Thibaut Garin et l'ensemble des collègues de Saint-Charles. Merci à Cyprien Lanteaume, Anthony Tendil, Christophe Matonti, Alexandre Lettéron pour vos conseils. Merci à Naomie Peters et Camille Ardeois pour leurs aides sur le manuscrit.

Merci à mes amis marseillais et nantais.

Merci à ma famille.

Merci à ma femme, Aurélie.

Contents

Abstract

The Yadana carbonate buildup is a mature gas field, located in the Andaman Sea, offshore Myanmar and producing since 1998. The reservoir is an isolated carbonate platform, Oligocene to Miocene in age, sealed below 1200 m of siliciclastic sediments. Predicting hydrocarbon resources and water flows during the production has become a major challenge for such mature carbonate gas fields. The present PhD work involves the implementation of a methodology that allows the construction of a detailed reservoir architecture that accounts for significant heterogeneity. The work is multiscale and multidisciplinary, covering discipline such as sedimentology, diagenesis, geochemistry, rock physics, geophysics and based on a large and comprehensive dataset including, cores, well logs, petrophysical measurements, production data and seismic data.

First, three types of carbonate factory produced sediment on top of the platform under prevailing oligophotic to mesophotic conditions and periods of varying particulate organic matter supplies. The limited lateral changes in facies and the layer-cake depositional architecture inferred from well correlations, and the seismic expression suggest a deposition on a flat shelf. Carbonate production and accumulation were mainly controlled by light penetration, nutrient content and hydrodynamic conditions which are related to changes in monsoonal intensity, terrestrial runoff during the early Miocene in the Andaman Sea. Secondly, with an average porosity of 28%, the diagenesis is an important controlling factor of the reservoir properties. Mud-supported, coral-rich sediments record significant early marine dissolution of aragonite and early lithification of the matrix and a major decrease in porosity (up to10%) below the gas-water contact suggests a major phase of porosity evolution during and/or after the hydrocarbon emplacement. By modifying drastically porosity and pore networks, the diagenesis largely controls the acoustic architecture and seismic expression of the reservoir. The well-to-seismic tie allowed to precisely evidencing the origin of the main seismic reflectors. They may form, within the gas zone, at the boundary between two diagenetic/acoustic units or result from the interference between reflection at the base and top of such intervals. Early marine lithification of coral-rich intervals generates high amplitude and continuous reflectors and a stratigraphy-cross-cutting reflector forming at a major and laterally continuous shift in porosity relates differential diagenetic evolution between the gas and the water zones. Finally, because the scattering of the elastic properties at a given porosity in carbonate is mainly relative to pore type variations, a rock physics inversion scheme based on DEM approaches

(Differential Effective Medium modeling; Xu and Payne 2009) has been developed to quantify the pore type effect from the well log and the seismic elastic properties. After the calibration of the method to the real pore type geometry from rock data, the inversion is performed (upscaling) on the 3D seismic data to map the geobodies relative to pore type variations. This approach allows a relevant prediction of geological seismic scale heterogeneity impacting for example the fluid flows and the water rises in the reservoir during the production.

Providing a robust framework for the characterization of the Yadana gas reservoir, the thesis gives further insights into the understanding of geological and environmental factors controlling Cenozoic isolated carbonate systems in South East Asia. This work highlights the interdependence existing between geology and seismic imaging and demonstrates that an integrated geological/geophysical characterization of carbonate reservoirs are essential for both the exploration and the production [illegible] resources.

Résumé

La plateforme carbonatée de Yadana est le réservoir principal d'un champ de gaz en Mer d'Andaman, au large des côtes Birmanes produisant depuis 1998. Le réservoir est d'âge Oligocène-Miocène et est scellé par 1200 m de sédiments silicoclastiques. Prédire les ressources en hydrocarbure et les mouvements des fluides durant la production est un challenge majeur pour ce champ devenu mature. Le présent travail de thèse met en place une méthodologie aboutissant à la construction détaillée de l'architecture du réservoir. Ce travail est multi-échelle, intégratif, multidisciplinaire couvrant des domaines tels que la sédimentologie, la diagenèse, la géochimie, la physique des roches, la géophysique et se base sur un large et complet jeu de données incluant des carottes, des diagraphies, des mesures petrophysiques, des données de production ainsi que des données de sismique 3D.

D'un point de vue sédimentologique, trois types d'usines à carbonates ont été identifiés, produisant les sédiments au sommet de la plateforme dans des conditions oligophotiques à mésophotiques. Les faibles modifications latérales de facies et l'architecture de dépôt en couches stratifiées déduite des corrélations de puits et de l'imagerie sismique suggèrent un dépôt sur un haut-fond à faible relief. La production et l'accumulation des carbonates étaient, au début du Miocène principalement contrôlé par la pénétration de la lumière, la teneur en éléments nutritifs et les conditions hydrodynamiques elles-mêmes liées d'intensité de la mousson, aux apports terrigènes et à l'activité des courants d'upwelling en mer d'Andaman.

Avec une porosité moyenne de 28%, la diagenèse est un facteur de contrôle important des propriétés réservoir. Les sédiments riches en coraux enregistrent une dissolution marine de l'aragonite ainsi qu'une lithification précoce de la matrice. L'analyse géochimique suggère que le hiatus de dépôt au sommet de la plateforme est lié à un ennoiement de la plate-forme. La diminution importante de la porosité (jusqu'à 10%) en dessous du contact gaz-eau suggère une phase majeure d'évolution de la porosité pendant et/ou après la mise en place des hydrocarbures. En modifiant considérablement la porosité et le réseau poreux, la diagenèse contrôle en grande partie l'architecture acoustique et sismique du réservoir. La calibration puits sismique a permis de mettre en évidence l'origine des réflecteurs sismiques. Ils se forment ainsi, dans la zone à gaz, à la limite entre deux unités diagénétiques ou résultent d'interférences entre les réflexions de la base et du sommet de ces intervalles. La lithification marine précoce des intervalles à coraux génère des réflecteurs de fortes amplitudes, continus, et assimilables à des lignes-temps

chronostratigraphiques. En revanche, un réflecteur diachrone, recoupant la stratigraphie, est généré au niveau d'un contraste de porosité au voisinage du contact eau-hydrocarbure. Enfin, une méthode d'inversion pétrophysique basée sur une approche DEM (*Differential Effective Medium theory*) a été développée et appliquée sur les données de sismique 3D. Cette approche a permis de prédire de manière pertinente les hétérogénéités géologiques ayant une incidence sur les écoulements de fluide et la montée du niveau d'eau dans le réservoir.

Fournissant un cadre géologique robuste à la caractérisation du réservoir de Yadana, la présente thèse apporte également des informations supplémentaires sur la compréhension des facteurs géologiques et environnementaux contrôlant les systèmes de carbonates isolés cénozoïques en Asie du Sud-Est. Ce travail met en évidence l'interdépendance existante entre la géologie et l'imagerie sismique et démontre que les caractérisations paléoenvironnementale et diagénétique sont essentielles à la fois en phase d'exploration, mais aussi en phase d'évaluation et de production d'hydrocarbures.

I. Introduction

1.1 Rationale

Carbonate reservoirs hold more than 50% of oil and gas reserves worldwide (Akbar et al., 2000; Roehl and Choquette, 1985). However, these reservoirs are complex, characterized by heterogeneities at all scales and physical properties are difficult to predict spatially. Heterogeneities in carbonates may be related to interactions between several processes such as diagenetic transformations or structural deformations. Compared to clastic sediments resulting from physical depositional processes, carbonates are mainly produced by the living within a large range of environmental conditions. In addition to controlling factors such as subsidence, eustasy and transport, the variability in terms of living factors (e.g., light, nutrient, initial topography, temperatures) are directly responsible for the complexity of carbonates at all scale of study and directly controlled the stratigraphic architecture of the carbonate accumulation (Hallock and Schlager, 1986; Pomar, 2001; Halfar et al., 2004;).

Additionally to deposition-related heterogeneities, transformations of carbonate sediment by physical and chemical (diagenesis) processes introduce additional heterogeneities. Diagenesis has the effect of modifying initial mineralogy, porosity of the rock and consequently have an important impact on petrophysical, mechanical and elastic behavior of carbonate rock. Diagenetic processes, such as cementation, dissolution, neomorphism, and compaction can occur in various types of diagenetic environments and at various stages of sediment evolution through times, which increase the difficulty to predict the spatial variations of reservoir properties in carbonates (Bathurst, 1974; Friedman, 1998, 1964; Saller and Moore, 1989; Tucker and Wright, 1990).

In this context, pore types in carbonate account for complex permeability-porosity and velocity-porosity relationships. It implies a major challenge for geoscientists to quantitatively estimate their influence on reservoir and acoustic properties. For example, in a purely calcitic limestone, the complexity of pore types such as moldic, vuggy, interparticle, intraparticle, crack and others may affect drastically permeability and seismic velocities at a given porosity (e.g., Anselmetti et al., 1997; Fournier and Borgomano, 2007). Thus, in Middle East carbonate reservoir Weger et al., 2009 show that at a given porosity of 25%, permeability variation ranges within four orders of magnitude, due to pore structure variations. In the same way, for a porosity of 25% in a purely calcitic limestone, a wide range of velocity of around 2000m/s is related to pore type variability (Eberli et al., 2003). Consequently, in exploration where data are often scarce and punctual, an unfortunate reality is that hydrocarbon resources in carbonates reservoirs are difficult to quantify and the recovery is usually low. Thus to match well heterogeneities to spatial reservoir scale heterogeneities, the prediction of the 3D distribution of reservoir properties requires therefore 1) to make the link between geological processes and properties (porosity, permeability, acoustic velocities) at various scales (micron scale to reservoir scale) and 2) to integrate and take benefits of both quantitative (seismic, porosity, permeability, acoustic velocities) and qualitative data (depositional facies, diagenetic features…). To carry out such links, two approaches are classically used in oil industry:

- ***From geology to geophysics (direct path)*****:** Geology gives critical information relative to the natural processes generating reservoir properties. For example, by the paleo-environmental analysis and the stratigraphic work, geoscientists deduce effects of natural processes on the stratigraphic architecture of carbonate systems and help to understand the spatial distribution of the reservoir properties only by knowing the rock at punctual localization (cores, cuttings…). The purpose here is to propose geological models which are consistent to rock data and seismic observations which honor the current knowledge on geological processes involving the production and the accumulation of carbonate sediments. For example, acoustic models may derive from stratigraphic forward models after conversion of depositional facies into rock properties (Lanteaume et al., 2018). By issuing strong geological hypotheses (*a priori*), geological approaches are the angular basis for many numerical modeling processes.

- ***From the geophysics to the geology (inverse path):*** directly related to innovation in seismic acquisitions, quantitative seismic data gives critical information to spatially estimates the distribution of facies and/or reservoir properties (Burgess et al., 2013; Eberli et al., 2003; Fournier and Borgomano, 2007; Rankey et al., 2019). In geophysics, inverse problems have been studied extensively and consists in determining causes knowing effects (e.g. Bard, 1974; Mendel, 1983; Tarantola, 2005). Concretely, aims of geophysical and petrophysical inversion methods consist to estimate (deconvolve) the subsurface elastic properties (density, wave velocity) from seismic measurements by using probabilistic methods and/or rock physics models (Buland et al., 2008; Duijndam, 1988; Grana, 2017; Grana and Della Rossa, 2010). In other words, the large amount of information contained in seismic measurements is used to spatially characterize and quantify the distribution of reservoir properties.

Both work approaches are classically developed in industry and require the intervention of many experts of varied disciplines (e.g., sedimentologist, stratigrapher, structuralist, petrophysicist, geophysicist and modeler). However, facing the increasing specialization tends to isolate the experts in their own complexities and preventing to integrate multi-scale analyses of the reservoir heterogeneties. The communication between disciplines is therefore needed and integrative approaches became essential to enhance efficiency of hydrocarbon resources exploration, characterization and production studies.

From the geoscientist's point of view, paleo-environmental study is paramount to understand the stratigraphic architecture and the layering of carbonate reservoir. Unfortunately, because of the subjective and purely qualitative nature of observations, and of many bias in the use of actualism in paleoenvironmental reconstructions, this type of study is difficult to be confidently integrated in within a complete direct or inverse workflow. In the same way, geoscientists must be perfectly aware of their own subjectivity when interpreting seismic data since there is certainly no single correspondence between a seismic image and geology (Bond et al., 2007; Rankey and Mitchell, 2003). On the other hand, from the geophysicist and the petrophysicist point of view, who are facing huge amounts of digital data, it is important to take into consideration the diversity of data in terms of scale, physical nature, uncertainties and most of all relevance for the study. Indeed, believing that quantification can replace judgment and personal experience and that objectivity of numbers reinforces the credibility of the results is illusory. Qualitative, naturalistic tools must be considered as a powerful tool bringing consistency and meaning to a complex set of diverse and varied data.

As a consequence, when considering the increasingly complex problems in Industry and Science, it becomes essential to develop integrative and multidisciplinary approaches which bridge gaps between disciplines. This is one of the main goals of the PhD thesis.

1.2 Scope of the thesis

The present thesis proposes an integrated geological and geophysical approach in order to characterize the carbonate reservoir of Yadana, which represents a major gas field in Southeast Asia (offshore Myanmar). This is a multi-scale and multidisciplinary approach integrating disciplines such as sedimentology, diagenesis, geochemistry, rock physics and geophysics (Fig. 1-1) and based on pre-existing and new quantitative data from seismic, and wells as well as qualitative data from naturalistic approaches.

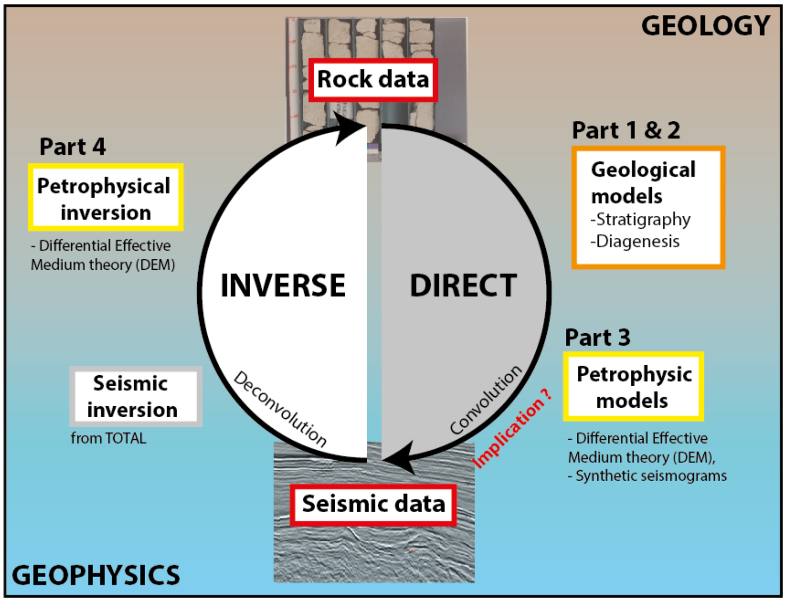

Figure 1-1: Workflow of the thesis integrating geological and geophysical paths.

From an industrial point of view, the ultimate goal is to enhance the prediction and the recovery of hydrocarbon resources and to improve the development strategies of this mature reservoir. The present thesis gives keys to understand multiscale geological heterogeneities (e.g., pore type variability, stratigraphic architecture…) in order to propose inputs for the optimization of numerical predictive models (deposition model, facies maps, well correlation, diagenetic models…). Another aim is also to highlight the uncertain and complex relationships between geology and geophysics. In this case, the question is to know how far we can go in the qualitative and quantitative interpretation of 3D seismic data.

From a scientific point of view, the reservoir of Yadana is an exceptional case study for Cenozoic tropical carbonate systems from Southeast Asia.

The first fundamental question is related to the sedimentology and the stratigraphy of the isolated carbonate buildup of Yadana. The carbonate rocks of Yadana are original because they are composed of sediments coming from a carbonate factory developing under the oligo-mesophotic zone. The question is to explain the deposition of these carbonates dominated by red algae and foraminifera in tropical regions generally the localization of euphotic carbonate factories (Pomar, 2001; Wilson, 2008a). Thus, the point is to understand the controlling factors (e.g., light penetration, nutrient supply, hydrodynamic energy…) inducing the deposition and the accumulation of carbonates in the Andaman Sea during the lower Miocene. Having hypotheses on controlling factors provide better predictions of lateral distribution of facies and stratigraphic heterogeneities. In other word, in a region close to a major river (Irrawady River), what was the role of terrestrial runoff into the deposition of carbonate sediments? What were the tectonic activity and the paleo-climatological conditions in this region during the early Miocene? Thus, through a detailed analysis of cores and seismic data, our study aims at establishing a robust depositional model and allows us to question the previous interpretations realized on the Yadana system that suggests the occurrence of a reef barrier and lagoonal facies (Paumard 2017).

Secondly, scientific issues concerning diagnesis consists to determinate the temporal and the spatial evolution of the porosity in the carbonate buildup of Yadana. This work is multiscale, first on the micro-scale, by highlighting on SEM the dissolution phases (early and/or late) that can modify the morphology of micritic grains, and at seismic scale by identifying the major subaerial emersion surfaces as well as the potential periods of karstification. With a chalky and very porous aspect of cores, the reservoir rocks of Yadana appear clearly dominated by microporosity. However, microporous reservoirs are complex and the origins of microporosity (early, late, meteoric diagenesis?) are still the subject of many studies (Budd, 1997; Lambert et al., 2006; Periere, 2011; Saller and Moore, 1989; Volery et al., 2010). So, in the case of Yadana, the objective is to establish the parasequence of the reservoir, to identify the main diagenetic features and the origin of the microporosity which strongly control the reservoir properties.

Then, by the use of rock physics, the thesis intends to clarify the physical link between the geology (sedimentology, stratigraphy and diagenesis) and the seismic imaging inside carbonate reservoir. Here the goal is to identify the physical factors controlling the acoustic properties in a carbonate reservoir at the logging and the seismic scale (e.g., fluids, mineralogy, porosity, porous type). So, what is the acoustic signature of oligo-mesophotic carbonates and is it really different from that of euphotic carbonates? Likewise, on the seismic scale, what is the geological significance of seismic reflectors? Can we systematically give a chronostratigraphic significance value to all the seismic reflectors in a carbonate reservoir? Finally, in the case of a mature reservoir as Yadana, we use new production data as the 4D seismic as a tool for qualitative interpretation and we show that 4D anomalies inside the reservoir can provide additional information about geological heterogeneities and their impact on the dynamic behavior of the reservoir during production.

In the last part of the thesis, as pore type is considered to be an important geological parameter to significantly control permeability, acoustic properties and seismic response of carbonate reservoirs, we develop an innovation petrophysical inversion method based on rock physics modeling (Differential Effective Medium theory; DEM) able to quantify pore type at the seismic scale. In this way, the seismic 3D data are quantitatively interpreted and the method led to the detection and the identification of seismic scale heterogeneities.

1.3 Yadana reservoir

The thesis focused on the carbonate reservoir of Yadana, located offshore Myanmar. The Andaman Sea (Moattama region) is a prolific region in terms of hydrocarbon resources (Racey and Ridd, 2015; Wilson, 2008b). In the northern part of the Sea, the Yadana Field is the main gas field.

Discovered in 1983 by MOC, this carbonate reservoir corresponds to an isolated carbonate platform (Late-Oligocene to Early Miocene) located at the top of a volcanic arc and sealed by more than 1000 m of clastic sediments. In July 1992, the French company TOTAL signed a contract with the State (Myanmar) company MOGE for blocks including the Yadana Field (M-5 and M6 blocks). The partnership successfully drilled four appraisal wells in 1993 (renamed here, WELL-1, WELL-2, WELL-3 and WELL-4). With an average porosity of 28% for an average permeability of 200mD, the Yadana field appeared to be a high-quality reservoir. In 1993 a first 3D seismic survey was acquired. The field has been producing gas since 1998, from 12 producer wells. The gas field extension is 65 km^2 with a gas column of 124 m of thickness. The production is mainly exported to Thailand via an offshore pipeline of 350 km and a 63 km-long onshore line to the Thai border (Min Aung, 2014). With recoverable resources of 6.05 to 6.41 TCF (Maw Win, 2011; Min Aung, 2014; Racey and Ridd, 2015), the production is estimated to 30 years (ending 2028).

More recently, in 2018 after 20 years of production new issues appeared for this mature field such as the origin and prediction of the water movement in the reservoir during gas production and the reduction of uncertainties for the ultimate recovery calculation. As for the exploration stage, the geological understanding of the field is essential during the development of the field. Coupled with a comprehensive dataset from 30 years of geological and geophysical studies, the analysis of seismic 4D effect is also a crucial issue in understanding the impact of geological heterogeneities on ultimate recovery and make decisions on further development of the gas field.

1.4 Thesis outline

The first chapter of the thesis discusses the factors controlling the deposition of the carbonate sediment of Yadana (e.g., light, nutrient content, nature of the substratum, temperature, water energy…). This part is relative to the detailed sedimentological analysis of cores and thin sections and integrates a biostratigraphic study on large benthic and planktonic foraminifera. From an industrial point of view, this part aims to characterize the sedimentary heterogeneities and to propose conceptual models of facies distribution.

Chapter 2 focuses on the diagenetic processes and aims at providing a parasequence and understanding the temporal and spatial evolution of the porosity within the reservoir. The study is mainly based on the analysis of petrographic data from rocks (cores, thin sections, SEM), geochemistry (strontium, carbon and oxygen stable isotopes, trace elements), permeability/porosity measurements. In this chapter, the diagenetic features are positioned in a chronological framework and interpreted in terms of diagenetic environments and processes.

The chapter 3 aims at linking the naturalistic approaches (Chapters 1 and 2) to petrophysics and geophysics. This work is based on the analysis of conventional logs, laboratory measurements (MICP, compressibility, XRD ...) and seismic data (3D, 4D). The chapter focuses the geological significance of seismic reflectors by using rock physics and synthetic seismic models. This part questions the chronostratigraphic value of seismic reflectors in carbonate systems and makes it possible to quantify the physical factors controlling elastic architecture of a carbonate reservoir (porosity, fluids, typical pores, mineralogy). Such an approach, coupled with the interpretation of 4D seismic, has been also implemented to detect and characterize in 3D major diagenetic heterogeneities which may significantly impact flows during production.

Finally, because pore type is a key factor controlling both the permeability and the elastic response of carbonate rocks, and in order to go further in the quantitative seismic reservoir characterization, chapter 4 proposes an innovative inversion method of 3D seismic data using Differential Effective Medium theory (Berryman, 1995; Xu and Payne, 2009). In this chapter the steps are the following: (1) qualitative and quantitative characterization of pore types of rock samples (2) Development and application of the inversion method to predict geophysical pore types at the well-log scale (1D). (3) Inversion of 3D seismic data to obtain the spatial distribution of geophysical pore types. (4) Interpreting such a spatial distribution in terms of diagenetic heterogeneities and/or reservoir unit. In this section, particular attention is paid to the calibration of the inversion results with respect to pore types observed on the rock data.

II. Sedimentology

Development patterns of an isolated oligo-mesophotic carbonate buildup, early Miocene, Yadana field, offshore Myanmar[1]

Thomas Teillet [1,2], François Fournier [1], Lucien F. Montaggioni [1], Marcelle BouDagher-Fadel [3], Jean Borgomano [1], Juan C. Braga [4], Quentin Villeneuve [1], Fei Hong [2]

[1] : Aix-Marseille Université, CNRS, IRD, CEREGE, UM34, 3 Place Victor Hugo, Case 67, 13331 Marseille cedex 03, France[2] : TOTAL, CSTJF, Avenue Larribau, 64000 Pau, France
[2] : TOTAL, CSTJF, Avenue Larribau, 64018 Pau Cedex, France
[3] : Postgraduate Unit of Micropaleontology, Department of Geological Sciences, University College London, Gower Street, London WC1E 6BT, U.K.
[4] : Departamento de Estratigrafía y Paleontología, Universidad de Granada, Campus Fuente Nueva 18002 Granada, Spain

Abstract: The development history of an oligo-mesophotic, Lower Miocene, isolated carbonate system (>160 m in thickness), forming the uppermost part of the Oligo-Miocene Yadana buildup (northern Andaman Sea), has been evidenced from the integration of sedimentological core studies from 4 wells (cumulated core length: 343 m), well correlations, seismic interpretation and analysis of the ecological requirements of the main skeletal components. Three types of carbonate factory operated on the top of the platform, depending on water depth, turbidity and nutrient levels: (1) a scleractinian carbonate factory developing under mesophotic conditions during periods of high particulate organic matter supplies, (2) an echinodermal carbonate factory occupying dysphotic to aphotic area of the platform coevally with the scleractinian carbonate factory, (3) a large benthic foraminiferal-coralline algal carbonate factories prevailing under oligo-mesophotic and oligo-mesotrophic conditions. The limited lateral changes in facies between wells, together with the seismic expression of the Yadana buildup, suggest a deposition on a flat shelf. Carbonate production and accumulation on the Yadana platform were

---

[1] Published in Marine and Petroleum Geology : https://doi.org/10.1016/j.marpetgeo.2019.08.039

mainly controlled by light penetration, nutrient content and hydrodynamic conditions. The scleractinian-rich facies resulted from transport of coral pieces developing on mesophotic environments (mounds?) and deposition in deeper, low light and mud-rich environments characterized by abundant communities of suspension feeders such as ophiuroids. Changes in monsoonal intensity, terrestrial runoff from the Irrawaddy River, upwelling currents and internal wave activity during the early Miocene are likely responsible for significant variations in water turbidity and nutrient concentration in the Andaman Sea, thus promoting the development of an oligo-mesophotic, incipiently drowned platform.

2.1 Introduction

Prolific sedimentological literature regarding tropical Cenozoic carbonate systems from Southeast Asia reveals a great diversity of carbonate factories in relation to a wide range of global and local environmental and climatic parameters such as temperature, nutrient content, light penetration and terrigenous inputs (e.g., Wilson, 2002; Wilson and Vecsei, 2005; Madden and Wilson, 2013; Nowak et al., 2013; Santodomingo et al., 2015). Usually, the concept of "tropical carbonate factory" is associated with a dominantly biological carbonate production in warm, well-illuminated, oligotrophic, and very shallow waters (e.g., Hallock and Glenn, 1986; Schlager, 2000, 2003; Pomar and Hallock, 2008). In such settings, carbonates are typically produced by various photosynthetic autotrophs including calcareous green and red algae, and by organisms with photosynthetic symbionts such as zooxanthellate coral and large benthic foraminifera, thus resulting in the so-called photozoan sediment association (James, 1997). These humid tropical environments that are generally considered unfavorable to the photozoan carbonate production (e.g., Wilson, 2002, 2008). Many modern and Cenozoic equatorial, Southeast Asian carbonate systems are associated with upwelling and/or terrestrial runoff, high turbidity and cool waters (Madden and Wilson, 2013). In such settings, nutrient-reliant biota often outweighs light dependent autotrophs (Tomascik et al., 2000; Wilson and Vecsei, 2005). At a regional scale, the combined effect of high nutrient supplies and low light penetration promotes the development of large scale isolated and/or land-attached oligophotic (sensu Pomar, 2001)

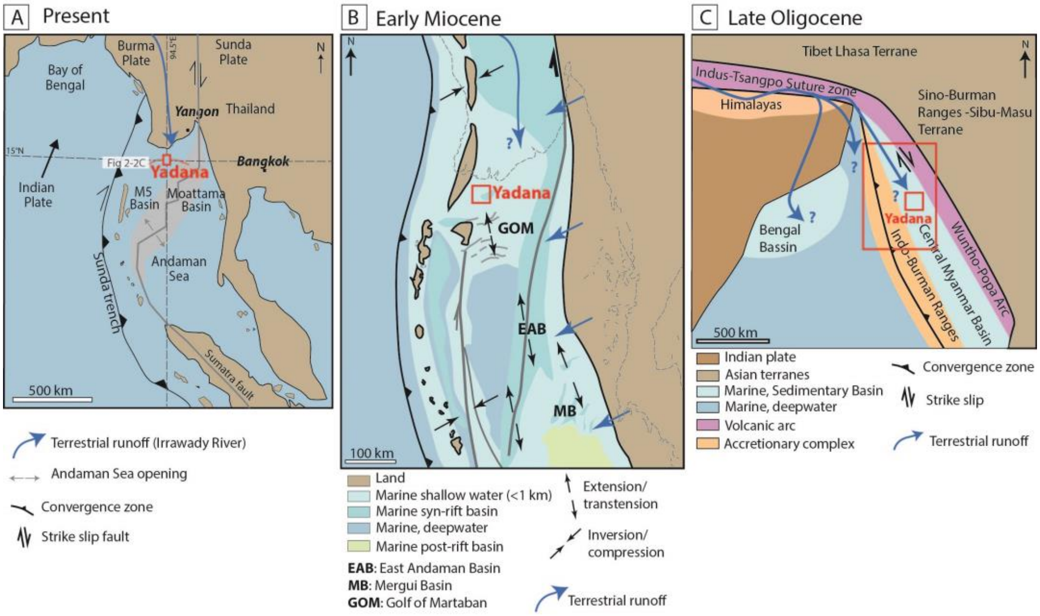

Figure 2-1 : (A) Location map of the Yadana field and tectonic setting of the Andaman Sea (after Curray2005); (B) and (C) Paleogeography of the Andaman Sea and environmental setting of the Yadana platform during the early Miocene (B) and late Oligocene (B) (modified from Licht2016; Morley 2015; Morley 2017).

platforms such as the modern Paternoster Platform (Burollet et al., 1986), Spermonde Platform (Renema and Troelstra, 2001), Kalukalukung Banks (Roberts and Phipps, 1988) and the Cenozoic Berai (Saller and Vijaya, 2002), Tonasa (Wilson and Bosence, 1996), Melinau platforms (Adams, 1965) and foreslope of Hawaiian Islands (Pyle et al., 2016). However in such carbonate platforms, even though oligophotic carbonate production dominates, reefal and/or non-reefal euphotic carbonate factories are coexisting (Wilson and Vecsei, 2005). The reconstruction of depositional models for ancient, coral-rich sedimentary systems has become a major issue in carbonate sedimentology since significant oligo-mesophotic scleractinian carbonate factories have been evidenced in modern and Cenozoic environments (e.g., Lesser et al., 2009; Kahng et al. 2010; Morsilli et al. 2012), thus questioning the common use of “tropical carbonate factory” concepts in paleoenvironmental interpretations.

The late Oligo-early Miocene Yadana carbonate platform is located in the Andaman Sea, offshore Myanmar (Fig.2-1). Three-dimensional seismic interpretation of the Yadana gas-bearing carbonate reservoir revealed that towards the upper part of the Yadana limestone (Upper Burman Limestone) the platform is transitioning from an attached to an

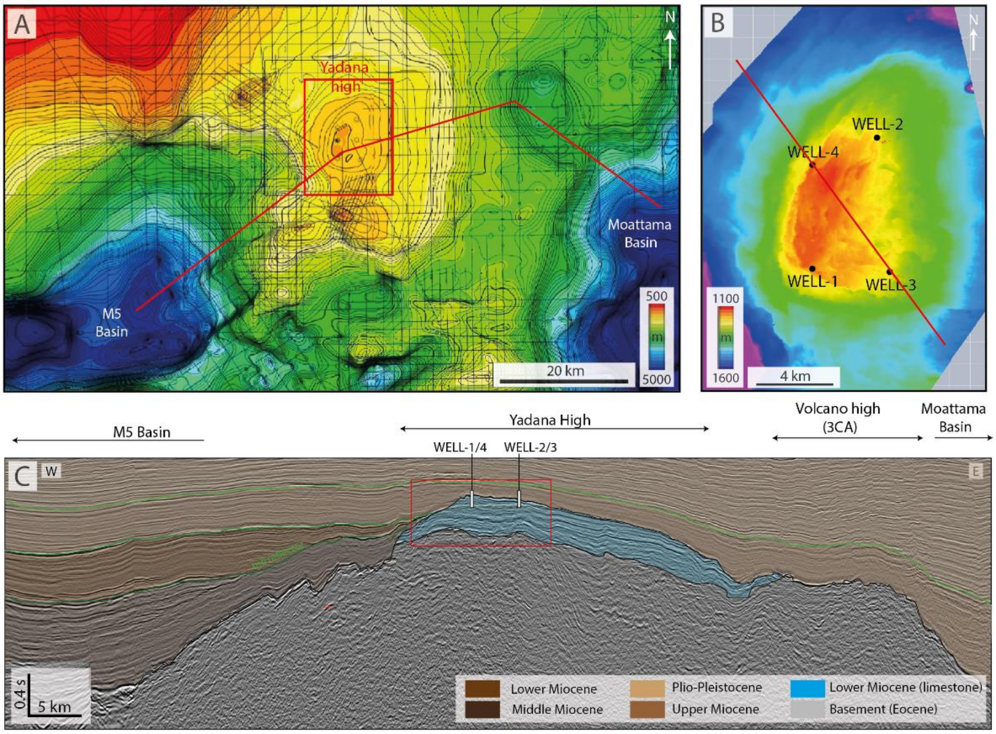

Figure 2-2 : Morphological and geophysical frame of the Yadana Field (A) Depth map of the top reservoir surface interpreted from 2D seismic data showing the Yadana High, the M5 and the Moattama basins. The red square represents the 3D seismic survey of the Yadana Field and the red line refers to the seismic profile (Fig. 2-2C). (B) 3D seismic survey of the Yadana Field, depth map of the top reservoir surface and well location. (C) Interpreted regional 2D seismic profile through the Yadana High (with location of projected WELL-1, WELL-2, WELL-3, WELL-4).

isolated configuration (Paumard et al., 2017). The analysis of seismic facies coupled with the use of modern analogues of tropical carbonate systems have led to interpret the Yadana buildup as an euphotic reef-rimmed carbonate platform (Paumard et al., 2017). The present study, on the basis of a detailed analysis of biological associations, sedimentological and diagenetic features from cores, aims at (1) revising the depositional model of the Upper Burman Limestone, previously established by Paumard et al. 2017, (2) assessing the impact of environmental factors such turbidity, light penetration, hydrodynamic energy and nutrient availability on carbonate production in tropical isolated carbonate platforms, (3) documenting the development of a coral-rich isolated carbonate system in mesophotic conditions, in Southeast Asia during the early Miocene and (4), linking changes in environmental conditions and carbonate production with the stratigraphic architecture of an isolated carbonate buildup with dominant oligo-mesophotic production. Such

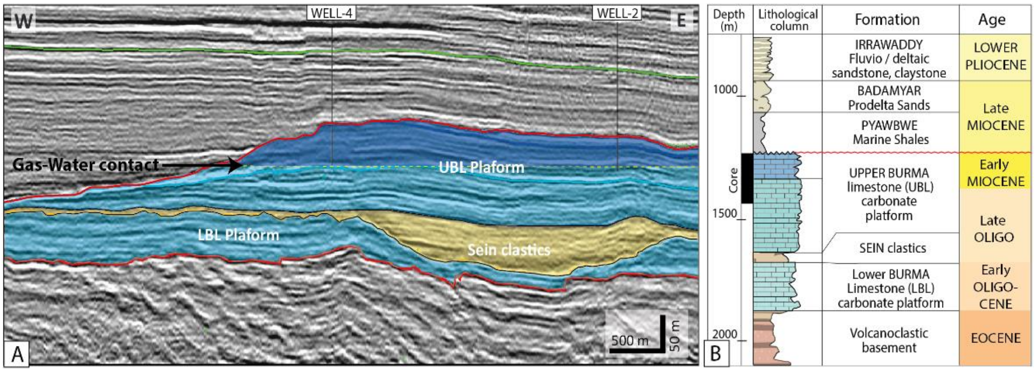

Figure 2-3 : Seismic architecture and stratigraphy of the Yadana carbonate platform (A) Interpreted 3D seismic profile (location on the Fig. 2-2B.) of the Yadana Field passing across the wells WELL-4 and WELL-2. The lithostratigraphic units and the gas water contact (yellow dotted lines) are shown (B). Lithostratigraphic column of the Yadana platform, name and age of the sedimentary units.

depositional models are also relevant in oil and gas industry since they may constrain the exploration targets and production strategies in carbonate settings with dominant oligo-mesophotic contributions.

2.2 Geological setting

During the Cenozoic, the regional geodynamic context strongly controlled the initiation, the development and the demise of Southeast Asian carbonate systems (Wilson and Hall, 2010). As a result of the oblique collision of the Indian-Australian plate beneath the Eurasian plate, the Sunda subduction zone formed during the early Eocene (Curray, 2005; Chakraborty and Khan, 2009), and induced the opening of the Andaman Sea as a back-arc basin. During the Oligocene to the early Miocene (Fig. 2-1), the Yadana carbonate buildup, 25 km to 30 km in size, developed at the top of a volcanic basement, located in the northern Andaman Sea (Racey, 2015). The volcanic basement has been interpreted as a volcanic arc separating the M5 fore-arc basin to the west from the Moattama back-arc basin to the east (Racey and Ridd, 2015) or alternatively as a volcanic ridge, created during the northward motion of the Indian plate above the Kerguelen island hotspot (Paumard et al. 2017) (Fig. 2-2).

Paumard et al. (2017) proposed a review of the stratigraphy and age of the Yadana carbonate platform based on a regional study integrating seismic and well data. The lowermost deposits from the Moattama Basin (Fig. 2-3) consists of Upper Eocene volcano-clastics sediments. The overlying Oligo-Miocene shallow-water carbonates may reach up to 700 m in thickness, and are subdivided into two distinct formations: the Lower Burman Limestone, and the Upper Burman Limestone. The Lower Burman Limestone, Chattian in age is composed of two distinct carbonate buildups separated by a SW-NE trending trough which is filled by the Sein Clastics Formation (late Chattian). The overlying Upper Burman Limestone has been interpreted as recording an upward transition from an attached platform to a single, reef-rimmed isolated carbonate buildup during the early Miocene. At the end of the Upper Burman Limestone deposition, a long-term depositional hiatus occurred from the early Miocene to the late Miocene. The Upper Burman Limestone carbonates are sealed by late Miocene (N16 planktonic zone) shales (Pyawbwe and Badamyar formations) from the Irrawaddy deltaic system. A major phase of eastward tilting of the Yadana platform, evidenced by seismic profiles (Fig. 2-2), occurred during the late Miocene (horizon M6: 8.2 Ma, after Paumard et al., 2017).

2.3 Material and Methods

Approximately 20 wells have penetrated the top of the Upper Burman Limestone. Four wells (WELL-1, WELL-2, WELL-3 and WELL-4), located in the western half of the buildup (Fig. 2-2B), have been selected in this study for a detailed sedimentological study, totalizing 343 m of cumulated length (WELL-1: 87.5 m, WELL-2: 84 m WELL-3: 59.5 m WELL-4: 112 m). The carbonate interval penetrated by core averages 160 meters.

Macroscopic core description and thin-section study under polarized-light microscopy provided the sedimentological framework for the present study. Around 700 thin sections were prepared from cores with an average spacing of 0.5 m and stained with red alizarin and potassium ferrocyanide. All thin sections were point counted on the basis of 300 points to quantify the bioclastic composition of the carbonates. Lithofacies have been defined based on sedimentary structures, depositional textures and biological composition identified from cores and thin sections. These lithofacies have been interpreted in terms of depositional environments by reference to modern and ancient analogues. The paleoenvironmental reconstructions have been constrained using light-dependent communities including coralline algae and large benthic foraminifera. Bathymetric zonation is based on the distinction between “euphotic” (maximal light intensity commonly associated with high wave energy), “mesophotic” (sufficient light for coral development,

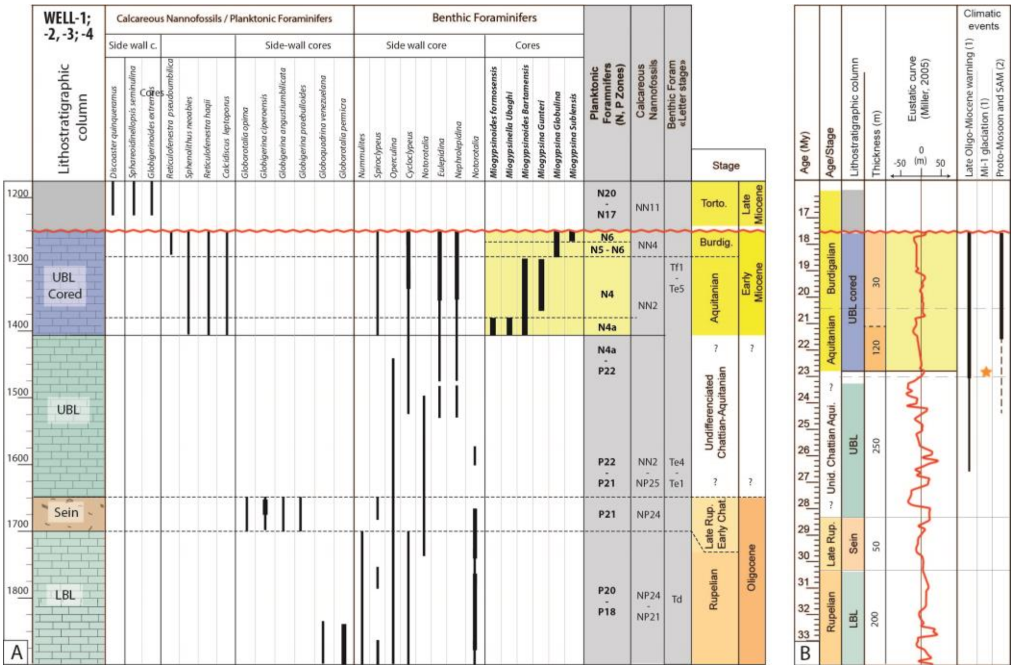

Figure 2-4 : Chronostratigraphic framework of the Yadana carbonate platform (A) based on planktonic and large benthic foraminifera from cores and side wall samples of the four wells (B) Chronostratigraphic framework of the Yadana field, eustacy (Miller, 2005) and global climatic events: (1) late Oligocene-early Miocene warming and Mi-1 glaciation (Holbourn, 2005), (2) intensity of Proto-monsoon and South Asian Monsoon (Betzler, 2016).

typically below normal wave base), “oligophotic” (sufficient light for coralline algae), and “dysphotic” (insufficient light for photosynthesis) and “aphotic” (Pomar, 2001).

The chronostratigraphic framework of the Yadana carbonate buildup has been revisited (Fig. 2.4) on the basis of: (1) a reappraisal of the available planktonic and benthic foraminiferal biostratigraphy, and (2) new taxonomic determinations of the benthic foraminiferal material from the studied Upper Burman Limestone cores (Fig. 2.5).

The benthic foraminiferal stratigraphy was based on the East Indian Letter Classification (Adams, 1970; BouDagher-Fadel, 1999; BouDagher-Fadel, 2015, 2018) and planktonic foraminiferal biostratigraphy on the zonation defined by Berggren et al. (1995) and modified by Wade et al. (2011), by using the time scale defined by Gradstein et al. (2012). The correlation framework between wells has been defined on the basis of: (1) biostratigraphic constraints, and (2) correlation of vertical changes in light penetration and trophic conditions.

The studied dataset includes 2D and 3D seismic surveys acquired by TOTAL. The 2D seismic profiles were acquired between 1993 and 1997 cover an area of ~14 200 km2.

The 3D seismic data were acquired in 2011, over an area of ~511 km2. The 3D volume is characterized by a bin spacing of 12.5 × 6.25 m and a trace sampling of 3 ms. The vertical resolution of the prestack time migrated data used in the present work is around 20 m within the carbonate reservoir. In addition to the gas water contact (GWC) that forms a well-identified flat spot, five seismic reflectors (TOP UBL, H9, H9A, H10B and H10), have been interpreted throughout the carbonate buildup from 3D seismic data.

2.4 Results

2.4.1 Biostratigraphy

The Upper Burman Limestone overlies the Sein siliciclastics of late Rupelian to early Chattian age as derived from the occurrence of *Paragloborotalia opima* (P20-P21). The age of the lower part of the UBL limestones (below the cored interval) is poorly constrained. The lowermost cored interval from the Upper Burman Limestone is early Aquitanian in age (N4a) as supported by the first co-occurrence of *Miogypsinella ubaghsi* (Fig 2.5) and *Miogypsinoides formosensis* (WELL-1, 1340.06 m). Above, the co-occurenceThe uppermost Upper Burman Limestone is recognized to be Burdigalian in age (N6) on the basis of the occurrence of *Miogypsina intermedia* (Fig 2.5), *Miogypsina globulina* and *Miogypsinoides dehaarti* (WELL-2 1272.23 m).

Calcareous nannofossils and planktonic foraminifera present in the shale overlying the UBL (*Discoaster quinqueramus*, *Sphaeroidinellopsis seminulina*, *Globigerinoides extremus*) are assigned to the Tortonian (N20-N17), thus suggesting a hiatus duration of approximatively 9 My at top of the Yadana platform (Burdigalian-Tortonian hiatus).

2.4.2 Lithofacies and paleo-environmental interpretations

Carbonate from the UBL interval are calcite-dominated limestones, with few partially dolomitized intervals. In decreasing order of abundance the main biological components observed on thin sections are: (1) non-geniculate coralline algae (42% of bioclasts on average; WELL-1=48%; WELL-2=41%; WELL-3=45%; WELL-4=33%), (2) larger benthic foraminifera (41% on average; WELL-1=38%; WELL-2=42%; WELL-3=41%; WELL-

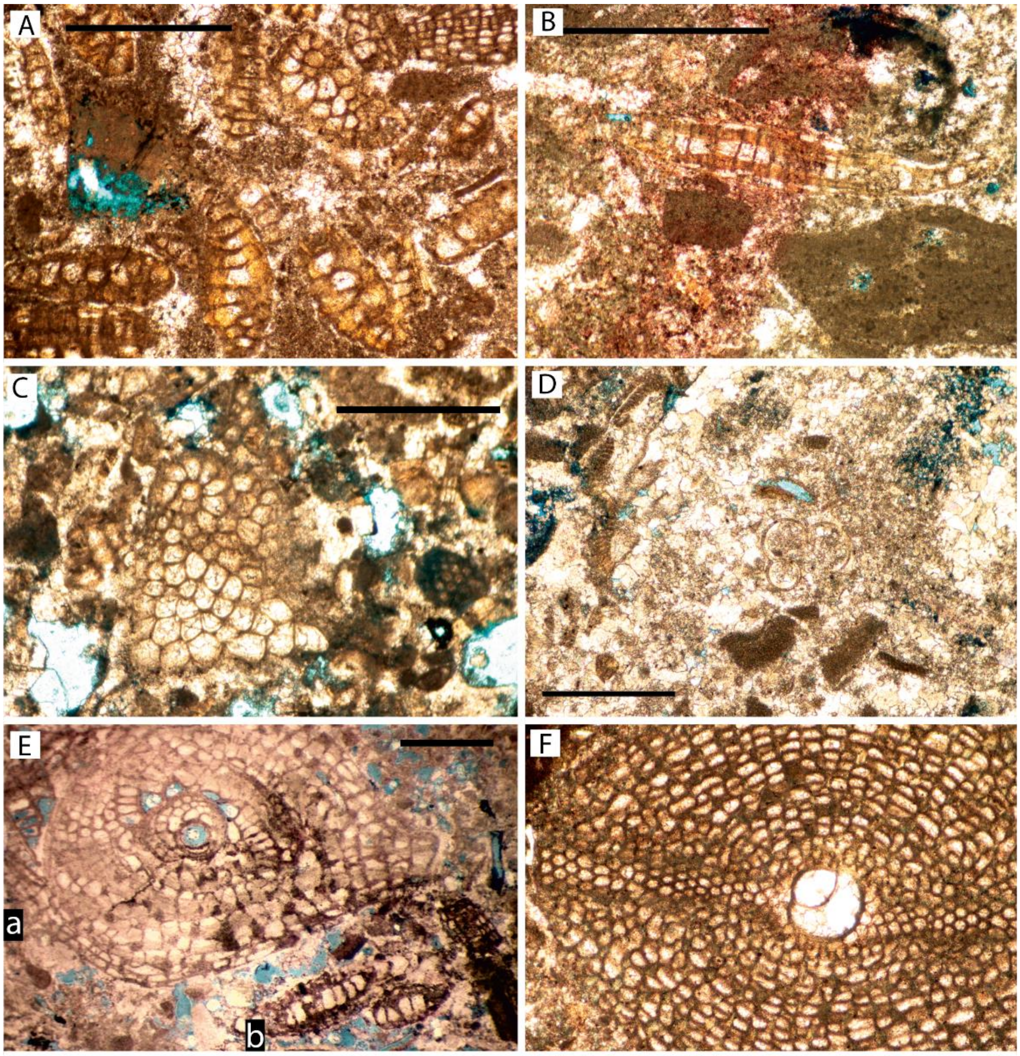

Figure 2-5 : Microphotographs of key large benthic foraminifera of the UBL formation. (A) WELL-2 1354, 95 mCD: *Miogypsinella ubaghsi* (Sin Hok, 1936). (B) WELL-3 1350, 24 mCD: *Miogypsina intermedia* (Drooger, 1952); (C) WELL-1 1254, 3 mCD: *Miogypsinoides bantamensis* (Tan Sin Hok, 1936). (D) WELL-2 1329, 22 mCD: *Globigerinoides primordius* (Blow and Banner, 1962), E) WELL-1 1243, 88 mCD: a - *Spiroclypeus tidoenganensis* (Van der Vlerk, 1925); b – *Miogypsina subiensis* (BouDagher-Fadel and Price, 2013). (F) WELL-1 1259, 50 mCD: *L. (Nephrolepidina) sumatrensis* (Brady, 1875). (Blow and Banner, 1962; Boudagher-Fadel and Price, 2013; Drooger, 1952; Tan Sin Hok, 1936; Van der vlerk, 1922).

4=41%) and (3) corals (16% on average; WELL-1=8%; WELL-2=20%; WELL-3=12%; WELL-4=25%). Subordinate components include echinoderms (5% on average), bryozoans, green algae and planktonic foraminifera. Five distinct lithofacies have been defined and interpreted in terms of depositional environments (Table 1):

LF1. Coralline algal floatstone to rudstone

The coralline algal floatstones to rudstones (Fig. 2-6 A-G) consist of spheroidal-ellipsoidal rhodoliths or pieces of branching coralline algae embedded within a coralline algal-foraminiferal wackestone to packstone matrix. The coralline algal association is composed of *Lithothamnion*, *Mesophyllum* and *Sporolithon*. Rhodoliths are heterometric, mostly with diameters ranging from 1 cm to 10 cm in cores and commonly displaying warty and branching growth forms. Loose pieces of branching and columnar (fruticose) coralline algae (particularly *Lithothamnion* and *Sporolithon*) may be dominant in some intervals. Loose and hooked *Mesophyllum* are present in very low amount. *Mastophoroids* are extremely rare or lacking. The foraminiferal assemblage is dominated by *Spiroclypeus tidoenganensis* and *Nephrolepidina sumatrensis,* with common occurrences of *Miogypsinoides, Miogypsinaand Heterostegina (Vlerkina).* Echinoderms, ectoprocts and planktonic foraminifera are occasional. *Sporolithon*. Rhodoliths are heterometric, mostly with diameters ranging from 1 cm to 10 cm in cores and commonly displaying warty and branching growth forms. Loose pieces of branching and columnar (fruticose) coralline algae (particularly *Lithothamnion* and *Sporolithon*) may be dominant in some intervals. Loose and hooked *Mesophyllum* are present in very low amount. Mastophoroids are extremely rare or lacking. The foraminiferal assemblage is dominated by *Spiroclypeus* tidoenganensis and *Nephrolepidina sumatrensis*, with common occurrences of *Miogypsinoides, Miogypsinaan Heterostegina (Vlerkina),* echinoderms, ectoprocts and planktonic foraminifera are occasional.

Interpretation: In LF1 facies, the coralline algal assemblage is dominated by the melobesioids *Lithothamnion*, *Mesophyllym* and *Sporolithon*. Such an assemblage is typical of lowlight environments, in oligo-mesophotic settings (Braga et al., 2010). In modern, tropical, low-turbidity environments, melobesioids have been shown to occur preferentially at water depths ranging from 30 m to 80 m (Adey, 1979; Braga and Aguirre, 2004). The co-occurrence of warty rhodoliths and pieces of branching coralline algae belonging to the same taxa may suggest that the isolated branches may derive from the fragmentation of branching rhodoliths during high-energy events (Bosence, 1983; Freiwald et al., 1994), such as storms, cyclones or internal waves. The foraminiferal assemblage dominated by large and

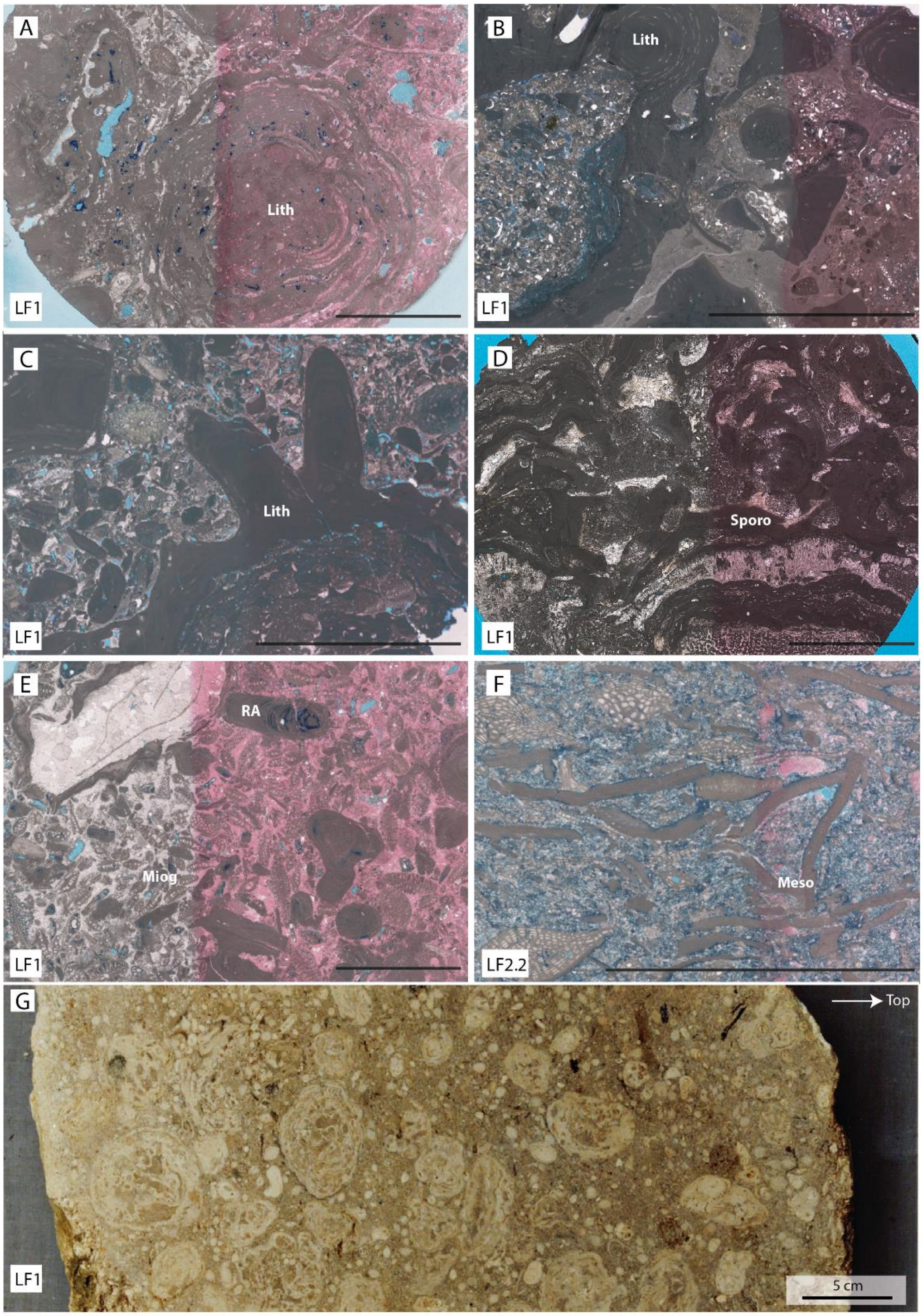
A
Lith
LF1
B
Lith
LF1
C
Lith
LF1
D
Sporo
LF1
E
RA
Miog
LF1
F
Meso
LF2.2
G
Top
LF1
5 cm

Figure 2-6 : Microphotographs (A—F) and core photograph (G) of coralline algal floatstones and rudstones (LF1): (A) WELL-3 1321.97 m: Coralline algal rudstone (LF1). Encrusting (rhodolith) and warty forms, possible *Lithothamnion* (Lith) with small conceptacles. (B) WELL-1 1251.25 m: Coralline algal floatstone (LF1). Branching *Lithothamnion* (Lith) with flat (and filled) conceptacles. *L. ramossissimum* type. (C) WELL-3 1323.40 m: Coralline algal floatstone (LF1) with a foraminiferal-red algal grainstone matrix. Encrusting and branching *Lithothamnion* (Lith) with flat conceptacles, L. ramossissimum type, (D) WELL-2 1262.68 m: Coralline algal floatstone (LF1). Abundant protuberant crusts of *Sporolithon* (Sporo), (E) WELL-3 1334.48 m: Coralline algal floatstone (LF1) with a foraminiferal grainstone matrix (LF1). Branching and encrusting forms of coralline algae (RA) associated with *Miogypsinoides* (Miog). (F) WELL-3 1340.90 m: Coralline algal with large benthic foraminiferal floatstone-wackestone (LF2.2). Laminar, loose *Mesophyllum* (Meso). (G) WELL-2 1345 m: Core picture of rhodolothic rudstone. Black bar length = 7 mm.

flat *Spiroclypeus* and Lepidocyclinids is typical of oligo-mesophotic environments, at water depths of 30 m or greater, but could live comfortably at 70 m depth (Hallock and Glenn, 1986; Noad, 2001). In contrast, benthic foraminifers like *Miogypsinoides*, *Miogypsina* and *Heterostegina (Vlerkina)* are common taxa in shallow-water, euphotic environments associated with seagrass beds (Fournier et al., 2004; BouDagher-Fadel, 2018; Hallock and Pomar, 2008; Maurizot et al., 2016) but were also reported from shallow mesophotic, mid-ramp environments (Bassi, 2005; Bassi et al., 2007; Rahmani et al., 2009). The mud-supported nature of LF1 suggests that the depositional environment was relatively sheltered or not permanently subject to wave action. As a consequence, the biological and textural features of LF1 facies likely reflect deposition in the shallowest part of the mesophotic zone, in an area located below the base of fair-weather wave action but experiencing episodic high-energy events.

LF2.1. Large benthic foraminiferal rudstone

The LF2.1 facies (Fig. 2-7A, B) consists of relatively thin (<1 m) accumulations of large benthic foraminifera, enriched in red algal fragments, with rare bryozoans and echinoderms which are typically interbedded within coralline algal floatstones (LF1). The intergranular spaces may be occupied by a peloidal grainstone matrix or occluded by sparry calcite cements. Large benthic foraminifera are usually centimetric in size (sometimes up to 2 cm) and most of them display broken edges. The foraminiferal assemblage is dominated by Lepidocyclina (Nephrolepidina) sumatrensis, L. (N.) oneatensis, and *Spiroclypeus*

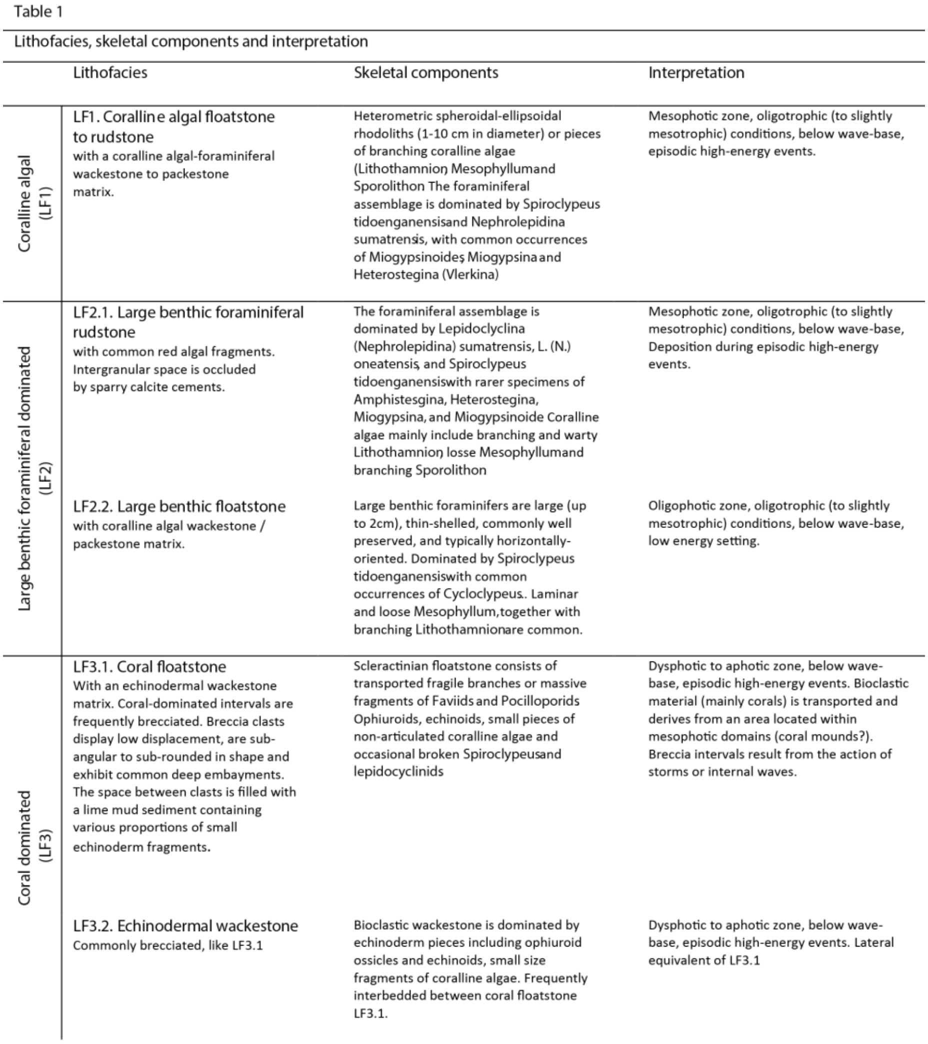

Table 1

Lithofacies, skeletal components and interpretation

	Lithofacies	Skeletal components	Interpretation
Coralline algal (LF1)	**LF1. Coralline algal floatstone to rudstone** with a coralline algal-foraminiferal wackestone to packestone matrix.	Heterometric spheroidal-ellipsoidal rhodoliths (1-10 cm in diameter) or pieces of branching coralline algae (Lithothamnion, Mesophyllum and Sporolithon The foraminiferal assemblage is dominated by Spiroclypeus tidoenganensis and Nephrolepidina sumatrensis, with common occurrences of Miogypsinoides, Miogypsina and Heterostegina (Vlerkina)	Mesophotic zone, oligotrophic (to slightly mesotrophic) conditions, below wave-base, episodic high-energy events.
Large benthic foraminiferal dominated (LF2)	**LF2.1. Large benthic foraminiferal rudstone** with common red algal fragments. Intergranular space is occluded by sparry calcite cements.	The foraminiferal assemblage is dominated by Lepidoclyclina (Nephrolepidina) sumatrensis, L. (N.) oneatensis, and Spiroclypeus tidoenganensis with rarer specimens of Amphistesgina, Heterostegina, Miogypsina, and Miogypsinoide Coralline algae mainly include branching and warty Lithothamnion, losse Mesophyllum and branching Sporolithon	Mesophotic zone, oligotrophic (to slightly mesotrophic) conditions, below wave-base, Deposition during episodic high-energy events.
	LF2.2. Large benthic floatstone with coralline algal wackestone / packestone matrix.	Large benthic foraminifers are large (up to 2cm), thin-shelled, commonly well preserved, and typically horizontally-oriented. Dominated by Spiroclypeus tidoenganensis with common occurrences of Cycloclypeus.. Laminar and loose Mesophyllum, together with branching Lithothamnion are common.	Oligophotic zone, oligotrophic (to slightly mesotrophic) conditions, below wave-base, low energy setting.
Coral dominated (LF3)	**LF3.1. Coral floatstone** With an echinodermal wackestone matrix. Coral-dominated intervals are frequently brecciated. Breccia clasts display low displacement, are sub-angular to sub-rounded in shape and exhibit common deep embayments. The space between clasts is filled with a lime mud sediment containing various proportions of small echinoderm fragments.	Scleractinian floatstone consists of transported fragile branches or massive fragments of Faviids and Pocilloporids Ophiuroids, echinoids, small pieces of non-articulated coralline algae and occasional broken Spiroclypeus and lepidocyclinids	Dysphotic to aphotic zone, below wave-base, episodic high-energy events. Bioclastic material (mainly corals) is transported and derives from an area located within mesophotic domains (coral mounds?). Breccia intervals result from the action of storms or internal waves.
	LF3.2. Echinodermal wackestone Commonly brecciated, like LF3.1	Bioclastic wackestone is dominated by echinoderm pieces including ophiuroid ossicles and echinoids, small size fragments of coralline algae. Frequently interbedded between coral floatstone LF3.1.	Dysphotic to aphotic zone, below wave-base, episodic high-energy events. Lateral equivalent of LF3.1

Table 1 : Lithofacies classification and paleoenvironmental interpretations of the UBL formation based on the main skeletal components and sedimentological attributes.

tidoenganensis with rarer specimens of *Amphistegina, Heterostegina, Miogyspina*, and *Miogypsinoides.* Coralline algae mainly include branching and encrusting, warty *Lithothamnion*, laminated, loose *Mesophyllum* and branching *Sporolithon*. The LF2.1 rudstone intervals are characterized by rapid (cm-scale) vertical and lateral changes of orientation of large benthic foraminifera (Fig. 2-7B).

Interpretation: The foraminiferal assemblage, dominated by *Nephrolepidina* and *Spiroclypeus* as well as the coralline algal association (*Lithothamnion-Mesophyllum-Sporolithon*) suggest that carbonate grains have been produced within the mesophotic zone (Braga et al., 2010). In addition, the lack or scarcity of mud matrix in intergranular spaces, with the poor state of preservation of large benthic foraminifera, suggest frequent turbulence, strong enough to winnow mud and to rework the large foraminiferal tests. The rare occurrence of *Amphistegina*, *Heterostegina*, *Miogyspina*, and *Miogypsinoides*, compared to LF1, may reflect that the source of sediment of the rudstones is located at greater depths within the mesophotic zone but may also result from preferential sorting of low-density bioclasts such as large and flat lepidocyclinids and *Spiroclypeus* (Jorry et al., 2006; Pomar et al., 2012; 2015).The low intergranular matrix content and the predominantly non-oriented nature of the large benthic foraminifera in LF2.1 suggest a bedload transportation and mass deposition during high-energy events such as storms or internal waves. In addition, the occurrence of LF2.1 rudstone beds within mesophotic LF1 coralline algal and foraminiferal floatstones and the mesophotic affinity of the biotic assemblage in LF2.1 also indicates that during such high-energy events the sediment was remobilized and then redeposited on top of the Yadana shelf in a similar range of water depth.

LF2.2. Large benthic foraminiferal floatstone

LF2.2 lithofacies consists of large benthic foraminiferal floatstone with a coralline algal wackestone/packstone matrix (Fig. 2-7C, D). Larger benthic foraminifera are up to 2 cm in diameter, thin-shelled, commonly well-preserved (unbroken), and typically horizontally oriented. The foraminiferal assemblage is dominated by *Spiroclypeus tidoenganensis* with common occurrences of *Cycloclypeus*, *Eulepidina*, *Nephrolepidina*, *Miogypsinoides* and Amphistegina. Planktonic foraminifers occur occasionally in LF2.2 lithofacies. Laminar and loose *Mesophyllum,* together with branching *Lithothamnion* are common components.

Interpretation: The foraminiferal assemblage dominated by very large and flat *Spiroclypeus, Cycloclypeus* and *Lepidocyclinids*, is typical of oligophotic environments, at

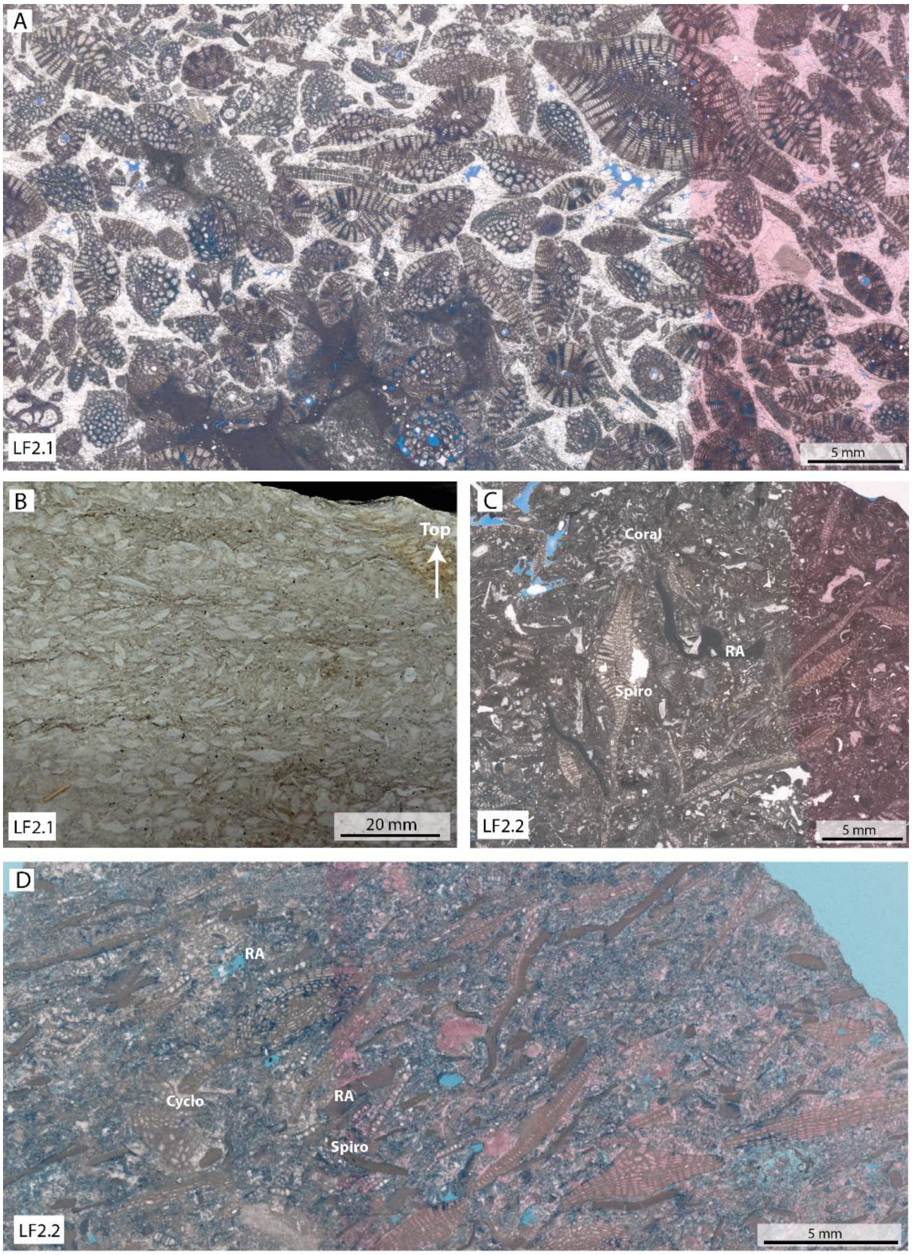

Figure 2-7 : Microphotographs of foraminiferal rudstones (LF2.1) and foraminiferal floatstone (LF2.2) (A) WELL-1 1319.49 m: Large benthic foraminiferal rudstone (LF2.1) with broken specimens of *Spiroclypeus* and Lepidocyclinids (Lepidocyclina spp). Space between bioclasts is filled by calcitic cement. (B) WELL-2 1291.8 m: Oriented core samples of lithofacies LF2.1. (C) WELL-1 1270.70 m: large benthic foraminiferal floatstone (LF2.2) with flat S*piroclypeus* (Spiro), laminar coralline algae (RA) and small pieces of coral (Coral). (D) WELL-3 1344.98 m: Large benthic foraminiferal floatstone (LF2.2) with flat-shaped *Cycloclypeus* (Cyclo), *Spiroclypeus* (Spiro) and laminar coralline algae (RA).

depths of 30 m or greater, but could grow comfortably at depths as great as 70 m (Hallock and Glenn, 1986; Noad, 2001). The occurrence of planktonic foraminifera in LF2.2 is consistent with such water depths. The coralline algal assemblage, dominated by *Mesophyllum* and *Lithothamnion*, is also indicative of relatively low-light conditions (e.g., Adey 1979; Bosence 1983; Rosler et al. 2015). The biological composition together with the well preservation state of flat-shaped large benthic foraminifera and the high proportion of micrite matrix strongly suggest that the LF2.2 floatstones were deposited in an oligophotic, low-energy environment.

LF3.1 Coral floatstone with echinoderm-rich wackestone matrix

LF3.1 lithofacies is a scleractinian-dominated floatstone consisting of thin branches of unidentified coral or massive fragments of merulinids and pocilloporids (Fig. 2-8, 2-9). Associated fossils included solitary coral. All are embedded in a wackestone matrix dominated by echinoderm fragments (mainly ophiuroids and some echinoids), small pieces of non-articulated coralline algae and occasional benthic foraminifera (mainly broken lepidocyclinids, *Spiroclypeus, Miogypsinoides* and *Amphistegina*). Some rare, well-preserved, flat-shaped lepidocyclinids and *Spiroclypeus* may represent autochthonous biota. The coralline algal assemblage, although poorly preserved, is prominently composed of *Mesophyllum* and *Lithothamnion*. Most of the corals are partially leached and filled with a finely bioclastic micrite (Fig. 2-8A, C, E) which is identical in nature and in physical continuity with the matrix in which they are embedded (faint ghost fabrics, sensu Sanders, 2003). Coral may also be replaced by calcite (Fig. 2-8B) or may be preserved as molds. Within the Upper Burman Limestone, LF3.1 has been encountered in four distinct, 5 to 10 m-thick intervals. Brecciated intervals (1 to 3 m-thick) may occur with LF3.1 units. In such breccia, clasts are gravel to pebble-sized (typically 0.5 to 5.0 cm diameter), sub-angular to sub-rounded in shape and commonly display deep embayments. The space between clasts is filled with a lime mud-supported sediment containing various proportions of fine-grained echinoderm fragments. The top of brecciated LF3.1 intervals are characterized by uneven, tightly indurated and brecciated surfaces with angular clasts (WELL-3 1295.5 m Fig. 2-9).

Interpretation: The biological assemblage in the matrix of LF3.1 floatstone is dominated by echinoderms and contains low amounts of light-dependent biota, which is not consistent with the deposition under euphotic conditions. Benthic foraminifers (mainly broken, flat-shaped lepidocyclinids and *Spiroclypeus*) are extremely scarce and likely derive from oligo-mesophotic environments. In addition, coralline algae are always broken and the assemblage

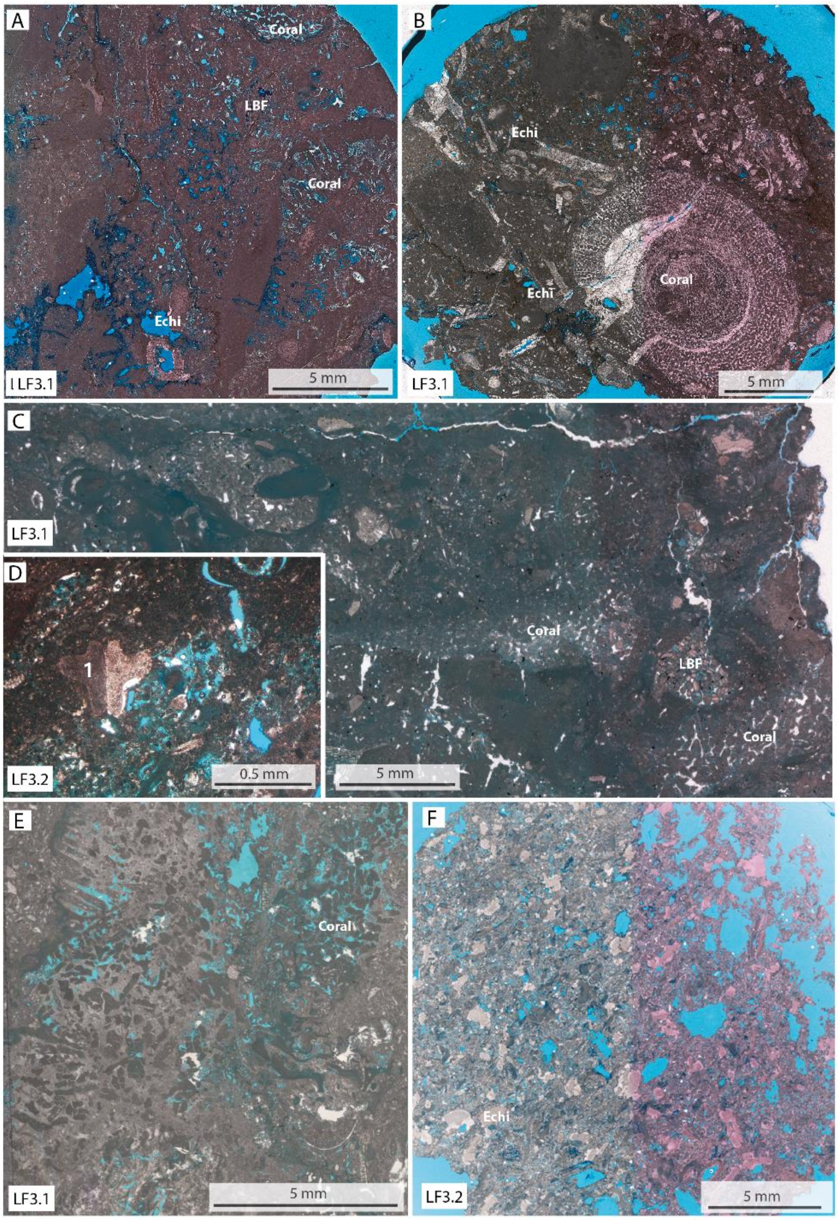

Figure 2-8 : Microphotographs of coral floatstones (LF3.1) and echinodermal wackestones (LF3.2) (A) WELL-1294.98 m: leached coral filled with lime mud (faint ghost texture) set in fine bioclastic wackestone matrices with rare large flat benthic foraminifers (LBF) and echinoderms (Echi). (B) WELL-2 1361.42 m: Cemented coral fragments in a wackestone-packestone bioclastic matrix dominated by echinoderm fragments (C) WELL-1 1294.7 m: leached coral in echinodermal wackestone. (D) WELL-4 1258.03 m: Section of ophiuroids with two stages of light extinction (1). (E) WELL-3 1311.84 m: Dissolved coral (LF3.1) filled with fine bioclastic micritic matrix (F) WELL-4 1326.22 m: Bioclastic packestone-wackestone with fragments of echinoderms (Echi) (LF3.2).

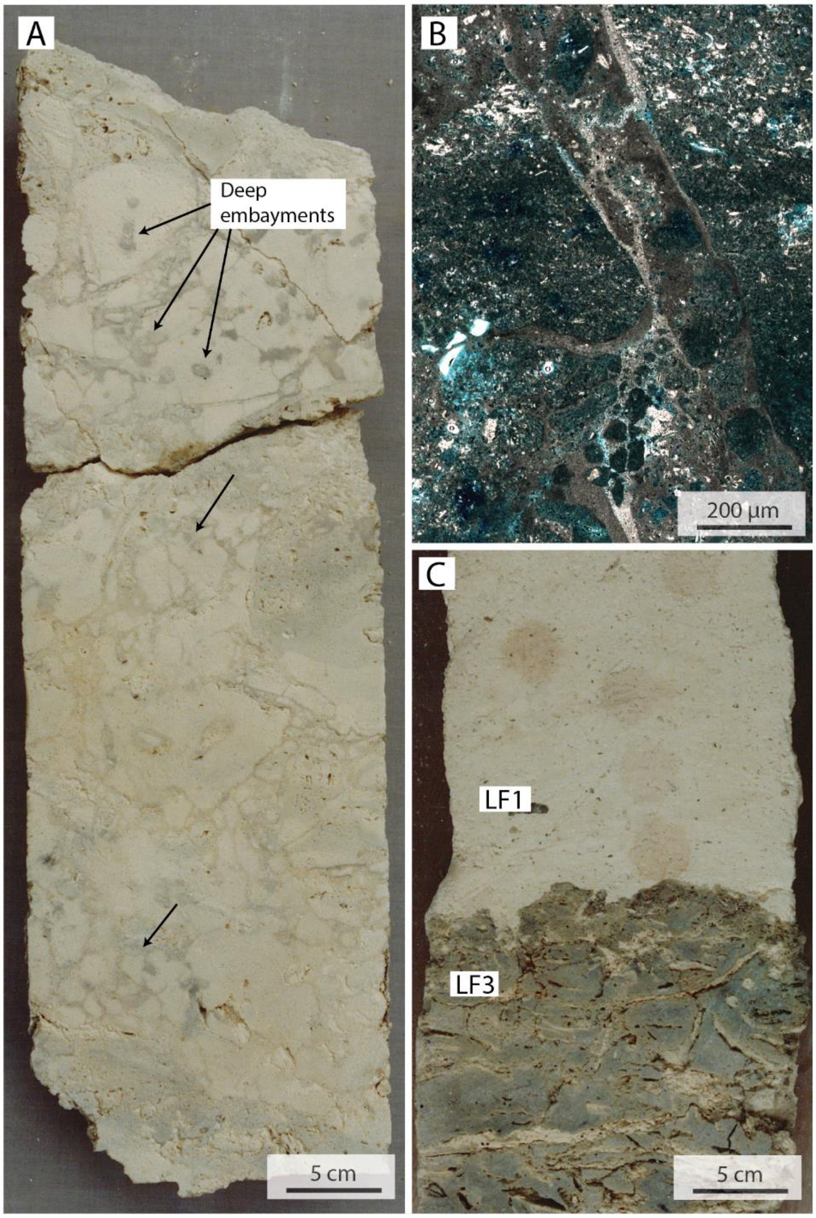

Figure 2-9 : Core photographs of brecciated LF3 intervals: (A) WELL-1 1256.6 m: brecciated coral floatstone with irregular-shaped clasts showing deep embayments. (B) WELL-4 1258.03 m: microphotograph showing a brecciated echinodermal wackestone (LF3.2). The sediment between clasts consists of lime mud. The clasts display irregular shapes with smooth edges which suggest that brecciation affected a relatively soft, partially lithified sediment; (C) WELL-3 1308.05 m: core photograph of a hardground surface, at the top of a carbonate breccia composed of poorly displaced, tight elements of coral-rich and echinodermal floatstone (LF3). The hardground is sharply overlain by high microporous, coralline algal-foraminiferal floatstone (diagenetic facies: G-DF1A). The space between clasts is filled by the overlying microporous sediment.

(*Mesophyllum* and *Lithothamnion*) is similar to that of LF1 and LF2. The fragmented nature of coral, red algae and most foraminifers strongly suggests that they have been transported. Assemblages of broken benthic foraminifers (lepidocyclinids, *Spiroclypeus*, *Miogypsinoides*) and coralline algae (*Mesophyllum* and *Lithothamnion*) indicate that the transported bioclastic material derives from an area located within the mesophotic domain. It is therefore likely that corals and associated benthic foraminifers and coralline algae were derived from nearby patches or mounds whose top has reached the mesophotic environment. The importance of coral-dominated carbonate factories in mesophotic settings has been recognized in various Cenozoic carbonate systems, in relation with nutrient rich and episodically agitated environments (e.g., Morsilli et al., 2012; Pomar et al., 2014) or with turbid waters (Santodomingo et al., 2015). Under such conditions, corals may develop by enhancing their heterotrophic strategy acting as suspension feeders (e.g., Anthony, 1999; Morsilli et al., 2012). The relative dominance of heterotrophs (echinoderms) and the lack of in situ light-dependent biota (larger benthic foraminifers, coralline algae and zooxanthelate coral) could reflect low light environments (dysphotic to aphotic) as a result of an increased water depth or water turbidity. In ancient and modern environments, occurrences of dense populations of ophiuroids are regarded as requiring the combination of three conditions (Aronson et al., 1997; Aronson, 2009) : low skeleton-crushing predation, low rates of sediment resuspension, and high flux of particulate organic matter. As a consequence, the development of coral patches in mesophotic settings, coeval with ophiuroid-rich sediment in dysphotic to aphotic area may be interpreted as resulting from high concentrations of suspended particulate organic matter in the water column and associated reduction in light penetration.

In brecciated intervals (Fig. 2-9), the similarity between the texture and composition of the intraclasts and those of the matrix in which they are embedded, the irregular shape of the clasts which display deep embayments, strongly suggest that brecciation affected a partially lithified lime-mud and therefore occurred early, in marine environments. Similar features of soft deformation and early brecciation have been interpreted by Bouchette et al. (2001) as resulting from water-wave cyclic loading. As a consequence, in spite of prevailing low-energy hydrodynamic conditions which are suggested by the lime-mud-supported nature of LF3.1, episodic high energy events are needed to: (1) break up and removed coral colonies, and (2) trigger sediment brecciation, clast deformation and reworking on the partially lithified sea bottom (Bouchette et al., 2001; Seguret et al., 2001). The angular nature of clasts at top of brecciated intervals and the sharp contact with overlying LF1 facies (Fig. 2-9) suggests that early brecciation processes affected well-lithified limestone and likely occurred during a period of depositional hiatus (hardground).

As a consequence, LF3.1 lithofacies is interpreted to have deposited in low light environment (dysphotic to aphotic), with high concentrations of suspended particulate organic matter, at the vicinity of mesophotic coral patches and subject to episodic high-energy events such as storms or internal waves causing sea-floor brecciation.

LF3.2 Echinoderm wackestone

The LF3.2 lithofacies is a bioclastic wackestone dominated by fragments of echinoderms, including ophiuroid ossicles and echinoids (Fig. 2-8D, F). Small size (<1 mm) fragments of coralline algae (*Mesophyllum* and *Lithothamnion*) are common. Isolated coral pieces and rare fragments of large benthic foraminifers may be present. LF3.2 facies commonly occurs as layers (0.10 to 1 m-thick) interbedded within LF3.1 coral floatstones.

Interpretation: The similarity in texture and biota between the echinodermal wackestone (LF3.2) and the matrix of the coral floatstone (LF3.1) strongly suggests that LF3.2 represents a lateral analogue of LF3.1, deposited in a dysphotic to aphotic environment. This contention is reinforced by the fact that LF3.2 and LF3.1 form thin (0.10 to 1 m) alternations. Since LF3.1 and LF3.2 essentially differ in their coral abundance, they may reflect a gradient of proximity to mesophotic coral patches.

2.4.3 Vertical and lateral changes in lithofacies and related environments

Vertical changes in lithofacies, related depositional environments and remarkable surfaces are summarized in Fig. 2-10 and 2-11 for each well in the cored intervals of the Upper Burman Limestone. All of the lithofacies have been interpreted as being deposited in low to moderate light environments, below the euphotic zone. In the cored sections, the Upper Burman Limestone is subdivided into meter-to-decameter-scale sedimentary units dominated either by LF1, LF2.1 and LF2.2 lithofacies (named units FA1 to FA6 in Fig. 2-10, 2-11) or by LF3.1 and LF3.2 lithofacies (units ES1 to ES5: Fig. 2-10, 2-11). Transitions between lithofacies are characterized mainly by gradual changes in biogenic composition. However, the upper part of coral-rich intervals (LF3.1 facies) is typically brecciated and topped by hardground surfaces (Teillet et al. 2019) (Fig. 2-9E, 2-10B, D).

The correlation framework and the well-to-seismic tie (Fig 2.12) revealed that the seismic reflectors roughly follow lithostratigraphic boundaries. For instance, the seismic marker H9B matches with the boundary between a lower, 10 m-thick interval of foraminiferal wackestones (LF2.2) and an upper, massive, interval containing rhodoliths, lepidocyclinids and *Spiroclypeus* (LF1). The stratigraphic correlation between wells reveals a lack of significant lateral change in lithofacies within the carbonate buildup. Such a stratigraphic architecture is indicative of a lack of significant topographic gradients on top of the buildup. The cored section of the Upper Burman Limestone (Aquitanian-Burdigalian) exhibits five main coral floatstone (LF3) intervals interbedded within foraminiferal-coral algal-dominated intervals (LF1-LF2).

2.4.4 Seismic interpretation

The 3D seismic records from, the Upper Burman Limestone interval is characterized by a set of flat, continuous, parallel, low to moderate amplitude reflectors (Fig. 2-13). There is no change in seismic facies or reflector morphology on the edges of the Yadana platform that could be interpreted as suggesting to the presence of reef barriers. The inter-well correlation of seismic markers is supported by the good lateral continuity of the seismic reflectors within the Upper Burman Limestone (Fig. 2-13A, B). The lack of significant lateral changes in amplitude, the flat morphology and the parallel pattern of the reflectors are strongly consistent with a layer-caked stratigraphic architecture (low lateral changes in lithofacies and thickness) as suggested by well correlations (Fig. 2-12). On the seismic profiles, reflectors from the Upper Burman Limestone appear sharply truncated at the northern margin (Fig. 2-13C). In addition, the very uneven shape of the UBL top surface on isochron maps (Fig. 2-13E, F) argues for a significant erosion of the Yadana buildup, after the Burdigalian and prior to the deposition of the overlying pro-delta shales during the Tortonian.

2.5 Discussion

2.5.1 The Yadana buildup: an early Miocene, isolated, oligo-mesophotic carbonate platform

The Yadana carbonate platform has been previously interpreted as a shallow-water, reef-rimmed carbonate platform based on seismic facies interpretations (Paumard et al., 2017).

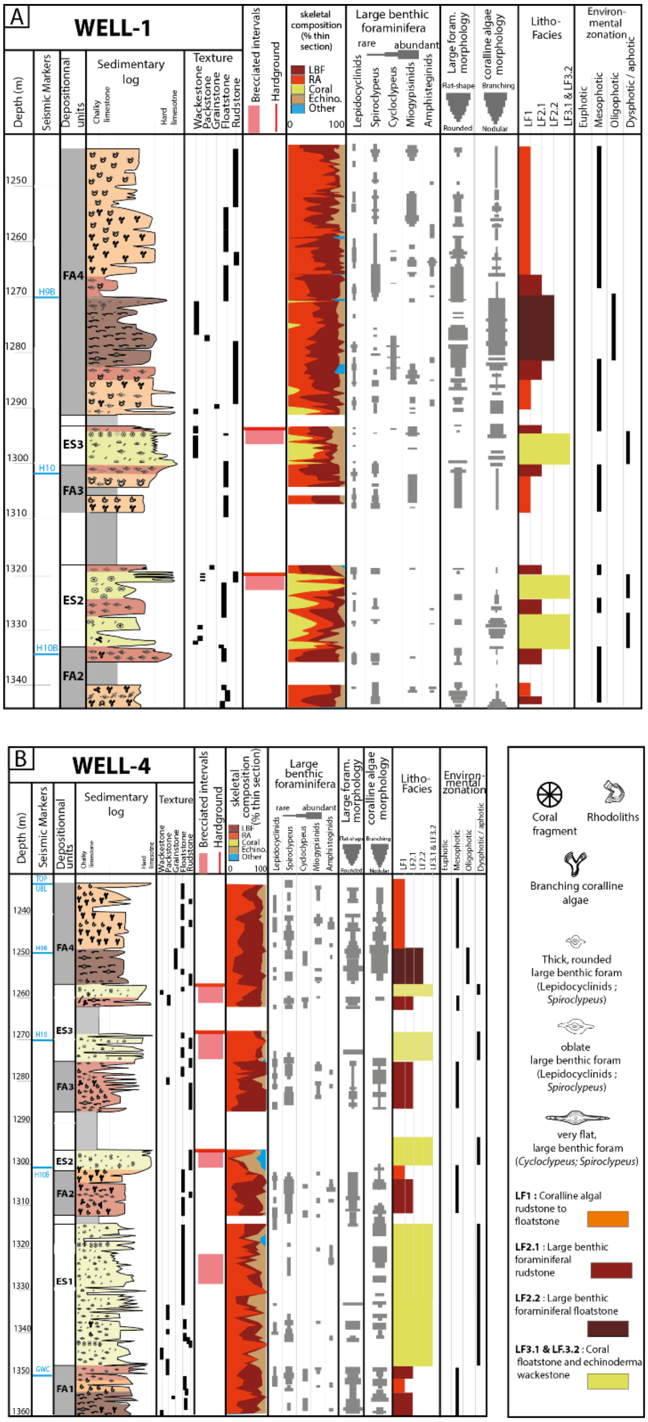

Figure 2-10 : Description of cores in terms of textures, bio-constituents, large benthic foraminiferal taxa, and morphologies, coralline algal morphologies and environmental interpretations: WELL-1 (A) and WELL-4 (B)

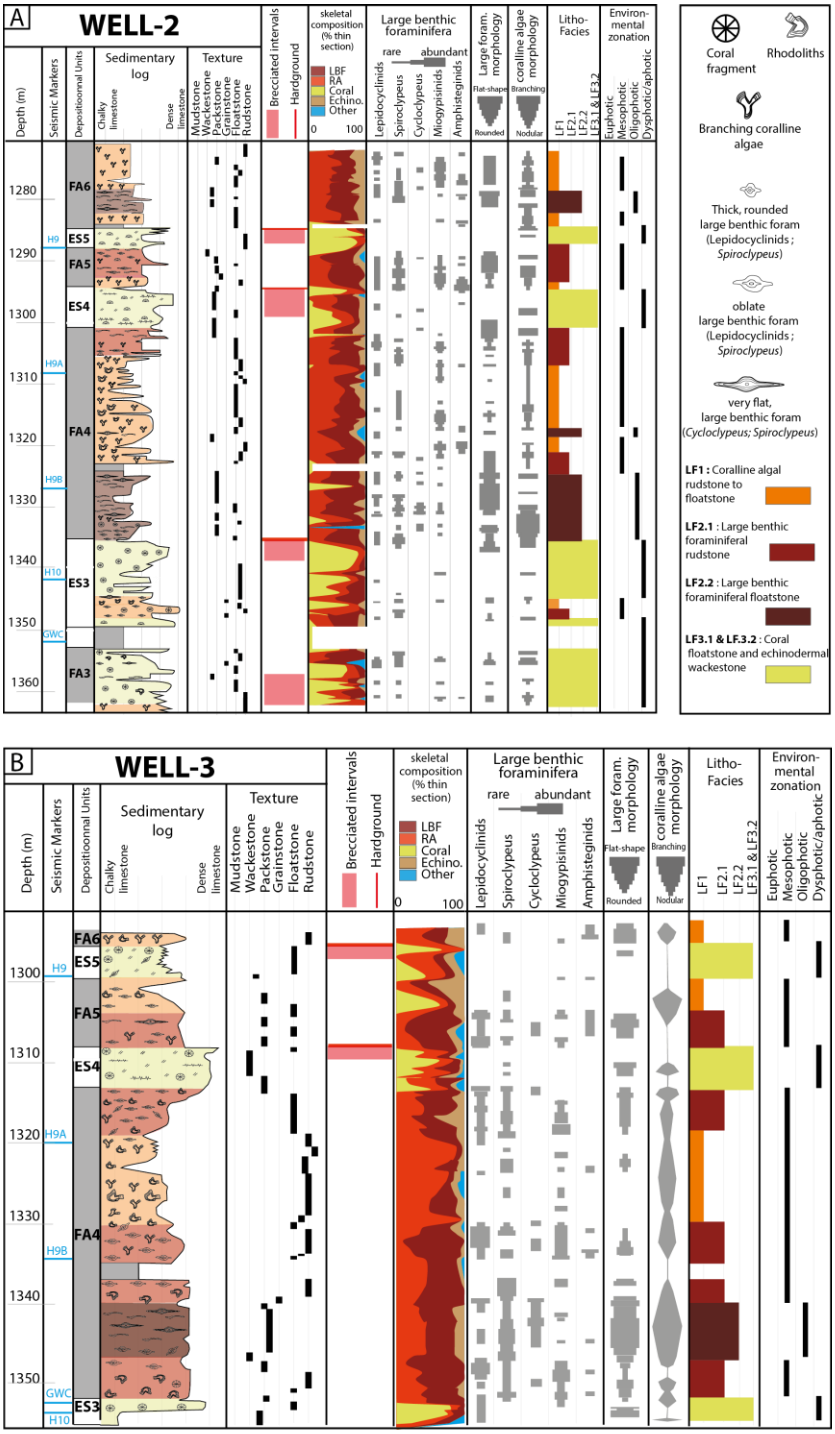

Figure 2-11 : Description of cores in terms of textures, bio-constituents, large benthic foraminiferal taxa, and morphologies, coralline algal morphologies and environmental interpretations: WELL-2 (A) and WELL-3 (B).

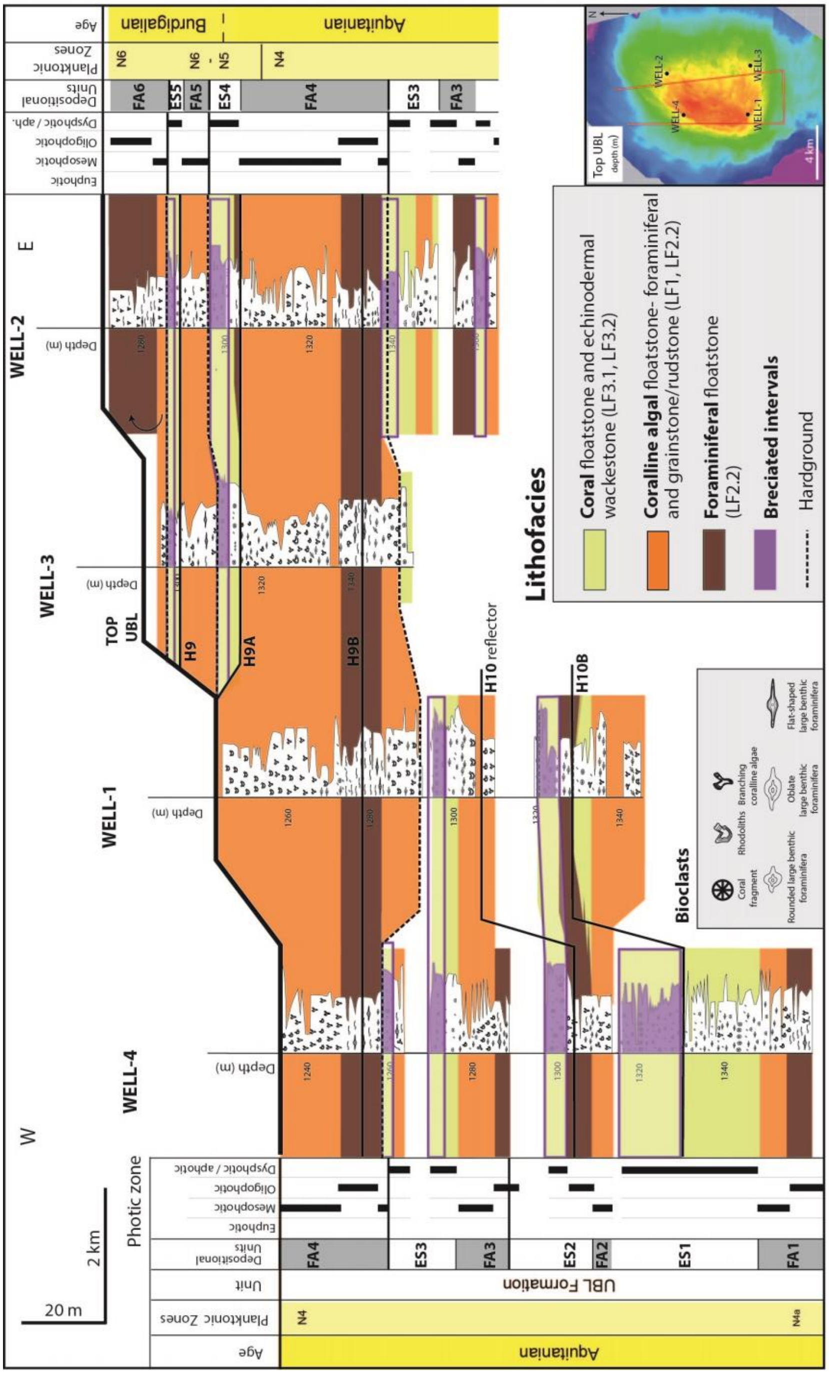

Figure 2-12 Well-correlations and stratigraphic architecture of the Yadana platform, based on large benthic foraminiferal biostratigraphy, well-to seismic ties (vertical resolution ~20 m) and correlation of lithofacies associations. Names of depositional units refer to coralline algal-foraminiferal carbonate factories (FA) and Echinodermal/Scleractinian carbonate factories (ES).

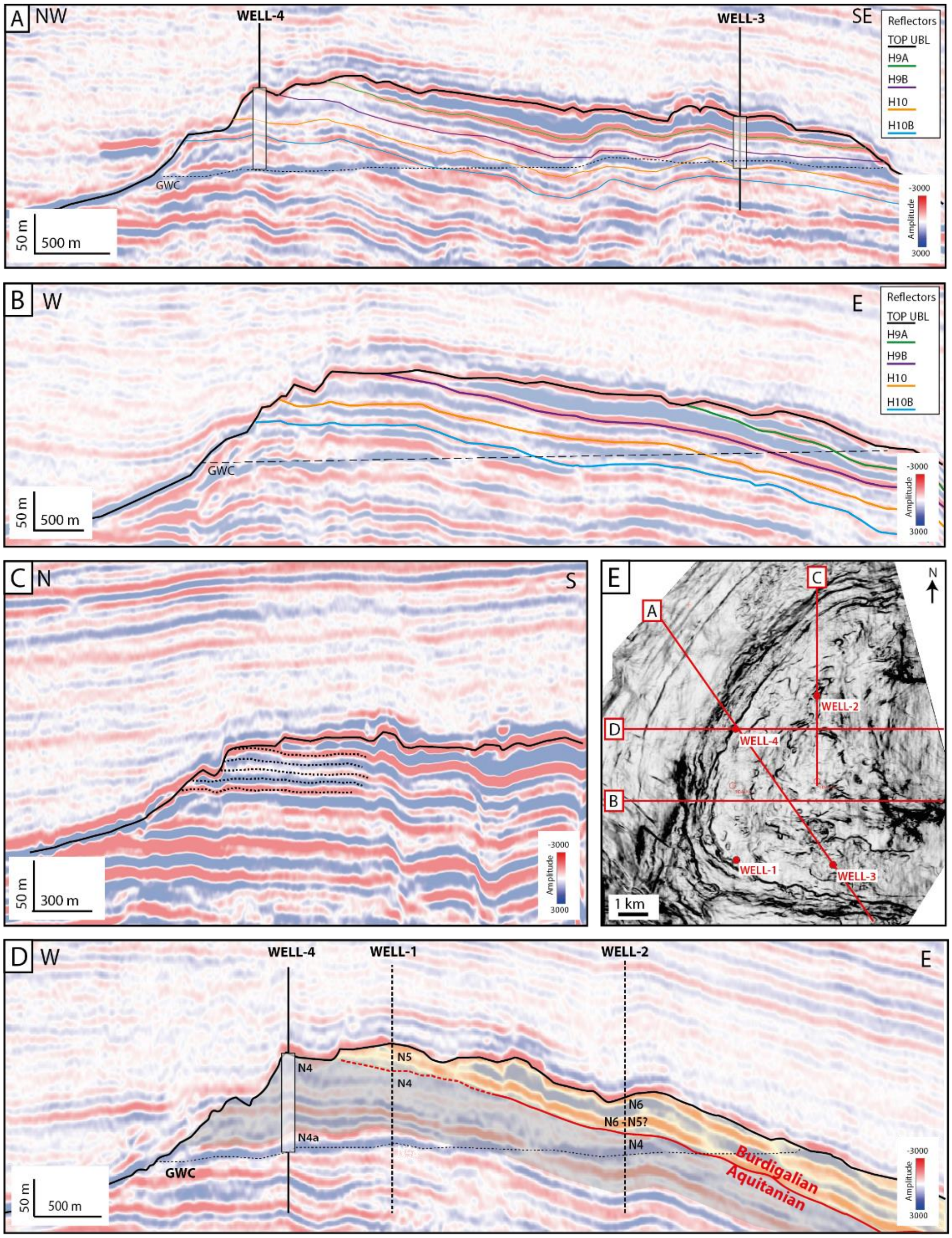

Figure 2-13 : Seismic geometries of the Yadana platform. The location of seismic profiles are indicated on Fig. 13E (red lines). (A) SE-NW-oriented, crossing through wells WELL-3 and WELL-4 and illustrating the main reflectors within the Upper Burman Limestone. (B) E-W-orientated profile, (C) N-S-oriented profile, and (D) W-E-oriented profile, through WELL-4 (WELL-1 and WELL-2 are projected). The gas water contact is identifiable on this line by a nearly horizontal reflector cross-cutting timelines. (E) Coherency map of the top reservoir surface.

Instead, the present environmental interpretations are based on: (1) interpretations of the skeletal components and the ecological requirements of the benthic communities from which they have derived, particularly light for autotrophs and food requirements for heterotrophs, (2) rock textures as indicative of water energy, (3) reconstruction of sedimentary geometries based on well correlations and 2D seismic cross section analysis. The isolated nature of the Yadana carbonate system during the Aquitanian and Burdigalian has been demonstrated by the three-dimensional interpretation of seismic data (Paumard et al., 2017). The lateral correlative potential of the lithofacies and their variability in thickness are indicative of a weak topographic gradient, at least in the western part of the buildup. In addition, the carbonate sediments from the Upper Burman Limestone are characterized by the absence of strictly euphotic constituents such as reef dwellings or seagrass-related biota. This suggests that the studied area around wells was not fed by sediments produced by an euphotic carbonate factory. In addition, the lack of lateral changes in the seismic facies and in thickness eastward, as revealed by the seismic data, supports the interpretation of a flat-topped platform for the whole early Miocene Yadana buildup.

The layer-caked architecture (= alternating echinodermal-scleractinian and foraminiferal-coralline algal intervals) of the Upper Burman Limestone is indicative of specific environmental conditions (light penetration, nutrient content, water depth) on the platform top at a given time. In contrast, the vertical changes in lithofacies (Fig. 2-10, 2-11, 2-12) can be interpreted in terms of changing environmental parameters such as nutrient supply, turbidity, water energy and water depth. The Upper Burman Limestone from the Yadana buildup has recorded three types of carbonate factory that operated on the top of the platform depending on the paleoenvironmental context (1) a scleractinian carbonate factory developing under mesophotic conditions in shallow(below fair-weather-wave-base), nutrient-rich waters, (2) an echinodermal carbonate factory occupying aphotic to oligophotic area of the shelf coevally with the scleractinian carbonate factory below fair-weather-wave-base, and (3) large benthic foraminiferal (LBF)-coralline algal carbonate factories prevailing under oligo-mesophotic and oligo-mesotrophic conditions below fair-weather-wave-base.

The scleractinian and the echinodermal carbonate factories (Fig. 2-14A)

Analysis of the biogenic components and textural features of LF3.1 and LF3.2 lithofacies reveal the existence of two coeval carbonate factories developing on top of the Yadana shelf. During LF3.1 and LF3.2 deposition, the top of the Yadana shelf was mainly located within the disphotic or possibly aphotic zone, and below the fair weather wave base. In such environments, skeletal carbonate production was dominated by echinoderms including a large proportion of ophiuroids. The abundance of ophiuroids in LF3.1 and LF3.2 suggests that prevailing environmental conditions favored the development of suspension feeders (McKinney and Hageman, 2007). The abundance of coral fragments scattered within echinodermal wackestones (LF3.1), together with broken, mesophotic benthic foraminifers and coralline algae, suggests the existence of a mesophotic scleractinian carbonate factory. However, in situ coral facies have not been encountered by cores.

In modern environments, mesophotic coral communities are known to include both zooxanthellate and azooxanthellate coral and occur in the lower half of the photic zone at depths down to 150 m (e.g., Kahng et al. 2010). In such environments, zooxanthellate coral may exhibit various photo-acclimatization strategies, but can also develop heterotrophic behavior, as suspension feeders, particularly when light significantly decreases with increasing depth or increasing turbidity, or during periods of high nutrient supplies (e.g., Muscatine et al., 1989; Alamaru et al., 2009; Chan et al., 2009; Lesser et al., 2009; Morsilli et al., 2012). In modern (Kahng et al., 2010, and references therein) and ancient lowlight environments, corals are known to form low-relief buildups such as in the late Eocene pro-delta environments from Spain (Morsilli et al., 2012). The strategy of forming mounds is believed to favor the development of suspension feeders since such reliefs promote turbulent currents capable of carrying picoplanktons and phytoplankton (Atkinson and Bilger, 1992; Ribes et al., 2003; Pomar and Hallock, 2008; Morsilli et al., 2012;). In the Yadana platform, corals from LF3.1 possibly derive from neighboring patches or mounds whose top is located in mesophotic environment. Since LF3.1 and LF3.2 mostly differ in their coral abundance, they may reflect a gradient of proximity to such a possible mound. In addition, the lateral changes in thickness (<10 m) of coral-rich units, as well as the lateral pinching out of some of these units, may advocate for the existence of localized sources of coral production, scattered on the Yadana shelf, promoting the formation of a mounded, low relief, top of platform morphology (Fig. 2-14A). The absence of visible morphologies on seismic profiles and the relatively flat and continuous expression of seismic reflectors may suggest that: 1) possible mounds have not been preserved, as a result of marine erosion processes, or 2) the height and lateral extension of these mounds are below the vertical and lateral resolution of the seismic (~ 20 m). The latter hypothesis would imply that the difference in elevation between the top of the mound (coral-dominated carbonate factory) which is located within the mesophotic zone and the dysphotic-aphotic platform (echinoderm-dominated carbonate

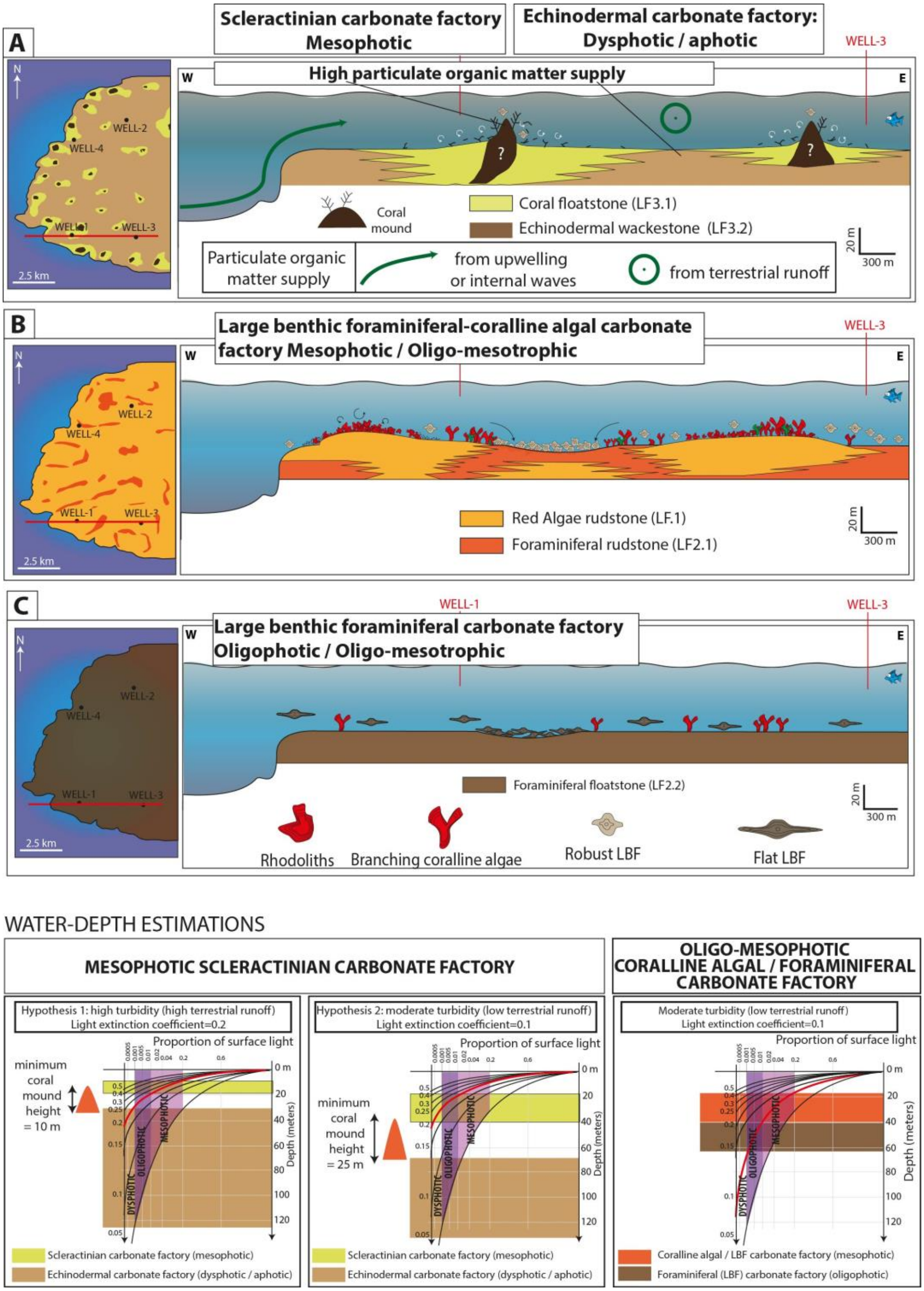
A
Scleractinian carbonate factory
Mesophotic
Echinodermal carbonate factory:
Dysphotic / aphotic
WELL-3
W
High particulate organic matter supply
E
N
WELL-2
WELL-4
WELL-1
WELL-3
2.5 km
?
?
Coral mound
Coral floatstone (LF3.1)
Echinodermal wackestone (LF3.2)
20 m
300 m
Particulate organic matter supply
from upwelling or internal waves
from terrestrial runoff
B
Large benthic foraminiferal-coralline algal carbonate factory Mesophotic / Oligo-mesotrophic
WELL-3
W
E
N
WELL-2
WELL-4
WELL-1
WELL-3
2.5 km
Red Algae rudstone (LF.1)
Foraminiferal rudstone (LF2.1)
20 m
300 m
C
WELL-1
WELL-3
W
Large benthic foraminiferal carbonate factory
Oligophotic / Oligo-mesotrophic
E
N
WELL-2
WELL-4
WELL-1
WELL-3
2.5 km
Foraminiferal floatstone (LF2.2)
20 m
300 m
Rhodoliths
Branching coralline algae
Robust LBF
Flat LBF
WATER-DEPTH ESTIMATIONS
MESOPHOTIC SCLERACTINIAN CARBONATE FACTORY
OLIGO-MESOPHOTIC CORALLINE ALGAL / FORAMINIFERAL CARBONATE FACTORY
Hypothesis 1: high turbidity (high terrestrial runoff)
Light extinction coefficient=0.2
Proportion of surface light
0.0005 0.001 0.005 0.01 0.02 0.04 0.2 0.6
minimum coral mound height = 10 m
0.5 0.4 0.3 0.25 0.2 0.15 0.1 0.05
DYSPHOTIC
OLIGOPHOTIC
MESOPHOTIC
0 m 20 40 60 80 100 120
Depth (meters)
Scleractinian carbonate factory (mesophotic)
Echinodermal carbonate factory (dysphotic / aphotic)
Hypothesis 2: moderate turbidity (low terrestrial runoff)
Light extinction coefficient=0.1
Proportion of surface light
0.0005 0.001 0.005 0.01 0.02 0.04 0.2 0.6
minimum coral mound height = 25 m
0.5 0.4 0.3 0.25 0.2 0.15 0.1 0.05
DYSPHOTIC
OLIGOPHOTIC
MESOPHOTIC
0 m 20 40 60 80 100 120
Depth (meters)
Scleractinian carbonate factory (mesophotic)
Echinodermal carbonate factory (dysphotic / aphotic)
Moderate turbidity (low terrestrial runoff)
Light extinction coefficient=0.1
Proportion of surface light
0.0005 0.001 0.005 0.01 0.02 0.04 0.2 0.6
0.5 0.4 0.3 0.25 0.2 0.15 0.1 0.05
DYSPHOTIC
OLIGOPHOTIC
MESOPHOTIC
0 m 20 40 60 80 100 120
Depth (meters)
Coralline algal / LBF carbonate factory (mesophotic)
Foraminiferal (LBF) carbonate factory (oligophotic)

Figure 2-14 : Depositional models for the flat-topped, oligo-mesophotic Yadana platform, for distinct paleooceanographic settings: (A) Mesophotic scleractinian mounds developing on top of a platform with dominant echinodermal carbonate production in dysphotic to aphotic conditions; the development of coral buildups results from significant supplies in particulate organic matter from various potential sources (upwelling currents, internal waves or terrigenous runoff); (B) Mesophotic, coralline algal-foraminiferal carbonate production prevailing on the platform top, under oligotrophic to mesotrophic conditions; (C) Oligophotic, large benthic foraminiferal carbonate production under oligotrophic to mesotrophic conditions; (D) Paleowater-depth estimates for the distinct carbonate factories. Two hypotheses of water turbidity are considered for the mesophotic coral mounds. The light-intensity zonation with depth is based on the proportion of surface light for different extinction coefficients of light (modified from Morsilli 2012). The lower limit of the euphotic, mesophotic and oligophotic zones depends on water transparency. Curves of light penetration for different extinction coefficients of light are based on Hallock 1986a, Kahng 2010).

factory) is less than 20 meters. This would be consistent with a steep light gradient within the water column and therefore with high turbidity (Fig 2.14). Such an interpretation is consistent with the size of mesophotic coral mounds (5-20 meters high) documented in Rupelian (Majella Mountain: Brandano et al., 2018) and Chattian (Salento Peninsula: Tomassetti et al., 2018) ramp systems from the Mediterranean area. Additionally, the coeval development of a scleractinian and an echinodermal carbonate factory may have been favored by increased influxes in suspended organic particulate matter that promoted both suspension feeding behavior of zooxanthelate coral at shallow depths in mesophotic, turbid waters (Anthony, 1999), and the development of ophiuroids in deeper,dysphotic to aphotic settings (Aronson et al., 1997; McKinney & Hageman, 2007). The occurrence of brecciated intervals within coral-floatstone intervals, together with the common fragmentation of large coral benthic foraminifera and coralline algae are indicative of episodic high-energy events that could have been generated by storms or internal waves (Morsilli and Pomar, 2012; Pomar et al., 2012). Finally, the pervasive, early dissolution of coral aragonite (faint ghost texture of coral floatstones) is indicative of undersaturated conditions at the sea bottom which may be related to (1) enhanced organic matter decay coupled with respiration in environments that are enriched in particulate organic matter (Sanders, 2003), and (2) the influx of cold, CO2-rich waters from upwelling currents (Feely et al., 2008).

The large benthic foraminiferal-coralline algal carbonate factories (Fig. 2-14B, C)

The foraminiferal and coralline algal-dominated carbonate sediments (LF1 and LF2.1) are found in 10 to 25 m-thick intervals that are correlatable between the studied wells (Fig. 2-12). All the identified biological constituents are indicative of mesophotic, oligo-mesotrophic conditions. The lack of euphotic biota within such intervals strongly suggests that there has been no euphotic carbonate factory on the Yadana buildup at that time. The large benthic foraminiferal-coralline algal carbonate factory, that was the source of carbonate sediment of LF1 and LF2.1, is therefore interpreted to have operated on the top of the Yadana shelf, under mesophotic conditions (Fig. 2-14B). The high micrite content in coralline algal floatstones LF1 advocates for a low-energy environment, below wave action. However, the usual disintegration of branching rhodoliths and the presence of the LBF rudstone LF2.1 argues for a repetitive alternation of low to high energy conditions. Another evidence of high-energy conditions could be the occurrence of thin (<1 m) beds of well-sorted foraminiferal rudstones (LF2.1) with dominantly non-oriented large benthic foraminifera, interbedded within coralline algal floatstones (Fig. 2-7B). Such rudstone deposits likely correspond to the remobilization of the mesophotic carbonate production and redistribution on top of the Yadana shelf during storm or internal wave events. Flat-shaped, large benthic foraminifers (*Spiroclypeus, Cycloclypeus* and *Eulepidina*) which are the dominant biota of LF2.2 are known to characterize oligophotic and oligo-mesotrophic environments (e.g., Buxton and Pedley 1989; Beavington-Penney and Racey 2004; Pomar et al. 2017). The lack of lateral changes in texture, biota and thickness between the wells for LF2.2 intervals in addition to the high micrite content are regarded as expressing a deposition on top of a low-energy platform rather than on a ramp system (Fig. 2-14C).

2.5.2 Factors controlling the development of mesophotic coral communities on the Yadana platform

As previously discussed, coralline algal and foraminiferal-dominated carbonate factories are linked to oligo-mesophotic settings associated with low-to-moderate turbidity and oligo-mesotrophic waters, while scleractinian and echinodermal carbonate factories developed coevally during periods of suspended particulate nutrient influxes.

Modern mesophotic carbonate buildups have been commonly reported from locations where surface waters are clear and oligotrophic, allowing sufficient light to penetrate to depths of 30–50 m, and where high fluxes of phytoplankton and zooplankton are supplied by internal waves (e.g., Hallock, 2001: Pomar et al., 2017). High fluxes of particulate organic matter would also explain the coeval development of echinoderm-dominated deposits in deeper (dysphotic to aphotic) setting. Such an interpretation is supported by various evidences of episodic high-energy events affecting scleractinian-echinoderm facies (LF3.1 and LF3.2) such as the transportation of mesophotic coral fragments into dysphotic-aphotic environments, and the common occurrence of brecciated intervals (Fig. 2-9). The Andaman Sea has been extensively studied for the occurrence of high amplitude (> 60 m) internal solitons (e.g., Osborne and Burch, 1980; Hyder et al., 2005; Jantzen et al., 2013). Locally, solitons are related to the occurrence of strong tidal currents in a stratified water column flowing over reliefs inducing abrupt changes in bathymetry, especially, over the sea—mounts from the Andaman volcanic arc (Hyder et al., 2005). Soliton induce perturbations of the depth of the pycnocline and generate strong currents (Apel et al., 1985). Such phenomena probably also occurred during the early Miocene, at a time when the topographic sill of the Andaman Arc was already formed and may have contributed to enriching shallow waters in nutrient by mixing with upwelled deeper waters.

An alternative interpretation would be a development of mesophotic coral communities in shallow, turbid waters with high particulate organic matter influx. Scleractinian-dominated bioconstructions that formed in turbid water under significant terrigenous inputs, have been shown to be common in the geological record (Sanders and Baron-Szabo, 2005) and particularly in Cenozoic shallow-water sedimentary systems from Southeast Asia (e.g., Wilson, 2005; Novak et al., 2013; Santodomingo et al., 2015, 2016). At present, the Irrawaddy River of Myanmar is one of the muddiest rivers (Licht et al., 2016) inflowing into the northern Andaman Sea and the Gulf of Martaban (Rao et al., 2005). It is the fifth-largest river in the world in terms of suspended sediment discharge, known to have been the major source of sediment within the Andaman Sea since the early Miocene (Licht et al., 2016). As a consequence, the Gulf of Martaban is one of the largest perennially turbid zones of the world's oceans. The suspended sediment levels and the area covered by the highly turbid zone have been shown to be strongly governed by the spring-neap tidal cycles (Ramaswamy et al., 2004). South of the Gulf of Martaban, in the Andaman Sea, around the location of the Yadana field, the nutrients supplied by the Irrawaddy River favor high concentrations of chlorophyll from algae and diatoms in the ocean (Ramaswamy et al., 2004). The late Oligocene and early Miocene paleogeography of the Andaman Sea is quite similar to the modern (Fig. 2-1A, B). So, the changes over time in sediment and nutrient inputs from the Irrawaddy River have most likely controlled changes in water turbidity and particulate nutrient concentration in the Yadana area. Periods of high terrigenous inputs may have favored the development of suspension feeders and driven the development of a dysphotic to aphotic echinodermal and mesophotic scleractinian carbonate factories. According to this interpretation, the change from a platform dominated by large benthic foraminifers and coralline algae to a dysphotic echinodermal platform may have occurred without increasing water depth (Fig 2.14D). As a consequence, in contrast to interpretations by Paumard et al. (2017), our sedimentological results do not support a deepening trend triggered by a rapid relative sea-level rise, toward the top of the platform.

Finally, the occurrence of upwelling currents may also have favored the development of mesophotic coral buildups on the Yadana platform. At present, monsoonal activity in the Andaman Sea is known to induce the formation of seasonal upwelling currents, particularly on the margin of Thailand (e.g., Chatterjee et al., 2017). The South Asian Monsoon (SAM), one of the most significant climatic components in the area is known to have occurred as early as the Oligocene-Miocene boundary (Fig. 2-4B) (Clift et al., 2008; Clift and Vanlaningham, 2010; Betzler et al., 2018). Seasonal upwelling currents, related to monsoonal activity, have been also reported to occur during the Late Miocene in the Andaman Sea (Chakraborty and Ghosh, 2016). The integration of various geochemical and mineralogical proxies by Clift et al. (2008) concluded that monsoon intensification started during the early Miocene (after ~24 Ma) and that at least 5 cycles of chemical weathering intensity have been recorded during the Aquitanian-Burdigalian interval. Changes in monsoonal activity during the early Miocene that is suggested by such alteration cycles in southeast Asia may have controlled cyclic terrestrial nutrient supplies and upwelling currents in the Andaman Sea. As a result, periods of strong upwelling activity and/or high terrestrial nutrient inputs may have favored the development suspension feeders on top of the Yadana platform and the formation of mesophotic coral patches, whereas oligo-mesophotic and oligo-mesotrophic carbonate factories dominated by coralline algae and large benthic foraminifera characterize periods of lower monsoonal intensity.

2.5.3 The significance of oligo-mesophotic carbonate factories in the Cenozoic of Southeast Asia

The concept of “tropical carbonate factory”, has been extensively used to typify carbonate paleoenvironments in various Cenozoic subtropical to tropical areas (Hallock and Glenn, 1986; Schlager, 2000; 2003). Nevertheless, an important number of recent studies in the Mediterranean region (e.g., Morsilli et al. 2012; Pomar et al. 2014, 2017, Brandano et al 2018) have increasingly identified facies associations and geometries which are significantly different from the standard modern tropical carbonate model based on reef systems and have pointed out the importance of the meso-oligophotic carbonate production by larger benthic foraminifers, red algae, associated to scleractinians. Brandano and Corda (2002) evidenced a lower-middle Miocene tropical ramp in the Central Appenines where the main carbonate production took place in the aphotic and oligophotic zone. Similarly, the role of mesophotic carbonate factories in Oligo-Miocene carbonate systems has been also evidenced in the Perla Field (offshore Venezuela, Caribbean domain), where most carbonate sediments have been shown to be produced in the oligo-mesophotic domain (Pomar, 2015).

In tropical, Cenozoic to modern environments from southeast Asia, heterozoan carbonate production has been shown to be significant and sometimes dominant in areas where upwelling and/or terrestrial runoff, high turbidity and cool waters occur (Halfar and Mutti, 2005; Madden and Wilson, 2013; Wilson and Vecsei, 2005). In such environments, heterotrophic and mixotrophic biota are more common than photosynthetic autotrophs (Tomascik et al., 2000). Additionally, most Southeast Asian Cenozoic platforms (including isolated platforms) have extensive development of oligophotic facies in moderate to deep photic zone (Wilson and Vecsei, 2005). Under conditions of high nutrient supply and high water turbidity, large scale, isolated and land-attached oligophotic platforms develop in modern environments (Paternoster platform: Burollet et al. 1986; Spermonde platform: Renema and Troelstra 2001; Kalukalukung banks: Roberts and Phipps 1988, Saya de Malha Bank: Hilbertz and Goreau 2002). Cenozoic counterparts have been also described: Berai platform (Saller and Vijaya, 2002); Tonasa platform (Wilson and Bosence, 1996); and Melinau platforms (Adams, 1965). In these carbonate systems, the oligophotic carbonate production dominates while a euphotic carbonate production may occur in some shallow water areas (Wilson and Vecsei, 2005), including barrier reefs or shoal rims (e.g., Paternoster and Berai Platforms), or localized patches/pinnacle reefs (e.g., Spermonde shelves). Shallow areas with euphotic carbonate production may be of very reduced extent in some banks or incipiently drowned platforms such as in the Wonosari and Kalukalukuangs platforms (Read, 1985). The present study shows that isolated carbonate systems with exclusive oligo-mesophotic and dysphotic-aphotic carbonate production existed during the early Miocene in Southeast Asia and that "incipiently drowned platform," conditions persisted throughout the entire early Miocene interval. On the Yadana platform, oligo-mesophotic carbonate production has been persistent during the early Miocene and has been likely promoted by the combination of repeated periods of high terrestrial runoff (Irrawaddy River), upwelling currents related to monsoonal activity and/or by deep-water mixing controlled by internal waves.

Carbonate production dominated by non-framework building biota has been evidenced in Oligo-Miocene, euphotic environments from the Indo-Pacific realm. Probably, the most significant non-framework building euphotic carbonate factory relates to foraminiferal and coralline algal and scleractinian production in seagrass environments. Isolated carbonate buildups with dominant seagrass-related carbonate production has been in the late Oligocene and early Miocene from the Malampaya buildup, Philippines, where changes in trophic states have operated (Fournier et al., 2004). The Malampaya and Yadana isolated systems show a number of similarities, including their predominantly aggrading stratigraphic architecture, the flat-topped morphology of the platform and the relative abundance of coral-rich facies. However, apart from coral, carbonate production in Malampaya is characterized by euphotic, seagrass-inhabiting benthic foraminifera (*Austrotrillina,* soritids, alveolinids, *Neorotalia*, *Miogypsina* and *Miogypsinoides*) whereas in Yadana the large foraminifers (Lepidocyclinids, *Spiroclypeus)* and encrusting coralline algae of oligo-mesophotic affinity are predominant. Additionally Euphotic carbonate production dominated by seagrass dwellers has been also recognized in the Aquitanian and Burdigalian ramps from Nepoui, New Caledonia (Maurizot et al., 2016), and from the Middle-to-Late Miocene Marion Plateau open platform (Conesa et al., 2005).

Accordingly, the study of the Yadana platform provides new insights into tropical carbonate production in Southeast Asia during the Cenozoic. Along with the classical euphotic, oligotrophic carbonate factory (Photozoan sensu James 1997), dominated by photosynthetic autotrophs and symbiont-bearing organisms including framework-building corals and large benthic foraminifera (e.g., Wilson and Evans, 2002; Saqab and Bourget, 2016), four tropical carbonate factories coexisted on top of Southeast Asian isolated buildups during the Miocene: (1) Seagrass-related, euphotic factory, (2) Oligo-mesophotic and oligo-mesotrophic large benthic foraminiferal and coralline algal factory, (3) a scleractinian carbonate factory developing under mesophotic conditions, (4) an echinodermal carbonate factory in disphotic to aphotic shelves. It also worth mentioning that these four carbonate factories characterize the Mediterranean Oligocene and the lower Miocene carbonate ramps (e.g. Brandano et al., 2017; Buxton and Pedley, 1989; Pomar et al., 2017)

2.6 Conclusion

Based on a detailed study of biological and sedimentological features from cores, well correlations and seismic expression, a revised depositional model of the early Aquitanian to mid Burdigalian carbonates from the Yadana platform is proposed and interpreted in terms of changes in turbidity, hydrodynamic water energy and nutrient availability.

(1) The layer-cake architecture inferred from seismic and well correlations, together with the low lateral changes in lithofacies suggest deposition on top of a flat-topped and open platform throughout the early Miocene interval. Oligo-mesophotic biological associations dominate whereas strictly euphotic constituents are lacking. Three types of carbonate factories operated at the top of the platform, depending on the paleoenvironmental context: (1) a scleractinian carbonate factory developing under mesophotic conditions during periods of particulate nutrient supplies, (2) an echinodermal carbonate factory occupying dysphotic to aphotic area of the shelf coevally with the scleractinian carbonate factory, and (3) large benthic foraminiferal-coralline algal carbonate factories prevailing under oligo-mesophotic and oligo-mesotrophic conditions.

(2) The three fundamental parameters controlling carbonate production on the Yadana platform were: (1) turbidity, (2) nutrient content, and (3) water energy. The dominantly low-energy setting of the oligo-mesophotic deposits suggests that deposition occurred below the fair-weather wave base. Changes from mesophotic to dysphotic-aphotic carbonate factories on the Yadana platform top through time may be related either to a change in water depth, or to a change in water transparency. The usual fragmentation of branching rhodoliths and the occurrence of brecciated intervals within early cemented coral-echinodermal lithofacies are indicative of frequent episodic high energy events such as storms, internal waves and/or cyclones.

(3) Finally, for the first time in the Oligo-Miocene from Southeast Asia, the case study documents the development history of a strictly oligo-mesophotic isolated carbonate platform with significant development of coral-rich deposits. Such events were likely responsible for changes in water turbidity and nutrient supplies as well as for the episodic occurrence of upwelling currents. Internal waves may also be regarded as a potential factor controlling both hydrodynamics and nutrient supplies. Such paleoceanographic conditions, characterized by variable trophic regimes, promoted development of an incipiently drowned platform, in oligo-mesophotic settings, during the whole early Miocene time interval.

III. Diagenesis

Diagenetic history and porosity evolution of an Early Miocene carbonate buildup (Upper Burman Limestone, Yadana gas field, offshore Myanmar)[2]

Thomas Teillet [1,2], *François Fournier* [1], *Franck Gisquet* [2], *Lucien F. Montaggioni* [1], *Jean Borgomano* [1], *Quentin Villeneuve* [1], *Fei Hong* [2]

[1] *: Aix-Marseille Université, CNRS, IRD, CEREGE, UM 34, 3 Place Victor Hugo, case 67, 13331 Marseille cedex 03, France*
[2] *: TOTAL, CSTJF, Avenue Larribau, 64018 Pau Cedex, France*

Abstract: The Miocene Yadana carbonate platform is a major offshore gas reservoir located in the Andaman Sea (offshore Myanmar). The integration of petrographic analysis of carbonate rocks, stable isotope measurements and seismic interpretation provided new insights into the diagenetic history of the Upper Burman Limestone reservoir. The high (28%) average porosity of the reservoir is dominantly related to strong development of microporosity, moldic and vuggy porosity. Mud-supported, coral-rich sediments record significant early marine dissolution of aragonite and early lithification of matrix that has led to the development of dense layers. Stable isotope and petrographic data from the top of the reservoir suggest that the long-term depositional hiatus (middle to late Miocene) was related to the platform drowning and non-deposition in a deep marine setting. Moderate dolomitization has affected the top and flanks of the platform during the depositional hiatus. Microporosity development and sparry calcite cementation mainly occurred in marine to marine shallow burial environments. A major decrease in porosity, averaging 10%, below the gas-water contact suggests a major phase of porosity evolution during and/or after the hydrocarbon emplacement which is mainly related to 1) increased moldic and vuggy porosity development within the gas zone, 2) microporosity preservation in loosely packed, subrounded micrites within the

---

[2] Published in Marine and Petroleum Geology: https://doi.org/10.1016/j.marpetgeo.2019.06.044

gas zone, and 3) microporosity reduction by calcite precipitation within the water zone leading to the development of densely packed, euhedral micrites.

3.1 Introduction

The diagenetic evolution of Cenozoic carbonate buildups, from the humid equatorial tropics of SE Asia, has been widely documented, in particular because these form the reservoirs of many hydrocarbon fields in the region (e.g. Fournier et al., 2004; Sattler et al., 2004; Wilson and Hall, 2010; Zampetti, 2010). The diagenetic history of such shallow-water carbonate systems is commonly driven strongly by the occurrence of intraformational subaerial exposure events that have severely modified the mineralogical patterns as well as the volume and structure of the pore networks (e.g., Sun and Esteban, 1994; Saller and Vijaya, 2002; Sattler et al., 2004; Fournier and Borgomano, 2007; Madden and Wilson, 2013). In such a context, best reservoirs commonly developed beneath subaerial unconformities in highstand carbonate buildups that have been subject to intense meteoric water leaching and karstification (Sun and Esteban, 1994; Moldovanyi et al., 1995; Vahrenkamp et al., 2004). Additionally, the later diagenetic evolution and the reservoir architecture of such shallow-water carbonates have been shown to be largely controlled by porosity and permeability distribution inherited from early stages of subaerial exposures (Fournier and Borgomano, 2007). In a few case studies such as the Miocene carbonates from the Liuhua oil field, offshore R.P. China (Sattler et al., 2004) and Miocene carbonate buildups from the Luconia Province (Zampetti, 2010), burial dissolution of carbonates has been proposed as a major process of porosity enhancement.

The Lower Miocene Yadana carbonate buildup (Upper Burman Limestone, offshore Myanmar) is known to be highly porous (av. porosity: 28%) and to be the main reservoir of a significant gas accumulation (Racey, 2015). Based on the integration of detailed petrographic analyses of cores, thin sections and SEM images, stable isotope (C and O) measurements, well logs and seismic interpretations, the present paper aims at: (1) reconstructing the diagenetic history and the porosity evolution of the Lower Miocene Yadana carbonate buildup, (2) identifying the main diagenetic processes that has controlled the development of a highly porous reservoir in carbonates with little meteoric diagenetic overprint, (3) constraining the timing and processes of evolution and preservation of micrite microfabrics and associated microporosity and (4) assessing the impact of gas emplacements on the late diagenetic evolution of the reservoir and on the porosity distribution within the carbonate buildup.

3.2 Geological setting

The structural framework and the marine and landmass geomorphology of the Andaman Sea area has been strongly controlled by the complex tectonic evolution of SE Asia during the Cenozoic (Hall, 2012, 2002, 1997; Lee and Lawver, 1995). During the Paleogene, the northeastward oblique subduction (Sunda subduction zone) of the Indian Plate beneath the Eurasian Plate (Fig. 3-1A) resulted in the opening of the Andaman Sea as a back-arc basin (Chakraborty and Khan, 2009; Curray, 2005). In addition, such an oblique subduction led to: 1) major dextral strike-slip movements along the Sagaing-Andaman-Sumatran fault system, 2) the formation of the Burmese microplate, and 3) rifting and spreading of the Andaman Sea within the back-arc basin (Chakraborty and Khan, 2009; Morley, 2012). During the Oligocene and early Miocene, the Yadana carbonate platform developed on the top of a volcanic ridge east of the Sunda subduction zone and between the M5 Basin and the Moattama Basin (Morley, 2013; Racey, 2015) (Fig. 3-1C).

The Moattama Basin contains Eocene to modern sediments. The lowermost deposits consist of Upper Eocene volcano-clastics sediments (Fig. 3-1E). The overlying Oligo-Miocene shallow-water carbonates may reach up to 700 m in thickness, and are subdivided into two distinct formations (Paumard et al., 2017). These are: (1) the Lower Burman Limestone Formation, late Oligocene in age, that is composed of two distinct carbonate platforms separated by a central incised valley filled by the Sein clastic formation and (2) the Upper Burman Limestone Formation, early Miocene in age, that is made up of one single carbonate platform, the top of which corresponds to the gas reservoir of the Yadana Field (Fig. 1D). A long-duration depositional hiatus (~10 Myr) is recorded at the top of the Upper Burman Limestones which are sealed by Upper Miocene (N17, planktonic zone) pro-delta shales (Pyawbwe and Badamyar formations) from the Irrawaddy deltaic system. A major phase of eastward tilting of the Yadana platform, evidenced by seismic profiles (Fig. 3-1D), occurred during the Late Miocene (horizon M6: 8.2 Ma, after Paumard et al., 2017). From the Pliocene to Pleistocene, the Moattama Basin became a major depocentre, with up to 10 km-thick terrigenous deposits supplied from the Irrawaddy deltaic system. The present study focusing on the uppermost part of the UBL Formation corresponding to the last 100 m of carbonates at the top of the western part of the platform (e.g., the gas reservoir; Figure 3-1).

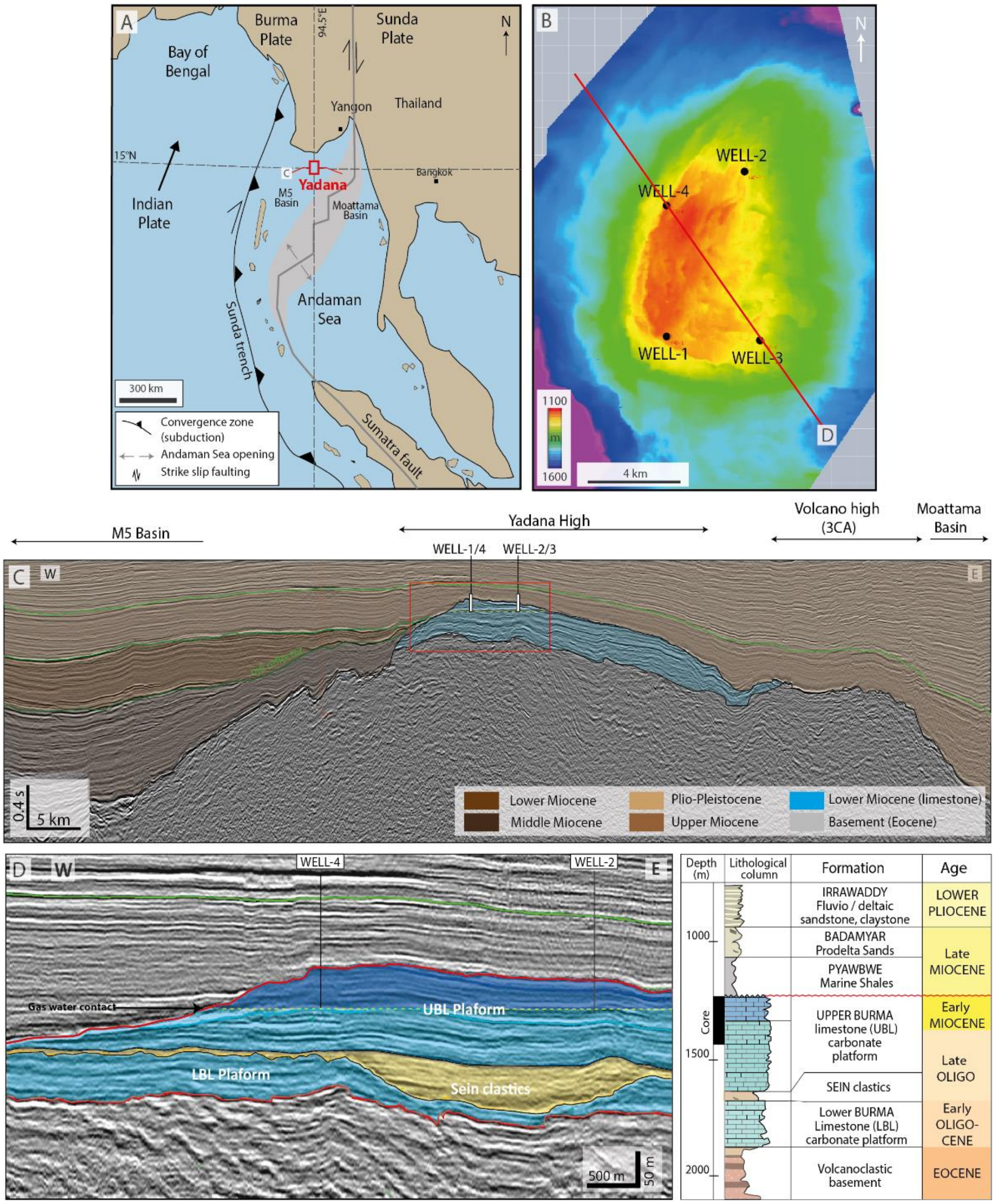

Figure 3-1 : Geographical and geological setting of the Yadana gas field: (A) Geographical and tectonic settings of the Andaman Sea and the Yadana Field (after [Curray, 2005]; (B) Depth map of top reservoir and well location. (C) Interpreted regional 2D seismic profile [two-way time) through the Yadana high (see location on A). (D) Interpreted seismic profile (depth) of the Yadana field crossing the wells WELL-4 and WELL-2, showing the lithostratigraphic units and the gas water contact (yellow dotted lines) (see location on A). (E). Lithostratigraphic column of the Yadana platform.

3.3 Data and Methods

The present work is based on the analysis of a subsurface database including well logs and cores. The Upper Burman Limestone has been penetrated by 20 wells. Four wells (WELL-1, WELL-2, WELL-3 and WELL-4) have been selected for the present study (location in Fig. 1B). A total of 343 m of cored sections are available through the reservoir (WELL-1: 87.5 mCD (meter Core Depth), WELL-2: 84 mCD WELL-3: 59.5 mCD WELL-4: 112 mCD). These were described in terms of lithology, depositional features (texture, biological associations) and diagenetic features.

A total of 694 thin sections have been prepared from cores (average spacing of 50 cm). The thin sections were impregnated with a blue epoxy resin and half-stained with alizarine-red and potassium ferrocyanide solution (Dickson, 1966) for the identification of carbonate minerals. Thin sections were observed under polarized-light microscopy for the characterization of depositional and diagenetic features as well as for the quantitative analysis of pore types. Macroporosity is defined as the pore space which is colored with blue epoxy and whose size exceeds 2 pixels (i.e., diameter> 10 µm) on scanned thin sections. The proportion of macroporosity on thin section is automatically extracted using the software ImageJ by gathering the blue pixels. Microporosity is defined as pores non-visible on thin section pictures or whose size is lower than 2 pixels (i.e., pore diameter <10 µm). The definition of microporosity used in the present work is therefore consistent with the definition given by Cantrell and Hagerty, 1999. The proportion of microporosity was semi-quantitatively estimated as the difference between the laboratory porosity measured on plugs and the macroporosity computed from thin-section image analysis. Although based on two-dimensional images, image analysis has been shown to provide accurate quantification of macroporosity in carbonate reservoirs (Haines et al., 2015). Petrographic analysis of thin sections was supported by observations of selected samples of cement under cathodoluminescence using an 8200 MKII Technosyn (20 kV and 600 mA; Technosyn, Cambridge, UK) coupled to an Olympus microscope (Olympus Optical Corporation, Tokyo, Japan) and a digital MRc5 camera (Zeiss, Göttingen, Germany). Micrite microfabrics were characterized by environmental scanning electron microscopy (SEM) images performed at Aix-Marseille University by using Philips XL30 ESEM®.

Laboratory porosity measurements have been performed on approximately 1000 core plugs. Vertical changes of porosity in cored and non-cored intervals have been also investigated by means of well-log data: a porosity log has been computed from density and neutron logs and corrected from gas effect.

Additionally, up to 1000 carbon and oxygen isotope ratios were measured at Erlangen University on bulk samples and selected carbonate components. Carbonate powders were prepared using a manual micro-drill and reacted with 100% phosphoric acid at 70°C using a Gasbench II connected to a ThermoFisher Delta V Plus mass spectrometer. All values are reported in per mil relative to V-PDB. Reproducibility and accuracy were monitored by replicate analysis of laboratory standards calibrated by assigning δ13C values of +1.95‰ to NBS19 and -47.3‰ to IAEA-CO9 and δ18O values of-2.20‰ to NBS19 and -23.2‰ to NBS18. Reproducibility for δ13 C and δ18O was ±0.06‰.

Elemental determinations of major (Al, Ca, Mg, Na, K, Ti, Fe, Mn, P, S in percent) and minor elements (including Cu, Pb, Zn As, U, Th, Sr, Ba in ppm) on whole rock and selected carbonate components (bioclasts, matrix and cement) were carried out at Bureau Veritas Commodities Canada Ltd., Vancouver, Canada on a total of 17 rock samples, by using inductively coupled plasma spectrometry (ICP-ES/MS) with a PerkinElmer ICP-MS ELAN® 9000 (PerkinElemer, Inc., 146 Waltham, Massachusetts, USA) which was calibrated using Bureau Veritas interlaboratory standards DS10 and Oreas 45Ea. Samples (~1 gram) were pulverized to a fine powder (~3.75 148 phi) and were digested by using the AQ250 Ultra Trace Geochemical aqua regia (HNO3-HCl) package for two hours at 95°C. Detection limits range from 1 to 5 ppm for minor elements 150 and average 0.01% for major elements.

3.4 Results

3.4.1 Depositional lithofacies of the Upper Burman Limestone

Skeletal grains are dominated by non-geniculate coralline algae and large benthic foraminifers (Fig. 3-2A, B, and C). Coral may be common in a few intervals (Fig 3-2D). Non-geniculate coralline-red algae are dominated by encrusting to branching forms, commonly forming nodules (rhodoliths) (Fig. 3-2A). The dominant genera are *Lithothamnion*, *Mesophyllum* and *Sporolithon*. Larger benthic foraminiferal association is characterized by Lepidocyclinids, *Spiroclypeus*, and *Cycloclypeus* commonly displaying flat-shaped morphologies (Fig. 3-2C). Scleractinian assemblage includes robust branching or massive forms and subordinate components include echinoderms, bryozoans, green algae and rare planktonic foraminifera. On the basis of textural and biological features, four

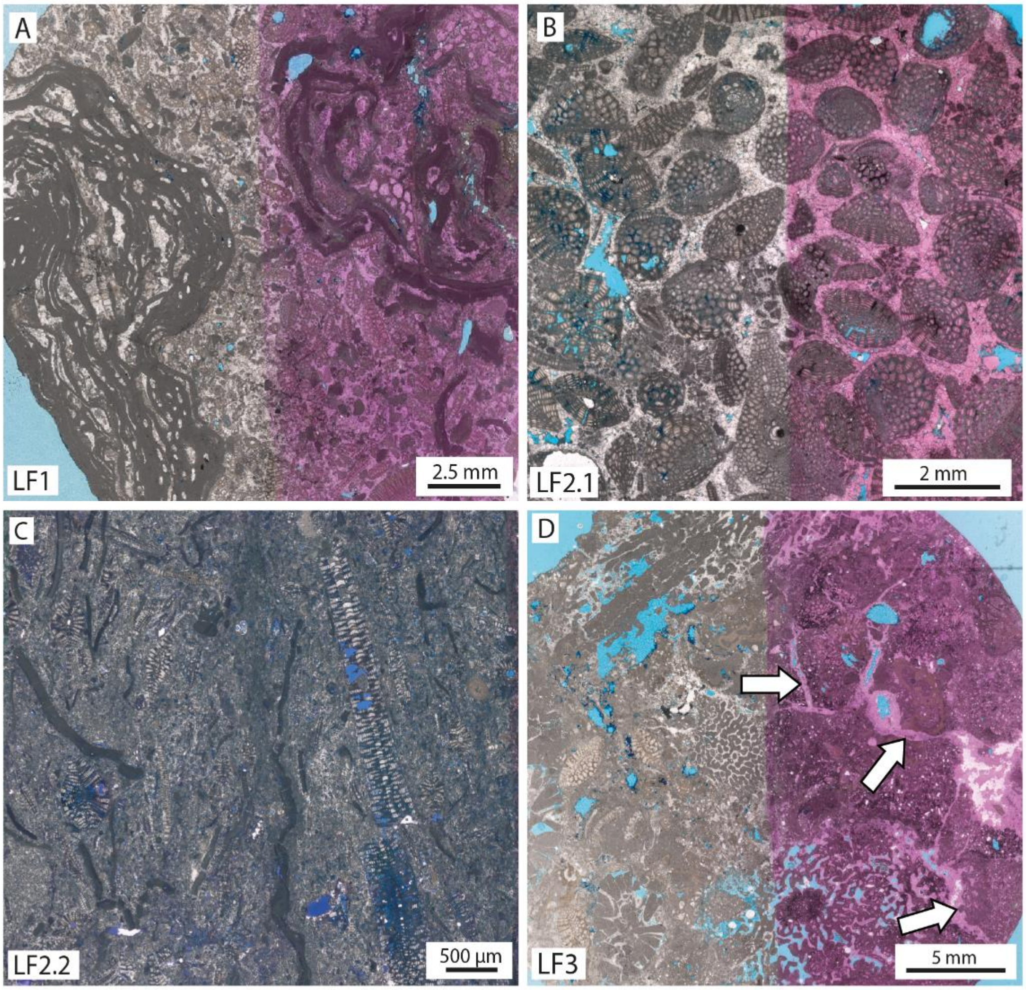

Figure 3-2: Microphotographs of lithofacies from the Upper Burman Limestone. (A) WELL-1 1284.15 mCD: Coralline algal rudstone (LF1). (B) WELL-1 1319.04 mCD: Large benthic foraminiferal rudstone (LF2.1). (C) WELL-2 1324.78 mCD: Large benthic foraminiferal floatstone (LF2.2). (D) WELL-1 1325.96 mCD: Coral floatstone (LF3) with curved fractures (arrow) indicating incipient brecciation.

lithofacies have been identified (Table 2): coralline algal and foraminiferal floatstone (LF1: Fig. 3-3A), large benthic foraminiferal 168 grainstone/rudstone (LF2.1: Fig. 3-3B) and floatstone (LF2.2: Fig. 3-3C), scleractinian echinodermal floatstone (LF3.1: Fig. 3-3D) and echinodermal wackestone (LF3.2).

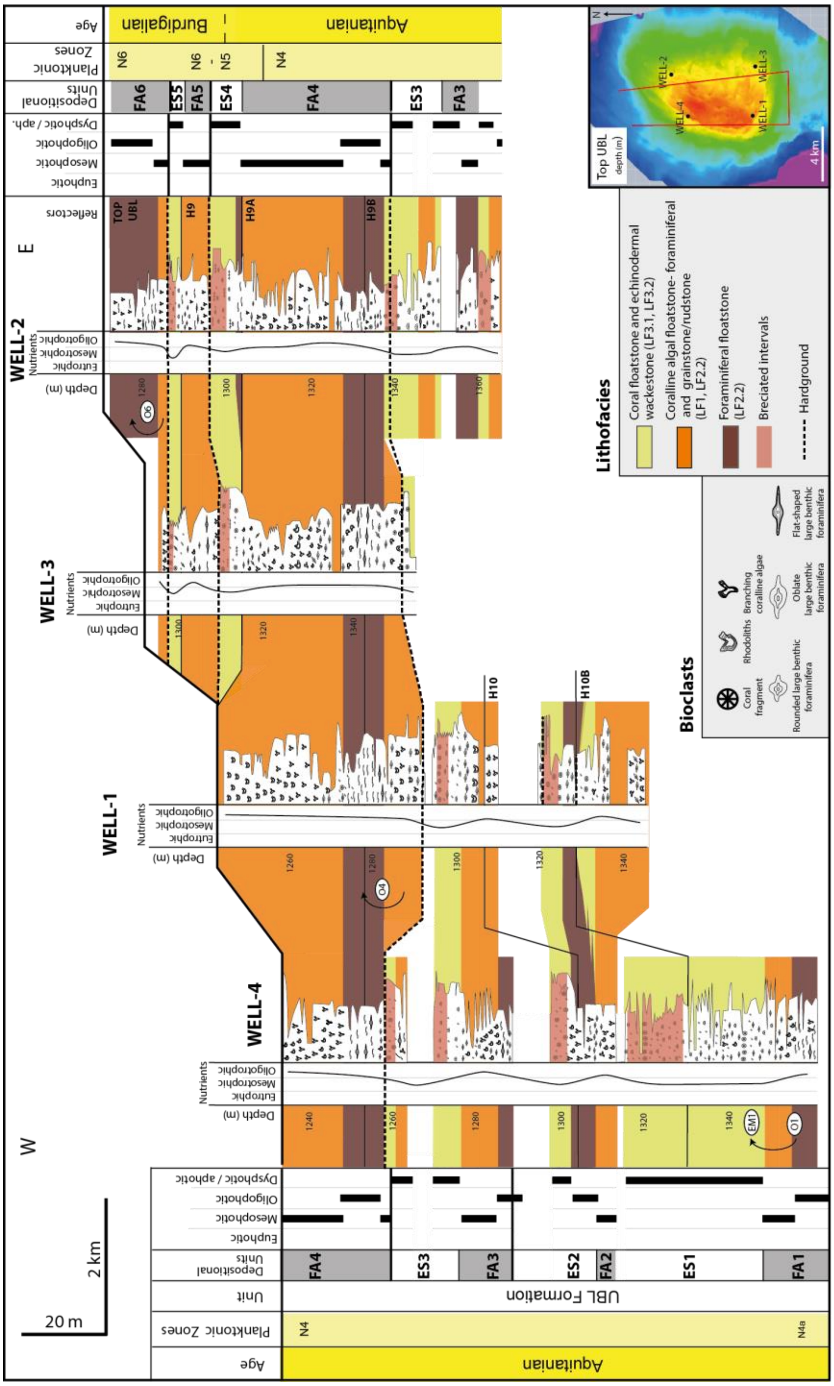

Figure 3-3: Well-correlations and stratigraphic architecture of the Yadana platform, based on large benthic foraminiferal biostratigraphy, well-to seismic ties (vertical resolution ~10 m) and correlation of key stratigraphic surfaces. Key seismic reflectors (H9, H9A, H9B, H10, and H10B) are positioned on the well-correlation panel.

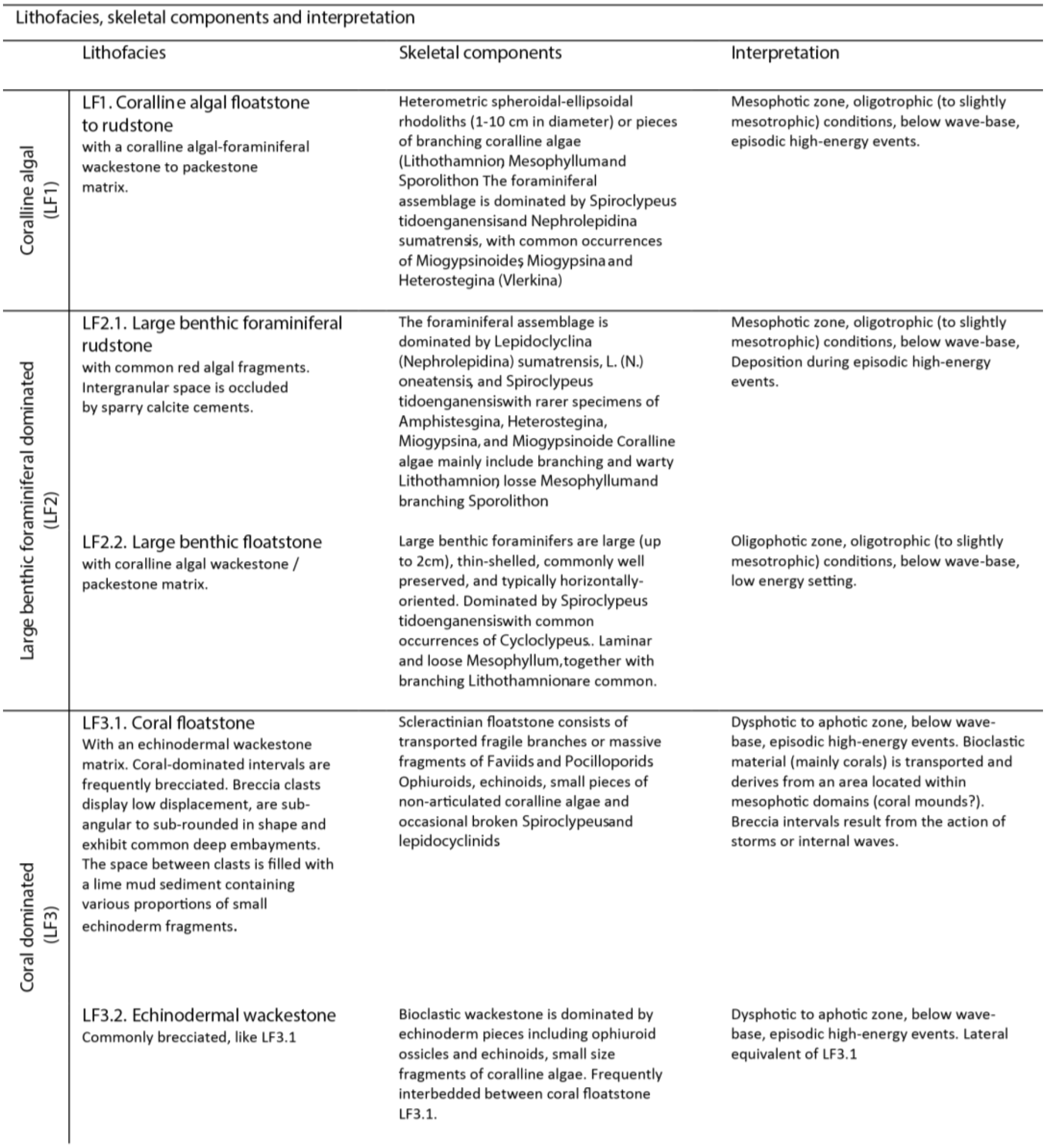

Lithofacies, skeletal components and interpretation

	Lithofacies	Skeletal components	Interpretation
Coralline algal (LF1)	**LF1. Coralline algal floatstone to rudstone** with a coralline algal-foraminiferal wackestone to packestone matrix.	Heterometric spheroidal-ellipsoidal rhodoliths (1-10 cm in diameter) or pieces of branching coralline algae (Lithothamnion, Mesophyllumand Sporolithon The foraminiferal assemblage is dominated by Spiroclypeus tidoenganensisand Nephrolepidina sumatrensis, with common occurrences of Miogypsinoides, Miogypsina and Heterostegina (Vlerkina)	Mesophotic zone, oligotrophic (to slightly mesotrophic) conditions, below wave-base, episodic high-energy events.
Large benthic foraminiferal dominated (LF2)	**LF2.1. Large benthic foraminiferal rudstone** with common red algal fragments. Intergranular space is occluded by sparry calcite cements.	The foraminiferal assemblage is dominated by Lepidocyclina (Nephrolepidina) sumatrensis, L. (N.) oneatensis, and Spiroclypeus tidoenganensiswith rarer specimens of Amphistesgina, Heterostegina, Miogypsina, and Miogypsinoide Coralline algae mainly include branching and warty Lithothamnion, losse Mesophyllumand branching Sporolithon	Mesophotic zone, oligotrophic (to slightly mesotrophic) conditions, below wave-base, Deposition during episodic high-energy events.
	LF2.2. Large benthic floatstone with coralline algal wackestone / packestone matrix.	Large benthic foraminifers are large (up to 2cm), thin-shelled, commonly well preserved, and typically horizontally-oriented. Dominated by Spiroclypeus tidoenganensiswith common occurrences of Cycloclypeus.. Laminar and loose Mesophyllum,together with branching Lithothamnionare common.	Oligophotic zone, oligotrophic (to slightly mesotrophic) conditions, below wave-base, low energy setting.
Coral dominated (LF3)	**LF3.1. Coral floatstone** With an echinodermal wackestone matrix. Coral-dominated intervals are frequently brecciated. Breccia clasts display low displacement, are sub-angular to sub-rounded in shape and exhibit common deep embayments. The space between clasts is filled with a lime mud sediment containing various proportions of small echinoderm fragments.	Scleractinian floatstone consists of transported fragile branches or massive fragments of Faviids and Pocilloporids Ophiuroids, echinoids, small pieces of non-articulated coralline algae and occasional broken Spiroclypeusand lepidocyclinids	Dysphotic to aphotic zone, below wave-base, episodic high-energy events. Bioclastic material (mainly corals) is transported and derives from an area located within mesophotic domains (coral mounds?). Breccia intervals result from the action of storms or internal waves.
	LF3.2. Echinodermal wackestone Commonly brecciated, like LF3.1	Bioclastic wackestone is dominated by echinoderm pieces including ophiuroid ossicles and echinoids, small size fragments of coralline algae. Frequently interbedded between coral floatstone LF3.1.	Dysphotic to aphotic zone, below wave-base, episodic high-energy events. Lateral equivalent of LF3.1

Table 2**:** Deposiotional lithofacies and skeletal components of the Upper Burma Limestone

3.4.2 Petrography of diagenetic features

The main diagenetic processes observed in cores are dissolution, cementation and dolomitization. Compaction is relatively weak with rare presence of stylolites in cemented intervals and open fractures.

Carbonate cements

Two distinct carbonate cements have been evidenced from petrographic analysis of thin sections: Isopacheous calcite cement (C1) and blocky calcite cement (C2).

Isopacheous calcite cement (C1) consists of isopacheous rims of scalenohedral, sparry, nonferroan (stained pink with Alizarin Red S and potassium ferricyanide) calcite crystals, dull brown under cathodoluminescence, averaging 10 µm in thickness (Fig. 3-4A, B, C). C1 cements may rim large intergranular pores in rudstones or moldic pores after dissolving aragonite bioclasts.

The blocky calcite cements (C2) consist of sparry, nonferroan calcite (50 to 250 µm) occluding intragranular pores in grainstone and rudstones (in gas and water zones), moldic/vuggy pores and fractures (mainly within the water zone) (Fig. 3-4A, C). Calcite cements C2 have been observed overlying calcite cement rims C1 (Fig.3-4A, B, C). These cements are zoned and composed of (Fig. 3-4B): (1) a first fringe of non-luminescent to dull calcite lining pore wall, (2) a fine and concentric dull to bright orange bands, and (3) a large internal zone occluding the pore and filled by a non-luminescent calcite. Large syntaxial sparry calcite cements (up to hundreds few microns) may also develop around echinoderm pieces in grainstone facies (Fig. 3-4C).

Neomorphic features

Calcitized aragonitic bioclasts (dominantly coral fragments) display two types of neomorphic features: Calcitized corals dominantly composed of equant calcite crystals (20 to 250 µm) (C2') (Fig. 3-4D). Calcitized coral composed of large (250-1000 µm), orange-brown under natural light, sparry calcite crystals (CX) (Fig. 3-4E, F). CX calcites are non-luminescent and have been encountered only within brecciated scleractinian-rich limestone (LF3 lithofacies).

Micrite microfabrics

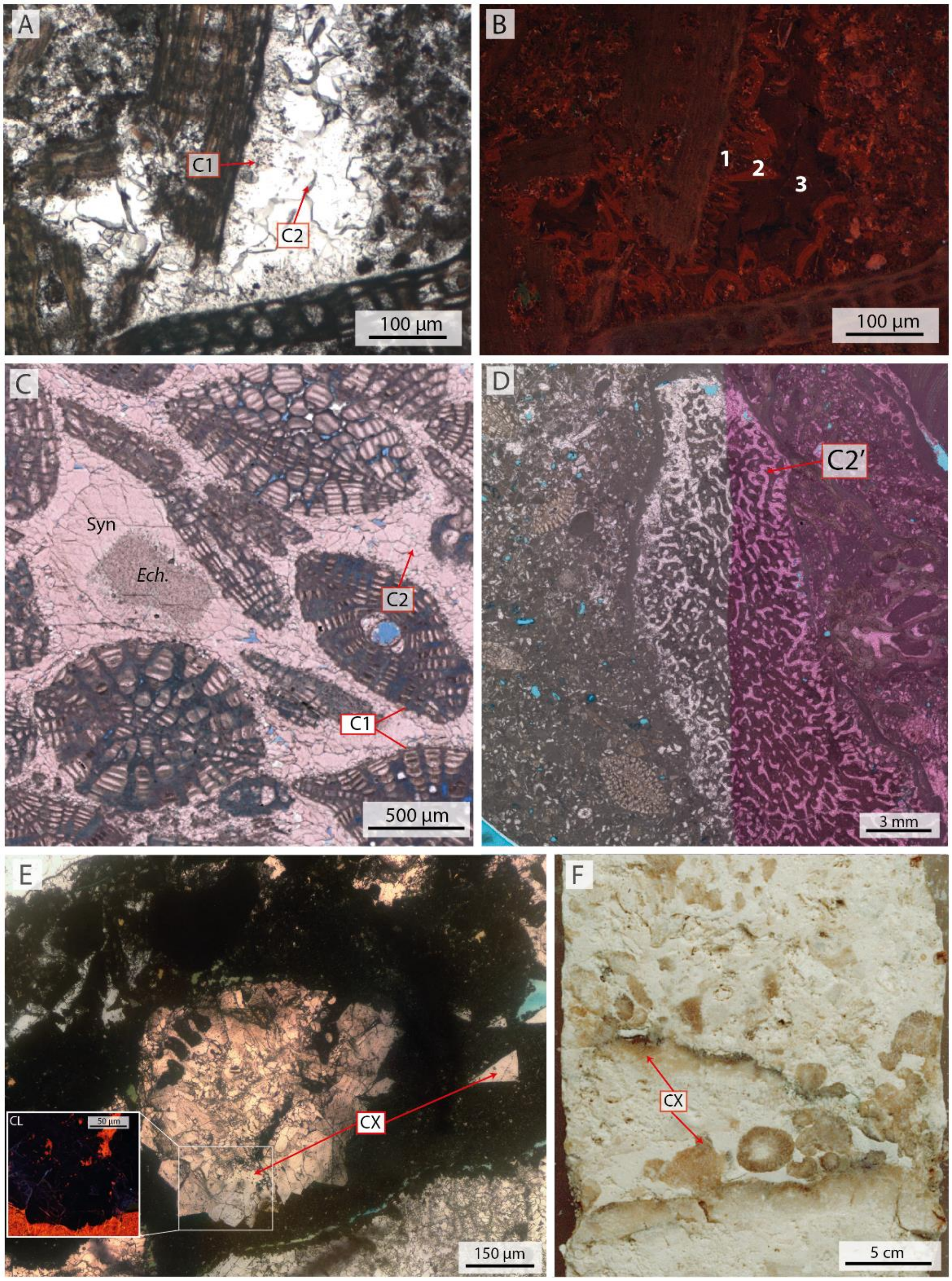
A
C1
C2
100 µm
B
1
2
3
100 µm
C
Syn
Ech.
C2
C1
500 µm
D
C2'
3 mm
E
CL
50 µm
CX
150 µm
F
CX
5 cm

Figure 3-4: Microphotographs of selected diagenetic features from the Upper Burman Limestone. (A, B): WELL-2 1355.6 mCD: Isopacheous rim cement C1 and blocky calcite cement C2 under polarized-light microscopy (A) and cathodoluminescence (B); Three zones are distinguished from cathodoluminescence: (1) C1 rim cement, lining the pore space, non-luminescent, (2) early phase of C2 cement formed by concentric, thin (20µm) bands with dull to bright luminescence and (3) later, non-luminescent, C2 cement (diagenetic facies: G-DF2). (C) WELL-3 1319.49 mCD: Isopacheous C1 rim cement and blocky calcite cement C2 infilling the intergranular pore space of a foraminiferal rudstone (diagenetic facies: G-DF2). A syntaxial calcite cement (Syn) develops around an echinoderm (Ech) fragment. (D) WELL-1 1328.03 mCD: equigranular sparry calcite replacing a coral fragment (C2'). (E) WELL-4 1326.45 mCD: Fragment of calcitized coral (CX) set in a micrite mud sediment which postdates the development of CX calcite overgrowths (red arrows) around the coral. (F) WELL-4 1337.7 mCD: core picture showing brownish calcitized coral (CX) within a brecciated interval.

Four main micrite microfabrics have been identified under SEM in both micritized bioclasts and micrite matrix (Fig. 3-5). In the gas zone, high porosity limestones (20-45%) exhibit dominantly loosely packed, anhedral, subrounded calcimicrites (M1 microfabric: Fig. 3-5A, B). Subhedral micrite particles may be present in smaller proportions within the M1 micrite (Fig. 3-5A). Such micrite may contain interparticle micropores that are larger than the average size of the micrite particles (around 1µm), with pore diameters ranging typically from 2 to 10 µm (=micro-vugs; Fig 3-5A). Micrite M1 commonly displays aggregates (5-10 µm) of coalescent micrite particles (Fig 3-5B). In a few intervals, M1 calcimicrites may coexist in samples with euhedral dolomicrite crystals (M4 microfabric: Fig. 3-5B). In gas-bearing limestone with porosity <20%, both micrite matrix and micritized allochems exhibit densely packed, coalescent, anhedral micrite crystals (M2 microfabric: Fig. 3-5C). The M2 micrite microfabric occurs typically in the matrix of coral-rich floatstones (lithofacies LF3). In the water zone, carbonates display low to moderate microporosity. In both matrix and micritized bioclasts, micrite crystals are mainly euhedral (M3 microfabric: Fig. 3-5D, E) and are coarser (typically 2-4µ) than gas-zone calcimicrites M1 and M2.

Additionally, euhedral crystals may encase smaller, rounded micrite particles (Fig. 3-5E). Finally, euhedral dolomicrite particles (from 0.5 to 4 µm) occur within micritized bioclasts (typically coralline algae) and matrix (Fig. 3-5F) from the water and the gas legs.

Dissolution features

Selective dissolution of aragonitic skeletal elements (mainly sclereactinians) and subsequent infill of the moldic pores by sediment (micrite mud and fine-grained skeletal fragments) are common diagenetic features in coral-rich lithofacies (LF3) (Fig. 3-6A, B). The sediment replacing the dissolved septae is of similar nature and in physical continuity with the lime mudstone matrix in which the coral fragments are embedded, thus leading to a faint-ghost fabric (sensu Sanders, 2003). Non-selective dissolution features affecting both aragonitic and calcitic bioclasts as well as micrite matrix may lead to the formation of moldic and vugs pores (Fig. 3-7A) which are devoid of any sediment or cement infill. Such dissolution features contribute significantly to the porosity of the reservoir (typically 5-20% of the rock volume) within the gas zone but are rarer or absent within the water zone.

Brecciation features

Brecciated intervals are common within coral floatstones (LF3.1) and echinodermal wackestones (LF3.2) lithofacies. Two distinct carbonate breccias have been identified:

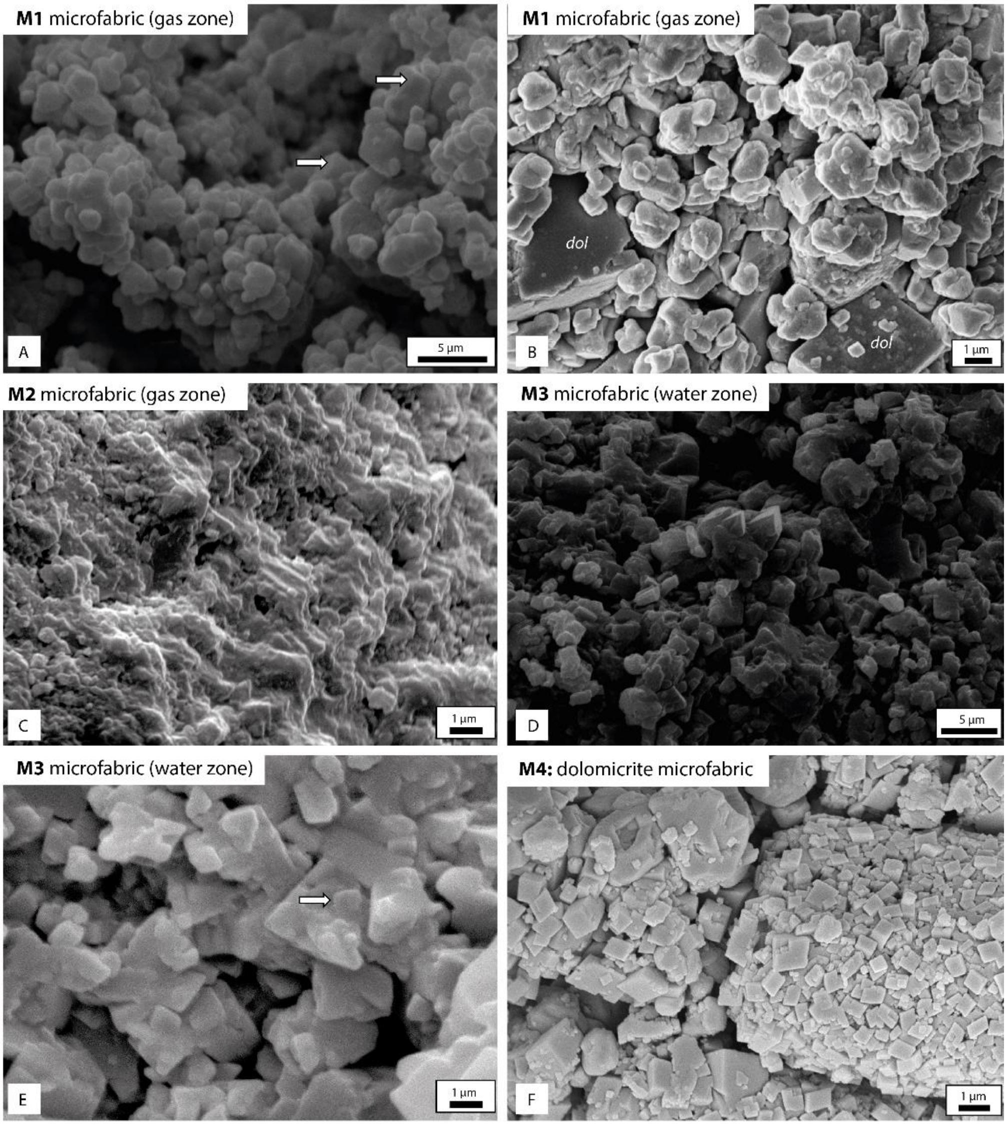

Figure 3-5: Micrite microfabrics identified under SEM: (A) Highly porous calcimicrite microtexture M1 showing loosely packed, dominantly anhedral, subrounded micrite particles. Such micrites display commonly microvugs (diameter: 5-10 µ) and relatively minor particle coalescence (gas zone). Few micrite particles exhibit subhedral morphology (arrow), (B) Highly porous calcimicrite microtexture M1, mixed with larger euhedral dolomicrosparite crystals (dol) (gas zone) (C) Low porosity calcimicrite microtexture M2 showing densely packed, strongly coalescent, anhedral micrite particles (gas zone). (D) Low porosity micrite microtexture M3 showing densely packed, subhedral to euhedral calcimicrite crystals (water zone) (E) Low porosity micrite microtexture M3 showing densely packed, euhedral calcimicrite crystals encasing smaller, rounded micrite particles (arrow) (water zone). (D) Euhedral dolomicrite (M4) replacing a coralline algae (gas zone).

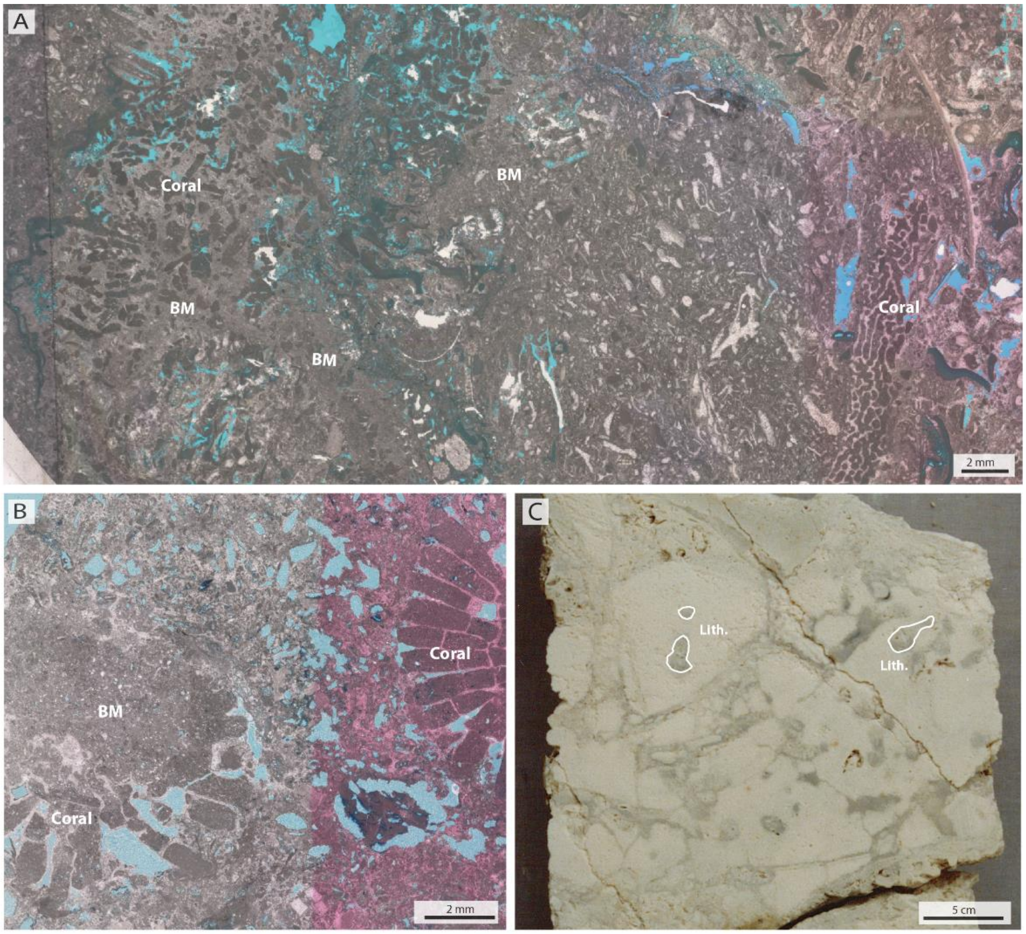

Figure 3-6: Micro-photographs of early marine dissolution features from the Upper Burman Limestone under polarized light microscopy: (A) WELL-3 1311.84 mCD: Coral floatstone whose scleractinian elements have been dissolved; the resulting moldic pores are infilled with a bioclastic micrite (MB) which is similar in nature to that of the floatstone matrix this leading to a faint-ghost fabric (diagenetic facies: G-DF4). (B) Close-up on dissolved coral calyces infilled by bioclastic mud lime (BM). (C) WELL-1 1256.6 mCD. Core samples showing a high microporous, brecciated coral (LF3) with lithophage burrows (Lith.) (Diagenetic facies: G-DF4).

- Type I breccia: thin beds (<20 cm) of low porosity (<20%) breccia, characterized by poorly sorted, irregular-shaped elements which are commonly interlocked and displaying very low displacement (Fig. 3-6C, 3-7C). Micrite within the fragments are tight (M2 microfabrics) and the space between fragments is filled with finely bioclastic wackestone material. The outlines of the clasts commonly display deep embayments (Fig. 3-6C).

- Type II breccia: thick interval (up to 10 m) of highly porous, loose breccia with large (up to 10 cm) angular and poorly sorted fragments which are composed of coral floatstones. In breccia type II, coral fragments are replaced by CX brownish calcite (Fig. 3-4F). The space between clasts may be partially filled with a finely bioclastic, matrix-supported sediment, but residual pore space may be preserved or filled by C2 sparry calcite cements.

Dolomitization

In various intervals, intragranular and matrix micrite is partially replaced by euhedral dolomite micro-rhombs (<50 µm) (Fig. 3-7B). As revealed by SEM observations (Fig. 3-5F), dolomicrite rhombs (M4 microfabric) are associated with M1 calcimicrites. Such dolomitized intervals do not clearly follow the stratigraphic architecture of the platform: they are common and scattered in some wells (e.g., WELL-2) and almost lacking laterally, in time-equivalent intervals (e.g., in WELL-1).

Stylolites

Compaction features are relatively scarce within the Upper Burman Limestone. In a few thin sections, stylolites are overprinted by dissolution vugs (Fig. 3-7E).

3.4.3 Definition of diagenetic facies

Diagenetic facies have been defined by the combination of selected petrographic, and petrophysical and geochemical parameters (Table 3): 1) diagenetic features, 2) micrite microfabrics, 3) range of porosity values and 4) pores type association. The significant decrease in average porosity below the gas-water contact (Fig. 3-8) and the distinct

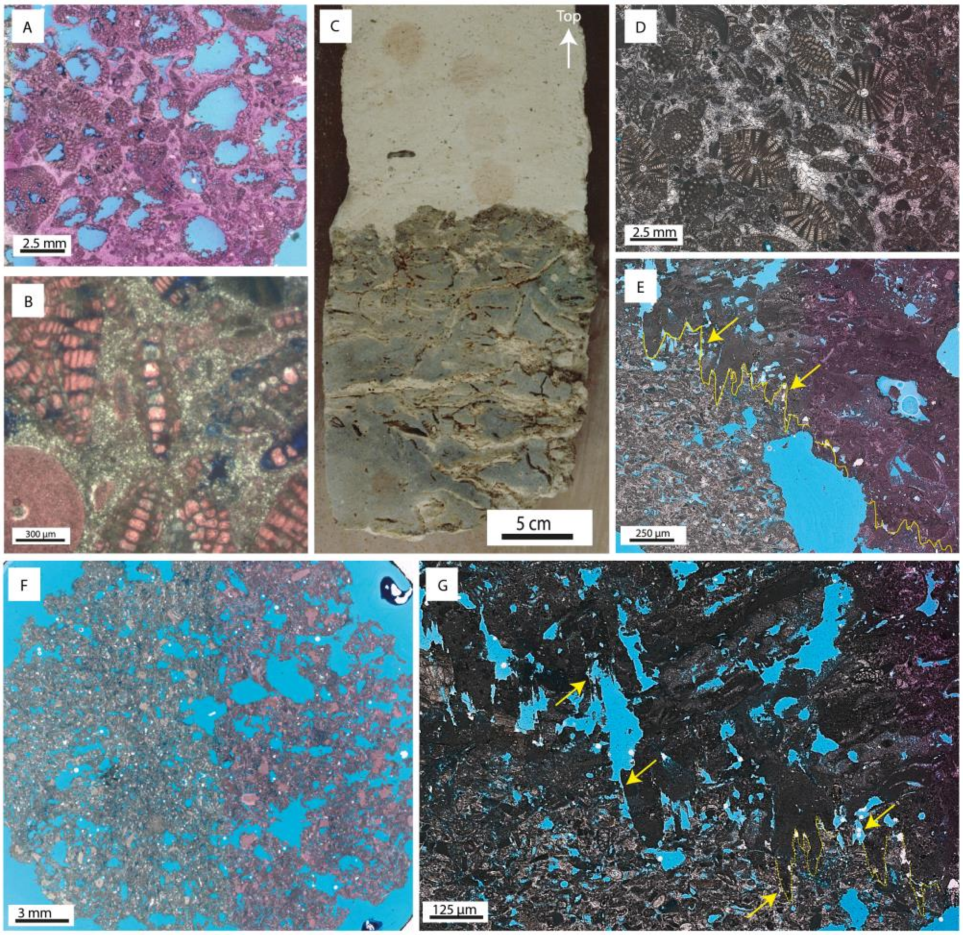

Figure 3-7: A) WELL-3 1319.92 mCD: microphotograph of a moldic pore and vugs within a foraminiferal grainstone. The intergranular pore space is entirely occluded by C2 sparry calcite (diagenetic facies: G-DF2) (C2). (B) WELL-4 1286 mCD: microphotograph of a foraminiferal packstone-floatstone whose matrix is partially replaced by dolomicrosparite (not stained by alizarine) (diagenetic facies: G-DF1C); (C) WELL-3 1308.05 mCD: core photograph of a hardground surface, at the top of a carbonate breccia composed of poorly displaced, tight elements of coral-rich and echinodermal floatstone (LF3) (diagenetic facies: G-DF4). The hardground is sharply overlain by high microporous, coralline algal-foraminiferal floatstone (diagenetic facies: G-DF1A). The inter-clast space of the hardground breccia is filled by the overlying microporous sediment. (D) WELL-2: 1354.56m CD: foraminiferal grainstone-rudstone from the water zone (diagenetic facies: W-DF1). The relatively low porosity (14%) of the sample is related to the lack of intergranular and moldic/vuggy macroporosity and to the microporosity reduction by calcite precipitation development within micritized bioclasts. (E) WELL-2 1284.56 mCD: microphotograph of a coralline algal-foraminiferal floatstone showing a stylolite (yellow line) which is overprinted by a dissolution vug (diagenetic facies: G-DF1A). (F) WELL-4 1347.14: Echinodermal floatstone 1096 showing pervasive moldic and vuggy porosity (G-DF1B). (G) Close up of (E) showing dissolution features affecting a stylolite (arrows).

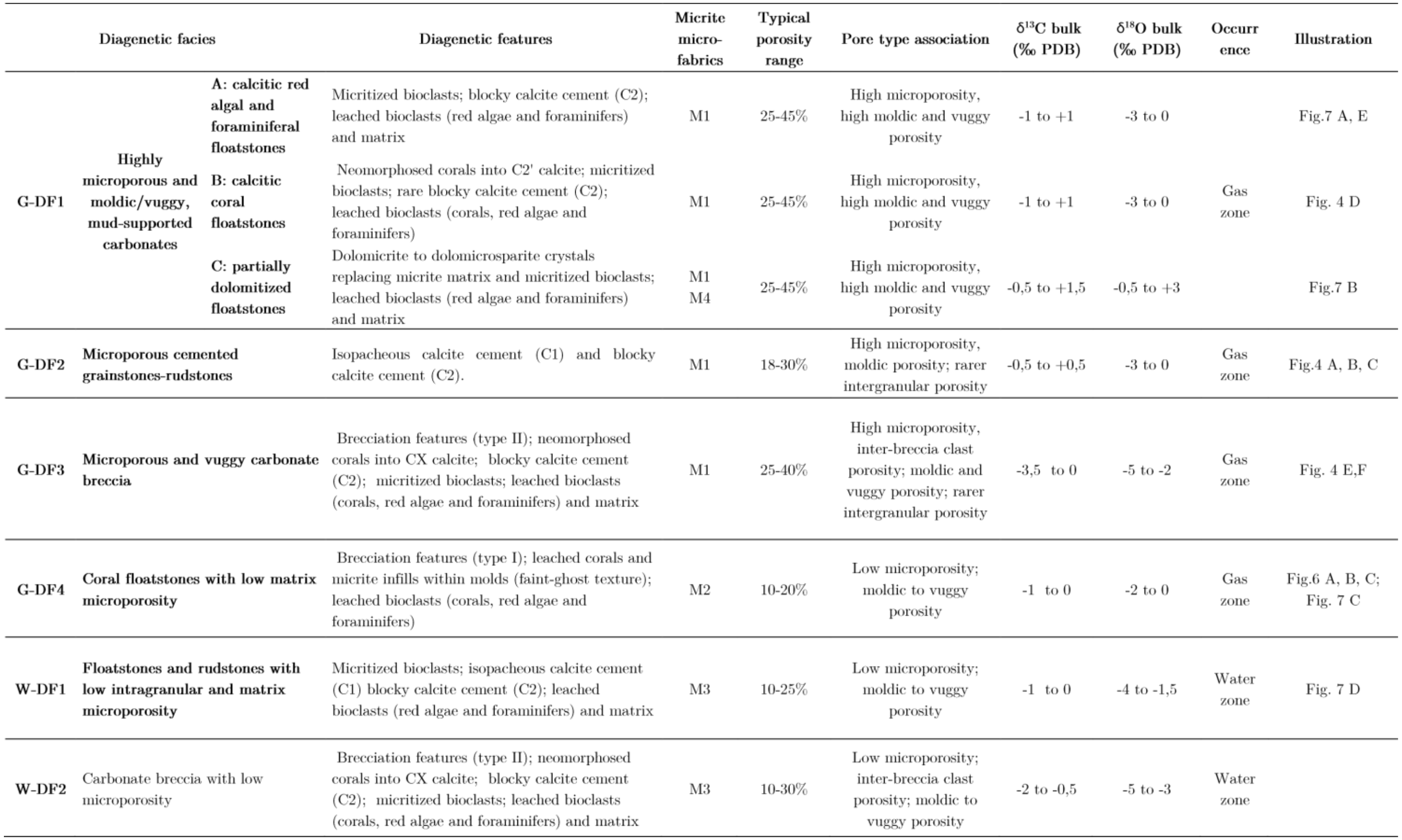

Diagenetic facies			Diagenetic features	Micrite micro-fabrics	Typical porosity range	Pore type association	δ¹³C bulk (‰ PDB)	δ¹⁸O bulk (‰ PDB)	Occurrence	Illustration
G-DF1	**Highly microporous and moldic/vuggy, mud-supported carbonates**	**A: calcitic red algal and foraminiferal floatstones**	Micritized bioclasts; blocky calcite cement (C2); leached bioclasts (red algae and foraminifers) and matrix	M1	25-45%	High microporosity, high moldic and vuggy porosity	-1 to +1	-3 to 0	Gas zone	Fig.7 A, E
		B: calcitic coral floatstones	Neomorphosed corals into C2' calcite; micritized bioclasts; rare blocky calcite cement (C2); leached bioclasts (corals, red algae and foraminifers)	M1	25-45%	High microporosity, high moldic and vuggy porosity	-1 to +1	-3 to 0		Fig. 4 D
		C: partially dolomitized floatstones	Dolomicrite to dolomicrosparite crystals replacing micrite matrix and micritized bioclasts; leached bioclasts (red algae and foraminifers) and matrix	M1 M4	25-45%	High microporosity, high moldic and vuggy porosity	-0,5 to +1,5	-0,5 to +3		Fig.7 B
G-DF2	**Microporous cemented grainstones-rudstones**		Isopacheous calcite cement (C1) and blocky calcite cement (C2).	M1	18-30%	High microporosity, moldic porosity; rarer intergranular porosity	-0,5 to +0,5	-3 to 0	Gas zone	Fig.4 A, B, C
G-DF3	**Microporous and vuggy carbonate breccia**		Brecciation features (type II); neomorphosed corals into CX calcite; blocky calcite cement (C2); micritized bioclasts; leached bioclasts (corals, red algae and foraminifers) and matrix	M1	25-40%	High microporosity, inter-breccia clast porosity; moldic and vuggy porosity; rarer intergranular porosity	-3,5 to 0	-5 to -2	Gas zone	Fig. 4 E,F
G-DF4	**Coral floatstones with low matrix microporosity**		Brecciation features (type I); leached corals and micrite infills within molds (faint-ghost texture); leached bioclasts (corals, red algae and foraminifers)	M2	10-20%	Low microporosity; moldic to vuggy porosity	-1 to 0	-2 to 0	Gas zone	Fig.6 A, B, C; Fig. 7 C
W-DF1	**Floatstones and rudstones with low intragranular and matrix microporosity**		Micritized bioclasts; isopacheous calcite cement (C1) blocky calcite cement (C2); leached bioclasts (red algae and foraminifers) and matrix	M3	10-25%	Low microporosity; moldic to vuggy porosity	-1 to 0	-4 to -1,5	Water zone	Fig. 7 D
W-DF2	Carbonate breccia with low microporosity		Brecciation features (type II); neomorphosed corals into CX calcite; blocky calcite cement (C2); micritized bioclasts; leached bioclasts (corals, red algae and foraminifers) and matrix	M3	10-30%	Low microporosity; inter-breccia clast porosity; moldic to vuggy porosity	-2 to -0,5	-5 to -3	Water zone	

Table 3 : Definition and properties of the diagenetic facies from the Upper Burman Limestone

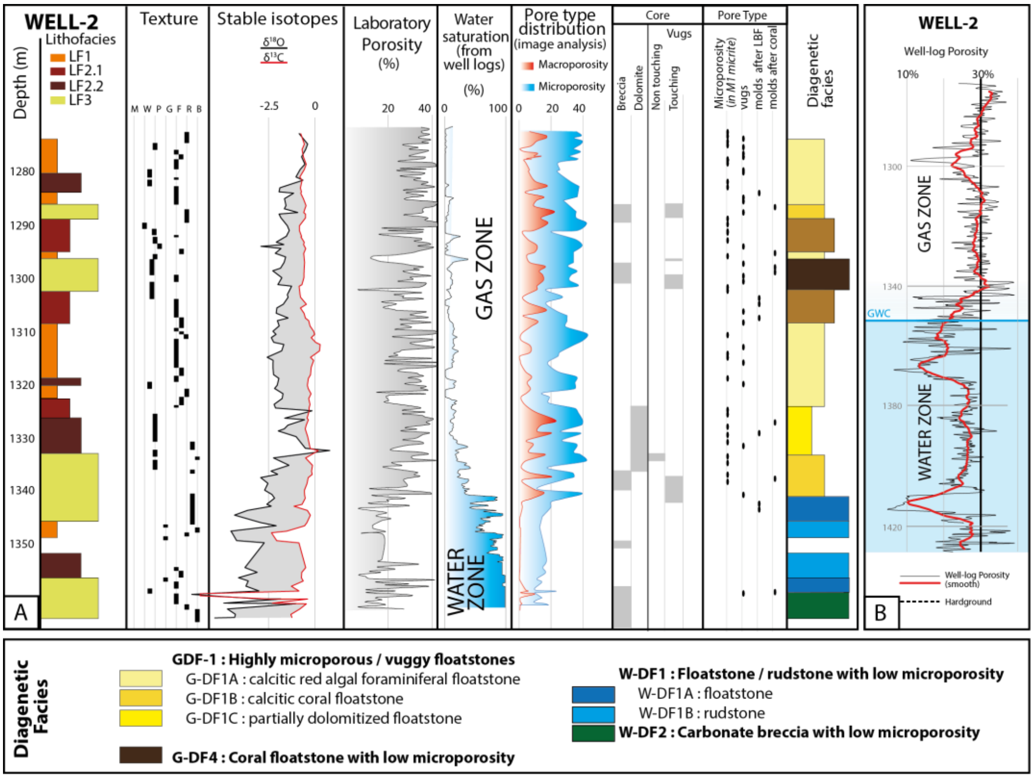

Figure 3-8: WELL-2 (A) cored intervals: lithofacies, depositional textures, carbon and oxygen isotope ratios, porosity (laboratory measurements on plugs), water saturation, pore type distribution (after image analysis of thin sections), diagenetic features and diagenetic facies. (B) Vertical variations of porosity within the Upper Burman Limestone, from well logs (dark curve) and smoothed values (moving average over a 2 meter-thick interval: red curve), showing the decrease in average porosity below the gas-water contact.

diagenetic features between the gas-bearing and the water-bearing reservoir led to differentiate the 2 zones in the facies classification. In the gas zone, in intervals where water saturation is lower than 50%, porosity average 28% (Fig. 3-8A, B), whereas at higher water saturation and particularly below the gas-water contact, porosity decreases significantly (average porosity: 18%) over a 30 meter-thick interval (Fig. 3-8B)

Within the gas zone, four main groups of diagenetic facies have been identified: 1) highly microporous and vuggy, mud-supported carbonates (G-DF1), 2) microporous cemented grainstones-rudstones (G-DF2), 3) microporous and vuggy carbonate breccia (G-DF3), 4) floatstones with low matrix microporosity (G-DF4). This diagenetic facies G-DF1 has been subdivided into 3 sub-facies: calcitic red algal and foraminiferal floatstones (G-DF1A), calcitic coral floatstones (G-DF1B), and partially dolomitized floatstones (G-DF1C).

Within, the water zone, two diagenetic facies have been recognized in the cored interval: 1) floatstones (W-DF1A) and rudstones (W-DF1B) with low intragranular and matrix microporosity, and 2) carbonate breccia with low microporosity (W-DF2).

3.4.4 Carbon and oxygen stable isotope signatures of selected carbonate components

Measurements of carbon and oxygen isotope ratios have been performed from selected carbonate components including red algae, benthic foraminifers, calcitized corals, cements, dolomite crystals and micrite matrix (Fig. 3-9). Calcitized corals C2' (δ18O= -4 to -0‰ V-PDB; δ13C= -0.5 to -0.3‰ V-PDB), red algae (δ18O= -0.6 to -2.2‰ V-PDB; δ13C= -0.4 to +0.7‰ V-PDB) and micritized large benthic foraminifera (δ18O= -0.7 to -2.9‰ V-PDB; δ13C= -0.5 to +0.1‰ V-PDB) display a relatively narrow range of carbon and oxygen signatures that are consistent with Miocene south-east Asian, shallow-water, marine calcite (Fig. 3-9A) (Ali, 1995; Madden and Wilson, 2013). Similar signatures are obtained for microporous micrites M1 (δ18O= -2.2 to -0.1‰ V-PDB; δ13C= -1.0 to +1.0‰ V-PDB) and densely packed micrites (δ18O= -2.3 to -0.7‰ V-PDB; δ13C= -0.6 to +0.2‰ V-PDB), whereas euhedral micrites M3 display slightly more negative δ18O values (δ18O= -2.9 to -2.7‰ V-PDB; δ13C = -0.6 to -0.4‰ V-PDB) (Fig. 3-9B).

Isopacheous cement (C1) displays a very narrow range of δ13C (from -0.0 to -0.7‰ V-PDB) and δ18O values (from -1.4 to -1.7‰ V-PDB) (Fig. 3-8C). In contrast, blocky calcite cement (C2) exhibits low variations of δ13 C (from -0.7 to +0.1‰ V-PDB) for a wide range of δ18O values (from -5.2 to -1.9‰ V-PDB) (Fig. 3-9C). Calcitized corals CX

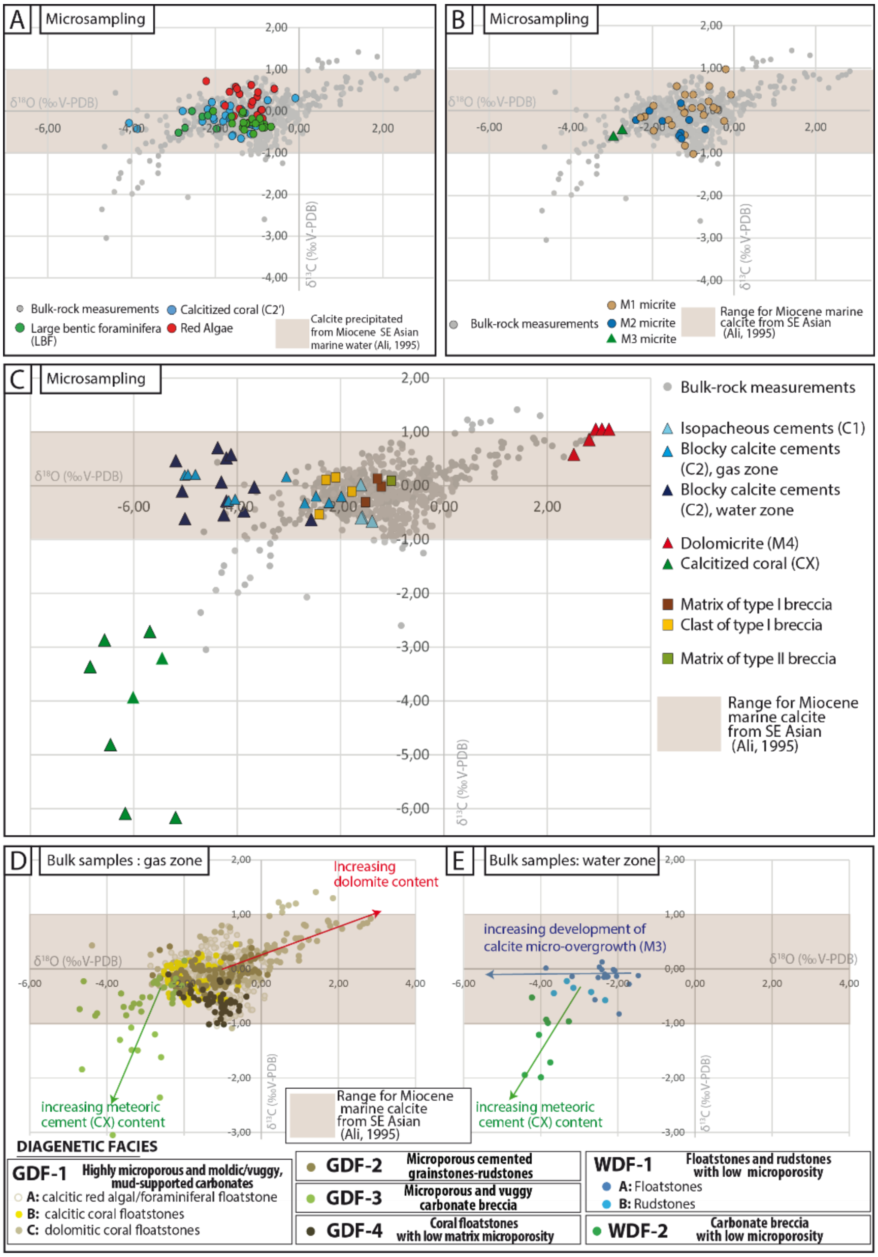

Figure 3-9: Carbon and oxygen isotopic signatures of the Upper Burman Limestone (A) δ18O-δ13C plot for selected bioclasts (large benthic foraminifera, coralline algae and calcitized corals) and bulk-rock measurements (gray dots) in the background (B) δ18O- δ13C plot for the 3 calcimicrite microfabrics identified in the Upper Burman Limestone, and bulk-rock measurements (gray dots) in the background (C) δ18O- δ13C plot for calcite cements, dolomite, as well as for carbonate breccia clasts and matrix; bulk-rock measurements (gray dots) are plotted in the background (D, E) δ18O- δ13C plots for bulk-rock measurements: samples are labeled according to the diagenetic facies within the gas zone (D) and water zone (E).

are significantly depleted in both δ18O and δ 13C compared to other carbonate components (δ18O: -5.2 to -6.8‰ V-PDB; δ13C: -2.7 to -6. ‰ V-PDB) (Fig. 3-9C). Finally, dolomite rhombs exhibit highly positive δ18O (from +2.6 to +3.1‰ V-PDB) and δ13C (from +0.8 to +1.0‰ V-PDB) values (Fig. 3-9C).

3.4.5 C and O isotopic signature of bulk samples

Measurements of carbon and oxygen isotope ratios have been conducted on bulk rock samples at a sampling increment averaging 0.50 m on cores from wells WELL-1, WELL-2, WELL-3 and WELL-4 (Fig. 3-9D). Bulk rock 18O and 13 C values are controlled by the 18O and 13 C signatures of the individual carbonate phases constituting the carbonate rock. They are therefore indicative of the processes that have significantly altered the original isotopic composition of the carbonate sediments. The 18O and 13 C domains identified for the different carbonate components (Fig. 3-9A, B, C), together with petrographic analysis of cores and thin sections, help interpret the vertical variations of the carbon and oxygen isotope ratios of bulk carbonates in cored intervals (Fig. 3-8, 3-10).

Within the gas zone, highly microporous mud-supported limestone (coralline algal/foraminiferal G-DF1A and coral floatstones G-DF1B) and grainstones/rudstones, (G-DF2) display δ13C values ranging from -1 to +0.5‰ and δ18 values ranging from - 2.8 to +0‰. Both oxygen and carbon isotope signatures are consistent with those of micritized bioclasts, micrite matrix and sparry calcite cements C1 and C2. In contrast, with the water zone, floatstones and rudstones (W-DF1) are marked by more negative δ18O values (below -2‰ V-PDB) (Fig. 3-9E). Highly negative δ18O values coupled with highly negative δ13C (below -1 ‰ V-PDB) correspond to brecciated intervals with calcitized coral (CX) from both gas (G-DF3) and water zones (W-DF2) (Fig. 3-9D, E). Increasing bulk δ18O values toward significantly positive values (>+1‰PDB) coupled with moderately positive δ13C (0 to +1‰ V-PDB) characterize intervals with significant dolomite content in bulk rock (G-DF1C) (Fig. 3-9D).

3.4.6 Major and trace elements

The concentration values for a selection of major and trace elements have been measured on bioclasts (calcitized corals, large benthic foraminifers and red algae), micrite matrix and cements as well as on bulk rock samples (Table 4). Strontium concentrations in micritized bioclasts (large benthic foraminifers and red algae) range from 407 to 551 ppm. Such values

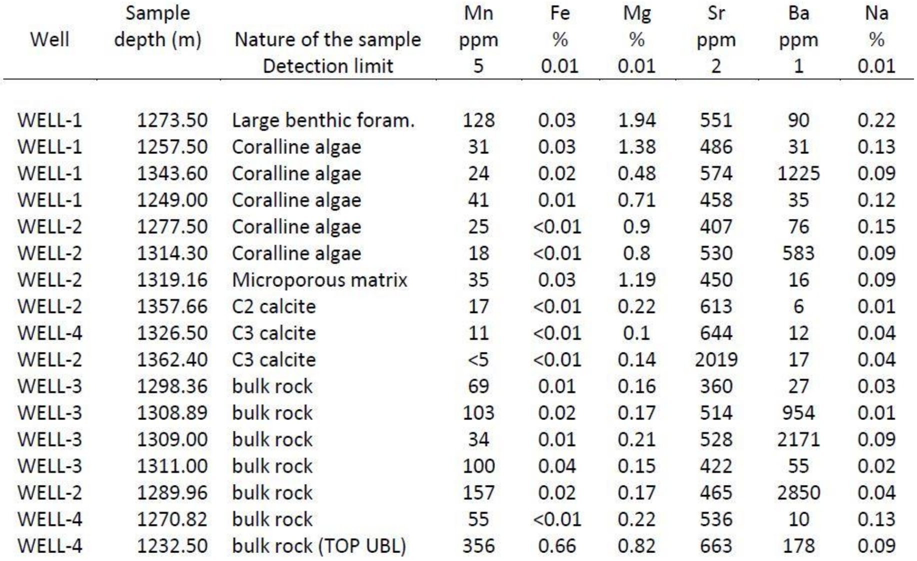

Well	Sample depth (m)	Nature of the sample Detection limit	Mn ppm 5	Fe % 0.01	Mg % 0.01	Sr ppm 2	Ba ppm 1	Na % 0.01
WELL-1	1273.50	Large benthic foram.	128	0.03	1.94	551	90	0.22
WELL-1	1257.50	Coralline algae	31	0.03	1.38	486	31	0.13
WELL-1	1343.60	Coralline algae	24	0.02	0.48	574	1225	0.09
WELL-1	1249.00	Coralline algae	41	0.01	0.71	458	35	0.12
WELL-2	1277.50	Coralline algae	25	<0.01	0.9	407	76	0.15
WELL-2	1314.30	Coralline algae	18	<0.01	0.8	530	583	0.09
WELL-2	1319.16	Microporous matrix	35	0.03	1.19	450	16	0.09
WELL-2	1357.66	C2 calcite	17	<0.01	0.22	613	6	0.01
WELL-4	1326.50	C3 calcite	11	<0.01	0.1	644	12	0.04
WELL-2	1362.40	C3 calcite	<5	<0.01	0.14	2019	17	0.04
WELL-3	1298.36	bulk rock	69	0.01	0.16	360	27	0.03
WELL-3	1308.89	bulk rock	103	0.02	0.17	514	954	0.01
WELL-3	1309.00	bulk rock	34	0.01	0.21	528	2171	0.09
WELL-3	1311.00	bulk rock	100	0.04	0.15	422	55	0.02
WELL-2	1289.96	bulk rock	157	0.02	0.17	465	2850	0.04
WELL-4	1270.82	bulk rock	55	<0.01	0.22	536	10	0.13
WELL-4	1232.50	bulk rock (TOP UBL)	356	0.66	0.82	663	178	0.09

Table 4: Concentrations of selected major and trace elements on bulk rock samples and various carbonate components.

are significantly depleted compared to values known in modern high-Mg calcite skeletal grains (typically higher than 1000 ppm) according to Veizer (1983). Such low values are likely consistent with Sr loss during high-Mg to low-Mg calcite transformation (Veizer, 1983). Strontium concentration in the blocky calcite cement C2 (613 ppm) is significantly lower than those expected in marine low-magnesium calcite (~1000 ppm). Corals neomorphiseds into calcite (CX) display the highest Sr concentrations with values of 644 and 2019 ppm. Manganese concentrations are generally low within micritized bioclasts (from 18 to 128 ppm), C2 (17 ppm) and CX (11 ppm) calcites. The iron concentrations in all of the measured samples are low (<0.04%). Magnesium concentrations are highly variable in the analyzed bioclasts (from 0.8 to 1.94%) and depleted in CX and C2 calcite (0.22 and 0.14% respectively). All of the analyzed samples have relatively high sodium concentrations ranging from 100 to 2200 ppm.

3.5 Discussion

3.5.1 Origin of diagenetic features and diagenetic environments

The integration of selected petrographic, petrophysical and geochemical parameters led to the definition of various diagenetic facies (Table 3, Fig. 3-10, 3-11) which are characterized by a specific paragenesis.

Highly microporous and vuggy, mud-supported carbonates from the gaz zone (G-DF1)

Within the gas zone, mud-supported carbonates (foraminiferal, coralline algal and coral floatstones) are characterized by significant proportions of dissolution vugs which have been shown to postdate stylolites, thus suggesting a late phase of leaching in burial environments. The significant drop in porosity (averaging 10%) below the gas-water contact, which is partly related to a decrease in moldic pore and vug abundance (Fig. 3-7A,3-7B; Fig 3-8 and Fig 3-11) strongly suggests that such a late stage of calcite dissolution occurred during and/or after gas emplacements.

In G-DF1 carbonates, dominant allochems (micritized coralline algae and large benthic foraminifers) have low-Mg mineralogy and exhibit highly microporous, subrounded micrite microfabric (M1) which is distinct from primary skeletal microfabrics. The carbon and oxygen isotopic signature of M1 micrites from micritized coralline algae and large benthic foraminifera are consistent with Miocene, south-east Asian, shallow-water, marine calcite values (Ali, 1995; Madden and Wilson, 2013), thus suggesting that the calcite from M1 micrites formed from marine pore fluids at the sea bottom or in marine, shallow burial conditions. The common occurrence of subrounded M1 micrite within the gas reservoir and its lack within the water zone may result from 1) preferential dissolution processes within the gas-bearing reservoir leading to rounded morphologies (Lambert et al., 2006; Volery et al., 2010; Léonide et al., 2014), or 2) preferential preservation of initially anhedral micrites within the hydrocarbon zone (Morad et al., 2016). In G-DF1 reservoirs, the micritic matrix mud displays the same micrite microfabric (M1) and the same range of carbon and oxygen isotope compositions as coralline algae and large benthic foraminifers (Fig. 3-9A), thus suggesting similar diagenetic evolution. Although it has been shown that anhedral and subrounded or knobby micrites may form early in the marine or shallow-burial environment without the intervention of a dissolution process (Morad et al., 2016; Lucia, 2017), the

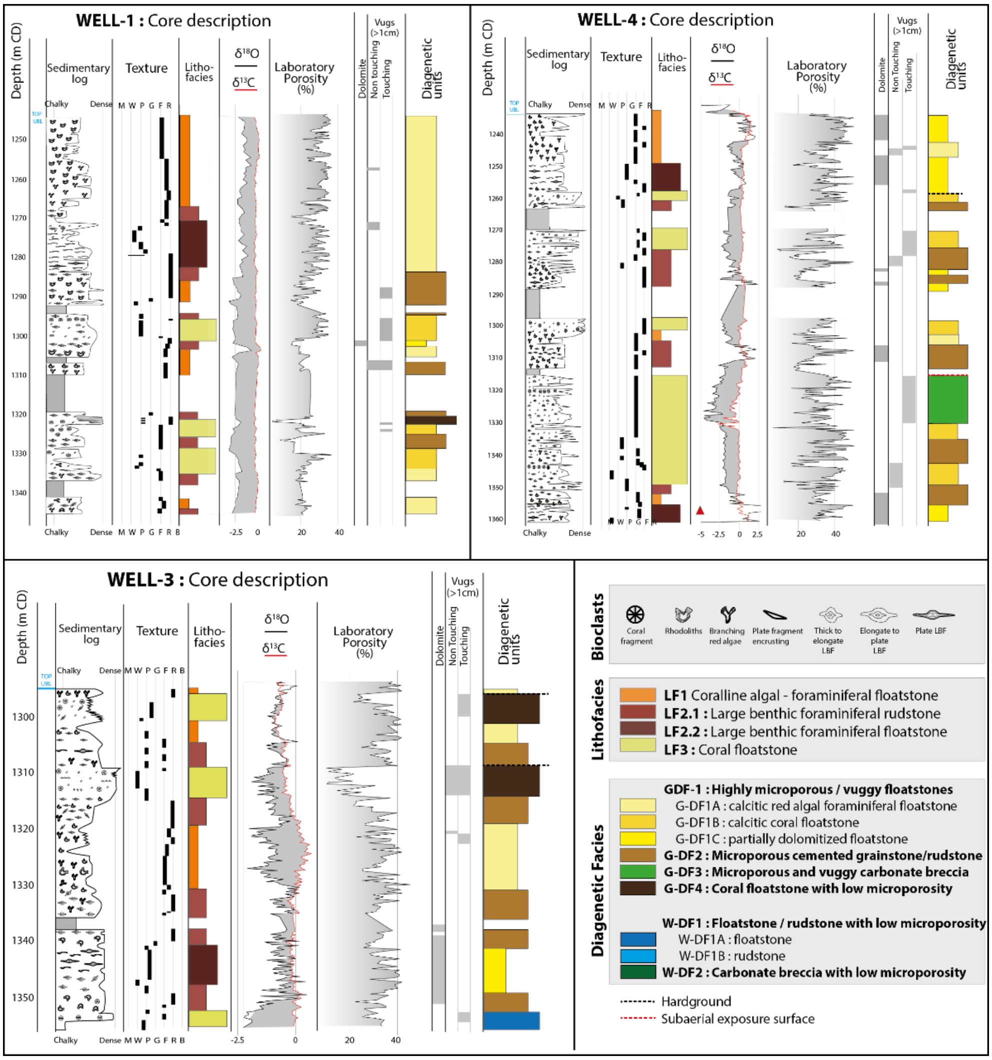

Figure 3-10: WELL-1, -3 and -4, cored intervals: lithofacies, depositional textures, carbon and oxygen isotope ratios, porosity (laboratory measurements on plugs), water saturation, dolomite and dissolution vug occurrence and diagenetic facies.

hypothesis of rounded micrite development during the late phase of leached that affected the gas zone cannot be ruled out.

Among the highly microporous and vuggy carbonates from the gas zone, coral-rich intervals (G-DF1B diagenetic sub-facies) exhibit distinct diagenetic patterns with regards to the early evolution of aragonitic components. In such intervals, coral are commonly dissolved and filled by a sediment which is closely similar to and in physical continuity with the matrix (=fossil ghost), thus forming a faint-ghost fabric (Fig. 3-6A, B). Filling

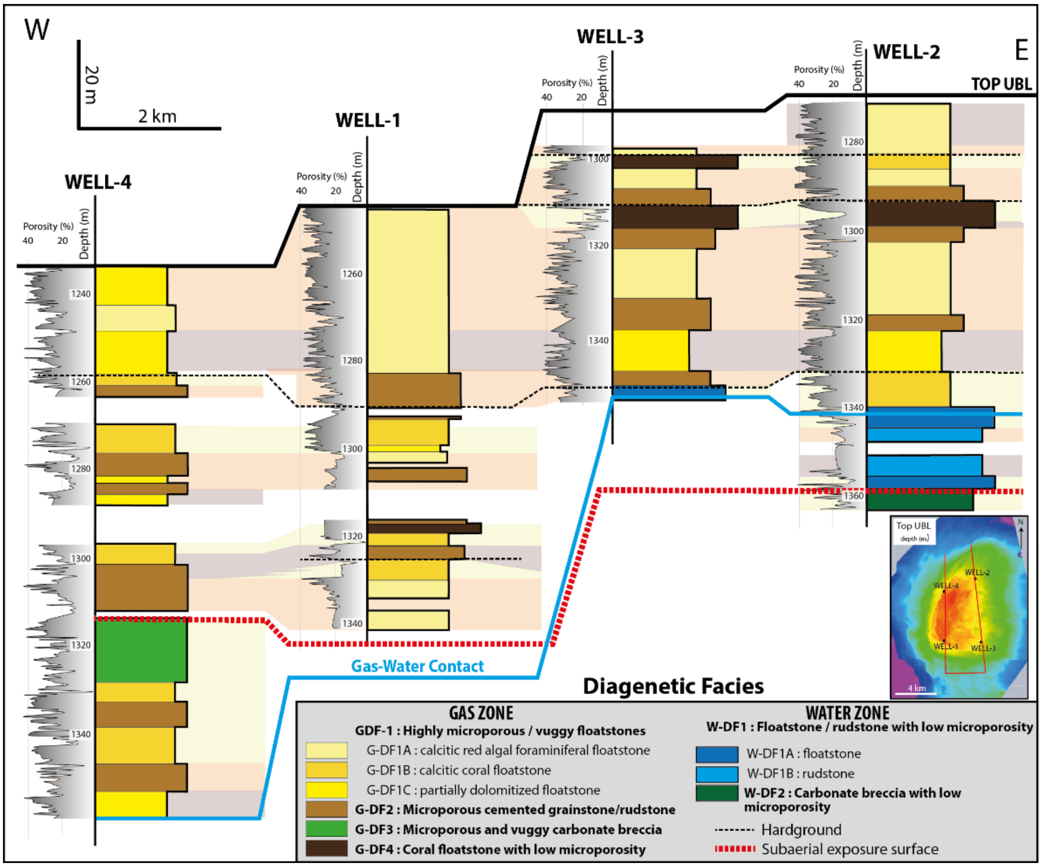

Figure 3-11: Diagenetic facies zonation of the four studied wells, vertical variations of plug porosity and remakarble surfaces (hardgrounds and potential subaerial exposure surface.

biomoulds with marine sediment below a subaerial exposure surface would require the existence of a continuous karstic porosity along which the sediment could infiltrate. The existence of such pathways is unlikely since in faint-ghost fabrics from Yadana, leached corals are generally sparse within the matrix, and typically non-touching. In contrast, the physical continuation of the biomould fill into the adjacent matrix or into the intragranular pore fill gives evidence of an early phase of aragonite dissolution in marine environments (Sanders, 2003).

Decameter-thick partially dolomitized intervals of mud-supported carbonates (foraminiferal floatstone LF2.2, echinodermal wackestone LF3.2) have been identified in Yadana wells (G-DF1C diagenetic facies). By considering the Zachos et al. (2001) range for Miocene seawater δ18O (from 0 to -1‰ SMOW), and by using the equation linking the fractionation factors for dolomite with temperature (Epstein et al., 1953; Irwin et al., 1977), the δ18O values of dolomite are consistent with a marine parent water at a temperature ranging from 12°C to 19°C. Such temperatures are significantly cooler than mean tropical sea surface temperatures (27-28.5°C in the modern Andaman Sea, after Rama Raju et al., 1981) which strongly suggests that dolomite formed from relatively deep marine water. The oxygen isotope signature of dolomite from Yadana is quite similar to that of Eocene carbonates from the Enewetak atoll (+2.1 to +2.7‰ PDB after Saller, 1984) and from most of Cenozoic carbonate islands (+2 to +4‰ PDB after Budd, 1997; Suzuki et al., 2006) where dolomitization has been interpreted to result from the circulation of cool, deep sea waters.

Microporous cemented grainstones-rudstones from the gas zone (G-DF2)

In foraminiferal and coralline algal grainstones-rudstones, the isopacheous rims of equigranular calcite (C1) around the bioclasts exhibit δ18O and δ13C values (Fig. 3-9C) which strongly suggest that they form in shallow marine environments (Ali, 1995). The calcite cement C2, that typically occludes entirely the intergranular porosity in grainstones and rudstones have δ13C values which are also consistent with a precipitation from marine water (Ali, 1995), but the significantly negative δ18O values (from -1.89 to -5.19‰PDB) would suggest a formation in shallow-burial conditions. By considering the Zachos et al. (2001) range for Miocene seawater δ18O (from 0 to -1‰SMOW), and by using the Anderson and Arthur (1983) equation, a temperature ranging from 20°C to 43°C has been estimated for C2 calcite formation, in the case of marine parent waters. In addition, the strontium concentration values in C2 (613 ppm) would be consistent with those for calcite precipitated from a shallow burial, deep marine water with a lowered Sr/Ca ratio with regards to surface seawater (Swart, 2015). Additionally, the extremely low Fe (<0.01%) contents and the relatively elevated Na concentration (100 ppm) in C2 support the interpretation of a non-meteoric origin for parent fluids, even though the possibility of contamination by Na from fluid inclusions cannot be discarded.

As for G-DF1 diagenetic facies, G-DF2 limestone is strongly affected by extensive non-selective dissolution features (vugs) cross-cutting stylolites. The lack of calcite cement within such vugs strongly suggest that dissolution postdates the formation of the early marine to marine shallow burial C2 cements.

Microporous and vuggy carbonate breccia from the gaz zone (G-DF3)

Highly porous carbonate breccia (G-DF3) form a 5 meter-thick interval with frequent brownish calcitized corals (CX). The negative signature in both δ13C (from -2.7 to -6.2‰ PDB) and 18O (from -5.2 to -6.9‰ PDB) would be consistent with calcitization processes controlled by meteoric water. By considering meteoric water temperatures ranging from 20 to 30°C, a 18O value of -2.5 to -6‰ V-SMOW has been calculated for the parent fluids by using the Anderson and Arthur (1983) equation. Such a value is consistent with the modern precipitation δ18O values recorded in the Andaman Islands (Laskar et al., 2011: +0.7 to -5.2‰ V-SMOW) and in low latitude in SE Asian area (Bowen & Wilkinson, 2002: -4 to -6‰ V-SMOW). In addition, the meteoric origin of CX calcite is also supported by the elevated strontium concentration (2019 ppm) since aragonite calcitization in meteoric environments has been shown to retain significant proportions of the original strontium amount, with final concentrations in calcite commonly higher than 2000 ppm, particularly in the vadose zone (Pingitore, 1976; Webb et al., 2009). Furthermore, the Sr/Ca and Mg/Ca weight ratio for CX calcite are within the range of published values for low-magnesium calcite replacing coral aragonite and also for interskeletal low-magnesium calcite in calcitized corals (Rabier et al., 2008). Calcite CX exhibit crystal overgrowths developing into the inter-clast space. These are sealed by finely bioclastic micrite of probable marine origin as suggested by its stable isotope signature (Fig. 3-9C; δ18O: -1‰ PDB; δ13C: +0.2‰ PDB). This suggests that coral calcitization and CX calcite overgrowth occurred during or after brecciation but prior to the marine micrite infill, and are therefore early diagenetic features. These indices strongly suggest that brecciation processes and calcitization of corals into CX occurred during an early, intraformational, stage of subaerial exposure.

Coral floatstones with low matrix microporosity from the gaz zone (GDF4)

The low to moderate porosity values (10-25%) for G-DF4 coral floatstones is related to the low interparticle microporosity within micrite (M2 microfabrics). As for G-DF1B diagenetic facies, early marine dissolution of aragonite is evidenced by the occurrence of faint-ghost textures. The carbon and isotope signatures of micrites and bulk carbonates from such dense G-DF4 intervals (Fig. 3-9B, D) suggest that M2 micrites formed and became lithified in marine environments. The brecciated limestone (type I breccia) typically occur at the top of G-DF4 intervals (Fig. 3-7C, 3-10, and 3-11). The clasts consist of para-autochthonous fragments of coral floatstone (LF3.1) displaying the densely packed, anhedral micrite M2. They are embedded within an echinoderm-rich wackstone matrix with M1 micrite, thus suggesting early lithification and early brecciation of the coral floatstone. This also strongly demonstrates that the densely packed, anhedral micrite M2 results from early lithification processes on the sea bottom. Tops of these brecciated intervals are commonly bored by lithophagous mollusks and are sharply overlain by LF1 or LF2.1 facies (Fig. 3-7C) thus suggesting hardground surfaces that formed during periods of non-deposition.

Low microporosity carbonates (W-DF1 and W-DF2) from the water zone

As revealed by laboratory measurements and counting on thin sections, the sharp decrease in porosity below the gas water contact is mainly related to low intragranular and matrix microporosity and in a decrease in moldic and vuggy pores (Fig. 3-8). Carbonates from the water zone display the same early diagenetic features as those evidenced in the gas zone: 1) micritization and high-Mg to low-Mg calcite conversion of foraminifera and coralline algae, 2) early marine dissolution of aragonite in coral-rich intervals (faint-ghost texture), 3) brecciation and calcitization of corals into CX below subaerial exposure surface; 4) occlusion of intergranular pore by C1 and C2 calcite. SEM observations of micrites from the water zone revealed a densely packed euhedral microfabric (M3: Fig. 5C). The occurrence of smaller (~1 µm) and rounded micrite particles which are encased within larger (~2-4µm) euhedral crystals may suggest that M3 euhedral micrite results from: 1) the transformation of rounded micrite into euhedral micrite and microspar (aggrading neomorphism), via precipitation of syntaxial calcite precipitation around micrite (Morad et al., 2016) or 2) recrystallization involving the dissolution of micrite and reprecipitation of euhedral calcite (Clift et al., 2008; Deville de Periere et al., 2011; Léonide et al., 2014; Volery et al., 2010). In addition, lower δ18O values have been measured in micritized benthic foraminifers from the water zone (δ18O = -2.7 to -2.9‰) compared to the gas zone (δ18O =-2 to -2.2‰), which likely results from an increase in precipitation temperature in the water zone, assuming similar oxygen isotopic composition of the porewaters (Dickson and Coleman, 1980). The stable isotope composition of such micrites probably reflects that of a mixture between a micrite precursor (anhedral micrite?) and calcite precipitation, thus only minimum temperatures of euhedral micrite formation can be obtained using δ18O values on micritized grains. By considering the Zachos et al. (2001) range for Miocene seawater δ18O (from 0 to -1‰ SMOW), and by using the Anderson and Arthur (1983) equation, a minimum temperature ranging from 23°C to 29°C has been estimated for calcite precipitation formation, in the case of marine parent waters. Higher temperatures (38-41°C) are obtained if precipitation is assumed to have occurred from evolved marine pore waters

(δ18O V-SMOW = +2‰ after Egeberg and Aagaard, 1989). The latter values are closer to that of the present-day reservoir temperature (55°C).

3.5.2 Diagenetic history of the Upper Burman Limestone

Petrographic and stable isotopic studies records allow the diagenetic history of the Upper Burman Limestone Formation to be reconstructed. The burial curve of the Yadana platform, the diagenetic model and the tectonic reconstruction of the region proposed in this paper are summarized in Fig. 3-12.

Step 1: Early Miocene: early marine and shallow-burial marine diagenesis

A major feature of early marine diagenesis of the coral-rich limestones (LF3.1 lithofacies), occurring at the sea bottom or near the sea bottom is extensive aragonite dissolution and subsequent marine sediment infills that led to the development of faint-ghost fabrics. Such early dissolution features have been interpreted as resulting from undersaturation of shallow-marine waters with increased organic matter degradation at the sea bottom (e.g. Reaves, 1986; Sanders, 2003). During periods of low sedimentation rates, low porosity M2 micrite microfabrics developed. Such an early lithification of mud matrix favored the early brecciation of LF3.1 and LF3.2 limestones. In coral-rich (LF3.1) and coralline algal-foraminiferal limestones (LF1 and LF2 lithofacies), the conversion of high-Mg into low-Mg calcite and the micritisation of bioclasts (red algae and large benthic foraminifers) probably occurred during early marine to shallow-burial, marine diagenesis, as suggested by marine, low temperature stable isotope signatures (Fig. 3-9B) of M1 micrites. In grain-supported sediments (LF2.1 lithofacies), minor calcite cementation occurred (C1 sparry calcite cement) in shallow-marine environments at water temperatures ranging from 18 to 24°C, as calculated from the range of 18O values of C1 calcite and Miocene seawater (0 to -1‰ SMOW, after Zachos et al., 2001).

Step 1′ : Early Miocene: intra-formational subaerial exposure

The scattered brownish calcitized corals (CX) with distinct meteoric isotope signatures are the only potential evidence of carbonate precipitated in freshwater in the whole Yadana core data set. Their occurrence within one correlatable brecciated interval may suggest the existence of one subaerial exposure event having interrupted the development history of

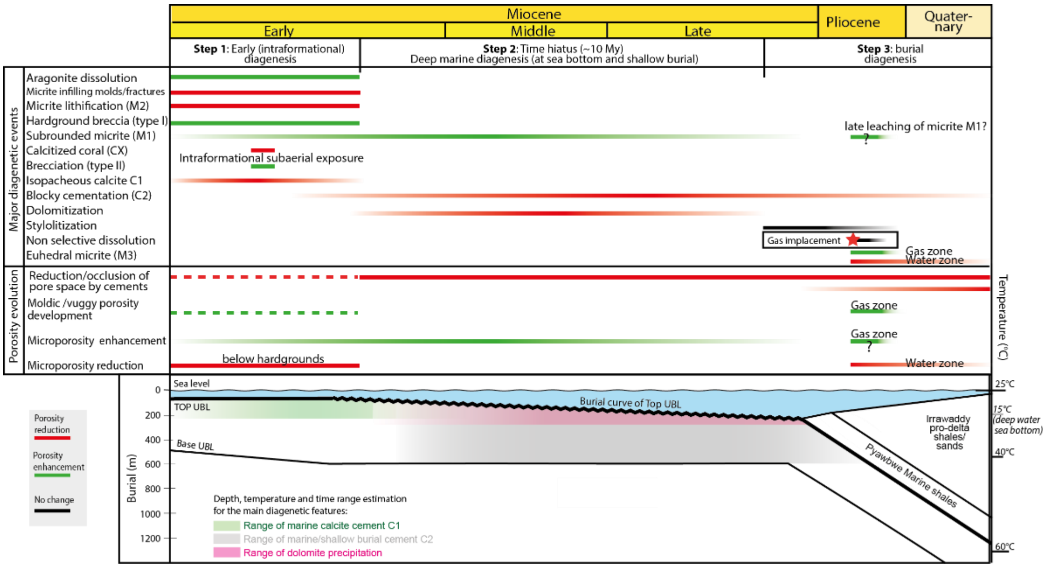

Figure 3-12: Paragenesis and porosity evolution of the Upper Burman Limestone and subsidence curve.

the Yadana carbonate platform. According to Miller et al. (2005), the amplitude of eustatic variations during the Early Miocene may have reached 30 m thus making possible the subaerial exposure during regional sea-level drops of shallow-water carbonates.

Step 2: Middle-Late Miocene: long-duration (~10 Myr) depositional hiatus

A 10 Myr-long hiatus (Burdigalian to Tortonian) has been evidenced between the top of the Upper Burman Limestone (Early Miocene) and the overlying shales forming the Pyawbwe Formation (Late Miocene) (see burial curve: Fig. 3-12). Contemporaneously, a significant depocenter developed to the west, in the M5 Basin resulting in the deposition of 1500 m thick terrigenous sediments during the Late Miocene. The uppermost Upper Burman carbonates as well as the limestones reworked at the base of the overlying marls do not present any petrographic or geochemical evidence of meteoric weathering. All of the bulk and micro-sampling isotope measurements performed in the uppermost Upper Burman carbonates are consistent with early marine or marine shallow burial signatures. In addition, no trend of decreasing δ13C, that could indicate a subaerial exposure surface at top of Yadana limestone (Matthews and Allan, 1982), has been evidenced in the cored intervals from the four studied wells (Fig. 3-8, 3-10). The more comprehensive interpretation for the long-duration hiatus occurring at top of Upper Burman limestones is the drowning of the Yadana platform during the Burdigalian which prevented shallow marine sedimentation from occurring. Long-term, marine depositional hiatuses are common features of submerged seamounts from the Pacific where Eocene to Miocene shallow-water carbonates are exposed in deep seawater at the top of seamounts (Takayanagi et al., 2012, 2007).

Even though microporosity development in Yadana may have started to develop during early marine diagenesis, high microporosity in calcitic sediments affected by cool seawater has been observed in Pacific atolls (Saller & Moore, 1989). The marine isotopic signature of dolomite, similarly to that from the Enewetak platform (Saller, 1984; Saller & Moore, 1989) indicates dolomitization of the Yadana carbonates by cool (12-19°C), marine water and therefore likely presumably occurred prior to significant burial. The occurrence of a dolomitized horizon on top of the reservoir, just below the overlying Pyawbwe Shales may suggest that dolomitization occurred during the period of non-deposition, in relatively deep-water setting. Similarly, dissolution and dolomitization in deep seawater have been described in slope sediments from the Bahamas (Mullins et al., 1985).

Step 3: Upper Miocene-Present: Cementation, euhedral calcimicrite development (M3) and late dissolution in burial environment

During the late Miocene, the opening and the spreading of the Andaman Sea resulted in increased subsidence in the Yadana area (Chakraborty and Khan, 2009; Curray, 2005). After a 10 My-long hiatus, the Yadana platform has become buried below approximately 1000 m-thick latest Miocene to Quaternary terrigenous marine sediments. Based on carbon and oxygen isotope signatures, the blocky calcite cements C2 that occludes most of the intergranular or intraskeletal porosity in the whole studied interval are regarded as having precipitated from marine pore water at temperatures ranging from 20 to 43°C. Such temperatures suggest that sparry calcite C2 cementation occurred therefore partially or entirely during the post-hiatus burial stage (Fig. 3-12).

The widespread development of open vugs is interpreted to have occurred during the burial stage since these dissolution features overprint calcite C2 cements and stylolites. In addition, the increased abundance in moldic and vuggy porosity in the gas zone strongly suggests that most of the burial dissolution occurred during and after the gas emplacement. The dominance of highly porous M1 micrites within the gas zone and its scarcity within the water zone may be related to a differential preservation of early-formed anhedral, subrounded micrites in a reservoir with high hydrocarbon saturation (Morad et al., 2016). However, the hypothesis of rounded micrite development by dissolution processes (Lambert et al., 2006) cannot be ruled out. Various potential sources for aggressive fluids that have been used to explain burial porosity creation in carbonates can be identified: 1) carbon dioxide and organic acids from kerogen (Mazzullo & Harris, 1991; Morad et al., 2000), 2) high inorganic CO_2 inputs from presumed metamorphic or igneous rocks (Beavington-Penney et al., 2008), 3) hydrocarbon biodegradation (Ehrenberg and Jakobsen, 2001), 4) hydrogen sulfide oxidation (Hill, 1990), 5) mixing corrosion (Esteban and Taberner, 2003), 6) thermochemical sulfate reduction (Machel, 2001), and 7) thermal convection (Bjørlykke et al., 1988).

Since late dissolution features are mostly located within the gas-bearing reservoir, water acidification by CO_2 and organic acids resulting from methane biodegradation (Behar and Albrecht, 1984) can be considered as a potential cause of undersaturation in the Yadana reservoir. CO2 is present within the gas zone (around 9% of the total gas volume) and may have contributed to significant carbonate undersaturation in residual water within the gas zone and at the gas migration front. As suggested by Lambert et al. (2006), dissolution could have occurred during gas emplacements, with organic acids and CO_2 moving downward with the advancing gas-water-contact. In this case, dissolved carbonates may have been transported downward into the water zone, together with water moving downward during gas emplacements, into the water zone and precipitated as calcite micro-overgrowths (M3 micrite) or C2 calcite within connected macropores. Dissolution may also have occurred after gas emplacements, by acidification of residual water saturation (Lambert et al., 2006), but in that case, a flow of residual water is needed to transport dissolved calcite (Ehrenberg et al., 2012) and maintain significant dissolution. The lack of preserved or relict sulfate, and sulfides in the Upper Burman limestone as well as the extreme scarcity of H2S (<4ppm) in the gas composition do not support the hypothesis of hydrogen sulfide oxidation or thermochemical sulfate reduction as major processes for secondary porosity development.

Finally, the major shift of porosity around the GWC (Fig. 3-8B) suggests a major phase of porosity evolution during and/or after the hydrocarbon emplacement which is mainly related to 1) differential moldic and vuggy porosity development within the gas zone, 2) microporosity preservation or enhancement in M1 micrites within the gas zone, and 3) microporosity reduction by calcite precipitation leading to densely packed, euhedral M3 microfabric.

3.5.3 Contrasting patterns of porosity evolution in Oligo-Miocene SE Asian carbonate hydrocarbon reservoirs

Isolated carbonate buildups are common in Cenozoic of SE Asia and are known to be significant hydrocarbon reservoirs : e.g., Liuhua platform (Sattler et al., 2004; Zampetti et al., 2005), Luconia platform (Bashah and Pierson, 2012; Epting, 1980; Sattler et al., 2004; Vahrenkamp, 1998), Malampaya platform (Fournier et al., 2004; Fournier and Borgomano, 2007). Such reservoirs are highly porous with porosity values commonly reaching 40%, and display a high proportion of secondary macropores (molds and vugs) and microporosity. Park et al. (1995) linked the increase in reservoir quality in the lower Miocene Batu Raja limestones from Indonesia to the repeated subaerial exposure events. Sun and Esteban (1994) emphasized the role of third-order sea-level drops and subsequent subaerial exposures on the regional development of Miocene carbonate reservoirs from South-East Asia. In addition, the development of elevated secondary porosity (moldic pores and microporosity) in the Luconia Province has been related to meteoric diagenesis during prolonged phases of subaerial exposure. However, for Zampetti et al. (2004), in the Luconia platforms, secondary porosity has been interpreted as having dominantly developed in burial environments. In the Liuhua isolated platform, there is little evidence of intraformational subaerial exposure events and secondary porosity has been shown to be largely related to burial leaching (Sattler et al., 2004). In the Tonasa Platform, central Indonesia (Eocene to Miocene), diagenetic features related to subaerial exposure are uncommon, mainly located around faulted highs, formed during the major-mid Oligocene eustatic fall although deposition occurred mainly close to sea surface on top of the platform (Arosi and Wilson, 2015). The scarcity of exposure-related features outside of faulted highs has been interpreted as resulting from the combined effect of relatively high subsidence rates and low rates of carbonate production and accumulation in foraminiferal-dominated carbonate systems (Arosi and Wilson, 2015; BouDagher-Fadel and Wilson, 2000; Wilson, 2008a).

Similarly, in Yadana, only one subaerial exposure event has been identified in the studied interval. The poor development of diagenetic features related to subaerial exposition is likely to be due to the low amplitude of eustatic variations during the Early Miocene and/or to high subsidence rates and in the case of effective emergence, the vadose zone is expected to be extremely reduced in thickness.

In contrast, the Oligo-Miocene Malampaya carbonate buildup (offshore Palawan, Philippines), was affected by cyclic, repeated subaerial exposure events recorded by thick (up to 5m) pedogenetized intervals (Fournier et al., 2004). However, in spite of such repeated subaerial exposure events, most of the secondary porosity (molds, vugs, microporosity) has been shown to have mainly developed during burial (Fournier and Borgomano, 2007; Warrlich et al., 2010, 2008).

The different Cenozoic South-East Asian carbonates have responded differentially to the development of low porosity intervals. In the Yadana platform, low porosity units within the gas zone are rare and related to early marine lithification of micrite matrix below hardgrounds. In the Miocene Zhujiang carbonates in the Liuhua Field (South-China Sea), tight intervals are related both to early meteoric phreatic and late burial calcite cementation (Sattler et al., 2004). In the Miocene E11 field from Central Luconia, low porosity intervals result from increased clay content and early marine and/or meteoric cementation (Warrlich et al., 2010). In the Malampaya field, low porosity units result from the late burial cementation of previously highly permeable pedogenetized intervals (Fournier & Borgomano, 2007). From the foregoing, it appears clear that in the different Cenozoic South-East Asian carbonate reservoirs, early depositional and diagenetic processes have played a key role in the development of low-porosity units.

However, the diagenetic analysis of the Yadana reservoir revealed, for the first time in Cenozoic carbonate reservoirs from SE Asia, a significant porosity reduction below a hydrocarbon-water contact which resulted from preferential calcite precipitations in water zone micrites. Such a process of late porosity reduction in carbonate reservoirs probably exists in other microporous carbonates from South East Asia, but the scarcity of cores in water zones limits its detection.

3.6 Conclusion

Petrographic and stable isotopic analyses allow the diagenetic history of the Upper Burman Limestone Formation to be reconstructed.

(1) The high (28%) average porosity of the Yadana gas reservoir is dominantly related to significant development of microporosity in micritized grains and matrix (loosely packed, subrounded micrite M1) as well as moldic and vuggy porosity.

(2) Mud supported, coral-rich sediments have undergone significant early marine dissolution of aragonite grains (faint-ghost texture) and lithification

to micrite matrix (densely packed and coalescent anhedral micrite M2), thus leading to the development of dense layers.

(3) One potential subaerial exposure surface correlatable through wells has been evidenced at the top of a brecciated interval which is characterized by the occurrence of scattered calcitized corals with negative $\delta^{13}C$ signature (CX calcite). With the exception of this thin (<10 m) interval, the Upper Burman carbonates show no petrographic or geochemical evidence of meteoric overprint.

(4) Stable isotope and petrographic data from the top of the UBL suggest that the associated long-term depositional hiatus (Middle to Late Miocene: ~10 Myr) was related to the platform drowning and non-deposition in a deep marine setting. Partial dolomitization, which affected preferentially the top and flanks of the platform, likely occurred during such a hiatus, in deep marine environment.

(5) Microporosity development and formation of loosely packed, subrounded micrites (M1 microfabric) likely mainly occurred in marine to marine shallow burial environments.

(6) The major decrease in porosity (averaging 10%) below the gas-water contact results from a major phase of porosity evolution during and/or after the gas emplacement. Such a porosity shift is mainly related to 1) increased moldic and vuggy porosity development within the gas zone, 2) microporosity preservation in loosely packed, subrounded micrites (M1) within the gas zone, and 3) microporosity reduction by calcite precipitations within the water zone leading to the development of densely packed, euhedral micrites (M3). The present findings provide therefore new insights into the porosity evolution in gas reservoirs from Cenozoic, South-East Asian carbonate buildups.

IV. Petrophysics & Geophysics

Origin of seismic reflections in a carbonate gas field, Lower Miocene (offshore Myanmar) [1]

Thomas TEILLET [1,2], François FOURNIER [1], Jean BORGOMANO[1], Fei HONG [2]

[1] : Aix-Marseille Université, CNRS, IRD, Cerege, Um 34, 3 Place Victor Hugo (Case 67), 13331 Marseille Cedex 03, France[2] : TOTAL, CSTJF, Avenue Larribau, 64000 Pau, France
[2] : TOTAL, CSTJF, Avenue Larribau, 64018 Pau Cedex, France

Abstract: The geological origin of seismic reflections, within a carbonate gas reservoir, has been determined on the basis of an integrative analysis of cores, well logs, pre-production and 4D time-lapse-seismic data. The gas reservoir is subdivided into meter to decameter-thick diagenetic units which are characterized by distinct contrasted acoustic properties. Low impedance units are dominant and consist of highly microporous and vuggy foraminiferal/coralline algal floatstones intervals whose porosity has been significantly enhanced in burial diagenetic environments. High to moderate acoustic impedance units (thickness: 1-20m) are related to various depositional and diagenetic fabrics: 1) early-lithified coral floatstones, 2) foraminiferal rudstone whose intergranular space is occluded by shallow burial sparry calcite and 3) carbonate breccia with neomorphosed corals occurring below an intra-formational subaerial exposure surface. Within the gas zone, seismic reflectors may form at the boundary between two diagenetic units or may result from the interference between reflection at the base and top of such intervals. A stratigraphy-cross-cutting reflection horizon has been shown to form at a major and laterally continuous shift in porosity which is related to a differential diagenetic evolution between the gas and the water zone, during or after hydrocarbon emplacements. Finally, the analysis of the geological origin of seismic reflections has been proved to help predict and mapping the major heterogeneities with a significant impact on flow during production.

---

[1] Published in Marine and Petroleum Geology : DOI : 10.1016/j.marpetgeo.2019.104110

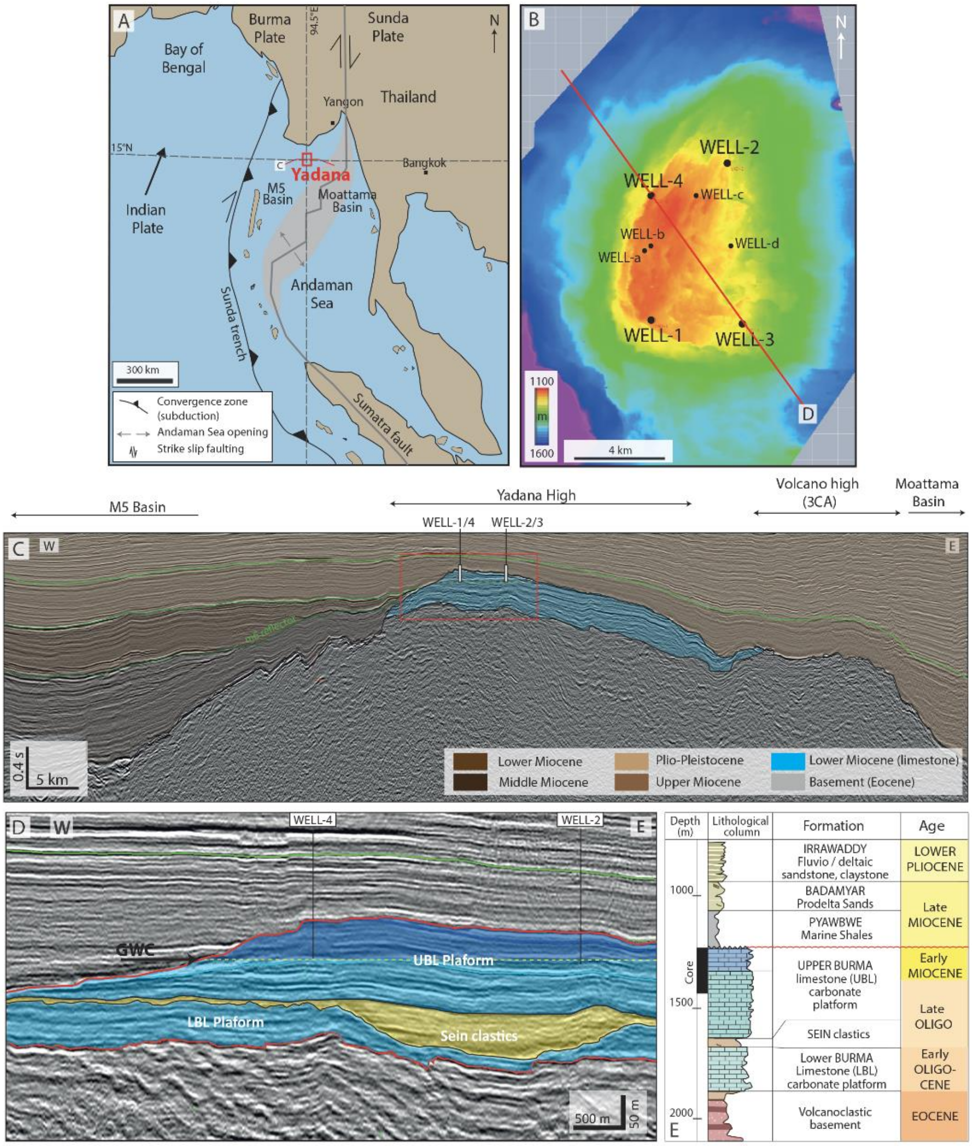

Figure 4-1 : Geographical and geological setting of the Yadana gas field: (A) Geographical and tectonic settings of the Andaman Sea and the Yadana Field (after (Curray, 2005); (B) Depth map of top reservoir and well location. (C) Interpreted regional 2D seismic profile (two-way time) through the Yadana high (see location on A). (D) Interpreted seismic profile (depth) of the Yadana field crossing the wells WELL-4 and WELL-2, showing the lithostratigraphic units and the gas water contact (yellow dotted line) (see location on A). (E). Lithostratigraphic column of the Yadana platform.

4.1 Introduction

Seismic reflection has become a major and indispensable geophysical method for imaging subsurface architecture of carbonate systems and reservoirs (Burgess et al., 2013; Eberli et al., 2003; Fournier and Borgomano, 2007; Rankey et al., 2019) and to reconstruct their evolution pattern and related controlling factors (Bachtel et al., 2004; Fournier et al., 2005; Lüdmann et al., 2018). Most seismic reflections in sedimentary rocks are composites resulting from several contrasts in acoustic impedance (Sheriff, 1977). In calcite-dominated carbonate reservoirs, such contrasts in acoustic impedance are mostly related to vertical changes in porosity and pore space architecture (Anselmetti and Eberli, 1999; Fournier and Borgomano, 2007). Seismic interpretation of carbonates is therefore highly challenging since such changes in porosity and pore network structure are strongly related to diagenetic history (Wagner, 1997). The seismic sequence stratigraphy method is based on the assumption that seismic reflections follow depositional surfaces and erosional unconformities (Tucker, 1993; Vail et al., 1977), and therefore, they have chronostratigraphic significance. In carbonate systems, the diagenetic evolution of the reservoir leads to a spatial porosity and pore type distribution that can significantly obliterate the depositional architecture in both siliciclastic and carbonates settings (e.g., Léonide et al., 2014; Zampetti et al., 2004). As a consequence, the seismic imaging of depositional features and the sedimentological and stratigraphic interpretation of seismic data may be significantly disturbed especially when the diagenetic evolution is multiphased and involves meteoric and burial processes (Fournier and Borgomano, 2007). However, the strong interaction between diagenetic architecture and seismic expression in carbonates represents a unique opportunity for detecting diagenetic bodies of exploration and exploitation significance from seismic data. On the basis of the integrated analysis (carbonate sedimentology, diagenesis, petroacoustics and seismic) of a Lower Miocene carbonate buildup (Upper Burma Limestone, Yadana gas field, offshore Myanmar) the present paper aims at: (1) identifying the depositional and diagenetic processes that controlled the evolution and the spatial distribution of acoustic properties within the carbonate buildup, (2) assessing the relative impact of depositional facies, diagenetic processes, and seismic resolution on the seismic expression of these carbonates, (3) testing the ability of seismic data to reveal diagenetic heterogeneity of significant impact on recovery and flow during hydrocarbon production.

4.2 Geological setting

The structural framework as well as the marine geomorphology of the Andaman Sea area has been strongly controlled by the complex tectonic evolution of SE Asia during the Cenozoic (Hall, 2002; Lee and Lawver, 1995). During the Paleogene, the northeastward oblique subduction (Sunda subduction zone) of the Indian plate beneath the Eurasian plate resulted in the opening of the Andaman Sea as a back-arc basin (Fig. 4-1A) (Chakraborty and Khan, 2009; Curray, 2005). In addition, such an oblique subduction led to: (1) major dextral strike-slip movements along the Sagaing-Andaman-Sumatran fault system, 2) the individualization of the Burma microplate, and 3) rifting and spreading of the Andaman Sea within the back-arc basin (Chakraborty and Khan, 2009; Morley, 2012). During the Oligocene and Early Miocene, the Yadana carbonate platform developed on the top of a volcanic ridge, located in the northern Andaman Sea, and separating the M5 fore-arc basin to the west from the Moattama back-arc basin to the east (Fig. 4-1B and C) (A. Racey, 2015; Morley, 2013). The lowermost deposits consist of Upper Eocene volcano-clastics sediments (Fig. 4-1D). The overlying Oligo-Miocene carbonates may reach up to 700 m in thickness, and are subdivided into two distinct formations (Paumard et al., 2017): 1) the Lower Burma Limestone formation (LBL), Late Oligocene in age, that is composed of two distinct carbonate platforms separated by a central trough which is filled by the Sein clastic formation and 2) the Upper Burman Limestone formation (UBL), Early Miocene in age, after benthic foraminiferal biostratigraphy, that is made of one single carbonate platform, the top of which corresponding to the gas reservoir of the Yadana field. A long-term depositional hiatus (~10 Myr) is recorded at the top of the UBL carbonates that are sealed by Late Miocene (N16, planktonic zone) pro-delta shales (Pyawbwe and Badamyar formations) from the Irrawaddy deltaic system. A major phase of eastward tilting of the Yadana platform, evidenced by seismic profiles, occurred during the Late Miocene (horizon M6: 8.2 Ma, after (Paumard et al., 2017). The Yadana gas field investigated in this study is located at the top (~100 m) of the west part of the platform, at depths ranging from 1240 mCD (core depth in meter) to 1350 mCD, corresponding to an overburden pressure of 2510 to 2550 psi (17 Mpa) and a temperature of 60°C.

The Yadana buildup has been regarded as a reef-rimmed platform by Paumard et al. (2017) on the basis of seismic facies interpretation, but the integration of paleoecological and sedimentological analysis of core data led to a revision of the former depositional models (Teillet et al., 2019b) and to the definition of three distinct carbonate factories operating on the top of an open platform: (1) a scleractinian carbonate factory developing under

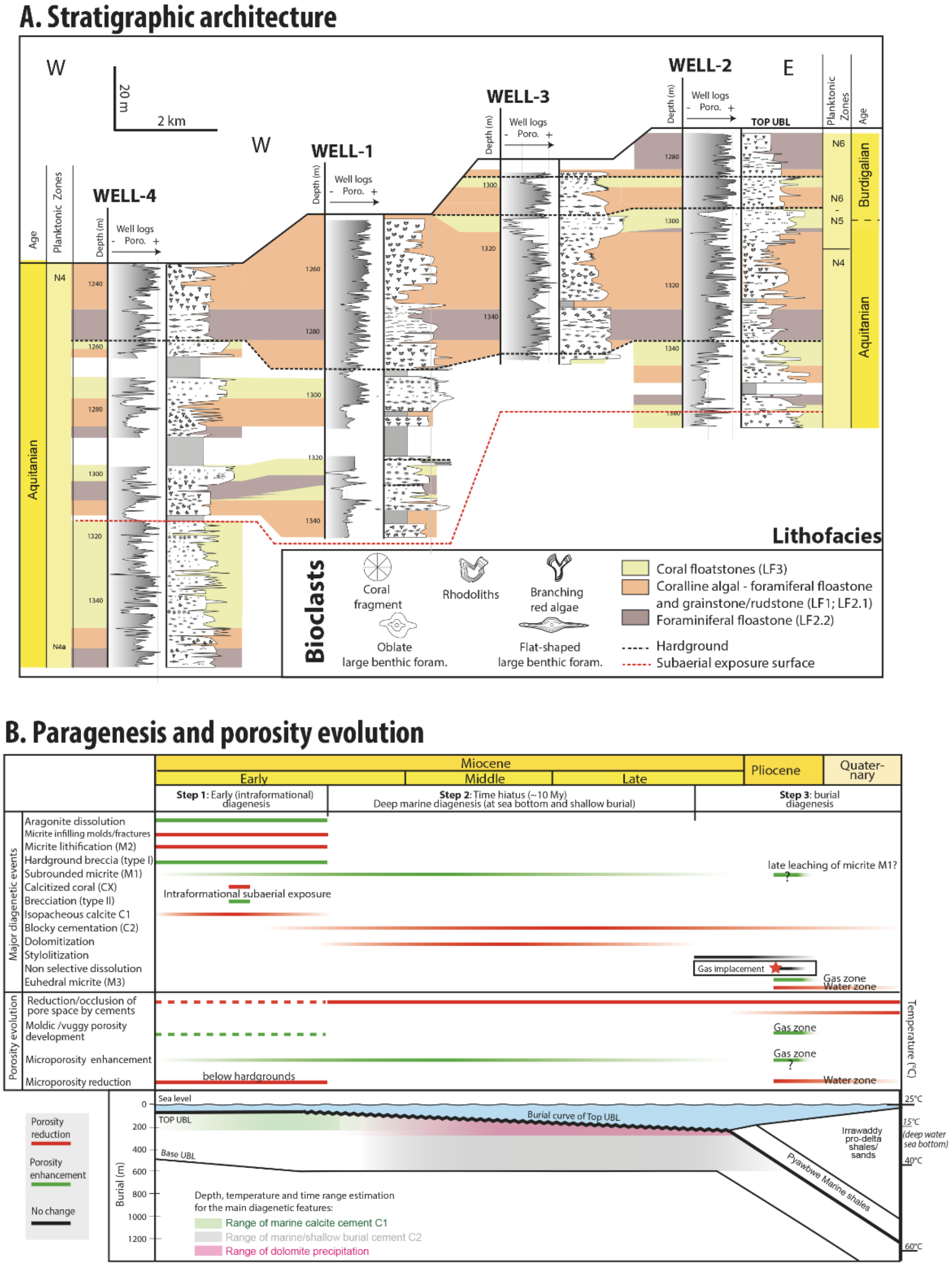

Figure 4-2: (A): Well-correlation panel showing the depositional architecture of the Upper Burman Limestone (after Teillet et al., in press 1); (B): Paragenesis and porosity evolution of the Upper Burman Limestone (after Teillet et al., in press 2)

mesophotic conditions during periods of high particulate organic matter supplies, (2) an echinodermal carbonate factory occupying dysphotic to aphotic area of the shelf coevally with the scleractinian carbonate factory, (3) a large benthic foraminiferal-coralline algal carbonate factories prevailing under oligo-mesophotic and oligo-mesotrophic conditions. The resulting depositional architecture of the carbonate buildup is displayed in Fig. 4-2A.

A scenario of diagenetic and porosity evolution of the Upper Burman Limestones has been proposed by (Teillet et al., 2019a)(Fig. 4-2B). The high (28%) average porosity of the reservoir is related to significant development of microporosity, moldic and vuggy porosity Mud-supported, coral-rich sediments record significant early marine dissolution of aragonite and early lithification of matrix that has led to the development of dense layers. One intra-formational subaerial exposure surface has been identified based on diagenetic features and stables isotopes. Teillet et al. 2019 interpreted the top of the reservoir as a long-term depositional hiatus (middle to late Miocene) which was related to the platform drowning and non-deposition in a deep marine setting. Moderate dolomitization has affected the top and flanks of the platform during the depositional hiatus. Microporosity development and sparry calcite cementation (C2 calcite cements) have been shown to have occurred in marine to marine shallow burial environments. A major decrease in porosity (up to 15%), below the gas-water contact suggests a major phase of porosity evolution during the hydrocarbon emplacement: 1) increased moldic and vuggy porosity development within the gas zone, 2) microporosity preservation or enhancement in loosely packed, subrounded micrites within the gas zone, and 3) microporosity reduction by calcite precipitations within the water zone leading to the formation of densely packed, euhedral micrites.

4.3 Data and methods

The Yadana field has been penetrated by 20 wells and covered by a three-dimensional seismic survey. Four cored (WELL-1, WELL-2, WELL-3, and WELL-4) and four uncored (WELL-a, WELL-b, WELL-c, WELL-d) wells have been selected for the present study (see location in Fig. 4-1B). The database is summarized in Table 5 and detailed below.

Carbonate rock sample database and petrographic analyses

The identification of depositional and diagenetic features is based on the study of a total of 343 m of cores located within the UBL interval (WELL-1: 87.5 mCD (meter Core Depth), WELL-2: 84 mCD WELL-3: 59.5 mCD WELL-4: 112 mCD). A total of 694 thin sections

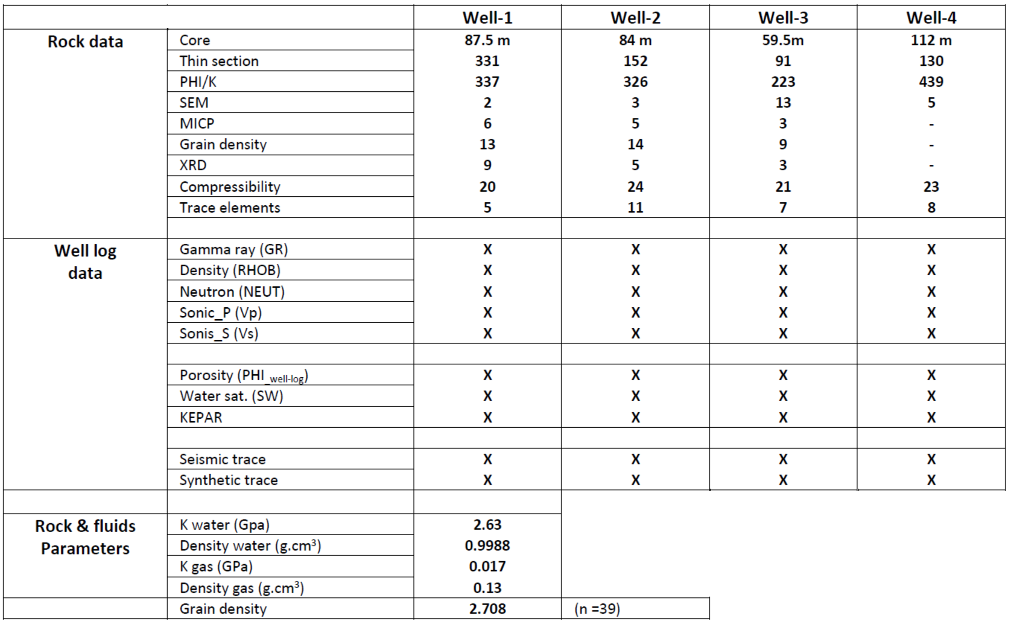

		Well-1	Well-2	Well-3	Well-4
Rock data	Core	87.5 m	84 m	59.5m	112 m
	Thin section	331	152	91	130
	PHI/K	337	326	223	439
	SEM	2	3	13	5
	MICP	6	5	3	-
	Grain density	13	14	9	-
	XRD	9	5	3	-
	Compressibility	20	24	21	23
	Trace elements	5	11	7	8
Well log data	Gamma ray (GR)	X	X	X	X
	Density (RHOB)	X	X	X	X
	Neutron (NEUT)	X	X	X	X
	Sonic_P (Vp)	X	X	X	X
	Sonis_S (Vs)	X	X	X	X
	Porosity (PHI $_{\text{well-log}}$)	X	X	X	X
	Water sat. (SW)	X	X	X	X
	KEPAR	X	X	X	X
	Seismic trace	X	X	X	X
	Synthetic trace	X	X	X	X
Rock & fluids Parameters	K water (Gpa)	2.63			
	Density water (g.cm^3)	0.9988			
	K gas (GPa)	0.017			
	Density gas (g.cm^3)	0.13			
	Grain density	2.708	(n =39)		

Table 5 : List of rock and well-log data. Elastic properties of fluids and mineralogical components.

have been prepared from cores (average spacing of 50 cm). The thin sections were impregnated with a blue-color epoxy resin and half-stained with alizarine red + potassium ferrocyanide solution for identification of carbonate minerals.

Thin sections were observed under polarized-light microscopy for the characterization of depositional and diagenetic features as well as for the quantitative analysis of pore types. Macroporosity is defined as the pore space which is colored with blue epoxy and whose size exceeds 2 pixels (i.e., diameter> 10 µm) on scanned thin sections. The proportion of macroporosity on thin section is automatically extracted using the software ImageJ by gathering the blue pixels. Microporosity is defined as pores non-visible on thin section pictures or whose size is lower than 2 pixels (i.e., pore diameter <10 µm). The definition of microporosity used in the present work is therefore consistent with the definition given by (Cantrell et al., 2015). The proportion of microporosity was estimated as the difference between the laboratory porosity measured on plugs and the macroporosity computed from thin-section image analysis. Petrographic analysis of thin sections was supported by observations of selected samples of cements under cathodoluminescence. Micrite microfabrics were characterized by scanning electron microscopy (SEM) images.

Petrophysical laboratory measurements

Laboratory helium porosity (PHI_plug) measurements have been performed on approximately 1300 core plugs at an interval of 50 cm in sub-atmospheric condition. Special core analysis (SCAL) consist of 14 MICP measurements giving information about the pore throat radius. Mercury was injected into cleaned and dried samples and initially evacuated, at pressure stages up to 345 MPa. Additionally, to include the mineralogical composition, density grain measurements, XRD analysis, element trace and fluorescence X analysis have been performed. The elemental trace determinations of major (Al, Ca, Mg, Na, K, Ti, Fe, Mn, P, S in percent) and minor elements (including Cu, Pb, Zn, As, U, Th, Sr, Ba in ppm) on whole rock and selected carbonate components (bioclasts, matrix and cements).

Well-log data and derived physical parameters

Conventional well log data of the 8 studied wells have been used in the present work. They include neutron (NEUT), density (RHOB), gamma ray (GR), photoelectric effect (PE) and P- and S-sonic logs. Water saturation (Sw), total porosity (PHI_welllog) and mineralogical composition have been estimated at TOTAL from the quantitative interpretation of well logs. P- and S-wave velocities of dry rocks have been estimated from sonic logs and by using the (Gassmann, 1951) fluid substitution relationship. Fluid physical parameters (bulk, shear moduli and density) are displayed in Table 1. Effective bulk moduli of fluid mixtures are calculated by using the empirical (Brie et al., 1995) mixing law. Core depths have been tied to log depths by matching vertical changes in plug porosity (PHI_plug) corrected from the overburden effect and well-log porosity (PHI_welllog) curves.

Rock physics modeling (DEM)

Differential Effective Models (DEM) (Norris, 1985; Zimmerman, 1991) have been used to model velocity-porosity transforms for various mineral compositions, porosity values, pore aspect ratios and fluid contents. Such an approach helps quantify the relative impact of mineralogy, pore volume and pore architecture on elastic moduli and velocities (Fournier et al., 2018; Xu and Payne, 2009).

Seismic data

The pre-production 3D seismic survey (base seismic) which has been used in the present work was acquired by TOTAL in 1993 and covers the Yadana, the Badamyar and the Sein gas fields (~511 km2). It is characterized by a trace spacing of 12.5 x 6.25 m and a signal sampling of 3 ms. A downward increase in acoustic impedance (positive reflection coefficient) is represented by a positive amplitude (SEG convention). The central signal frequency within the carbonate buildup averages 45 Hz which implies a vertical resolution ranging 20 m. A monitor 3D seismic survey was acquired in 2012 after 14 years of production. In the present study, four key seismic reflection horizons have been defined within the gas-bearing interval (H9, H9A, H9B, H10 and H10B) from the pre-production 3D seismic survey. Additionally the expression of a seismic reflection which is located at the pre-production (i.e., initial) gas-water contact (IGWC) has been analyzed in both pre-production and monitor 3D seismic data.

Integrative workflow for seismo-diagenetic characterization of the Yadana reservoir.

The following workflow has been adopted to assess the geological significance of seismic reflections within the Yadana carbonate gas reservoir:

(1) Sedimentological and diagenetic study based on petrographic description of cores and thin sections, cathodoluminescence, and interpretation of carbon and oxygen isotope ratios (Teillet et al., 2019a; 2019b).
(2) Interpretation of the relationships between depositional fabrics, diagenetic products, and physical properties (porosity, P-wave velocity, acoustic impedance).
(3) Identification of diagenetic units on the basis of cores and well-log data; these are defined as carbonate rock intervals characterized by a pattern of diagenetic evolution, and a range of reservoir and acoustic properties.
(4) Well-to-seismic ties.
(5) Determination of the relationship between seismic reflections and the major depositional surfaces and diagenetic unit boundaries.

4.4 Results

4.4.1 Depositional lithofacies

The UBL carbonates are characterized by a relatively monotonous, 100m-thick succession of bioclastic limestones. The biota is dominated by non-geniculate coralline algae and large benthic foraminifers. On the basis of textural and biological features, five lithofacies have been identified and summarized in Table 6: Coralline algal rudstone to floatstone (LF1: Fig 4-3F, 4-3I, 4-3K), large benthic foraminiferal rudstone (LF2.1: Fig 4-3A, 4-3E) to floatstone (LF2.2), scleractinian-echinodermal floatstone (LF3.1: Fig.4-3C, 4-3D, 4-3G, 4-3J) and echinodermal wackestone (LF3.2).

4.4.2 Diagenetic features

Petrographic analysis of cores and thin sections revealed a variety of diagenetic features related to carbonate cementation, neomorphism, dissolution, brecciation, dolomitization and compaction:

Carbonate cements

Two distinct cements have been evidenced from petrographic analysis of thin sections. The isopacheous calcite cement (C1) consists of isopacheous rim of scalenohedral, sparry, non-ferroan calcite crystal averaging 10 µm in thickness which may occupy intergranular or moldic pores after dissolving aragonite bioclasts. The cement (C2) consists of blocky, sparry, non-ferroan calcite (50 to 250 µm) occluding intergranular pores (Fig. 4-3A) in grainstone rudstones (in gas and water zones), moldic/vuggy pores and fractures (mainly in the water zone). Calcite cements C2 have been observed overlying calcite cements C1.

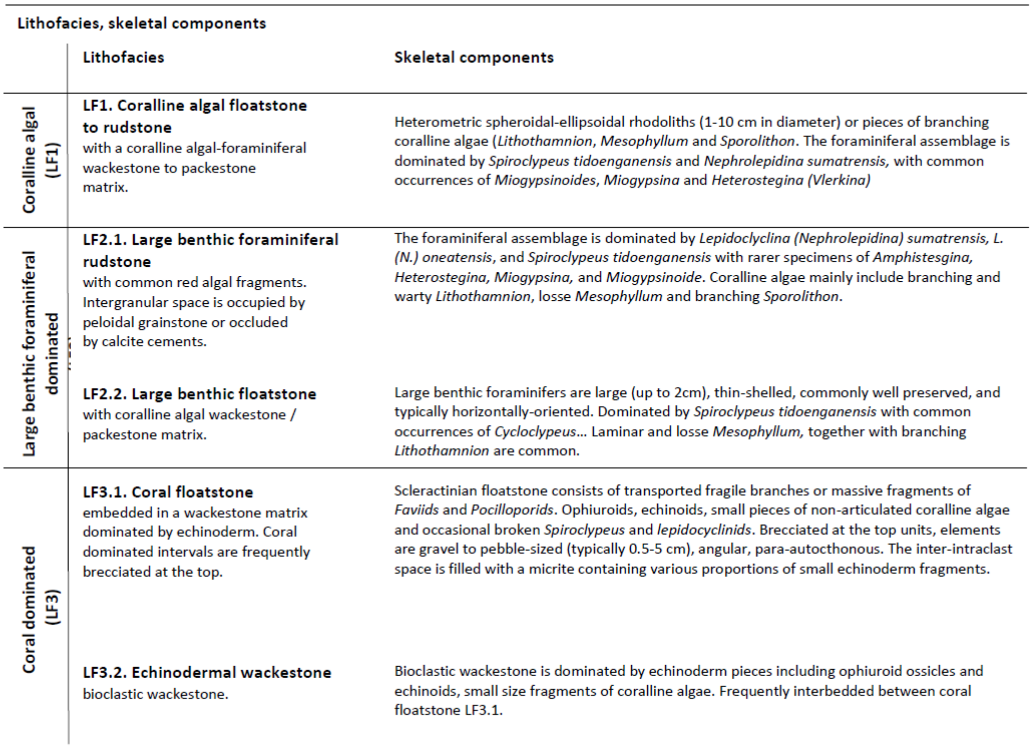

Lithofacies, skeletal components

	Lithofacies	Skeletal components
Coralline algal (LF1)	**LF1. Coralline algal floatstone to rudstone** with a coralline algal-foraminiferal wackestone to packestone matrix.	Heterometric spheroidal-ellipsoidal rhodoliths (1-10 cm in diameter) or pieces of branching coralline algae (*Lithothamnion*, *Mesophyllum* and *Sporolithon*. The foraminiferal assemblage is dominated by *Spiroclypeus tidoenganensis* and *Nephrolepidina sumatrensis*, with common occurrences of *Miogypsinoides*, *Miogypsina* and *Heterostegina (Vlerkina)*
Large benthic foraminiferal dominated	**LF2.1. Large benthic foraminiferal rudstone** with common red algal fragments. Intergranular space is occupied by peloidal grainstone or occluded by calcite cements.	The foraminiferal assemblage is dominated by *Lepidoclyclina (Nephrolepidina) sumatrensis, L. (N.) oneatensis*, and *Spiroclypeus tidoenganensis* with rarer specimens of *Amphistesgina, Heterostegina, Miogypsina,* and *Miogypsinoide*. Coralline algae mainly include branching and warty *Lithothamnion*, losse *Mesophyllum* and branching *Sporolithon*.
	LF2.2. Large benthic floatstone with coralline algal wackestone / packestone matrix.	Large benthic foraminifers are large (up to 2cm), thin-shelled, commonly well preserved, and typically horizontally-oriented. Dominated by *Spiroclypeus tidoenganensis* with common occurrences of *Cycloclypeus*... Laminar and losse *Mesophyllum*, together with branching *Lithothamnion* are common.
Coral dominated (LF3)	**LF3.1. Coral floatstone** embedded in a wackestone matrix dominated by echinoderm. Coral dominated intervals are frequently brecciated at the top.	Scleractinian floatstone consists of transported fragile branches or massive fragments of *Faviids* and *Pocilloporids*. Ophiuroids, echinoids, small pieces of non-articulated coralline algae and occasional broken *Spiroclypeus* and *lepidocyclinids*. Brecciated at the top units, elements are gravel to pebble-sized (typically 0.5-5 cm), angular, para-autocthonous. The inter-intraclast space is filled with a micrite containing various proportions of small echinoderm fragments.
	LF3.2. Echinodermal wackestone bioclastic wackestone.	Bioclastic wackestone is dominated by echinoderm pieces including ophiuroid ossicles and echinoids, small size fragments of coralline algae. Frequently interbedded between coral floatstone LF3.1.

Table 6 : Depositional lithofacies and skeletal components of the Upper Burman Limestone.

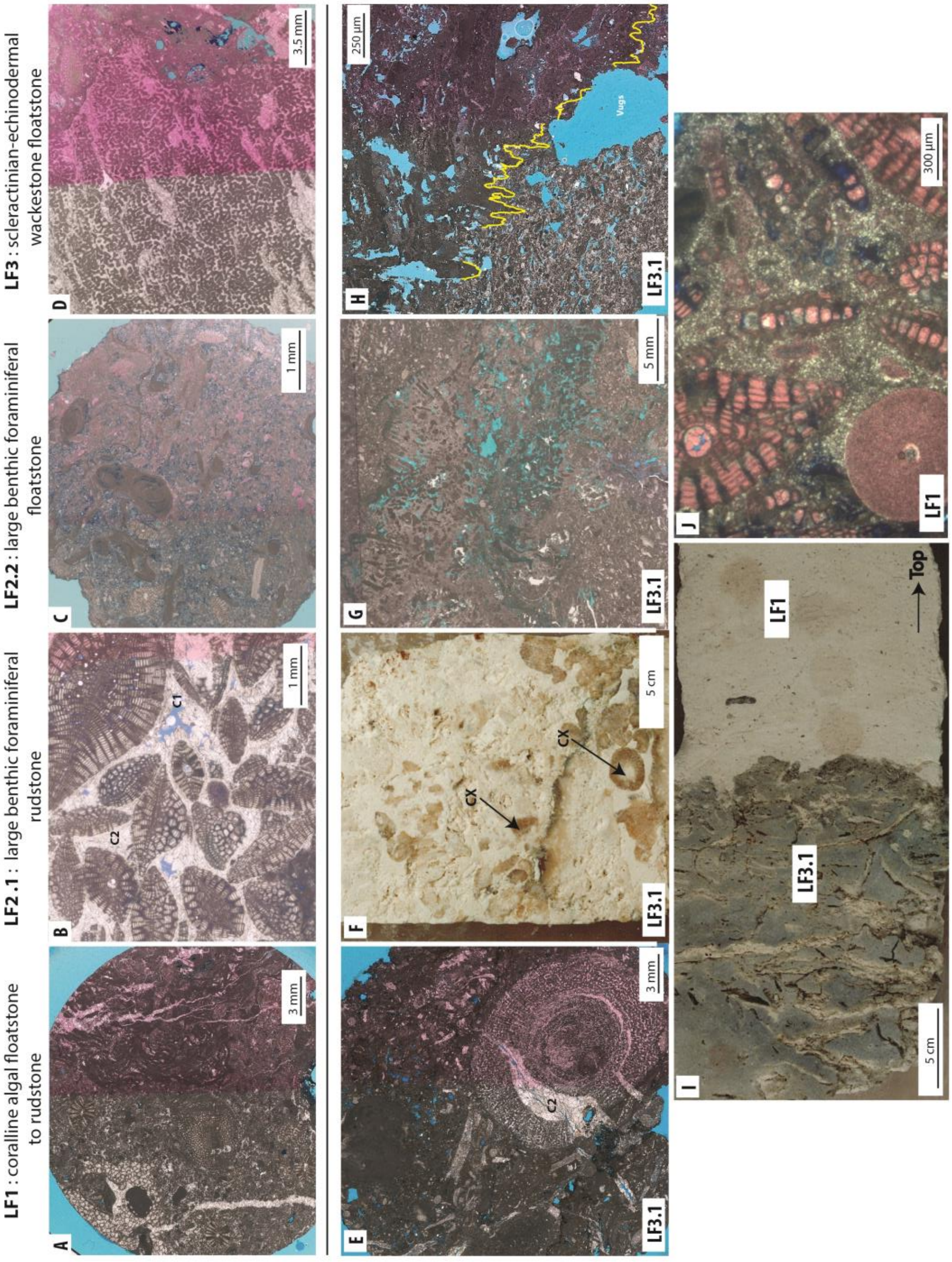
LF1 : coralline algal floatstone to rudstone
LF2.1 : large benthic foraminiferal rudstone
LF2.2 : large benthic foraminiferal floatstone
LF3 : scleractinian-echinodermal wackestone floatstone
A
3 mm
B
C1
C2
1 mm
C
1 mm
D
3,5 mm
E
C2
3 mm
LF3.1
F
CX
CX
5 cm
LF3.1
G
5 mm
LF3.1
H
Vugs
250 µm
LF3.1
I
5 cm
LF3.1
LF1
Top
J
300 µm
LF1

Figure 4-3: (A) WELL- 2 1345.40 mcD: Foraminiferal coralline algalfloatstone-rudstone (lithofacies LF1) with low microporosity in the water zone (diagenetic facies: W-DF1b); (B): WELL-3 1319.49 mCD; Isopacheous C1 rim cement and blocky calcite cement C2 infilling the intergranular pore space of a foraminiferal rudstone(lithofacies LF2.1; diagenetic facies G-DF2); (C) WELL-3 1330.30 mcD: red algal/foraminiferalfloatstone (lithofacies LF1) with high matrix and intraskeletal microporosity and vuggy porosity (diagenetic facies: G-DF1a); (D) WELL-1 1328.03 mCD equigranular sparry calcite (C2′) replacing a coral fragment; (E) WELL-21361.42 mcD: Coral and echinodermalfloatstone (lithofacies LF3.1) in the water zone. Tight with low microporosity (diagenetic facies: W-DF1a); (F) WELL-4 1337.7mCD; core picture showing brownish calcitized coral (CX) within a brecciated interval (lithofacies LF3.1; diagenetic facies: G-DF3); (G) WELL-3 1311.84 mCD: Coralfloatstone (lithofacies LF3.1) whose scleractinian elements have been dissolved; the resulting moldic pores are infilled with a bioclastic micrite which is similar innature to that of thefloatstone matrix thus leading to a faint-ghost fabric (diagenetic facies: G-DF4); (H) WELL-2 1284.56 mCD: microphotograph of a coralline algal-foraminiferalfloatstone (lithofacies LF1) showing a stylolite (yellow line) which is overprinted by a dissolution vug (diagenetic facies: G-DF1a); (I) WELL-3 1308.05mCD: core photograph of a hardground surface, at the top of a carbonate breccia composed of poorly displaced, tight elements of coral-rich and echinodermalfloatstone (lithofacies LF3.1; diagenetic facies: G-DF4). The hardground is sharply overlain by highly microporous, coralline algal-foraminiferalfloatstone (lithofaciesLF1; diagenetic facies: G-DF1a). The inter-clast space of the hardground breccia isfilled by the overlying microporous sediment; (J) WELL-4 1286 mCD: microphotograph of a foraminiferal packstone-floatstone whose matrix is partially replaced by dolomicrosparite (not stained by alizarine) (diagenetic facies G-DF1c).

Neomorphic features

Calcitized aragonitic bioclasts (dominantly coral fragments) display two types of neomorphic features: 1) calcitized corals composed of equant calcite crystals (20 to 250 µm) (C2') (Fig. 4-3B) and 2) calcitized corals composed of large (250-1000 µm), orange-brown under natural light, sparry calcite crystals (CX) (Fig. 4-3C). The CX calcites have been encountered only within brecciated scleractinian-rich limestones (LF3 lithofacies).

Dissolution features

Selective dissolution of aragonitic skeletal elements (mainly scleractinian) and subsequent infill of the moldic pores by sediment (micrite mud and fine-grained skeletal fragments) are common diagenetic features in coral-rich lithofacies (LF3). The sediment replacing the dissolved septae is of similar nature and in physical continuity with the lime mudstone matrix in which the coral fragment is embedded, thus leading to a faint-ghost fabric (sensu Sanders, 2003, Fig. 4-3D). Non-selective dissolution affecting both aragonitic and calcitic bioclasts as well as micrite matrix may lead to the formation of moldic pores (Fig. 4-3E) and vugs overprinting stylolites (Fig. 4-3F) and devoid of any sediment or cement infill.

Brecciation features

Brecciated intervals are common within coral floatstones (LF3.1) and echinodermal wackestones (LF3.2) lithofacies. Two distinct carbonate breccias have been identified.

- Thin beds (<20 cm) of low porosity (<20%) breccia (Type I breccia), characterized by poorly sorted, irregular-shaped elements which are commonly interlocked and displaying very low displacement (Fig. 4-3G).

- Type II breccia: thick interval (up to 10 m) of highly porous, loose breccia with large (up to 10 cm) angular and poorly sorted fragments which are brownish calcite (Fig. 4-3D). The space between clasts may be partially filled with a finely bioclastic, matrix-supported sediment, but residual pore space may be preserved or filled by C2 sparry calcite cements.

Dolomitization

In various intervals, intragranular and matrix micrite is partially replaced by euhedral dolomite micro-rhombs (<50 µm) (Fig. 4-3H). Dolomitization affects preferentially coralline-algal and foraminiferal lithofacies (LF1, LF2.1 and LF.2.2)

Stylolites

Compaction features are relatively scarce within the Upper Burman Limestone. In a few thin sections, stylolites are overprinted by dissolution vugs (Fig.4-3F).

Micrite microfabrics

Four main micrite microfabrics have been identified under SEM in both micritized bioclasts and micrite matrix. In the gas zone, high porosity limestones (20-45%) exhibit dominantly loosely packed, anhedral, subrounded calcimicrite crystals, typically 1-2 µm in diameter (M1 microfabric: Fig. 4-4A, B). M1 micrites commonly display microvugs (2-10 µm in diameter) and aggregates (2-10 µm) of coalescent micrite particles (Fig.4-3A, B). In gas-bearing limestones with porosity <20%, both micrite matrix and micritized allochems exhibit densely packed, coalescent, anhedral micrite crystals (M2 microfabric: Fig. 4-4C). The M2 micrite microfabric occurs typically in the matrix of coral-rich floatstones (lithofacies LF3). In the water zone, in both matrix and micritized bioclasts, micrite crystals are mainly euhedral (M3 microfabric: Fig. 4-4D, E) and are coarser (typically 2-4µ) than gas-zone calcimicrites M1 and M2. Additionally, euhedral crystals may encase smaller, rounded micrite particles (Fig. 3E). Finally, euhedral dolomicrite particles (from 0.5 to 4 µm) occur within micritized bioclasts (typically coralline algae) and matrix in both water and gas zone (Fig. 4-4F).

4.4.3 Pore type characterization

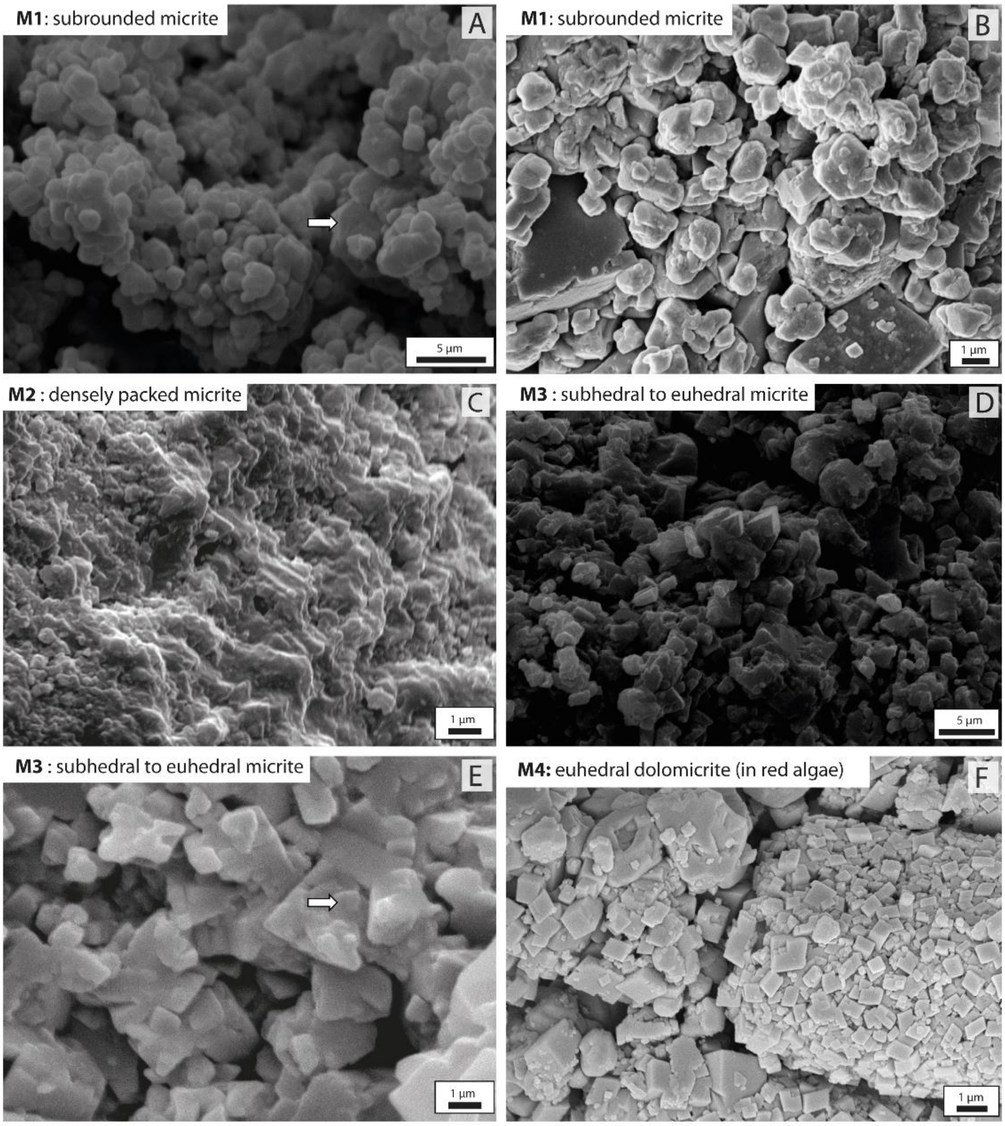

Figure 4-4: Micrite microfabrics identified under SEM: (A) Highly porous calcimicrite microtexture M1 showing loosely packed, dominantly anhedral, subrounded micrite particles. Such micrites display commonly microvugs (diameter: 5-10 µ) and relatively minor particle coalescence (gas zone). Few micrite particles exhibit subhedral morphology (arrow), (B) Highly porous calcimicrite microtexture M1, mixed with larger euhedral dolomicrosparite crystals (dol) (gas zone) (C) Low porosity calcimicrite microtexture M2 showing densely packed, strongly coalescent, anhedral micrite particles (gas zone). (D) Low porosity micrite microtexture M3 showing densely packed, subhedral to euhedral calcimicrite crystals (water zone) (E) Low porosity micrite microtexture M3 showing densely packed, euhedral calcimicrite crystals encasing smaller, rounded micrite particles (arrow) (water zone). (D) Euhedral dolomicrite (M4) replacing a coralline algae (gas zone).

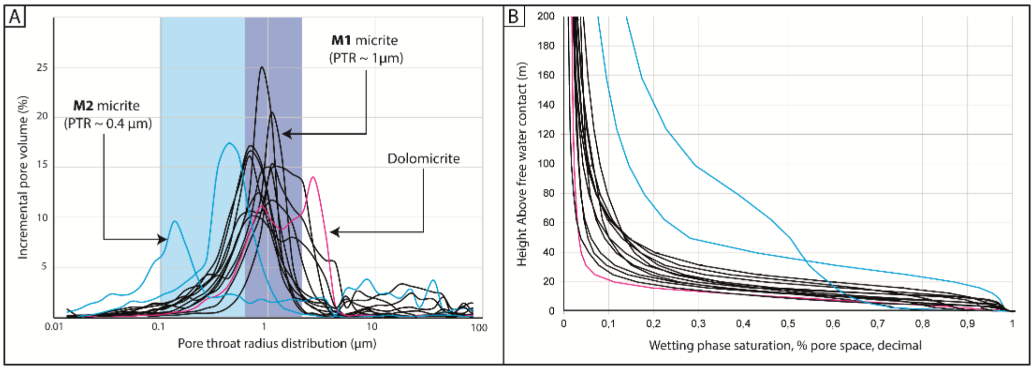

Figure 4-5: Mercury injection capillary pressure (MICP) data on selected samples. (A) Pore throat size distribution curves. (B) Primary drainage capillary pressure curves converted to a height above free water level.

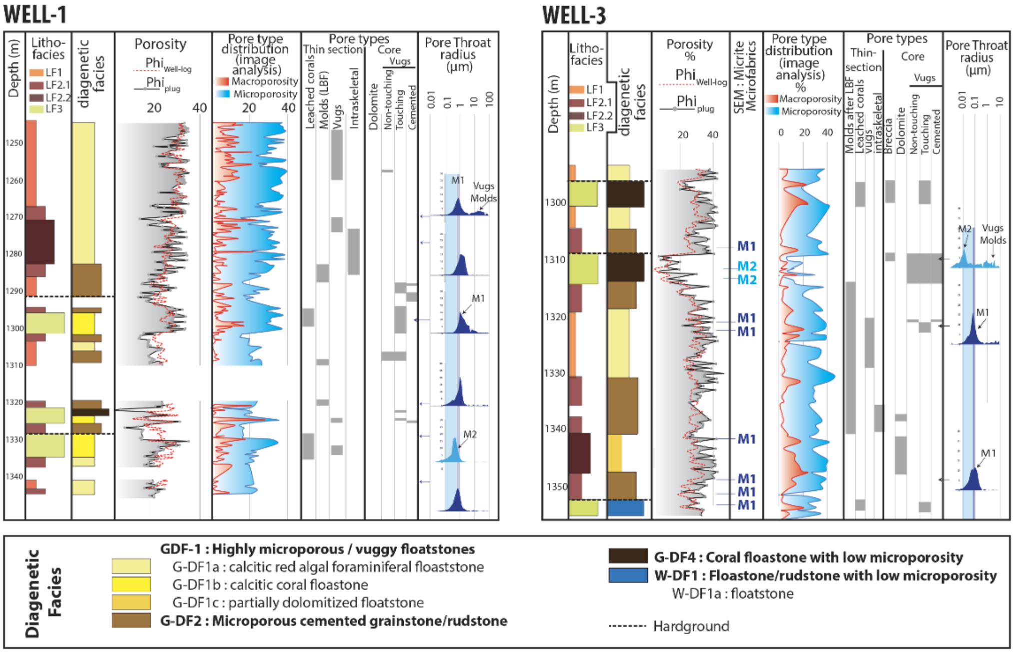

Figure 4-6 : WELL-1 and -3, cored intervals: lithofacies, diagenetic zonations, porosity from well logs and plugs, pore type distribution on thin sections (Digital Image Analysis) and cores and pore throat radius measurement (MICP).

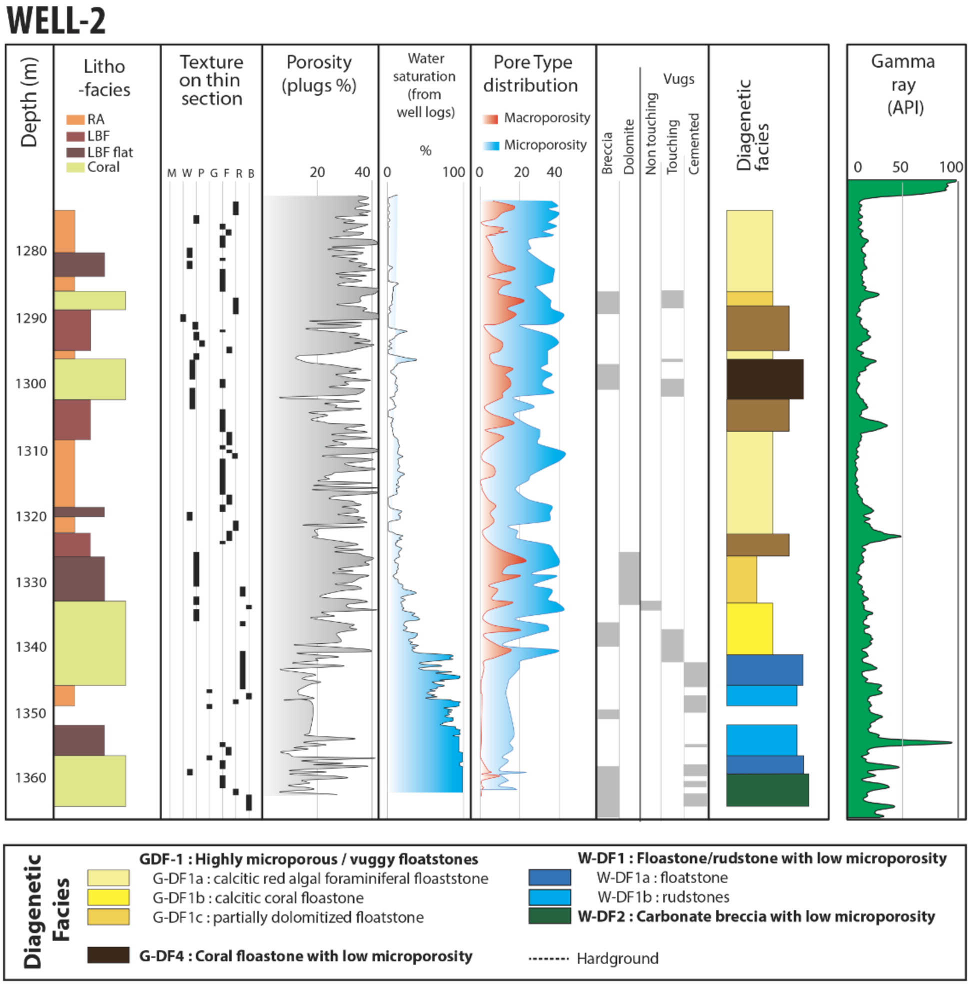

Figure 4-7 : WELL-2 cored intervals: lithofacies, textures on thin sections, porosity and saturation from well logs, pore type distribution on thin sections (Digital Image Analysis) and cores and diagenetic zonation and gamma ray.

The analysis of 320 thin sections shows that macroporosity ranges from 0 to 15% and represents in average only 25% of the total porosity (PHI_plug) (Pore type distribution log, red curve on Fig 4-6 and 4-7) while 75% of the pore volume is microporosity. (Blue curve on Fig 4-6 and 4-7). Macropore space is composed of a mixture of various pore types: (1) mesovugs (pore diameter between 10 and 100 µm) located within leached micrite matrix (M1); (2) moldic pores (pore diameter: from 20 µm to 5 cm) mainly after leaching benthic foraminifers, coralline algae or corals; (3) macro-vugs (>100 µm) affecting both matrix and/or allochems; (4) intercrystalline pores in dolomitic limestone (pore size: 10-50 µm); and (5) intergranular pores (50-200 µm) which are very uncommon in the studied samples.

Microporosity is both located in micrite matrix and micritized allochems. MICP measurements performed on 14 samples revealed that microporosity in the UBL limestones is characterized by three classes in terms of pore throat radius distribution (Fig. 4-5). The first group, including 11 of the 14 samples, has a unimodal distribution with modal pore throat radii ranging from 0.6 to 1.2 µm. This group corresponds to samples with micrite microfabrics M1 (Fig. 4-3A, B). The second group (only 2 samples) displays a unimodal distribution with a pore throat radius lower than 0.6 µm. These samples are coral-rich limestones with micrite microfabric M2 (Fig. 4-4C). Finally, one sample of dolomitic wackestone displays a bimodal distribution with pore throat radii of 0.8 µm and 3 µm likely which are likely to be related respectively to micropores in M1 micrite and intercrystaline porosity between dolomite rhombs.

4.4.4 Diagenetic zonation of the Upper Burman Limestone

A diagenetic layering of the cored interval of the Upper Burman Limestone has been performed based on the identification of diagenetic facies. The diagenetic facies have been defined from the combination of petrographic and petrophysical parameters (Table 7): 1) diagenetic features, 2) micrite microfabrics, 3) range of porosity values, 4) pore type associations. The significant decrease in average porosity below the gas-water contact (Fig. 5) and the distinct diagenetic features observed in the gas-bearing and water-bearing reservoir led to differentiate the 2 zones in the facies classification. In the gas zone, in intervals where water saturation is lower than 50, porosity average 28%, whereas at higher water saturation and particularly below the gas-water contact, porosity decreases significantly (average porosity: 18%) over a 30 meter-thick interval (Fig. 4-7). Within the gas zone, four main groups of diagenetic facies have been identified: 1) highly microporous and vuggy, mud-supported carbonates (G-DF1), 2) microporous cemented grainstones-rudstones (G-DF2), 3) microporous and vuggy carbonate breccia (G-DF3), 4) floatstones with low matrix microporosity (G-DF4). This diagenetic facies G-DF1 has been subdivided into 3 sub-facies: calcitic red algal and foraminiferal floatstones (G-DF1A), calcitic coral floatstones (G-DF1B), and partially dolomitized floatstones (G-DF1C). Within, the water zone, two diagenetic facies have been recognized in the cored interval: 1) floatstones (W-DF1A) and rudstones (W-DF1B) with low intragranular and matrix microporosity, and 2) carbonate breccia with low microporosity (W-DF2).

Diagenetic facies			Diagenetic features	Micrite micro-fabrics	Typical porosity range	Pore type association	$\delta^{13}C$ bulk (‰ PDB)	$\delta^{18}O$ bulk (‰ PDB)	Occurrence	Illustration
G-DF1	**Highly microporous and moldic/vuggy, mud-supported carbonates**	**A: calcitic red algal and foraminiferal floatstones**	Micritized bioclasts; blocky calcite cement (C2); leached bioclasts (red algae and foraminifers) and matrix	M1	25-45%	High microporosity, high moldic and vuggy porosity	-1 to +1	-3 to 0	Gas zone	Fig.7 A, E
		B: calcitic coral floatstones	Neomorphosed corals into C2' calcite; micritized bioclasts; rare blocky calcite cement (C2); leached bioclasts (corals, red algae and foraminifers)	M1	25-45%	High microporosity, high moldic and vuggy porosity	-1 to +1	-3 to 0		Fig. 4 D
		C: partially dolomitized floatstones	Dolomicrite to dolomicrosparite crystals replacing micrite matrix and micritized bioclasts; leached bioclasts (red algae and foraminifers) and matrix	M1 M4	25-45%	High microporosity, high moldic and vuggy porosity	-0,5 to +1,5	-0,5 to +3		Fig.7 B
G-DF2	**Microporous cemented grainstones-rudstones**		Isopacheous calcite cement (C1) and blocky calcite cement (C2).	M1	18-30%	High microporosity, moldic porosity; rarer intergranular porosity	-0,5 to +0,5	-3 to 0	Gas zone	Fig.4 A, B, C
G-DF3	**Microporous and vuggy carbonate breccia**		Brecciation features (type II); neomorphosed corals into CX calcite; blocky calcite cement (C2); micritized bioclasts; leached bioclasts (corals, red algae and foraminifers) and matrix	M1	25-40%	High microporosity, inter-breccia clast porosity; moldic and vuggy porosity; rarer intergranular porosity	-3,5 to 0	-5 to -2	Gas zone	Fig. 4 E,F
G-DF4	**Coral floatstones with low matrix microporosity**		Brecciation features (type I); leached corals and micrite infills within molds (faint-ghost texture); leached bioclasts (corals, red algae and foraminifers)	M2	10-20%	Low microporosity; moldic to vuggy porosity	-1 to 0	-2 to 0	Gas zone	Fig.6 A, B, C; Fig. 7 C
W-DF1	**Floatstones and rudstones with low intragranular and matrix microporosity**		Micritized bioclasts; isopacheous calcite cement (C1) blocky calcite cement (C2); leached bioclasts (red algae and foraminifers) and matrix	M3	10-25%	Low microporosity; moldic to vuggy porosity	-1 to 0	-4 to -1,5	Water zone	Fig. 7 D
W-DF2	Carbonate breccia with low microporosity		Brecciation features (type II); neomorphosed corals into CX calcite; blocky calcite cement (C2); micritized bioclasts; leached bioclasts (corals, red algae and foraminifers) and matrix	M3	10-30%	Low microporosity; inter-breccia clast porosity; moldic to vuggy porosity	-2 to -0,5	-5 to -3	Water zone	

Table 7: Definition and properties of the diagenetic facies from the Upper Burman Limestone

4.4.5 Physical factors controlling elastic properties at log scale

The impact of selected parameters (fluid content, mineralogical composition, porosity and pore shape) on the P-wave velocities measured from well logs in the Upper Burman Limestone, has been assessed.

Fluid effect:

The Fig 4-8A and 4-8B display graphs of P-wave velocity derived from sonic logs versus porosity (PHI_log). At a given porosity, P-wave velocity values (Vp) are significantly higher for water-saturated rocks (below the gas-water contact) compared to gas-saturated rocks. The shift in velocity averages 500 m/s for porosity values higher than 25%. Water-saturated P-wave velocity values have been calculated from velocities in the gas zone by using Biot-Gassman substitution theory (Gassmann, 1951). For porosity values below 30%, the range of P-wave velocities predicted after Biot-Gassman water substitution from the gas zone remarkably matches with that of the water zone (Fig. 4-8B). For porosity higher than 30%, the predicted water-saturated Vp value on the gas-bearing interval remains significantly lower than those from the water zone, at a given porosity (Fig. 4-8B).

Mineralogic effect:

Gamma ray from well logs (Fig. 4-7), petrographic observations of thin sections as well as laboratory mineralogical analyses of rock samples (trace element, XRD and fluorescence: Table 3) revealed a dominantly calcitic mineralogy with the occurrence of scattered, partially dolomitized intervals (see distribution in thin section: Fig. 4-3H). In such intervals dolomite content typically ranges from 5 to 15% with rare occurrences at concentrations up to 30%. In addition, XRD and fluorescence analyses (Table 3) indicate that silica concentrations are very low (<0.47%) suggesting a very low terrigenous content. Additionally, the very low values of gamma ray (GR), typically ranging from 10 to 20 API with rare peaks at 40 API, suggest very low clay content (Fig. 4-7). To quantify the impact of mineralogy on the acoustic properties of the Yadana reservoir, DEM models of spheroidal inclusions have been computed for various mineralogical compositions of the host. By keeping a constant pore aspect ratio (0.13: reference pore aspect ratio, after Xu and Payne, 2009 and constant gas saturation (Sw=0%), the substitution of 25% of dolomite in the host material (Fig. 4-8C) leads to a minor increase in Vp value (typically less than 3% at porosity>20%). This results in a very low terrigenous content. Additionally, the very low

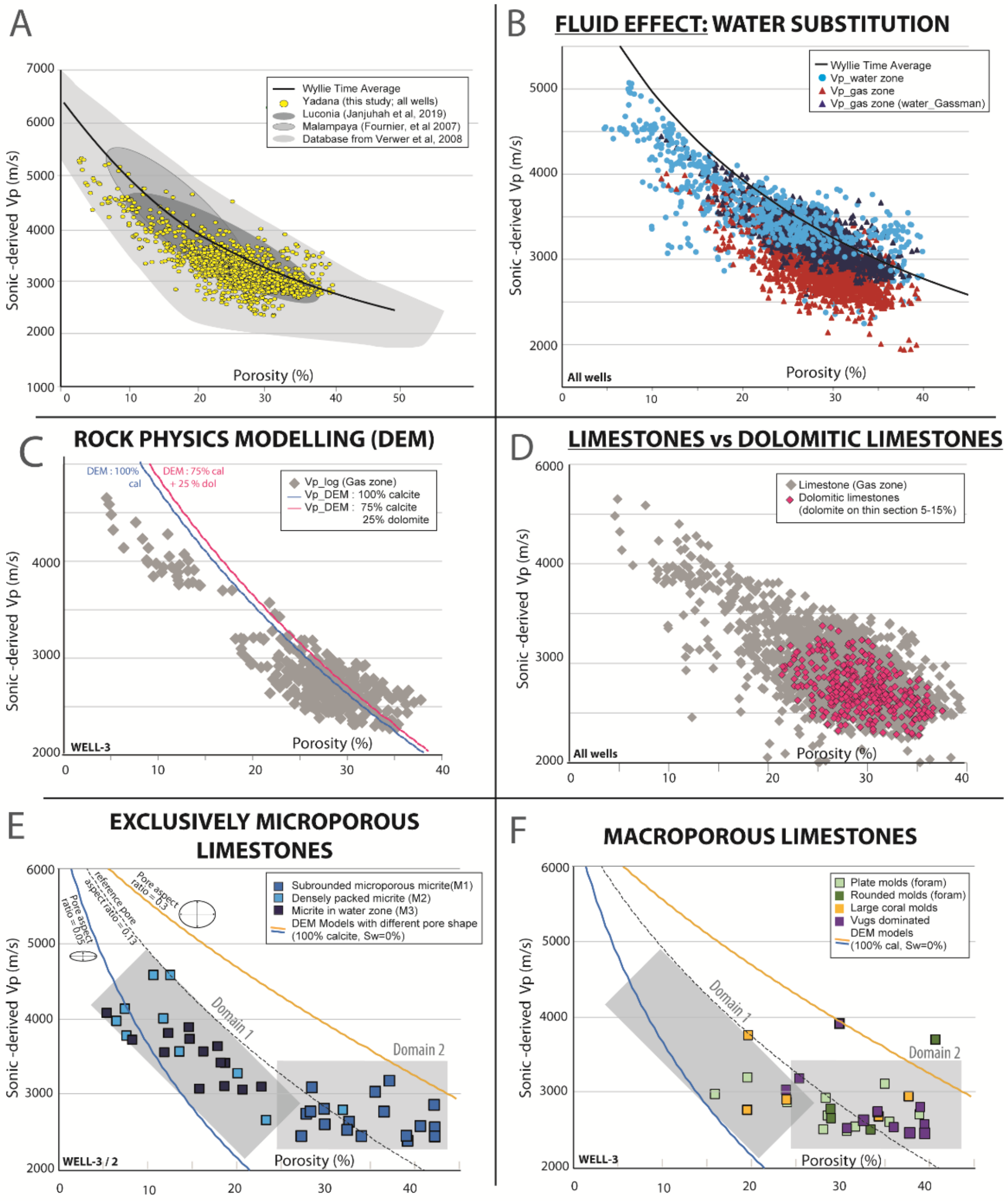
A
7000
6000
5000
4000
3000
2000
1000
Sonic -derived Vp (m/s)
Porosity (%)
0
10
20
30
40
50
Wyllie Time Average
Yadana (this study; all wells)
Luconia (Janjuhah et al, 2019)
Malampaya (Fournier, et al 2007)
Database from Verwer et al, 2008
B
FLUID EFFECT: WATER SUBSTITUTION
5000
4000
3000
2000
Sonic -derived Vp (m/s)
All wells
Porosity (%)
0
10
20
30
40
Wyllie Time Average
Vp_water zone
Vp_gas zone
Vp_gas zone (water_Gassman)
C
ROCK PHYSICS MODELLING (DEM)
DEM : 100% cal
DEM : 75% cal + 25 % dol
Vp_log (Gas zone)
Vp_DEM : 100% calcite
Vp_DEM : 75% calcite 25% dolomite
4000
3000
2000
Sonic -derived Vp (m/s)
WELL-3
Porosity (%)
0
10
20
30
40
D
LIMESTONES vs DOLOMITIC LIMESTONES
6000
4000
3000
2000
Sonic -derived Vp (m/s)
Limestone (Gas zone)
Dolomitic limestones (dolomite on thin section 5-15%)
All wells
Porosity (%)
0
10
20
30
40
E
EXCLUSIVELY MICROPOROUS LIMESTONES
6000
5000
4000
3000
2000
Sonic -derived Vp (m/s)
Pore aspect ratio = 0.05
reference pore aspect ratio = 0.13
Pore aspect ratio = 0.3
Subrounded microporous micrite(M1)
Densely packed micrite (M2)
Micrite in water zone (M3)
DEM Models with different pore shape (100% calcite, Sw=0%)
Domain 1
Domain 2
WELL-3 / 2
Porosity (%)
0
10
20
30
40
F
MACROPOROUS LIMESTONES
6000
5000
4000
3000
2000
Sonic -derived Vp (m/s)
Plate molds (foram)
Rounded molds (foram)
Large coral molds
Vugs dominated
DEM models (100% cal, Sw=0%)
Domain 1
Domain 2
WELL-3
Porosity (%)
0
10
20
30
40

Figure 4-8 : Figure 4-8: Well-log Vp-porosity crossplots of the Upper Burman Limestone Formation. (A) Comparison with other carbonates case studies (Fournier and Borgomano, 2007; Verwer et al. 2008; Janjuhah, 2019); (B) Fluid effect on Vp-porosity relationship: comparison between log measurements (from all of the studied wells) in the water zone (light blue dots), in the gas zone (red triangles) and the corresponding water-substituted values (dark blue triangles) calculated by using Gassmann relationship; (C) Mineralogy effect on Vp: calculation of Vp-porosity relationships by using DEM models on spheroidal inclusions (aspect ratio=0.13) set in a carbonate mineral phase with various calcite and dolomite proportion, and values measured from logs in the gas zone from WELL-3; (D) Well log-derived Vp-porosity crossplot for limestones and dolomitized limestones from the gas zone (all wells); (E) Well log-derived Vp-porosity crossplot for intervals (WELL-2 and -3) displaying microporosity only; samples are labeled as a function of micrite microfabrics and DEM curves are displayed for various aspect ratios (calcitic host); (F) Well, log-derived Vp-porosity crossplot for macroporous intervals (WELL-3); samples are labeled as a function of dominant pore types observed on thin sections.

values of gamma ray (GR), typically ranging from 10 to 20 API with rare peaks at 40 API, suggest very low clay content (Fig. 4-7). To quantify the impact of mineralogy on the acoustic properties of the Yadana reservoir, DEM models of spheroidal inclusions have been computed for various mineralogical compositions of the host. By keeping a constant pore aspect ratio (0.13: reference pore aspect ratio, after Xu and Payne, 2009 and constant gas saturation (Sw=0%), the substitution of 25% of dolomite in the host material (Fig. 4-8C) leads to a minor increase in Vp value (typically less than 3% at porosity>20%). This result is consistent with the Vp-porosity plot from Fig. 4-8D where the range of P-wave velocity values from dolomitized intervals largely overlaps that of purely calcitic limestones.

Pore type effect:

P-wave velocity versus porosity plots (Fig 4-8D) exhibit a wide range of values, at a given value of porosity and for a given mineralogy and fluid. Such a scattering in velocity values is commonly interpreted as representing the pore type effect on acoustic properties (Eberli et al., 2003). To quantify such a pore type effect, DEM models of spheroidal inclusions within a calcitic host have been computed (Fournier et al., 2018) and compared with well log-derived porosity and P-wave velocity (Fig. 4-8E and 4-8F). Results for intervals with exclusive microporosity (and lacking macroporosity) revealed two domains of porosity and equivalent aspect ratio values which correspond to two distinct micrite microfabrics (Fig. 4-8E):

- *Domain 1 (porosity: 5-20%; equivalent aspect ratio<0.13):* This domain represents less than 20% of samples and matches with the soft-pore domain (Xu and Payne, 2009). The corresponding samples are limestones whose matrix and micritized grains are made of a densely packed micrite (M2 and M3. microfabric) (Fig. 4-4C).
- *Domain 2 (porosity: 20-43%; equivalent aspect ratio>0.13):* This domain represents more than 80% of the samples and corresponds to the highly micro-mesoporous limestones whose micritized grains and matrix are dominated by M1 microfabrics (Fig. 4-8E).

The range of velocity and porosity values for samples with macroporosity (Fig. 4-8F) largely overlaps that of pure microporous samples. Since the proportion of microporosity is always dominant (in average 75% of the whole pore volume), it is likely that the acoustic properties of macroporous limestones are largely controlled by those of the microporous host and therefore by micrite mirofabrics.

4.4.6 Geological control on acoustic properties and petroacoustic layering

As evidenced in the previous section, vertical variations of acoustic impedance within the gas reservoir are mainly related to changes in porosity, in pore network structure, and in a minor proportion to changes in dolomite content (Fig. 4-9). The depositional architecture of Yadana has been built based on vertical lithofacies changes in cores and well correlations (Fig. 4-9B). Well correlations are based on the 4 key markers identified from cores: 1) the transition from N5 to N6 biostratigraphic zones in the upper part of the cored interval; 2) a 10 meter-thick foraminiferal floatstone unit (LF2.2 lithofacies) identified on the four cored wells, with flat *Spiroclypeus* and *Cycloclypeus*, interpreted as representing a maximum deepening interval, 3) a subaerial exposure surface (Teillet et al., 2019) and 4) the transition from N4a to N4 biostratigraphic zones identified in the lower part of the cored interval. The Fig. 9A indicates that a significant overlap exists between the ranges of porosity, velocity and acoustic impedance for the distinct lithofacies. This implies that spatial variations of petroacoustic properties cannot be related to the depositional architecture only. A petroacoustic layering of the Yadana reservoir has been also performed (Fig. 4-9A) based on the identification of diagenetic facies (Fig. 4-7) and associated acoustic properties. Contrasted ranges of porosity, P-wave velocity and acoustic impedance are evidenced for the distinct diagenetic facies and three main groups (Group 1 to 3) of diagenetic facies were identified according to their petroacoustic signature (porosity, and acoustic impedance):

Petroacoustic group 1: Highly microporous and vuggy floatstones from the gas zone (G-DF1):

Highly microporous and vuggy floatstones (G-DF1) is the most common diagenetic facies from the gas-bearing interval (80%). They include purely calcitic limestones with M1 micrite microfabrics (G-DF1a and G-DF1b), and partly dolomitized limestones (G-DF1c). These diagenetic facies display a very similar and narrow range of porosity (mode: 30%) and low acoustic impedance (5600-6000 kg.m^2.s-1).

Petroacoustic group 2: Microporous cemented grainstone/rudstone and breccia from the gas zone (G-DF2 and G-DF3):

The diagenetic facies G-DF2 and G-DF3 are characterized by slightly lower porosity values compared to G-DF1 (mode: around 26%) and higher acoustic impedance (typically ranging from 6000 to 7000 kg.m^2.s-1). In such highly microporous diagenetic facies, lower porosity and higher acoustic impedance values are related to increased calcite cementation of intergranular pores (C2 blocky calcite) in grainstone-rudstone (G-DF2) and significant number of calcitized corals (CX) in breccia (G-DF3).

Petroacoustic group 3: Low microporosity coral floatstones from the gas zone (G-DF4), floatstone-rudstone and breccia from the water zone (W-DF1, and W-DF2):

The diagenetic facies G-DF4 within the gas-bearing zone as well as W-DF1 and W-DF2 within the water zone are characterized by: 1) a wide range of porosity values, ranging from 5% to 35%, but usually lower than 20% and 2) a wide range of acoustic impedance values, typically higher than 7000 kg.m^2.s-1 and up to 10000 kg.m^2.s-1. In the gas-bearing zone, the relatively low value of modal porosity (21%) of G-DF4 compared to other diagenetic facies appears largely related to the relatively low interparticle microporosity within densely packed matrix micrite (M2 microfabrics) in coral-rich intervals. In the water zone, low porosity and high acoustic impedance values in W-DF1 and W-DF2 diagenetic facies are related to significant development of micro-calcite overgrowths within intragranular and matrix micrite (M3 micrite microfabric).

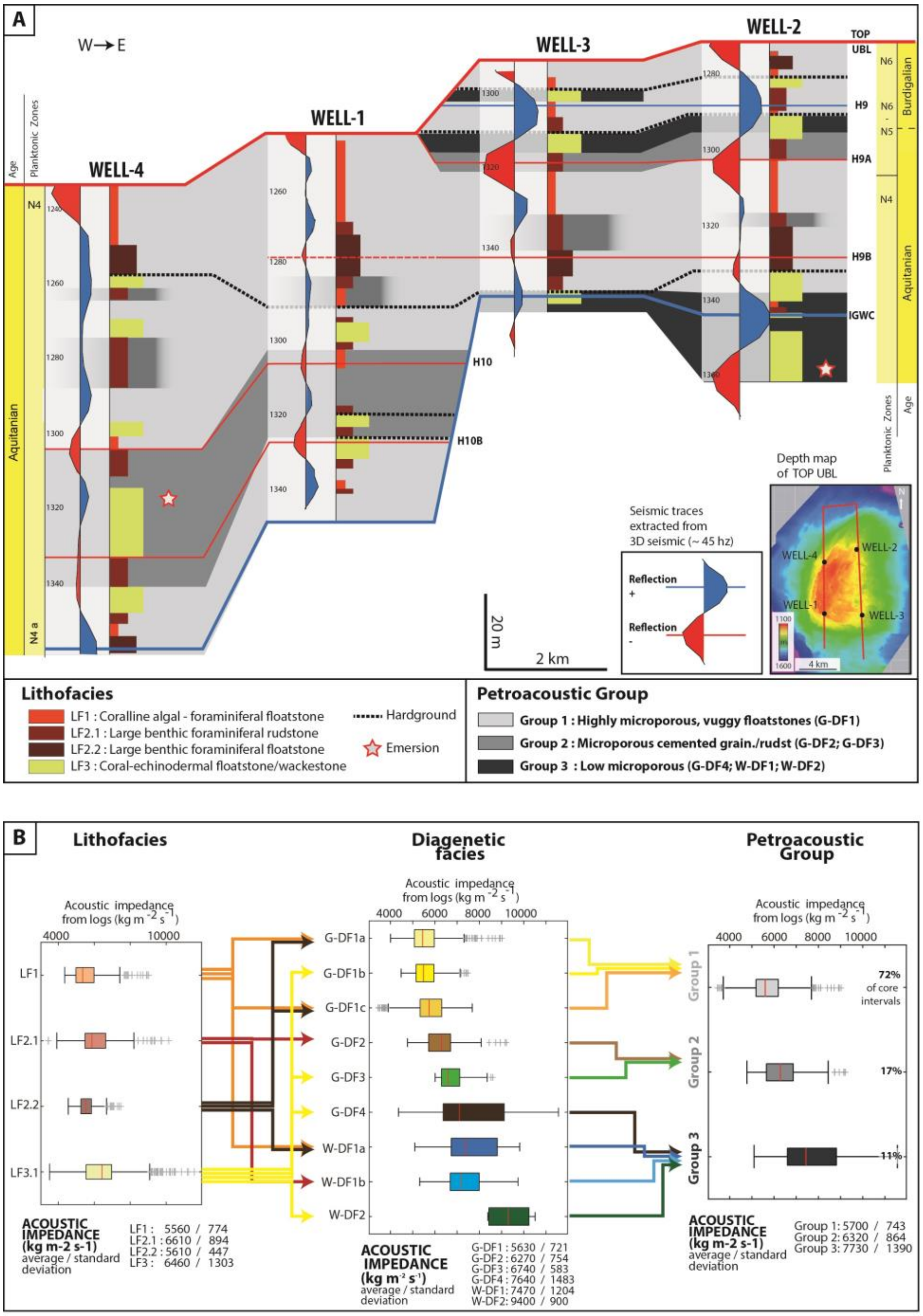

Figure 4-9 : (A): Petroacoustic architecture of the Yadana reservoir (Upper Burman Limestone) showing the weak correspondence between lithofacies and petroacousticzonations; seismic traces at wells are reported. (B) Diagram showing the genetic correspondence between lithofacies, diagenetic facies and petroacoustic groups andtheir respective ranges of acoustic impedance values.

4.4.7 Well-to-seismic tie

Synthetic seismograms have been computed from the well logs (Fig. 4-10) in order to identify the geological origin of seismic reflectors. A good fit is obtained between reflections of the synthetic seismogram calculated for the four cored wells and the actual seismic traces extracted at well location.

Within the gas-bearing interval, reflections are commonly low in amplitude, particularly in WELL-1 and WELL-4 (Fig. 4-10), where seismic and synthetic traces are relatively smooth. The highest amplitude reflections located in WELL-2 and WELL-3 and below the GWC (H9A, H9B, H10 and H10B) occurs at the vicinity of high reflection coefficients (in absolute value) that are mostly related to boundaries between petroacoustic units. In the pre-production 3D seismic data, a major seismic reflection occurs at the gas-water contact (IGWC= initial, pre-production gas-water contact) imaged on seismic profiles as a high amplitude, continuous, nearly horizontal but uneven reflector (Fig. 4-11).

4.4.8 Analysis of 4D seismic data

The pre-production 3D seismic survey (Base 1993, Fig. 4-12A) has been compared to a 3D monitor seismic (Fig. 4-12B). Three major results regarding changes in seismic expression during production have been revealed: 1) the flat spot evidenced from the pre-production seismic around the IGWC is still present on the monitor seismic, at the same location, after 14 years of production (Fig. 4-12A, 4-12B); 2) subsidence of the reservoir top during production ranges from 2 to 8 meters (Fig. 12A, 4-12B); 3) differential water rise occurred between eastern (~50 m) and western (~10 m) platform as revealed by the spatial distribution of 4D velocity anomalies (Fig. 4-12E and 4-12F). The top of the main anomaly is interpreted as the syn-production gas water contact (PGWC, Fig. 4-12F).

4.4.9 Geological significance of seismic reflections within the gas-bearing reservoir (pre-production 3D seismic)

In the gas-bearing reservoir, five main reflection horizons (from top to base: H9, H9A, H9B, H10, H10A), interpretable throughout the Yadana buildup, have been identified and evaluated for their geological significance. The contribution of individual contrasts in acoustic impedance to the composite seismic amplitude has been quantified by comparing the synthetic seismograms computed from a selection of reflection coefficients with the full

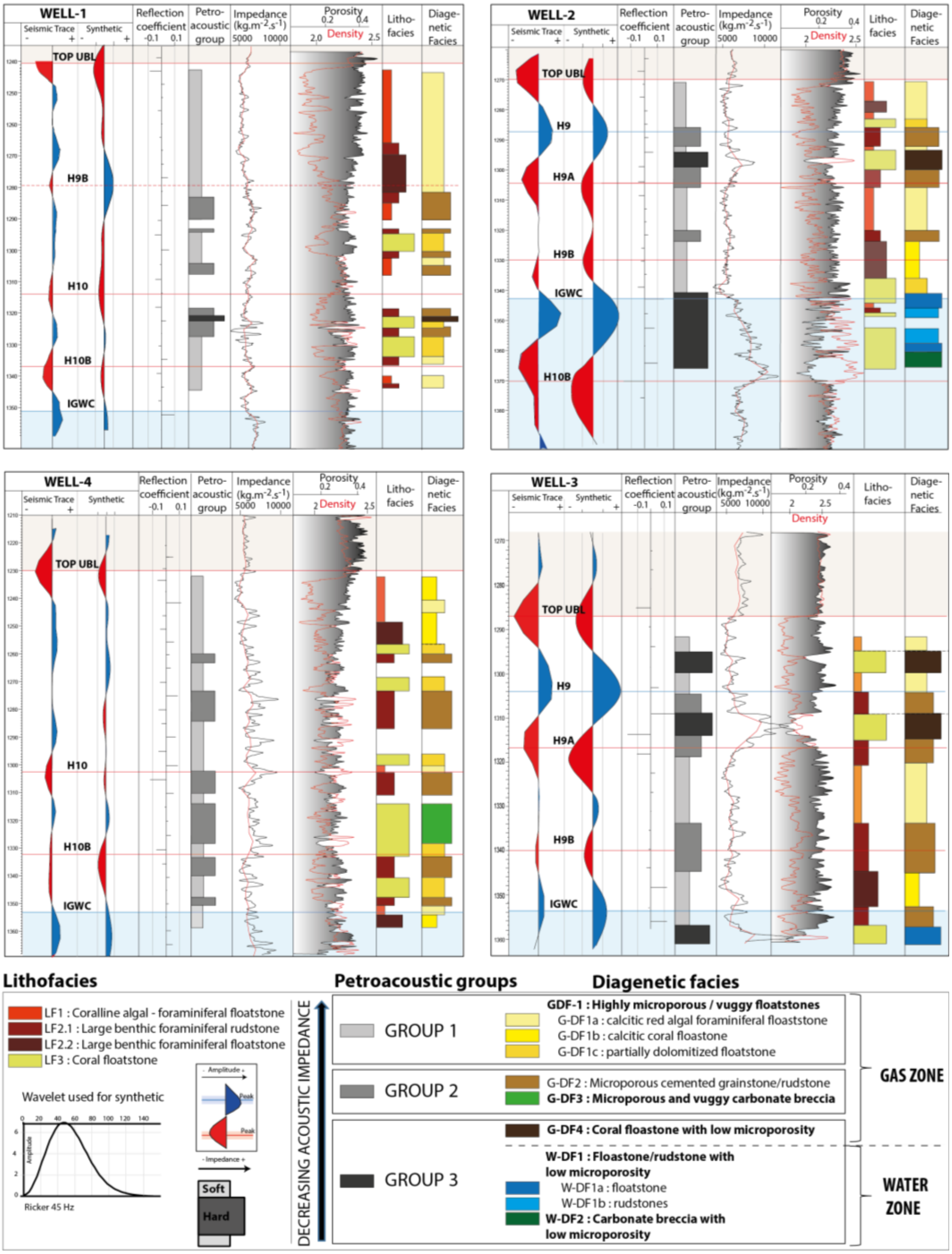

Figure 4-10: Well-to-seismic tie for WELL-1, -2, -3 and -4. Seismic trace is extracted from the pre-production (1993) 3D seismic at the well location. Synthetic seismograms have been computed by a 45 Hz Ricker wavelet.

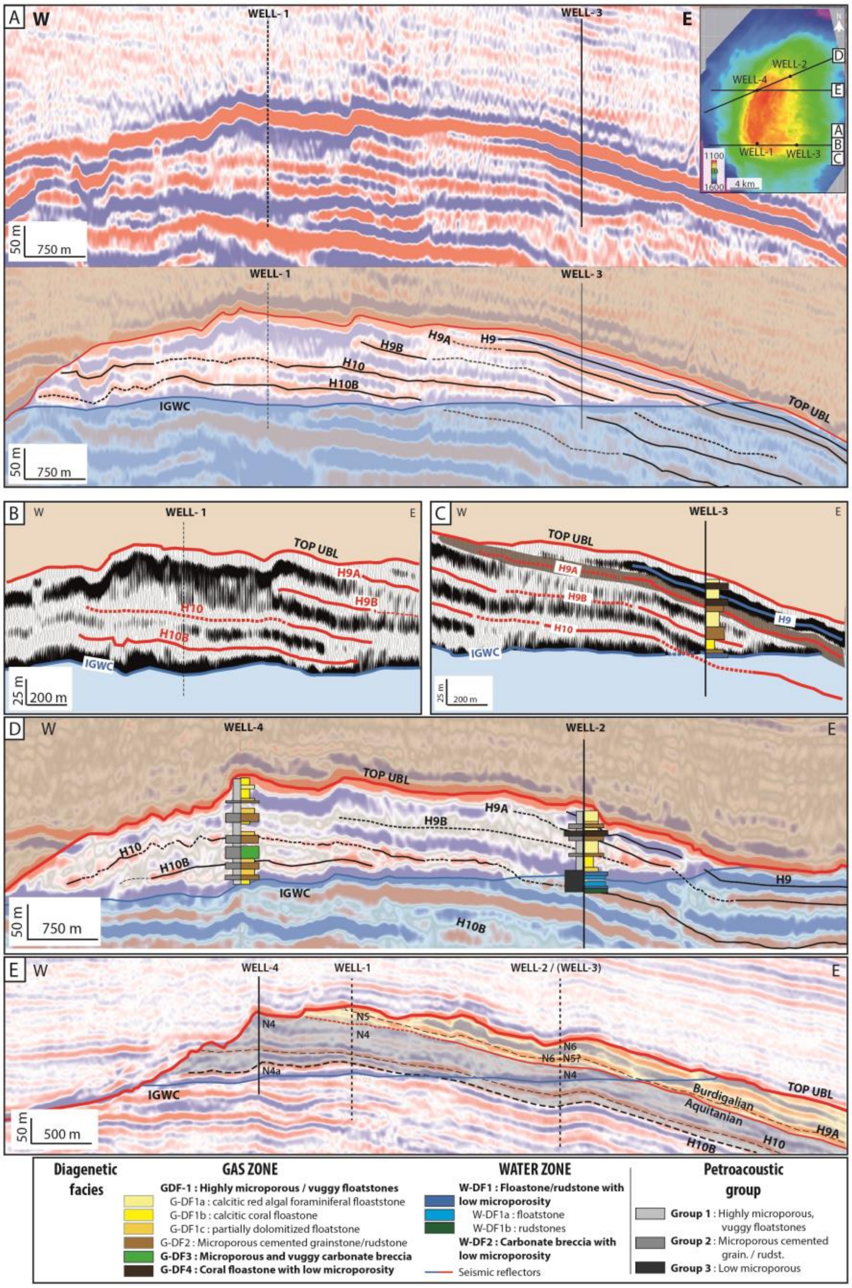

Figure 4-11: Seismic profiles across the Yadana platform (pre-production 3D seismic). (A) W-E oriented profile, crossing wells WELL-3 and WELL-4, illustrating the main reflection horizons within the Upper Burman Limestone (H9, H9A, H9B, H10, H10B and IGWC). (B) and (C) close-up around well location of the profile displayed in(A). (D) W-E oriented profile, crossing wells WELL-4 and WELL-2, with cored sections and diagenetic zonations. (E) Comparison between biostratigraphic zonation ofthe Yadana buildup (from Teillet et al., in press1) and seismic reflections.

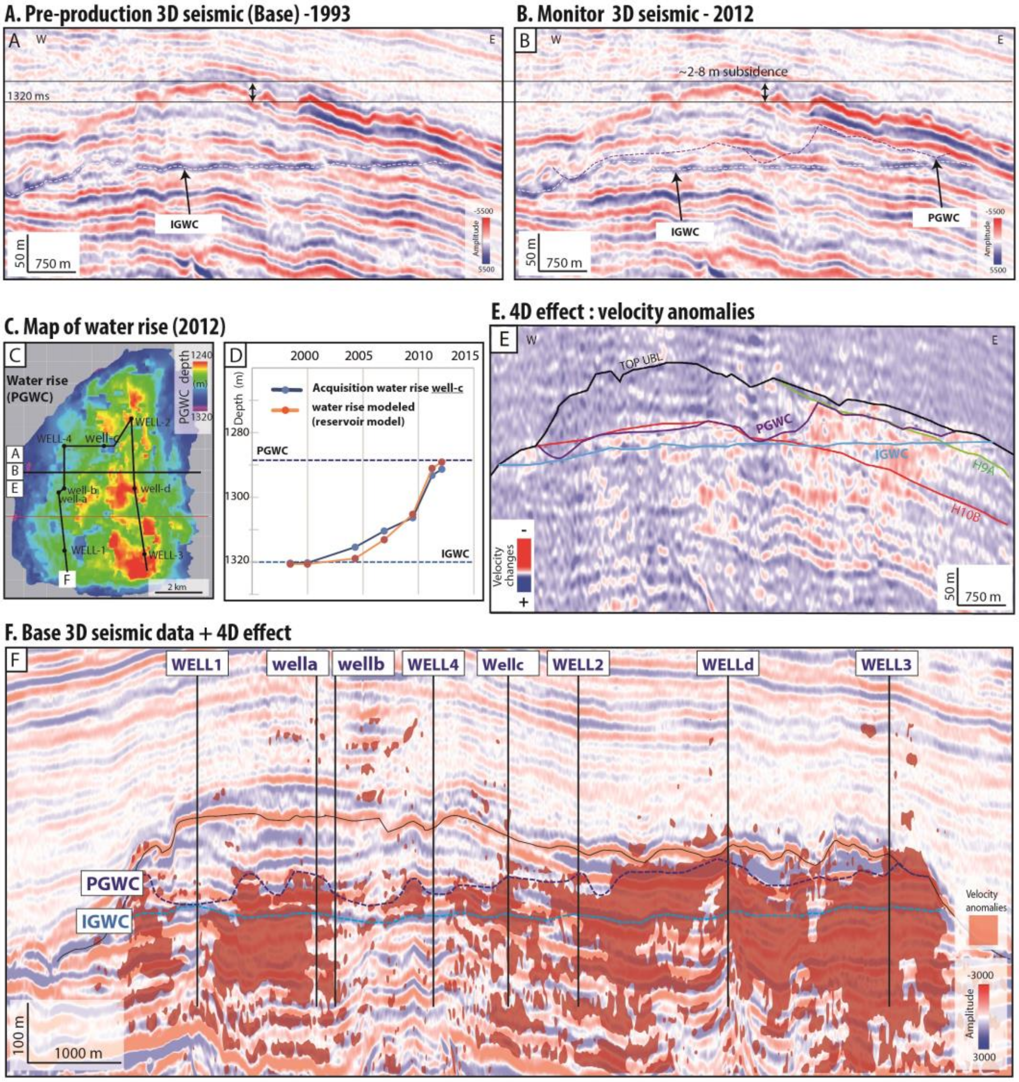

Figure 4-12: Time-lapse seismic analysis. (A) and (B) W-E oriented profile from the pre-production 3D seismic survey (1993) and from the monitor 3D seismic (2012) respectively. (C) Map of the water rises in 2012 (initially at 1320 m before production). (D) Water rises during production at WELL-c. (E) W-E profile (same as (A) and (B)) showing velocity change between Monitor and Base seismic data. (F) Seismic reflectivity profile crossing all the studied wells (localization on Fig. 1B) and velocity anomalies (red).

synthetic seismogram (Fig. 4-13). The match between the full synthetic seismic and the partial synthetic seismic is considered as good when the difference in amplitude is lower than 20% and when the shift in peak location is lower than T/10 T being the period of the wavelet (for a frequency mode around 50 Hz T averages 20 ms in the gas reservoir).

H9 (WELL-2 and WELL-3): positive in amplitude and located just below the TOP UBL, the seismic reflection is mostly controlled by two successive positive reflection coefficients, which represent a trend of increasing upward porosity at the transition between a coral floastone unit with low microporosity (GDF-4 diagenetic unit) and the overlying microporous foraminiferal rudstone (G-DF2) and foraminiferal/coralline algal floatstone (G-DF1) (Fig. 4-13A).

H9A (WELL-2 and WELL-3): The amplitude of reflection is dominantly controlled by reflection coefficients from the base and top of a 10 meters-thick, moderate porosity (<20 %) coral-rich unit (G-DF4 diagenetic facies), interbedded within highly microporous limestones (porosity <30-35%; G-DF1 units) (Fig. 4-13B). As a consequence, H9A is not related to a single acoustic interface, but instead represents the composite contribution of a whole sub-seismic scale (i.e., below vertical seismic resolution) diagenetic units.

H10 (WELL-1 and WELL-4): In the western part of the buildup, H10 reflection amplitude is mainly controlled by negative reflection coefficients (Fig. 4-13C), which represent a trend of decreasing upward porosity at the transition between a highly microporous foraminiferal/coralline algal floatstone (G-DF1) and the overlying, moderate porosity (<25 %) interval, dominated by cemented foraminiferal rudstones (G-DF2 diagenetic unit). Reflector H10 laterally pinches out to the east by interfering with the flat-spot reflection at the initial gas-water contact (IGWC) (Fig. 4-11A).

H10B (WELL-1, WELL-2 and WELL-4): In the western part of the platform the H10B amplitude is mainly controlled by a negative reflection coefficient at the base of a moderate microporous carbonate breccia with calcitized corals (GDF3 diagenetic unit) (Fig. 4-13D). Eastward (WELL-2, Fig. 4-10, 4-11D) H10B significantly interferes with the IGWC flat spot.

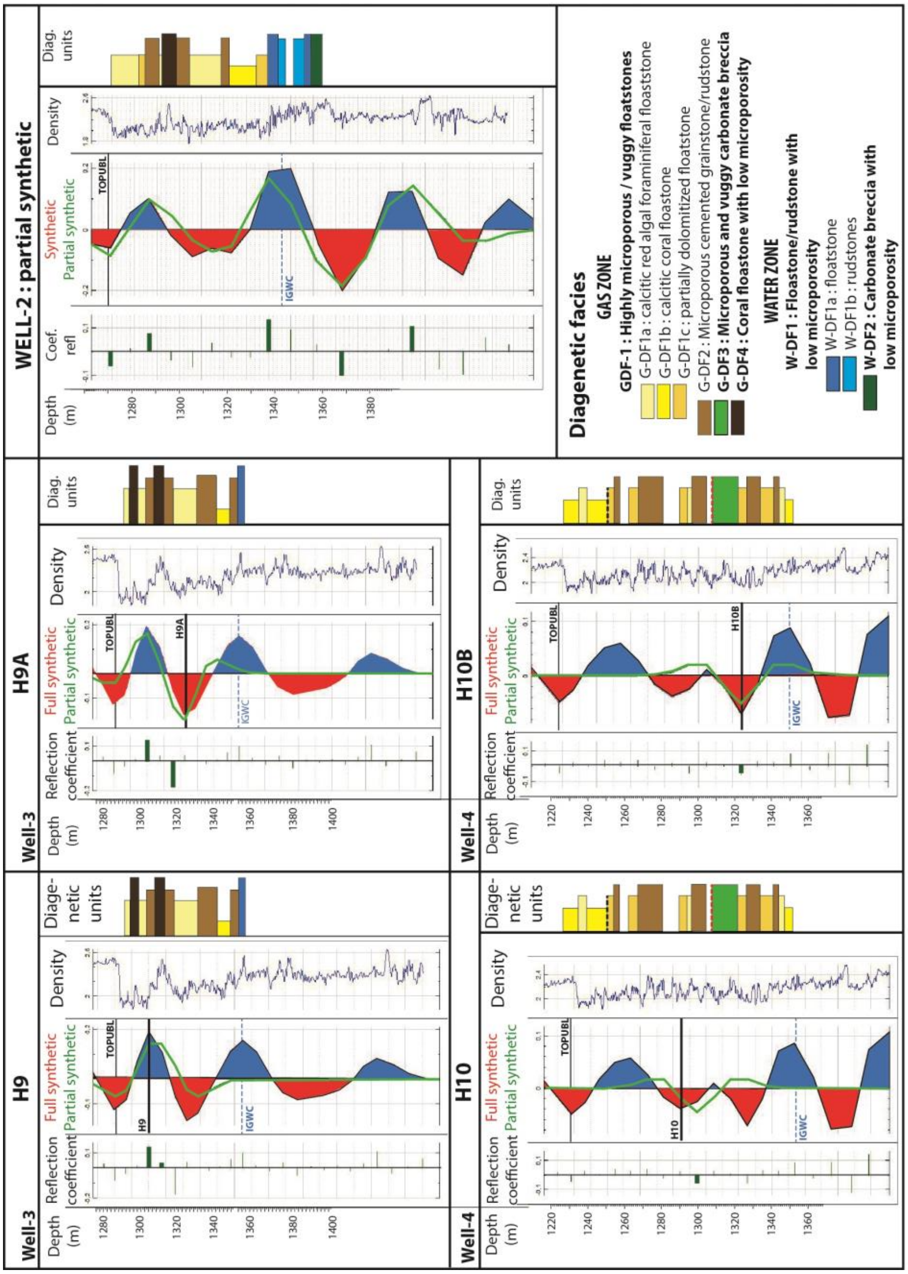

Figure 4-13**:** Comparison between full synthetic seismograms (computed from the full succession of reflection coefficients) and partial synthetic seismograms (from aselection of reflection coefficients) in order to assess the impact of each acoustic interface on the seismic trace.

4.5 Discussion

4.5.1 Depositional vs. diagenetic control on seismic reflection in carbonate gas reservoirs

Based on well-to-seismic tie and partial synthetic seismogram computation, the geological origin of the main seismic reflection from the gas reservoir (from pre-production 3D seismic data) has been determined. Seismic reflections have been shown to result from : 1) a vertical, transitional change in acoustic impedance, over 1-10 meter-thick intervals, at the boundary between two diagenetic units (H9, H10, H10B), or 2) the interference from two opposite-polarity reflections at top and base of a sub-seismic scale diagenetic unit (H9A).

Reflection horizon H9 has been shown to result from an upward decrease in acoustic impedance at the transition between a G-DF4 diagenetic unit and overlying G-DF2/G-DF1 intervals which are mostly related to a downward decrease in porosity (Fig. 4-10 and 4-14). The significant shift in porosity (averaging 10%) between G-DF1/GDF2 and G-DF4 intervals results from both 1) early micrite cementation in marine environment (G-DF4) and 2) differential porosity enhancement or preservation as well as moldic and vuggy porosity development (G-DF1/GDF2) during late burial diagenesis (Teillet et al. 2019a). Coral floatstone intervals with low microporosity (GDF-4) have been interpreted to form during periods of high nutrient supplies associated with episodic high-energy events such storms or internal waves (Teillet et al., 2019b) and represent therefore time-correlatable units. The chronostratigraphic value of such a dense horizon is also supported by biostratigraphic constrains since the boundary between N4 and N5/N6 planktonic zones occurs in both WELL-2 and WELL-3 at the base of the G-DF4 unit (Fig. 4-9, 4-11E). As a consequence, in spite of the diagenetic control on porosity and acoustic properties, the main acoustic contrasts and associated seismic reflectors are conforming to depositional's timeline. Such an apparent paradox results from the importance of initial petrophysical properties (porosity and permeability), related to depositional textures and early diagenesis, on the subsequent evolution of pore network and acoustic properties (Fournier and Borgomano, 2007). Similarly, the composite reflection H9A is also controlled by porosity contrasts at the boundary of a low-microporosity G-DF4 units which developed during the early marine diagenesis and have been enhanced during burial diagenesis by late dissolution processes (Teillet et al., 2019a).

For both H9 and H9B horizons, the acoustic contrasts originating reflection occur at the boundary of coral-rich intervals and are therefore conform to lithofacies changes.

However, such contrasts in acoustic impedance are created by differential early and later diagenetic evolution between coral-rich deposits and encasing foralgal facies. Early cementation of micrite mud matrix is restricted to some coral-rich floatstone intervals (G DF4) and the resulting reduction in porosity and permeability likely reduced or impeded the development of further secondary porosity (microporosity and moldic/vuggy porosity) which is widespread in foralgal facies (G-DF1a, G-DF2). In contrast, when the coral-rich intervals have not undergone early cementation (G-DF1b), their subsequent diagenetic evolution is similar to that of the encasing foralgal facies, and no significant contrast likely to generate a reflection forms at their boundaries. This clearly demonstrates that changes in lithofacies alone are not sufficient to generate reflections but they must be accompanied by differential diagenetic evolution

The H10 reflection horizon is controlled by an upward decrease in porosity at the transition between highly microporous floatstones (G-DF1) and overlying microporous, cemented foraminiferal rudstones (G-DF2). In that case the shift in porosity is likely mostly related to differential volume of micropores between foraminiferal/coralline algal floatstones where both grains and matrix are microporous and cemented foraminiferal rudstones where intergranular space is occluded by sparry calcite C2 and microporosity is exclusively intragranular. As a consequence, the acoustic impedance contrast occurs at the boundary between two intervals which are characterized by distinct depositional textures even though pore network and acoustic properties have been significantly transformed during shallow and deeper burial (Teillet et al., 2019a).

H10B reflection forms at an acoustic impedance contrast at the base of a brecciated interval (G-DF3) which has been interpreted to develop during an intra-formational stage of subaerial exposure as suggested by its carbon and oxygen stable isotope signature (Teillet et al., 2019a). Since the thickness of such a meteorically altered interval is low (<10 m) compared to seismic resolution (~20 m), H10B reflection horizon can be regarded as being conformed to the intra-formational exposure surface and therefore to be a valuable seismic stratigraphic marker.

As a consequence, the analysis of the main seismic horizons from the Yadana gas reservoir clearly show that the acoustic contrasts generating the reflections result from differential patterns of diagenetic evolution at the interface between intervals characterized by distinct lithofacies.

4.5.2 Origin of time-transgressive seismic reflections in carbonate gas reservoirs

The pre-production (1993) 3D seismic displays a relatively flat but uneven seismic horizon occurring at the gas-water contact (IGWC=Initial Gas-Water Contact), and cross-cutting the main seismic reflections identified in the gas reservoir (Fig. 4-11 and 4-12). Surprisingly, the IGWC reflector remained unchanged in syn-production (2012) 3D seismic (Fig. 4-13, 4-14) while the upward displacement of the gas-water contact may have reached 50 ms (TWT). In addition no seismic reflection occurs at the syn-production (2012) gas-water contact position (Fig 4-13B). Two possible origins can be therefore inferred from the persistence of a flat spot at the pre-production gas-water contact: 1) the fluid effect related to residual gas in the reservoir after production is sufficient to generate a significant and laterally continuous shift in acoustic impedance around the IGWC; 2) the flat spot is controlled by a shift in the acoustic impedance around the IGWC, which is related to differential porosity evolution between the gas and the water zone.

The comparison between the seismograms calculated from water substitutes and actual density and sonic logs (Fig. 4-14A and B) shows that the position and the amplitude of the IGWC reflector are weakly affected by fluid saturation and therefore predicts the persistence of a time-transgressive reflector after gas production. As a consequence, the IGWC reflection horizon is essentially related to the vertical and lateral variations of the intrinsic properties of the carbonate reservoir (porosity, mineralogy and velocity). A significant decrease in porosity has been evidenced in all of the studied wells, below the IGWC, within a 20 to 30 meter-thick intervals (Fig. 4-14): the shift in average porosity between the uppermost 10 meters from the pre-production water zone and the lowermost 10 meters from the gas zone may reach 7 % in the western part of the reservoir and gradually decreases eastward, down to 0.2% (Fig. 4-14C). The vertical variation in porosity is related with an increased abundance of moldic/vuggy pores and micropores in the gas zone and with a widespread development of euhedral calcite precipitations (micrite M3) in the water zone (Fig. 4-5). Such a significant and laterally continuous change in porosity and pore network structure below the IGWC has been interpreted to result from a major phase of diagenetic evolution during and/or after the hydrocarbon emplacement (Teillet et al., 2019a) which is mainly related to 1) increased moldic and vuggy porosity development within the gas zone, 2) microporosity preservation or enhancement in loosely packed, subrounded micrites within the gas zone, and 3) microporosity reduction by calcite precipitation within the water zone leading to the development of densely packed, euhedral micrites (M3 micrite). As a consequence, the time-transgressive, IGWC reflection marks a major, reservoir-scale, diagenetic boundary.

Flat-spot reflections marking fluid contacts are extremely rare in carbonate reservoirs likely because of the relative stiffness of carbonate rocks which lowers fluid effect on velocity and because of the high vertical variability of porosity and acoustic impedance: fluid contacts generate reflection coefficients which are much smaller than those induced by porosity changes (e.g Simm and Bacon, 2014). Diagenetic seismic reflection cross-cutting strata reflectors have been documented in various diagenetic settings. Most of the published examples concern bottom-simulating reflectors which are related to diagenetic transformation of Opal-A into Opal-CT in biosiliceous deep-water deposits (e.g. (Davies and Cartwright J, 2002; Hammond and Gaither, 1983; Nouzé et al., 2009). In addition, kilometer-scale geobodies, delineated by stratigraphy-cutting reflectors and characterized by fault-related cementation within porous chalk, have been evidenced from high-resolution 3D seismic in the Upper Cretaceous from the North Sea (Smith et al., 2018). Stratigraphy-cutting reflectors of mixed depositional and diagenetic origin have been also reported at the transition between shelf margin grainstones and slope wackestones from a Permian prograding carbonate platform from Texas (Zeng and Kerans, 2003). The Yadana subsurface database documents an example of diagenetic, stratigraphy-cross-cutting reflector which is related to differential porosity evolution within the gas and the water zone, during and/or after gas emplacements.

4.5.3 Origin of seismic reflection in carbonate hydrocarbon reservoirs: comparison with other Cenozoic SE Asian case studies

The synthesis of published case studies of carbonate gas reservoirs from SE Asia (Table 5) show that the main reflection horizon occur at the boundary between decameter-scale acoustic units where acoustic impedance is mainly controlled by porosity changes.

In the Miocene Elk-Antelope field (offshore Papua New Guinea), some high amplitude reflections coincide with sedimentological facies boundaries, but other reflectors may occur at porosity changes which are purely diagenetic and not facies-dependent (Wilson and Goldberg, 2010). In the same gas field, the boundaries of dolomitized intervals are not characterized by major changes in acoustic impedance and are not related to major seismic reflections, thus suggesting that the mineralogical control is not of prime importance in such carbonate reservoirs.

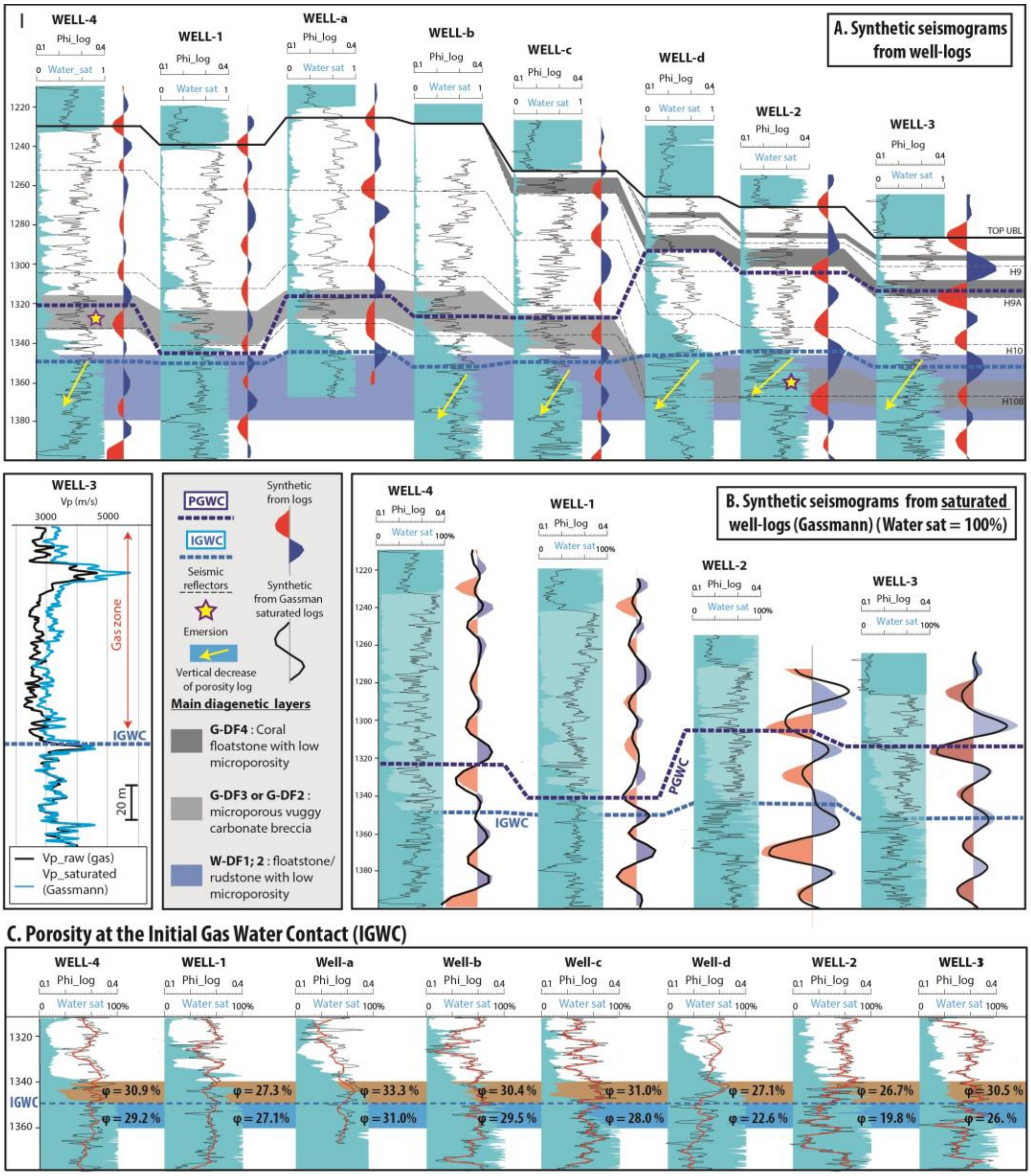

Figure 4-14: Fluid saturation vs. diagenetic control on the IGWC reflector: (A) Well correlation panel with porosity, saturation logs and synthetic seismograms. (B) Comparison between seismograms computed from pre-production well logs and seismograms calculated from water-substituted well logs (through the whole reservoir interval), using the Gassmann relationship; effects of changing effective pressure are not considered. (C) Comparison between average porosity over a 10 meter-thick window, above (brownish interval) and below (blue interval) the initial gas water contact (~1350 mcD), showing a systematic downward decrease in porosity for all of the studied wells.

In Miocene carbonate hydrocarbon reservoirs from Luconia Province, offshore Sarawak (Zampetti et al., 2004) and Liuhua, offshore R.P. China (Zampetti et al., 2005), the main seismic reflectors mark the boundary of 10 to 100 meter-thick acoustic units whose properties are largely controlled by the late dissolution and/or late cementation processes. In spite of the late diagenetic origin of the acoustic boundaries, seismic reflections have been shown to roughly follow the original depositional architecture.

In the Oligo-Miocene Malampaya carbonate gas field, offshore Palawan (Fournier and Borgomano, 2007), seismic reflections are generated at the boundary between 10 to 80 meter-thick diagenetic units. Low impedance units may correspond to highly porous intervals (>20%) dominated by matrix microporosity and/or moldic/vuggy porosity which developed during repeated stages of subaerial exposure as well as during burial. High-impedance units are characterized by pedogenetic and dissolution features developed during repeated stages of subaerial exposure and by pervasive late burial sparry calcite cementation. The seismic horizons located at the top of high-impedance diagenetic units are major intra-formational unconformities associated with significant depositional hiatus and have therefore a chronostratigraphic value. In contrast reflections generated at their base have a questionable chronostratigraphic value since the late burial cementation processes have been shown to be independent of depositional facies.

As a consequence the present findings from the Yadana reservoir are consistent with the previous studies from various Oligo-Miocene carbonate reservoirs from SE Asia, in that diagenetically controlled boundaries can generate reflection events. However, the Yadana case study provided two additional results that complement the understanding of the origin of seismic reflections in carbonates: 1) thin diagenetic units (below vertical resolution) may generate continuous seismic reflections (H9A reflector); 2) stratigraphy-cross-cutting reflection horizons of diagenetic origin may form at the gas-water contact as a result of differential porosity evolution in the gas and water zones during and/or after gas emplacements.

4.5.4 Genesis of seismic reflectivity: implications for seismic interpretation and fluid flow prediction

The few published examples of deeply buried, neritic carbonate reservoirs for which the geological significance of seismic reflectors has been assessed (Fournier and Borgomano, 2007; Wilson and Goldberg, 2010; Zampetti et al., 2005, 2004), indicate that their chronostratigraphic value is variable. The use of 3D seismic data for detailed reconstruction of the stratigraphic architecture of carbonate systems involves calibration between seismic traces and petrographic, sedimentological and diagenetic data from well cores. The present study has shown that even though the main seismic reflection are fundamentally related to diagenetic boundaries, they may nevertheless be conformed to depositional surfaces, mainly in the following cases: 1) acoustic contrasts are related to changes in carbonate production and/or early diagenetic processes in response to oceanographic or climatic changes (Eberli, 2002; this study) or 2) the acoustic properties of the diagenetic units are inherited from meteoric processes associated with an intra-formational subaerial exposure surface (Fournier and Borgomano, 2007). The diagenetic-acoustic units can be thin, sub-seismic in thickness, as evidenced by reflection H9A which results from reflection at boundaries of a 10 m-thick (~ λ/10), early-lithified coral floatstone interval.

In contrast, the chronostratigraphic significance of reflections generated at a depositional texture interface or within the same lithologic unit by vertical variation of cementation or late dissolution is more doubtful. Finally, in the Yadana case study some reflection appear to be indisputably diachronous, like the IGWC reflection horizon which marks a late diagenesis boundary, associated with hydrocarbon emplacements. Determining the geological significance of reflection horizons is therefore required prior to any seismo-stratigraphic analysis of carbonate reservoirs.

Such a recommendation also concerns seismic stratigraphic approaches based on seismic facies analysis. Various studies have used a correspondence between seismic facies and depositional facies and environments (e.g., Paumard et al., 2017). Such an approach can only be valid if the geological significance of seismic facies has been previously calibrated to well cores. For example, seismic facies which are characterized by continuous, parallel and sub-horizontal reflection horizons are extremely common in isolated carbonate buildups, and these have been reported from back-reef settings of rimmed platforms (Baechle and Eberli, 2014), seagrass dominated euphotic open platform (Fournier and Borgomano, 2007) or oligo-mesophotic shelves with foralgal carbonate production (Teillet et al., 2019b). The occurrence, continuity and amplitude of seismic reflection horizons from isolated carbonate systems are largely determined by their zonation into seismic (>λ/4) to sub-seismic scale (down to at least λ/10) diagenetic units. Such a diagenetic zonation can affect carbonate sediments deposited in various environments, especially if late diagenetic processes predominate (Zampetti et al., 2005, 2004). The use of seismic facies approaches without calibrations to cores, in deeply buried carbonate reservoirs which have been subject to polyphase diagenetic evolution, is therefore not recommended.

The detection and mapping of significant horizontal heterogeneities which can impact fluid flow during hydrocarbon production are another major implication of the analysis of seismic reflection genesis (Fig. 4-15). In Miocene carbonate gas fields from Central Luconia (Offshore Sarawak), extended and laterally continuous, meter to decameter-scale lithologic (argillaceous flooding events) and diagenetic (tightly cemented and karstified intervals below exposure surfaces) units have been shown to represent major heterogeneities of a strong impact on pressure behavior and GWC rise during production (Warrlich et al., 2019). In the Yadana field, the monitor 3D seismic evidences an uneven rise of the GWC during production, ranging from 10 m in the western part of the accumulation to 50 m to the east. In the western area, the GWC was initially located below a moderate porosity, brecciated G-DF3 unit, whose base is marked by the H10B reflector and which is related to meteoric diagenetic processes during an intra-formational stage of subaerial exposure. Such a diagenetic unit acted as a baffle during gas production and favored a preferential GWC rise in the western area of the reservoir, where the IGWC was located above the G-DF3 unit (and above H10B: Fig. 4-15B, C). Around WELL-3, the PGWC is locally parallel with and below the H9A horizon related with a thin (<10 m), early lithified coral-floatstone (G-DF4 diagenetic unit) which suggesting that such a low to moderate porosity units behaved as a baffle during production. As a consequence, the

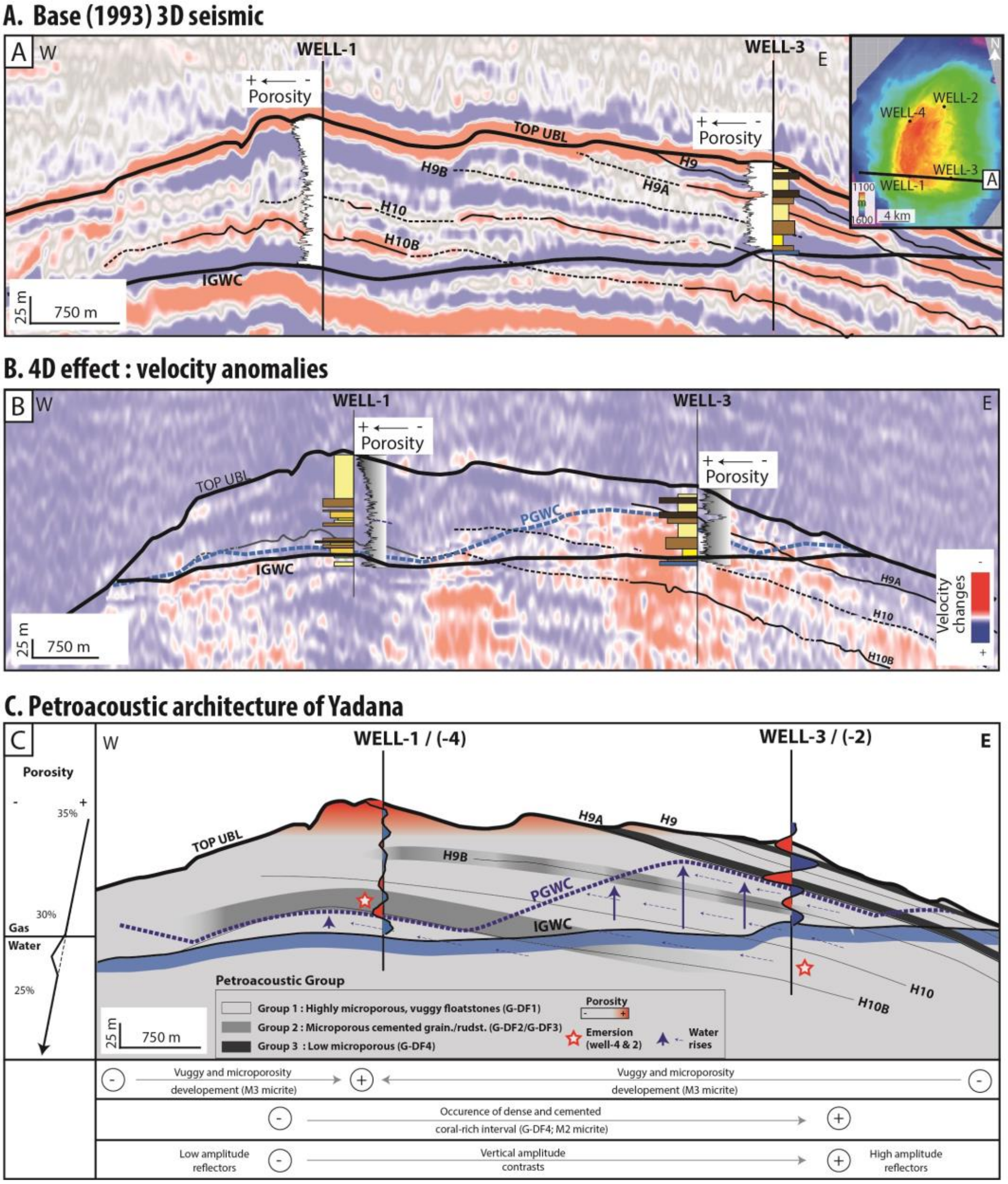

Figure 4-15: Seismic reflectivity, diagenetic/petroacoustic architecture of the Yadana reservoir and fluid flow during production. (A) W-E-oriented reflectivity profile across WELL-1 and WELL-3. (B) Velocity change (between monitor and base seismic) and position of the initial (IGWC) and syn-production (PGWC) gas-water contact, and (C) Interpretative correlation panel showing the impact of the petroacoustic/diagenetic architecture of the reservoir on the uneven rise of the gas-water contact: in the western area, water is baffled below a moderately porous G-DF3 diagenetic unit whereas in the eastern part, water can rise significantly up to the coral-rich dense intervals (G-DF4 units) from the uppermost reservoir.

analysis of the diagenetic significance of seismic reflections may help predict and mapping major heterogeneities which baffles or accelerate flow during production. Additionnally, higher permeabilities parallel to depositional bedding rather than across bedding may have enhanced the differential water rise but this effect alone could not explain the step-like shape of the gas-water contact (Fig. 12E, 15B). Two types of horizontal baffle for flow can be therefore identified and mapped throughout the Yadana buildup: (1) the brecciated and moderately porous unit related to intra-formational subaerial exposure (G-DF3/reflection H10B) and (2) the early lithified and low porous coral-rich intervals (G-DF4/reflection H9A).

4.6 Conclusion

(1) Within the gas reservoir, acoustic properties distribution is mainly determined by the reservoir zonation into meter to decameter-thick intervals which are individually characterized a dominant diagenetic facies (G-DF1 to G-DF4). Such diagenetic facies are defined by a typical range of porosity, a dominant pore type association and a set of diagenetic features. Low impedance units are highly microporous and vuggy foraminiferal/coralline algal floatstones intervals (G-DF1) whose total porosity has beensignificantly enhanced in burial environment, during or after the gas emplacement. High to moderate impedance units may correspond to 1) thin (<10 m), laterally continuous intervals of coral floatstones whose matrix has been partly cemented during early marine diagenesis (G-DF4), 2) foraminiferal rudstone geobodies of variable thickness (<1 m to>10 m) whose intergranular space is occluded by sparry calcite cements formed in shallow burial environments (G-DF2) and 3) relatively thick (up to 20 m) and laterally continuous coral breccia interval whose aragonite has been calcitized during an intra-formational stage of subaerial exposure (G-DF3).

(2) Below the pre-production gas-water contact, both microporosity and moldic/vuggy macroporosity significantly drop (up to 15% decrease) as a result of a differential diagenetic evolution between gas and water zones during and/or after hydrocarbon emplacements: carbonate leaching occurred in the gas zone whereas calcite precipitations developed within the micrite in the water zone. Within the gas zone, the acoustic architecture is predominantly driven by the diagenetic architecture. The Yadana reservoir

is subdivided into meter-decameter scale petroacoustic units whose acoustic impedance is mainly related to porosity and pore type.

(3) Seismic reflections may form at the boundary between two diagenetic units or may result from the interference between reflection at the base and top of such intervals. The acoustic contrasts generating the reflections result from differential patterns of diagenetic evolution at the interface between intervals characterized by distinct lithofacies. Changes in lithofacies alone, without differential diagenetic evolution, do not create sufficient acoustic contrast to induce seismic reflection..

(4) A stratigraphy-cross-cutting reflection horizon form at a diagenetic boundary which coincides with the pre-production gas-water contact. This horizon remains at the same location after gas-production and rising gas-water contact.

(5) The combined analysis of water rises from time-lapse seismic data and of the diagenetic significance of seismic reflections has been proved to help predict and mapping the major heterogeneities which matter for flow during production. By using such an approach, two types of horizontal baffle for flow have been identified throughout the Yadana buildup: (1) the brecciated and moderately porous unit related to intra-formational subaerial exposure (G-DF3 diagenetic unit/reflection H10B) and (2) the early lithified and low porous coral-rich intervals (G-DF4 diagenetic unit/reflection H9A).

(6) The present approach which assimilates and analyze large and diverse data sets should be applicable to other mature carbonate gas fields. The integration of petrographic, sedimentological and diagenetic inputs appears to be the key for the identification and 3D characterization of the relevant heterogenities which impact on flow during production and for improving the use of quantitative seismic approaches in reservoir studies.

V. Geophysical Pore Type inversion

Integration of cores, well-logs, and seismic data for geophysical pore type inversion in the carbonate gas reservoir of Yadana, offshore Myanmar[4]

Thomas TEILLET [1,2], François FOURNIER [1], Luanxiao ZHAO [3], Jean BORGOMANO [1], Fei HONG [2]

1 : Aix-Marseille Université, CNRS, IRD, Cerege, UM 34, 3 Place Victor Hugo (Case 67), 13331 Marseille cedex 03, France
2 : TOTAL, CSTJF, Avenue Larribau, 64018 Pau Cedex, France
3 : State Key Laboratory of Marine Geology, Tongji University, Shanghai, China

Abstract: The present work shows the potentiality of the geophysical pore type (α_P) inversion, a rock physics inversion scheme, to characterize pore type distribution quantitatively from well-log and seismic data. The method detects laterally extended (100-1000 meters) sub-seismic to seismic scale (>5 meters thickness) geological heterogeneities which are interpretable in terms of depositional and diagenetic fabrics. Based on detailed petrographical and petrophysical analysis of carbonates rock, the geophysical Pore type parameter (α_P) is fitted with facies and pore type characterization at the micro (SEM, MICP) and the macro scale (Digital Image Analysis of thin sections, cores scans) and revealed to be an upscalable parameter whose depositional/diagenetic interpretation may be performed at both well-log and seismic scales. Applied to the seismic data of an early Miocene carbonate gas reservoir (Yadana gas field, Offshore Myanmar), the inversion allowed to quantitatively map the spatial distribution of the geophysical pore type (α_P) and discriminate two main associations of diagenetic geobodies. The reservoir is composed of: (1) a highly microporous background (~80% of the reservoir interval) mainly consisting of foraminiferal red algae floastone to rudstone with vuggy and moldic porosity characterized by moderately low α_P (0.11-0.20) and (2) interbedded by thin stratiform cemented coralian floatstone/brecciated units (5-10 m; ~20% of the reservoir) with low microporosity and macroporosity exhibiting a low α_P values (<0.11).

---

[4] Manuscript ready to submitted in Geophysics

5.1 Introduction

Carbonate reservoirs are complex to characterize due to the common presence of severe and multiscale heterogeneities. Consequently, the prediction of reservoir properties in these reservoir has become a major challenge for hydrocarbon exploration and development because of the colmplex pore structure of carbonate rock which result from a variety of depositional processes and subsequent diagenetic transformations (e.g., Zampetti et al., 2004; Fournier and Borgomano, 2007; Warrlich et al., 2010; Brigaud *et al.* 2010). Pore structure is considered to be an important geological parameter that significantly control permeability, acoustic properties and seismic response of the reservoir (Anselmetti and Eberli, 1999; Eberli et al., 2003; Kenter et al., 2007; Sun et al., 2006). In a purely calcitic reservoir, P- and S-wave velocities exhibit a wide range of values at a given porosity and the resulting scattering in velocity-porosity transforms has been shown to be related to the variety of pore network architectures in carbonate rocks (e.g., Anselmetti and Eberli, 1993; 1999; Eberli et al., 2003; Fournier et al., 2018).

Petroacoustic modeling of carbonate rocks has been shown to be a relevant approach to predict porosity and pore network architectures from seismic data and to be the foundation of petrophysical inversion methods to detect and quantify pore type variations and the associated seismic heterogeneities (e.g Buland *et al.* 2008; Xu and Payne, 2009; Grana & Della Rossa 2010; Dou *et al.* 2011; Karimpouli *et al.* 2013; Zhao *et al.* 2013; Gharechelou *et al.* 2015; Grana & Mukerji 2015; Wang *et al.* 2017). In this respect, the Differential Effective Medium (DEM; Norris 1985; Zimmerman 1991; Berryman 1992, 1995) theory is a rock physics approach which makes possible to compute effective property of rocks with various mineralogical composition, porosity and pore shapes (e.g Baechle *et al.* 2008; Fournier and Borgomano 2009; Dou *et al.* 2011; Zhao *et al.* 2013; Guo *et al.* 2017; Liu & Wang 2017; Karimpouli *et al.* 2018). By using DEM theory, Fournier *et al.* (2011, 2018) defined the effective pore aspect ratio (EPAR) α_P parameter as the aspect ratio of an oblate spheroid (i.e., ratio of the polar to equatorial lengths) that is acoustically equivalent to the actual pore network. In this way, α_P has been proved, in various carbonate case studies, to be a relevant tool for characterizing pore types and diagenetic features from acoustic measurements at rock-plug and well-log scales (Hairabian et al., 2014; Fournier *et al.,* 2014; 2018). It is worth mentioning that the actual complex pores in carbonates

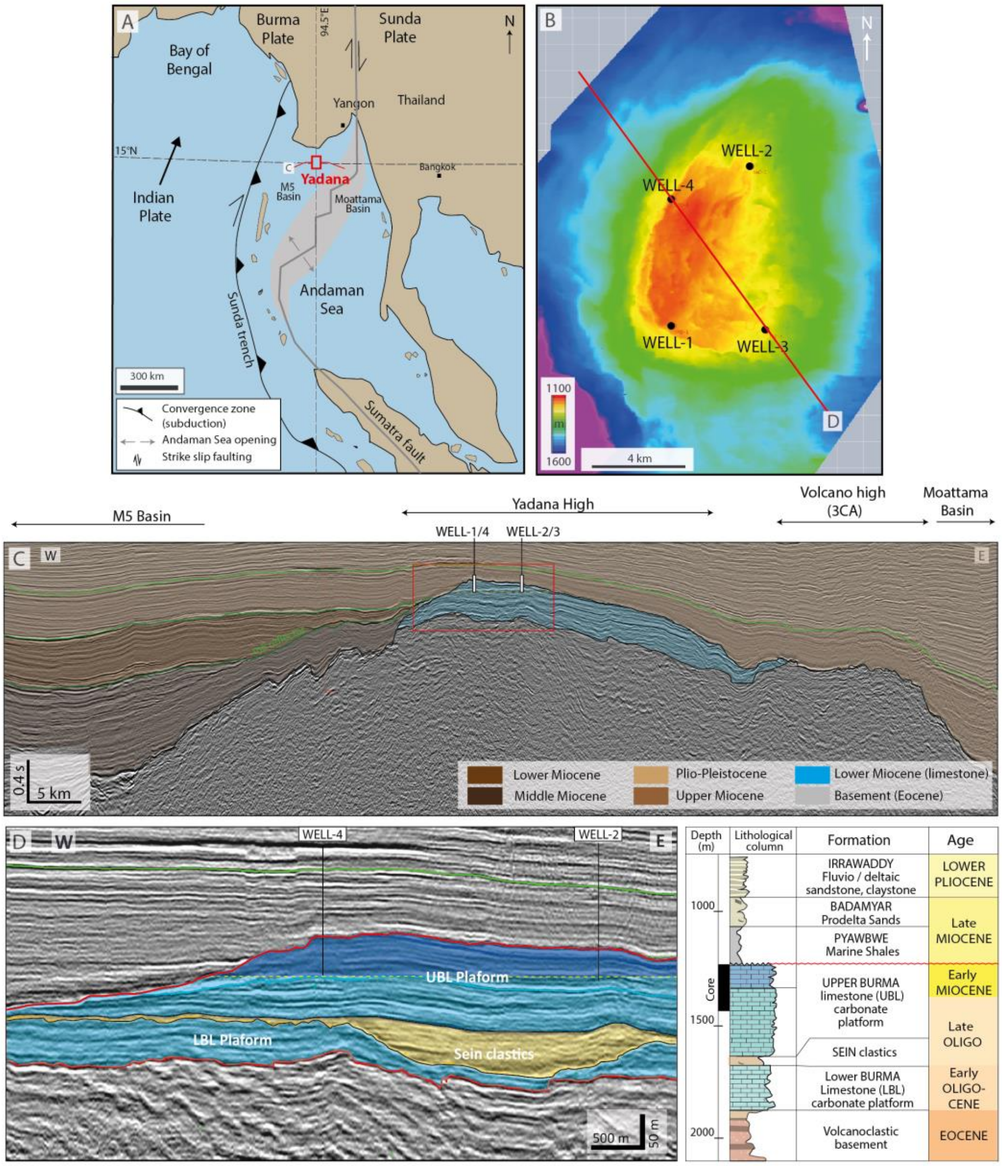

Figure 5-1 : Geographical and geological setting of the Yadana gas field: (A) Geographical and tectonic settings of the Andaman Sea and the Yadana Field (after (Curray, 2005); (B) Depth map of top reservoir and well location. (C) Interpreted regional 2D seismic profile (two-way time) through the Yadana high (see location on A). (D) Interpreted seismic profile (depth) of the Yadana field crossing the wells WELL-4 and WELL-2, showing the lithostratigraphic units and the gas water contact (yellow dotted line) (see location on A). (E). Lithostratigraphic column of the Yadana platform.

are rarely ellipsoidal in shape, and α_p should be regarded only as a proxy of the effective pore stiffness imprinted by diagenetic processes. At seismic scale, a DEM-based rock physics modeling approach has been also used to invert effective pore aspect ratio from seismic data (Zhao et al., 2013) in order to detect seismic-scale geobodies characterized by distinct pore types. Seismiwave cannot see the individual pores or cracks at microscopic scale, but only see the average pore stiffness at the seismic wavelength scale. As a consequence, seismic-derived pore aspect ratios represent the average elastic effective properties of complex pore structures at seismic scale and therefore characterize geophysical pore types.

The objectives of the present work are: 1) to qualitatively and quantitatively characterize pore types associations from the Yadana gas reservoir (early Miocene, Offshore Myanmar) using core data and to relate them to the depositional and diagenetic evolution of the carbonate system, and 2) to propose a DEM-based methodology which integrates the α_p approach (Fournier et al., 2018) and its ability to detect pore types and diagenetic features and the geophysical pore type approach (Zhao et al., 2013) in order to provide a 3D diagenetic inversion of the carbonate gas reservoir.

Such a diagenetic inversion aims at detecting and mapping seismic-scale heterogeneities of significant impact on hydrocarbon recovery during production.

5.2 Geological setting

The Yadana gas field is located in the Andaman Sea, offshore Myanmar, 60 km south of Irrawady River delta (Fig. 1A, 1B). The Yadana field was discovered in 1983 from the lower Miocene Upper Burman Limestone formation and dry gas production began in 1998 (Racey and Ridd, 2015). The geodynamic context of the Andaman Sea (Chakraborty and Khan, 2009; Curray, 2005; Morley, 2013, 2012) is largely controlled by the oblique collusion of the Indian—Australian plate beneath the Eurasia plate, the Sunda Subduction (Hall, 2012, 2002, 1997; Lee and Lawver, 1995) (Fig. 1A). The carbonate platform of Yadana has settled on top of a volcanic ridge (Yadana High) which separates the M5 basin to the west from the Moattama Basin to the east (Fig. 1C). The lower part of the carbonate buildup (Lower Burman Limestone; LBL Formation, Oligocene) is composed of two distinct platforms separated by a central canyon (Zuckmeyer et al., 2017). Above the LBL formation, the Upper Burman Limestone (UBL) Formation (early Miocene) consists of a single isolated platform, 25 to 30 km in diameter and up to 300 m in thickness and represents the gas-bearing reservoir (Fig. 1B, 1C). The gas column occupies the uppermost 150 meters of the Upper Burman Limestone (Fig 1D) and the platform is topped by an uneven, erosive surface (TOP UBL) which is overlain by the late Miocene siliciclastic deposits of the Pyawady Formation.

5.2.1 Depositional lithofacies

The Yadana buildup has been regarded as a reef-rimmed platform by Paumard et al. (2017) on the basis of seismic facies interpretation, but the integration of facies and paleoenvironmental analysis of core data led to a revision of the former depositional models (Teillet et al., 2020) and to the definition of three distinct carbonate factories which occupied the top of an isolated platform at different stages of the buildup development: (1) a scleractinian carbonate factory developing under mesophotic conditions during periods of high particulate organic matter supplies, (2) an echinodermal carbonate factory occupying dysphotic to aphotic area of the shelf coevally with the scleractinian carbonate factory, (3) a large benthic foraminiferal-coralline algal carbonate factories prevailing under oligo-mesophotic and oligo-mesotrophic conditions.

The Upper Burman Limestone is characterized by a relatively monotonous, 100m-thick bioclastic carbonate succession whose skeletal components are dominated by non-geniculate coralline algae and large benthic foraminifers. Coral may be common in a few intervals. Non-geniculate coralline-red algae are dominated by encrusting to branching forms, commonly forming nodules (rhodoliths). Larger benthic foraminiferal association is characterized by lepidocyclinids (*Nephrolepidina* and *Eulepidina*), *Spiroclypeus*, *Cycloclypeus* commonly displaying flat morphologies. Additional skeletal components include echinoderms, bryozoans, and rarer planktonic foraminifera. Based on depositional textures and biota, five lithofacies have been identified (Teillet et al., 2020) and summarized in Fig. 2A. Coralline algal rudstone to floatstone (LF1), large benthic foraminiferal rudstone (LF2.1) to floatstone (LF2.2), scleractinian-echinodermal floatstone (LF3.1) and echinodermal wackestone (LF3.2). The depositional architecture of Yadana has been built based on vertical lithofacies stacking pattern in cores as well as foraminiferal biosstratigraphic constrains (Teillet et al., 2019; 2020) (Fig. 2B).

A. Lithofacies

LF1 Coralline algal floatstone to rudstone with a coralline algal-foraminiferal (Lithothamnion, Mesophyllum)wackestone to packestone matrix. Heterometric rhodoliths or pieces of branching red algae. Foraminiferal assemblage dominated by Spiroclypeus sp. and Nephrolepidina sp.

LF2.1 Large benthic foraminiferal rudstone with common red algal fragments. Intergranular space is occupied by peloidal grainstone or occluded by calcite cements. Dominated by Lepidocyclina, Spiroclypeus and rarer Amphistegina, Miogypsina. Coralline algae mainly include branching and warty forms.

LF2.2 Large benthic foraminiferal floatstone with coralline algal wackestone / packestone matrix. Large benthic foraminifers are large (up to 2 cm) thin shelled commonly preserved. Spiroclypeus and common Cycloclypeus. Laminar and losse Mesophyllum, together with branching Lithothamnion.

LF3 Coral float. and echinodermal wackestone (LF3.1) embedded in a wackestone matrix dominated by echinoderm **(LF3.2).** Consists of transported fragments of Scleractinian (Faviids, Pocilloporids) dominated intervals are frequently brecciated at the top. Elements are gravel to pebble-sized,para-autochtonous. Intergranular space is filled micrite.

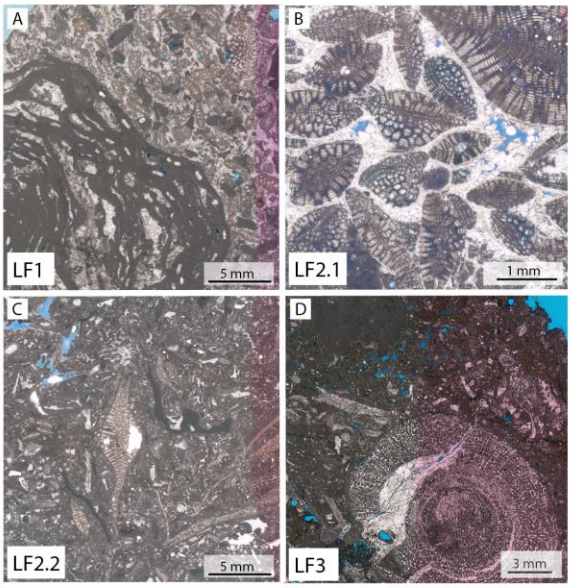

Figure 5-2A: Depositionnal lithofacies of the Upper Burman Limestones (after Teillet er al., 2019, 2020).

5.2.2 Diagenetic zonation of the Upper Burman Limestone

A diagenetic layering of the cored interval of the Upper Burman Limestone has been performed, based on the identification of diagenetic features. A detailed description of the diagenetic features identified in the Yadana reservoir is displayed in the Fig. 5-3 and discussed in Teillet et al. (2019a). The diagenetic facies have been defined by combining petrographic and petrophysical attributes (Table 8): 1) diagenetic features, 2) micrite microfabrics, 3) range of porosity values, 4) pore type associations. The significant decrease in average porosity below the gas-water contact (Fig. 5-2B) and the distinct diagenetic features observed in the gas and water legs (Teillet et al. 2019a) led to differentiate the 2 zones in the facies classification.

Within the gas zone, four main groups of diagenetic facies have been defined: 1) highly microporous and vuggy, mud-supported carbonates (G-DF1), 2) microporous cemented grainstones-rudstones (G-DF2), 3) microporous and vuggy carbonate breccia (G-DF3), 4) floatstones with low matrix microporosity (G-DF4). This diagenetic facies G-DF1 has been subdivided into 3 sub-facies: calcitic red algal and foraminiferal floatstones (G-DF1a), calcitic coral floatstones (G-DF1b), and partially dolomitized floatstones (G-DF1c).

Within, the water zone, two diagenetic facies have been identified in the cored interval (Fig. 5-3): 1) floatstones (W-DF1a) and rudstones (W-DF1b) with low intragranular and matrix microporosity, and 2) carbonate breccia with low microporosity (W-DF2). According to Teillet et al. 2019a, the diagenetic layering of the cored interval of the Upper Burman Limestone based on the identification of diagenetic facies is presented in the Fig. 5-4.

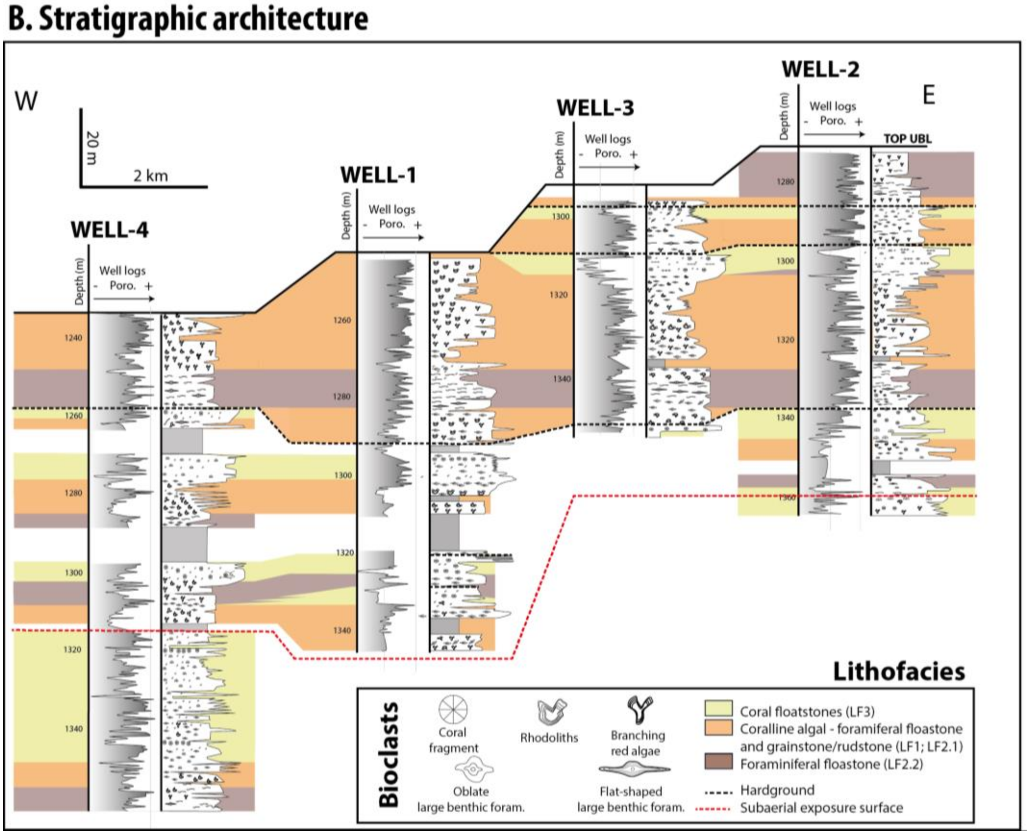

B. Stratigraphic architecture

Figure 5-2B: Stratigraphic architecture of the Yadana platform based on large benthic foraminiferal biostratigraphy, well to seismic tie and correlation of lithofacies stacking patterns (after Teillet et al., 2019, 2020).

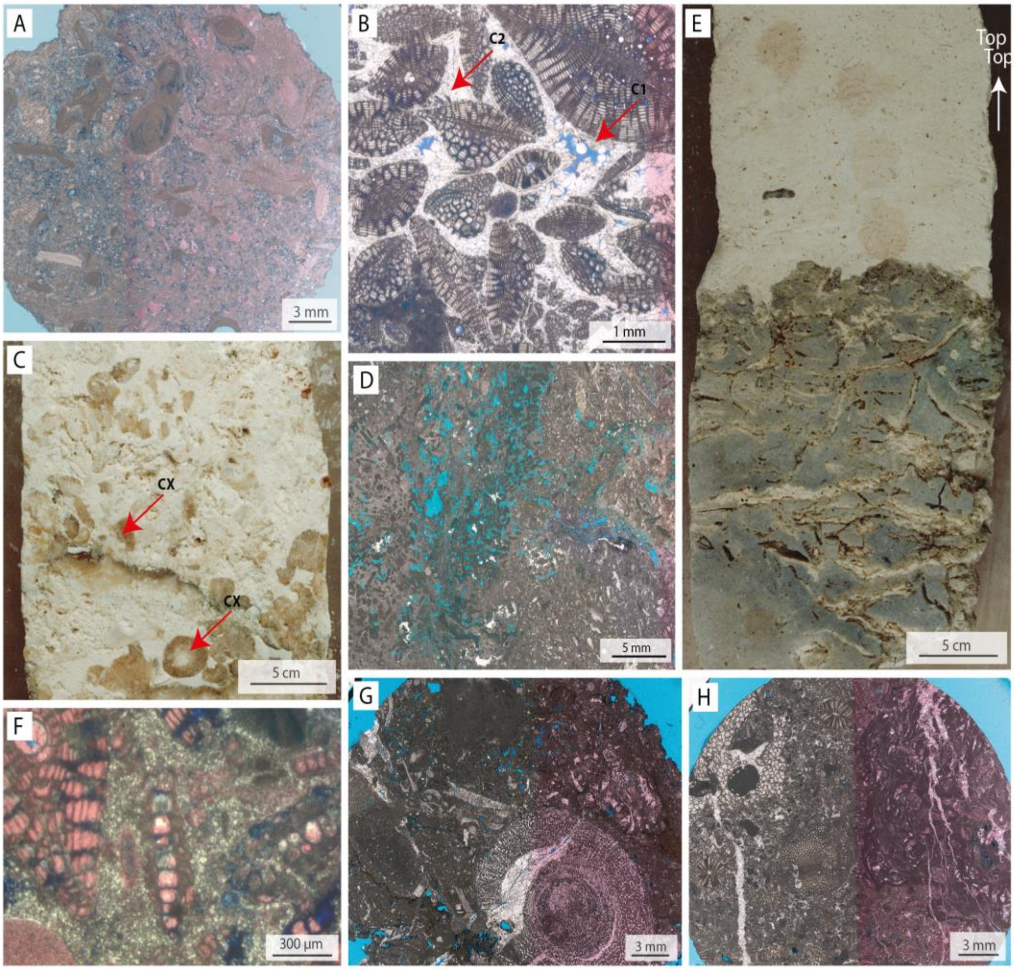
A
3 mm
B
C2
C1
1 mm
E
Top
Top
5 cm
C
CX
CX
5 cm
D
5 mm
F
300 µm
G
3 mm
H
3 mm

Figure 5-3 : (A) WELL-3 1330.30 mcD : red algal/foraminiferal floatstone (lithofacies LF1) with high matrix and intraskeletal microporosity and vuggy porosity (diagenetic facies : G-DF1a); (B): WELL-3 1319.49 mCD; Isopacheous C1 rim cement and blocky calcite cement C2 infilling the intergranular pore space of a foraminiferal rudstone (lithofacies LF2.1; diagenetic facies G-DF2).(C) WELL-4 1337.7 mCD; core picture showing brownish calcitized coral (CX) within a brecciated interval (lithofacies LF3.1; diagenetic facies: G-DF3); (D) WELL-3 1311.84 mCD: Coral floatstone (lithofacies LF3.1) whose scleractinian elements have been dissolved; the resulting moldic pores are infilled with a bioclastic micrite which is similar in nature to that of the floatstone matrix thus leading to a faint-ghost fabric (diagenetic facies: G-DF4); (E) WELL-3 1308.05 mCD: core photograph of a hardground surface, at the top of a carbonate breccia composed of poorly displaced, tight elements of coral-rich and echinodermal floatstone (lithofacies LF3.1; diagenetic facies: G-DF4). The hardground is sharply overlain by highly microporous, coralline algal-foraminiferal floatstone (lithofacies LF1; diagenetic facies: G-DF1a). The inter-clast space of the hardground breccia is filled by the overlying microporous sediment; (F) WELL-4 1286 mCD: microphotograph of a foraminiferal packstone-floatstone whose matrix is partially replaced by dolomicrosparite (not stained by alizarine) (diagenetic facies G-DF1c); (G) WELL-2 1361.42 mcD: Coral and echinodermal floatstone (lithofacies LF3.1) in the water zone. Tight with low microporosity (diagenetic facies: W-DF1a); (H) WELL- 2 1345.40 mcD: Foraminiferal coralline algal floatstone-rudstone (lithofacies LF1) with low microporosity in the water zone (diagenetic facies: W-DF1b).

	Diagenetic facies		Diagenetic features	Micrite micro-fabrics	Typical porosity range	Pore type association	δ^{13}C bulk (‰ PDB)	δ^{18}O bulk (‰ PDB)	Occurrence	Illustration
G-DF1	**Highly microporous and moldic/vuggy, mud-supported carbonates**	**A: calcitic red algal and foraminiferal floatstones**	Micritized bioclasts; blocky calcite cement (C2); leached bioclasts (red algae and foraminifers) and matrix	M1	25-45%	High microporosity, high moldic and vuggy porosity	-1 to +1	-3 to 0	Gas zone	Fig.7 A, E
		B: calcitic coral floatstones	Neomorphosed corals into C2' calcite; micritized bioclasts; rare blocky calcite cement (C2); leached bioclasts (corals, red algae and foraminifers)	M1	25-45%	High microporosity, high moldic and vuggy porosity	-1 to +1	-3 to 0		Fig. 4 D
		C: partially dolomitized floatstones	Dolomicrite to dolomicrosparite crystals replacing micrite matrix and micritized bioclasts; leached bioclasts (red algae and foraminifers) and matrix	M1 M4	25-45%	High microporosity, high moldic and vuggy porosity	-0,5 to +1,5	-0,5 to +3		Fig.7 B
G-DF2	**Microporous cemented grainstones-rudstones**		Isopacheous calcite cement (C1) and blocky calcite cement (C2).	M1	18-30%	High microporosity, moldic porosity; rarer intergranular porosity	-0,5 to +0,5	-3 to 0	Gas zone	Fig.4 A, B, C
G-DF3	**Microporous and vuggy carbonate breccia**		Brecciation features (type II); neomorphosed corals into CX calcite; blocky calcite cement (C2); micritized bioclasts; leached bioclasts (corals, red algae and foraminifers) and matrix	M1	25-40%	High microporosity, inter-breccia clast porosity; moldic and vuggy porosity; rarer intergranular porosity	-3,5 to 0	-5 to -2	Gas zone	Fig. 4 E,F
G-DF4	**Coral floatstones with low matrix microporosity**		Brecciation features (type I); leached corals and micrite infills within molds (faint-ghost texture); leached bioclasts (corals, red algae and foraminifers)	M2	10-20%	Low microporosity; moldic to vuggy porosity	-1 to 0	-2 to 0	Gas zone	Fig.6 A, B, C; Fig. 7 C
W-DF1	**Floatstones and rudstones with low intragranular and matrix microporosity**		Micritized bioclasts; isopacheous calcite cement (C1) blocky calcite cement (C2); leached bioclasts (red algae and foraminifers) and matrix	M3	10-25%	Low microporosity; moldic to vuggy porosity	-1 to 0	-4 to -1,5	Water zone	Fig. 7 D
W-DF2	Carbonate breccia with low microporosity		Brecciation features (type II); neomorphosed corals into CX calcite; blocky calcite cement (C2); micritized bioclasts; leached bioclasts (corals, red algae and foraminifers) and matrix	M3	10-30%	Low microporosity; inter-breccia clast porosity; moldic to vuggy porosity	-2 to -0,5	-5 to -3	Water zone	

Table 8: Definition and properties of the diagenetic facies from the Upper Burman Limestone (after Teillet et al., 2019).

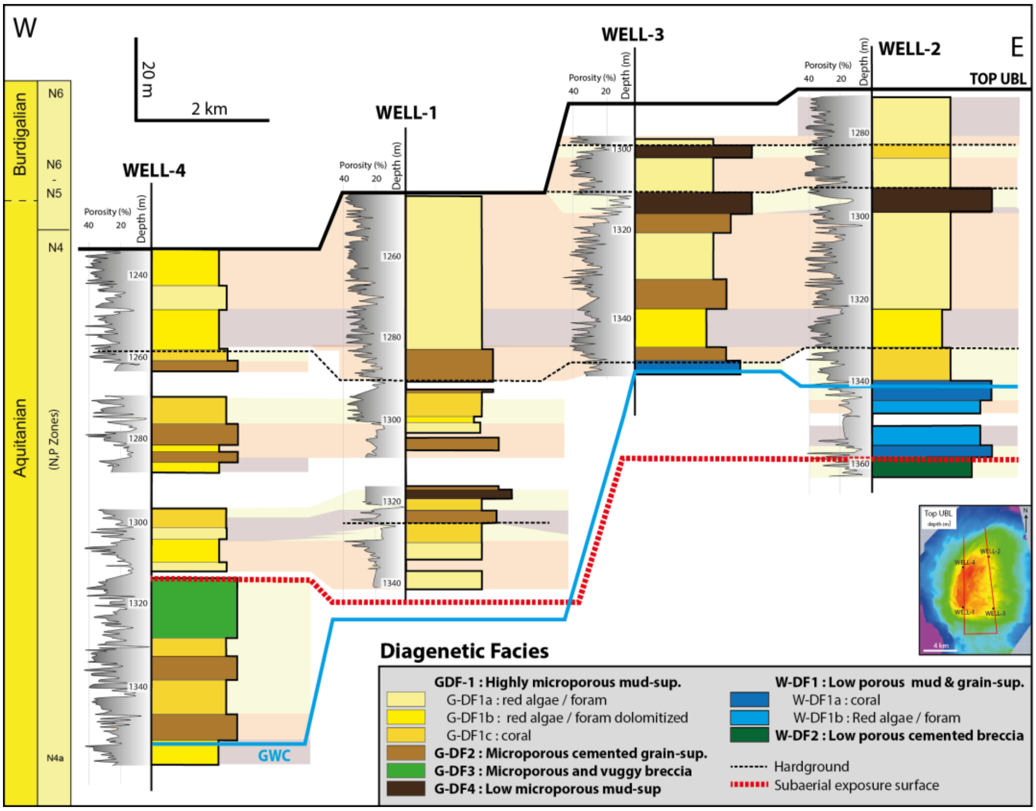

Figure 5-4 : WELL-1, -3 and -4, cored intervals: lithofacies, depositional textures, carbon and oxygen isotope ratios, porosity (laboratory measurements on plugs), water saturation, dolomite and dissolution vug occurrence and diagenetic facies (after Teillet et al., 2019).

5.3 Data set and Method

The Yadana field has been penetrated by 20 wells and covered by a three-dimensional seismic survey. Four cored (WELL-1, WELL-2, WELL-3, and WELL-4) have been selected for the present study (see location in Fig. 5-1B). The database is summarized in Table 9 and detailed below.

Petrographic analysis

The identification of depositional and diagenetic features is based on the study of a total of 343 m of cores located within the UBL interval (WELL-1: 87.5 mcDs (meter Core Depth), WELL-2: 84 mCD WELL-3: 59.5 mCD WELL-4: 112 mCD). A total of 694 thin sections have been prepared from cores (average spacing of 50 cm). The thin sections were impregnated with a blue dye epoxy resin and half-stained with alizarine-red and potassium ferrocyanide solution (Dickson, 1966) for the identification of carbonate minerals. Thin sections were observed under polarized-light microscopy for the characterization of depositional and diagenetic features as well as for the quantitative analysis of pore types. Macroporosity is defined as the pore space which is colored with blue epoxy and whose size exceeds 2 pixels (i.e., diameter> 10 µm) on scanned thin sections. The proportion of macroporosity on thin section is automatically extracted using Digital Image Analysis (DIA) and the software ImageJ by gathering the blue pixels. Microporosity is defined as pores non-visible on thin section pictures or whose size is lower than 2 pixels (i.e., pore diameter <10 µm). The definition of microporosity used in the present work is therefore consistent with the definition given by Cantrell and Hagerty (1999). The proportion of microporosity was semi-quantitatively estimated as the difference between the laboratory porosity measurement on plugs and the macroporosity estimated from thin-section image analysis. Although based on two-dimensional images, image analysis has been shown to provide accurate quantification of macroporosity in carbonate reservoirs (Haines et al., 2015). Micrite microfabrics were characterized by scanning electron microscopy (SEM) images performed at Aix-Marseille University using a Philips XL30 ESEM ®.

Laboratory measurements

Laboratory helium porosity ($PHI_{\_plug}$) measurements have been performed on approximately 1300 core plugs at an interval of 50 cm in sub-atmospheric condition. Special

		Well-1	**Well-2**	**Well-3**	**Well-4**
Rock data	Core	**87.5 m**	**84 m**	**59.5m**	**112 m**
	Thin section	**331**	**152**	**91**	**130**
	PHI/K	**337**	**326**	**223**	**439**
	SEM	**2**	**3**	**13**	**5**
	MICP	**6**	**5**	**3**	**-**
	Grain density	**13**	**14**	**9**	**-**
	XRD	**9**	**5**	**3**	-
Well log data	Gamma ray (GR)	**X**	**X**	**X**	**X**
	Density (RHOB)	**X**	**X**	**X**	**X**
	Neutron (NEUT)	**X**	**X**	**X**	**X**
	Sonic_P (Vp)	**X**	**X**	**X**	**X**
	Sonis_S (Vs)	**X**	**X**	**X**	**X**
	Porosity ($PHI_{\_well\text{-}log}$)	**X**	**X**	**X**	**X**
	Water sat. (Sw)	**X**	**X**	**X**	**X**
	Geophysical Pore type (aK)	**X**	**X**	**X**	**X**
	Seismic trace	**X**	**X**	**X**	**X**
	Synthetic trace	**X**	**X**	**X**	**X**
Rock & fluids Parameters	K_{water} (Gpa)	**2.63**	Kcalcite	**76.8**	
	$Density_{water}$ (g.cm^3)	**0.9988**	$Density_{calcite}$	**2.71**	
	K_{gas} (GPa)	**0.017**			
	$Density_{gas}$ (g.cm^3)	**0.13**			
	Grain density (g.cm^3	**2.708** (n=39)			

Table 9: Rock, well-log and physical properties of water, gas and minerals.

core analysis (SCAL) consists of a total of 14 Mercury Injection Capillary Pressure (MICP) measurements giving information about the pore throat radius distribution of the sample. Mercury was injected into cleaned and dried samples and initially evacuated, at pressure stages up to 345 MPa. At each step of the pressure, the volume of injected mercury gives the wetting phase.

Well-log data

Conventional well logs data of the four studied wells have been used in the present work. They include neutron (NEUT), density (RHOB), gamma ray (GR) and P- and S-sonic logs. Water saturation (S_w), total porosity ($PHI\_\_{welllog}$) and mineralogical composition have been estimated at TOTAL from the quantitative interpretation of well logs. Core depths have been tied to log depths by matching vertical changes in plug porosity ($PHI_{\_plug}$) corrected from the overburden effect and well-log porosity ($PHI_{\_welllog}$) curves.

Geophysical data

The 3D seismic survey for the Geophysical Pore Type inversion was acquired by TOTAL in 1993 and covers the entire Yadana gas field (~511 km^2). Trace sampling is 3 ms, lateral spacing is 12.5 x 6.25 m and the central signal frequency within the carbonate buildup averages 45 Hz for a vertical resolution of 20 m within the reservoir (Fig. 5-5). The time to depth conversion is based on check-shots and well to seismic tie using synthetic seismograms. Elastic models (impedance) has been computed from the acoustic poststack inversion performed by CGG Group and based on the approach implemented by Coulon *et al.* (2006).

Rock physics modeling at well-log and seismic scale: the Geophysical Pore type approach

Differential Effective Medium (DEM) methods have been used to model velocity-porosity transforms for various mineral compositions, porosity values, pore aspect ratios and fluid contents. According to such an approach, a two-phase composite material is modelled by incrementally adding inclusion of one phase (phase2: pores) to the host phase (phase 1: mineral) (Norris, 1985; Zimmerman, 1991; Mavko *et al.* 2009). The methodology helps quantifying the relative impact of mineralogy, pore volume and pore architecture on elastic moduli and velocities at plug or well-log scale (Fournier et al., 2011; 2018; Hairabian, 2014) as well as at seismic scale (Xu & Payne 2009; Zhao et al., 2013). A geophysical pore type α_{P_log} has been defined as the matching parameter between the P-wave velocity (V_P) derived from well logs or seismic data and that computed from DEM modeling of an effective medium composed of oblate spheroidal voids included within a mineral host. In the present approach, a P-wave velocity-derived aspect ratio (α_P) is used instead of a bulk-modulus derived parameter (α_K in Fournier *et al.*, 2018) in order to adapt the methodology to databases where S-wave sonic logs and/or S-wave impedance 3D inversion models are not available.

According to the geophysical pore type inversion scheme implemented by Xu and Payne (2009) and Zhao et al. (2013), the pore system is composed of two pore types of

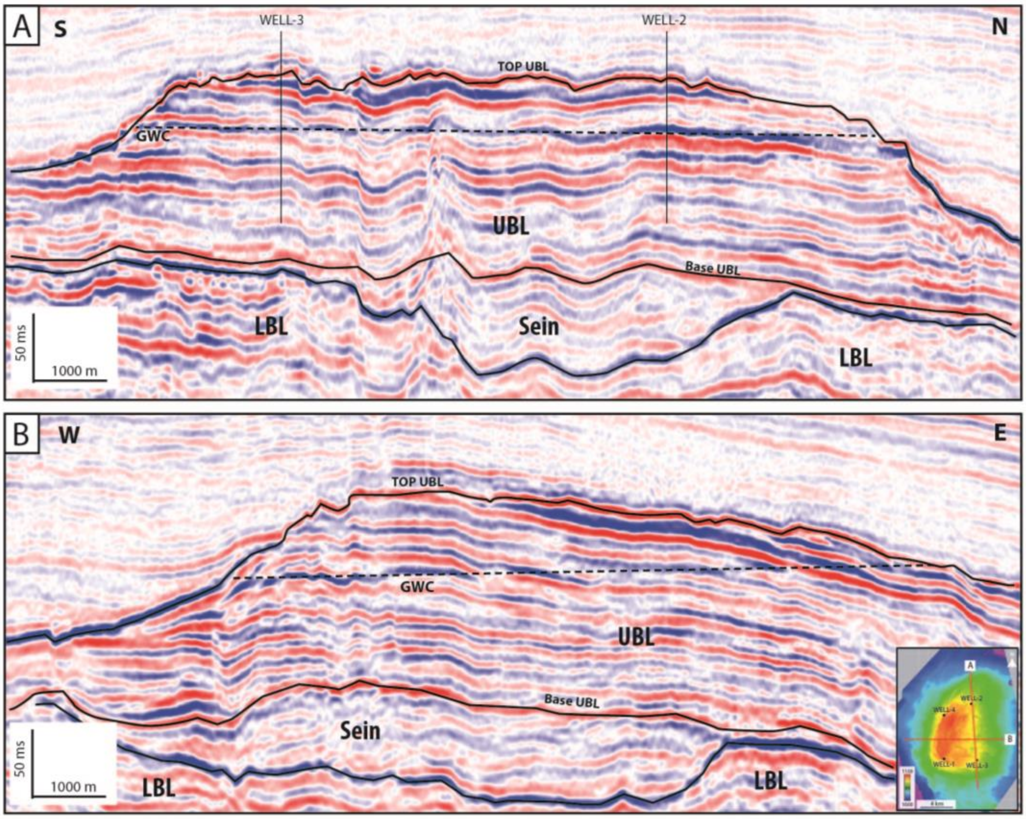

Figure 5-5 : N/S (A) and W/E (B) section of stacked seismic data (amplitude) crossing the Yadana platform. UBL: Upper Burman Limestone Formation; LBL: Lower Burman Limestone Formation; GWC: Gas Water Contact; Sein : Sein Clastic Formation.

fixed aspect ratio (stiff pore + reference pore or soft pore + reference pore) and the computation provides the relative proportion of these two pore types. In the present work the former algorithm of Zhao et al. (2013) has been modified in order to compute one single geophysical pore type from seismic data. In the present work, α_{P_log} and α_{P_seis} represent the geophysical pore type derived respectively from well-log and from seismic data respectively.

The computation of the geophysical pore type α_P has performed according to the following scheme: (Fig. 5-6):

1) At a given location within the reservoir, a set of $V_{P\_measured}$ and porosity ($Phi_{measured}$) values is extracted from well logs (at well location) or from poststack seismic inversion model to serve as adjusting parameters to the inversion.
2) Bulk and shear moduli of the mineral phase are computed using mixing law Voigt and Reuss-Hill equations (Mavko et al., 1998), based on the mineralogical composition of the rock and on individual moduli of each mineral.
3) Dry spheroidal pores with a given aspect ratio are included within the mineral host and effective bulk and shear moduli of the resulting dry porous medium are computed by using DEM equations (cf. appendix).
4) Bulk and shear moduli (K_{DEM}, μ_{DEM}) of the fluid saturated composite medium are calculated by using Gassmann equation. The fluid modulus is modeled using Wood's suspension model to take into account the fluid saturation effect.
5) Grain density ρ_g is computed as the arithmetic average of individual mineral density, weighted by mineral volume fractions, and the bulk density $_B$ of the fluid saturated mineral composite with spheroidal inclusions is calculated as follows: $\rho_B = (1-\varphi).\rho_g + \varphi.\rho_{fl}$, where ρ_{fl} being the density of pore fluid.
6) The effective P-wave velocity of the fluid saturated mineral composite with spheroidal inclusions ($V_{P\ modeling}$) is computed from K_{DEM}, μ_{DEM}, and from the bulk density.
7) The value of α_P is determined by matching $Vp_{modeling}$ with the actual P-wave velocity which derives from well logs or seismic inversion.

Similarly to α_K (Fournier et al., 2018), α_P value should not be considered as a geometrical descriptor of the actual pore shape but as an index of the impact of pore network structure on P-wave velocity. The mineral and fluid properties used for the DEM modeling and $_P$ computations are reported in Table 9. The spatial estimation of porosity and fluid saturation used for the computation of α_{P_seis}, are derived from static reservoir modeling

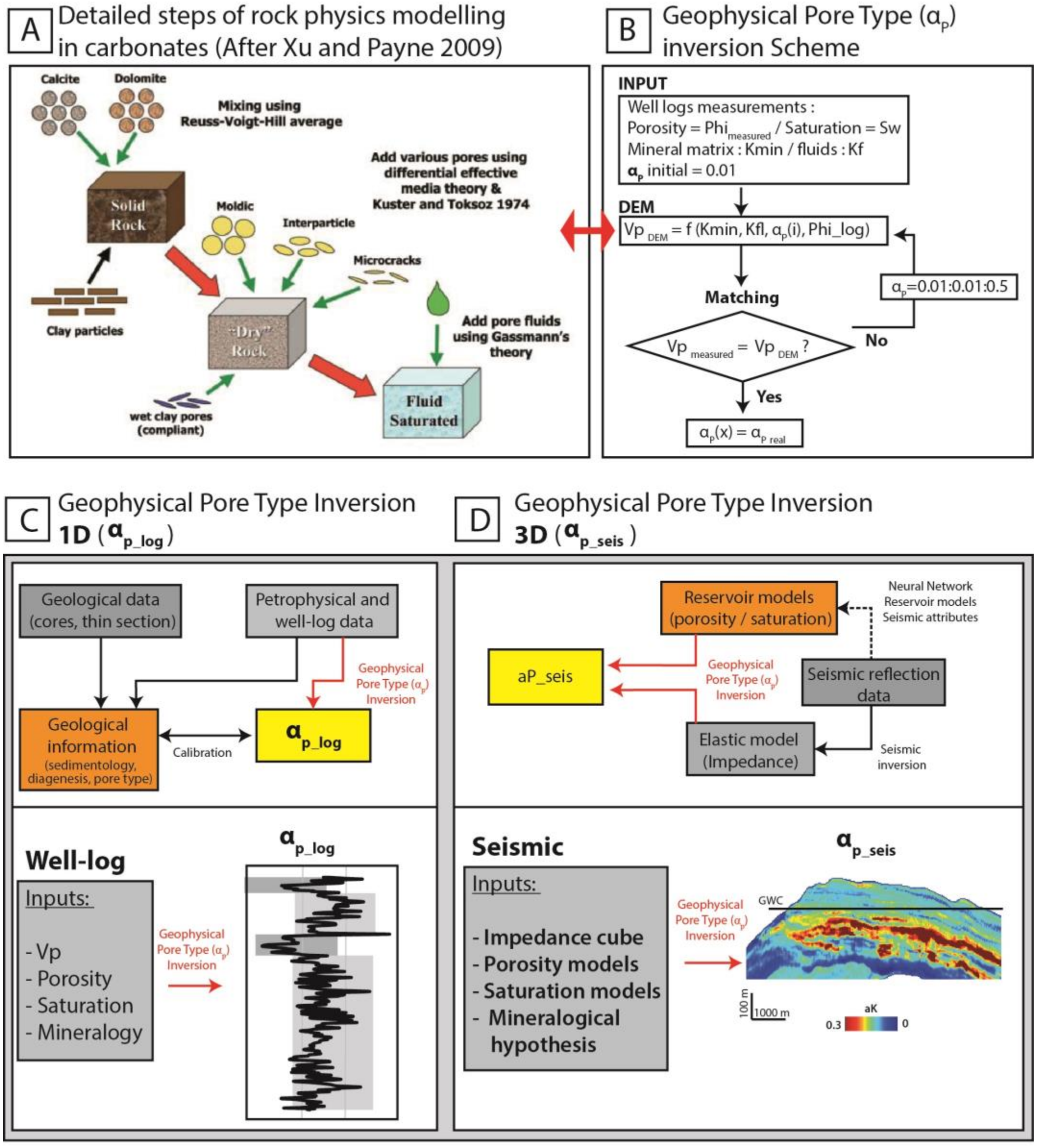

Figure 5-6 : Workflows of rock physics modeling and the Geophysical Pore Type Inversion: (A) Detailed steps of rock physics modeling (DEM) in carbonates (from Xu and Payne 2009). (B) Scheme of Geophysical Pore Type (α_P) Inversion (algorithm on Matlab). (C) 1D inversion from well-logs data (α_{P_log}). (D) 3D inversion from seismic data (α_{P_seis}).

approaches which are based on geostatitiscal methods (Sequential Gaussian Simulation; SGS), driven by all the available well logs, seismic attributes and deterministic facies maps.

5.4 **Results**

5.4.1 Pore type characterization

Pore network characterization is based on core and thin section analysis (petrography; Fig. 5-3 and 5-7A), SEM observations (Fig. 5-7B) and mercury injection capillary curves (MICP: Fig. 5-7C). Digital Image Analysis (DIA) has been used to estimate macroporosity (pore diameter>10 µm) from thin section microphotographs (Fig. 5-7D). The remaining fraction of porosity, which is lower than the threshold of the image analysis (<10 µm) represents the microporosity and has been estimated as the difference between the laboratory porosity measured on plugs and the macroporosity computed from DIA. Such an approach, applied to 320 thin sections, indicates that macroporosity ranges from 0 to 15% and represents in average only 25% of the total porosity (PHI_plug) (Fig. 5-7D), while 75% of the pore volume is microporosity (Fig. 5-7D). Macropore space is composed of a mixture of various pore types: (1) mesovugs (pore diameter between 10 and 50 µm) located within leached micrite matrix (M1); (2) macro-vugs (>50 µm) affecting both matrix and/or allochems; (3) moldic pores with pore diameter: from 50 µm to 5 cm which affect mainly benthic foraminifers but also coralline algae or corals; (4) intercrystalline pores in dolomitic limestone (pore size: 10-50 µm); and (5) intergranular pores (50-200 µm) which are relatively scarce in the studied samples.

Microporosity is both located in micrite matrix and micritized allochems. MICP measurements performed on 14 samples revealed that three distinct micropore networks can be distinguished in the Yadana gas-bearing based on throat radius distribution (Fig. 5-7C). A first group of samples (11 samples) exhibits a unimodal pore throat radius distribution centered around a dominant pore throat radius of 0.6 to 1.2 µm and corresponding to samples with the highly porous, anhedral to subrounded micrite microfabrics M1 defined by Teillet et al. 2019a (Fig. 5-7B). A second group of samples (only 2 samples) displays a unimodal distribution with a pore throat radius lower than 0.6 µm corresponding to coral-rich limestone with moderate porosity and a densely packed micrite microfabric M2 (Fig.5-7B). Finally, one sample of dolomitic wackestone displays a bimodal distribution with two dominant pore throat radii of 0.8 µm and 3 µm, which are

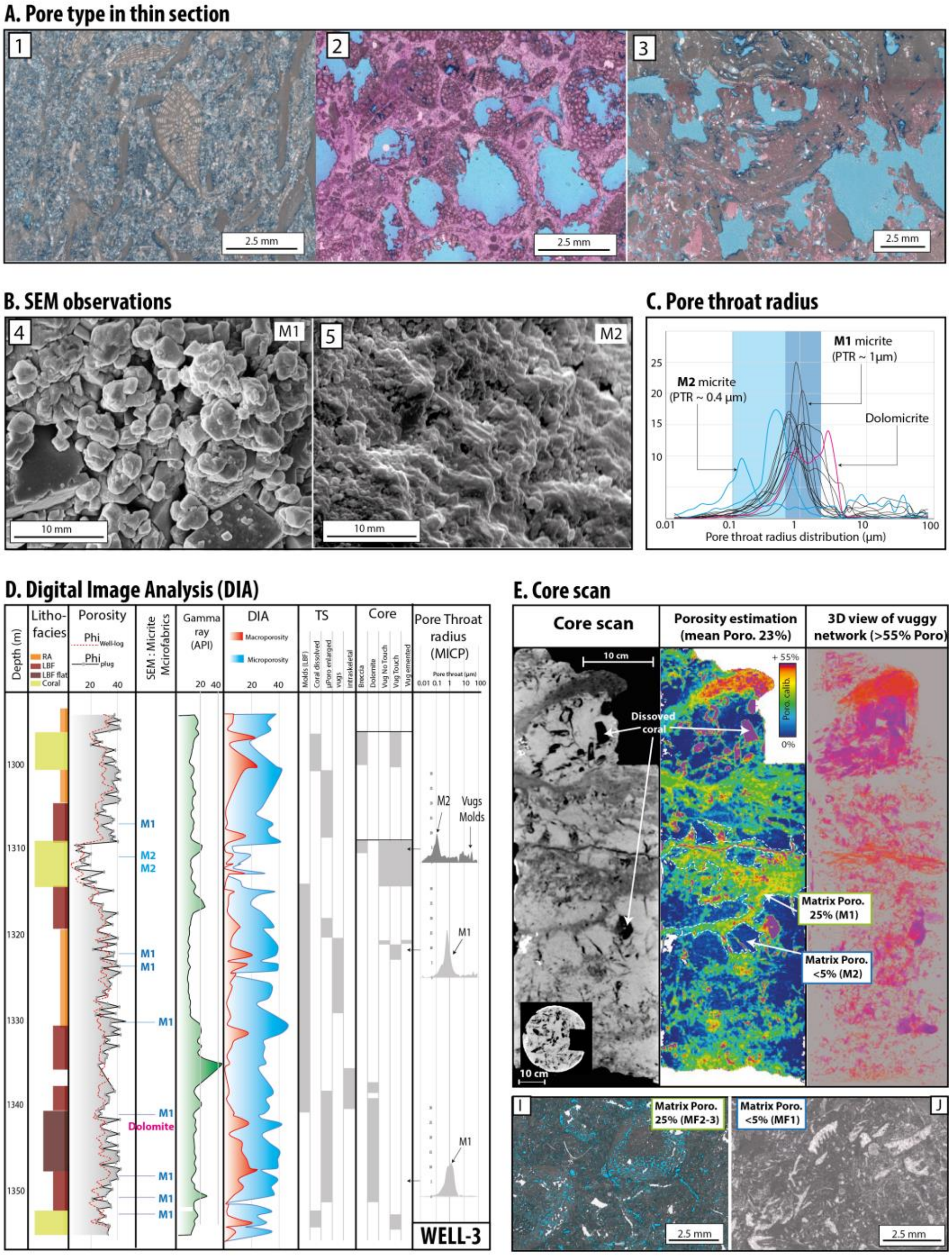

Figure 5-7 : Pore type characterization. (A) Main pore types on thin sections: (1) mesoporosity, (2) moldic pores, (3) vugs. (B) SEM observation of micrite microfabrics (4) subrounded micrite; M1, (5) cemented tight micrite; M2 (C) Pore Throat radius measurement. (D) WELL-3 cored intervals with lithofacies, well-log and plug porosity, pore type distribution on thin sections (Digital Image Analysis) and cores and pore throat radius measurement (MICP). (E) Scanned interval of a core sample (WELL-3 1308 mcD) illustrating porosity heterogeneities at core scale.

likely to be related respectively to micropores in M1 micrite and intercrystaline porosity between dolomite rhombs.

Finally, a piece of core (length: 0.20 m), from a brecciated, coral-rich interval (WELL-3 1308 mCD), has been scanned to characterize porosity heterogeneity at the pluri-centimetric scale (Fig. 5-7E). The calculated porosity of the full piece of core is 23% but therefore two types of heterogeneities: (1) A Dense cm-sized area with low porosity (porosity<15%, area in blue in Fig. 5-7E) including sometime moldic pores of coral fragments (purple area). SEM observations have shown that micrite from these area displays a densely packed M2 micrite microfabric (Fig. 5-7B). (2) A highly porous area (porosity> 30%, area in green to yellow, Fig. 5-7E) that surrounds the low porous zones, whereas the matrix on SEM is made by the very porous loosely packed and subrounded micrite microfabric M1 (Fig. 5-7B). The degree of pore type heterogeneity highlighted by a core scan (cm scale) can therefore be considered to be partly responsible for the existing gap between porosity measured from plugs (cm scale) and well-log measurements (dm scale) (Fig. 5-7D). Consequently, the interpretation of sonic log velocity measurements and other well-log derived parameters such as α_P must integrate such heterogeneities and associated pore type diversity.

5.4.2 Geophysical Pore Type inversion from well-log data (1D)

The Geophysical Pore Type inversion in 1D consists in computing the α_{P_log} parameter by matching DEM velocity models with well-log-derived velocity. The inversion has been performed on 4 wells (WELL-1, -2, -3 and -4) (Fig. 8). For the computations, the limestones of Yadana has been considered to be exclusively calcitic. Such an assumption is based on the following facts: 1) dolomite has been found in thin and scattered intervals in cores where dolomite volume fraction typically ranges from 5 to 15 % (Teillet et al. 2019a); 2) the gamma ray (GR) logs of the four selected wells are very low typically ranging from 10 to 20 API with rare peaks at 40 API, which suggest very low clay content (Fig. 7D); 3) uncertainty analysis of DEM models predicts that substitution of 15% of dolomite or 2% of clay in the host calcitic material led to minor variations in α_P computation (<5%; Teillet et al., 2019a). As a consequence, the low relative proportions of dolomite and clay in the Yadana reservoir are considered to have a negligible impact on α_{P_seis} inversion.

The computed α_{P_log} from 0.03 to 0.30, with an average value of 0.13 and rarely exceeds 0.20 (Fig. 5-8A, B). In α_{P_log}—porosity plots (Fig. 5-8B, 5-9), two groups of limestone with distinct petroacoustic signatures are distinguished according diagenetic

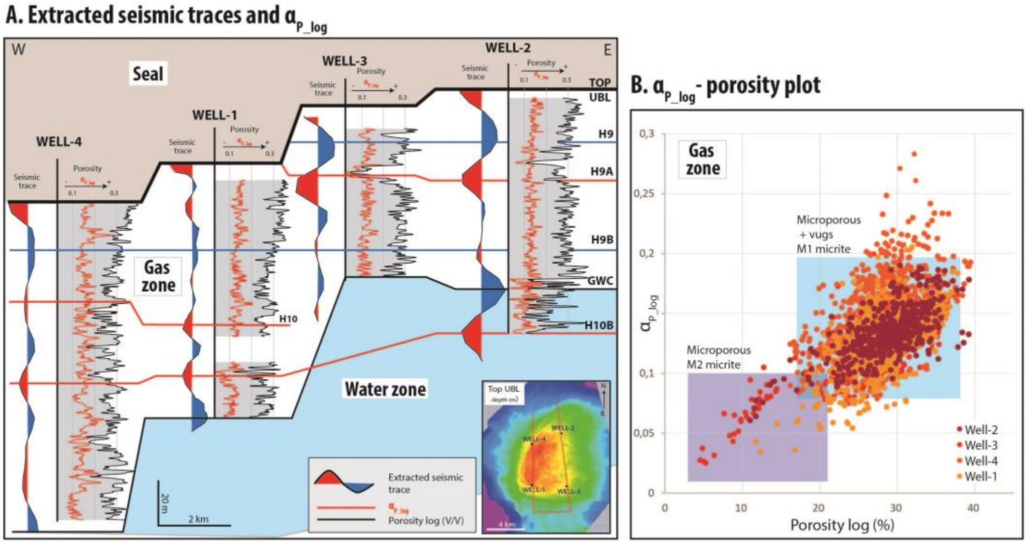

Figure 5-8 : Geophysical Pore Type Inversion of well-log data (a_{P_log}; 1D): (A) Well-correlations based on seismic reflectors (H9A, H9B…), logs of α_{P_log} for the four wells (red) associated to porosity logs and seismic traces extracted at well localization. (B) α_{P_log}–porosity crossplot calculated from well logs of WELL-1, -2, -3 and -4.

facies and relate to distinct proportion of microporosity and differences in terms of macro pore types and microfabrics.

Within the gas interval (Fig. 5-9A), the group 1 corresponds to the highly micro and mesoporous limestone (porosity: 20-40%) characterized by moderately low α_{P_log} ranging from 0.11 to 0.20. This group represents more than 80% of the cored intervals, matches with the reference pore to stiff pore domain of Xu and Payne (2009). Group 1 integrates various diagenetic facies: highly microporous red algal/foraminiferal floatstones (G-DF1), microporous cemented grainstone/rudstone (G-DF2) and microporous coral-rich breccia (G-DF3)(Fig. 9A). All of these carbonate rocks are characterized by (1) less than 10 % of macroporosity (e.g., moldic pores of foraminifera/coral and vugs; Fig. 10B), (2) a high proportion of microporosity reaching 20% to 30% of the total porosity (Fig. 5-7D; blue curve DIA logs) and (3) a loosely packed, anhedral to subrounded calcimicrite microfabric M1 (Fig. 7B, 9B) presenting a unimodal pore throat radius of 1 µm (Fig. 5-7C).

Group 2 samples correspond to low porosity (<20%) limestones characterized by very low α_{P_log} values ranging from 0.03 to 0.11. This group represents less than 20% of the cored intervals and matches with the soft-pore domain of Xu and Payne,

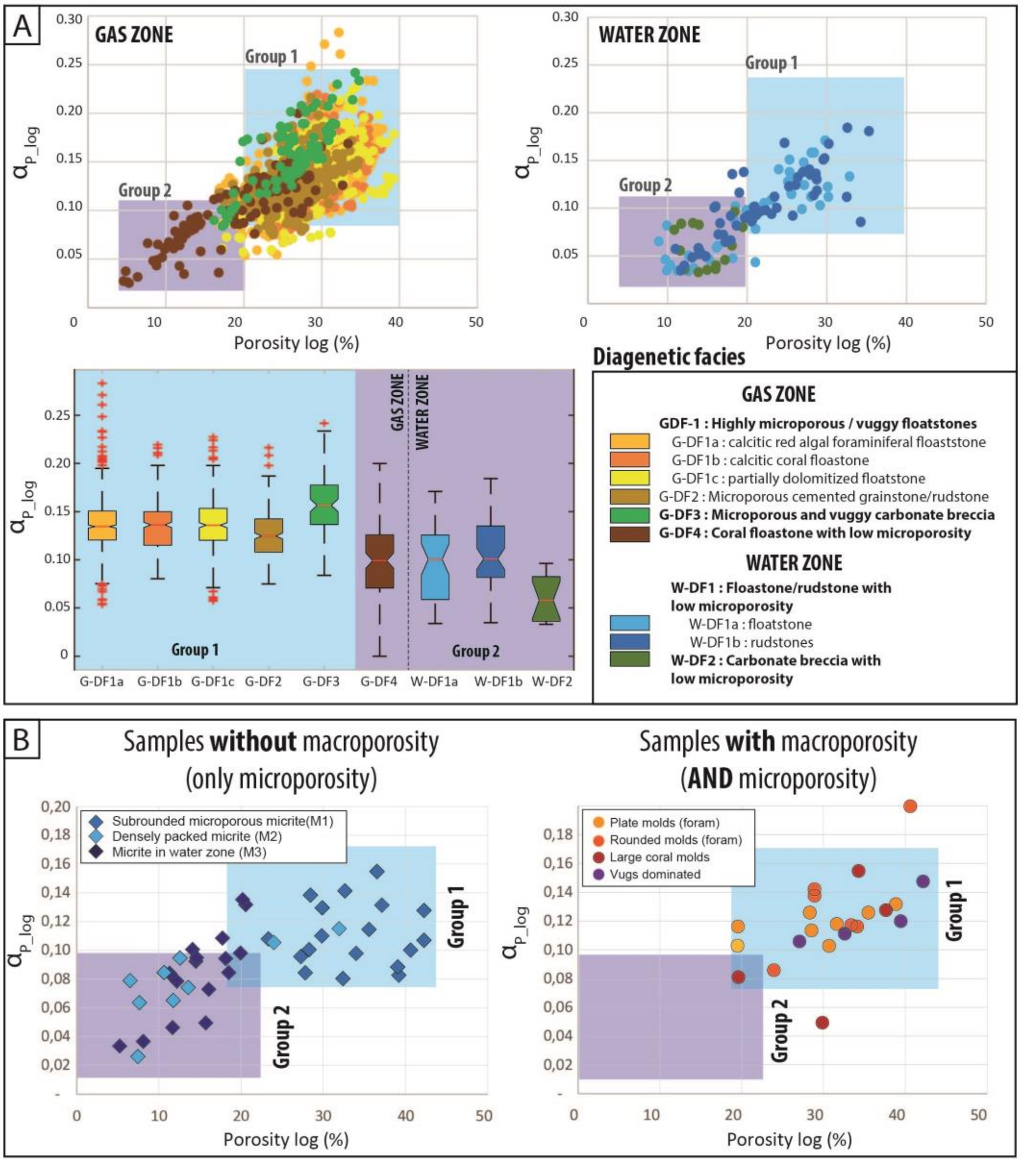

Figure 5-9 : α_{P_log} of Yadana carbonates. (A) Crossplot and box plot of α_{P_log}—calculated from well-log data as function of diagenetic facies. (B) α_{P_log}—calculated from well-log data as function of porosity for limestone without/with macroporosity. Samples are labeled as a function of dominant pore type on thin section.

(2009). Group 2 samples belong, in the gas interval,l to early cemented coral-rich floatstones intervals (G-DF4). Such limestones are characterized by(1) a densely packed micrite microfabric M2, (2) a low proportion of macroporosity (<10%), (3) a low proportion microporosity (<20%; Fig. 5-7D) and a (3) pore throat radius lower than 0.4 µm (Fig. 5-7C). In the water leg, the calibration of α_{P_log} is more difficult because of the limited number of available core data below the gas water contact expected at the base of the WELL-2 (Fig. 5-8A). In this specific interval, high α_{P_log} (>0.15) is very uncommon (Group 1) and the transition with the water zone is associated with a negative shift of α_{P_log} with values rarely exceeding 0.10. These values are consistent to the petroacoustic signature of the Group 2 (Fig. 5-9A) and could refer in terms of diagenetic facies to the low microporous limestones floatstone to rudstone (W-DF1) and/or the cemented carbonate breccia (W-DF2). Both of these diagenetic facies have a low proportion of macroporosity and microporosity and are composed of a dense micrite microfabric (M3; Teillet et al., 2019a).

5.4.3 Geophysical Pore Type inversion from seismic data (3D)

The Geophysical Pore Type inversion from seismic data consists in computing the α_{P_seis} parameter by matching the acoustic impedance calculated from DEM velocity models, geostatistical porosity and fluid saturation models, with the poststack inverted acoustic impedance cube (Fig. 5-10A, B).

As for the well-log inversion, the reservoir has been considered to be exclusively calcitic. The quantitative match between upscaled logs of porosity and the acoustic impedance computed from a moving average (Tiwary et al. 2009) and seismic inversion data at well location shows a relatively good agreement (Fig. 5-10C).The inversion is applied on four selected seismic profiles through the Yadana reservoir (Fig. 5-10D, 5-11). Within the gas zone, at well locations a good match is obtained between the major trends of the upscaled α_{P_log} and the α_{P_seis} (Fig. 5-11C and 5-11D). However, a moderate shift, averaging 0.02 is evidenced between α_{P_log} and α_{P_seis} modal values (0.13 and 0.11 respectively).

Above the GWC, the spatial variations of α_{P_seis} of the four inverted profiles appears globally homogeneous and show relatively low variations of α_{P_seis} outside the range of 0.05 to 0.15 (dark blue to light green color on Fig. 5-10D, 5-11A, 5-11B). These low

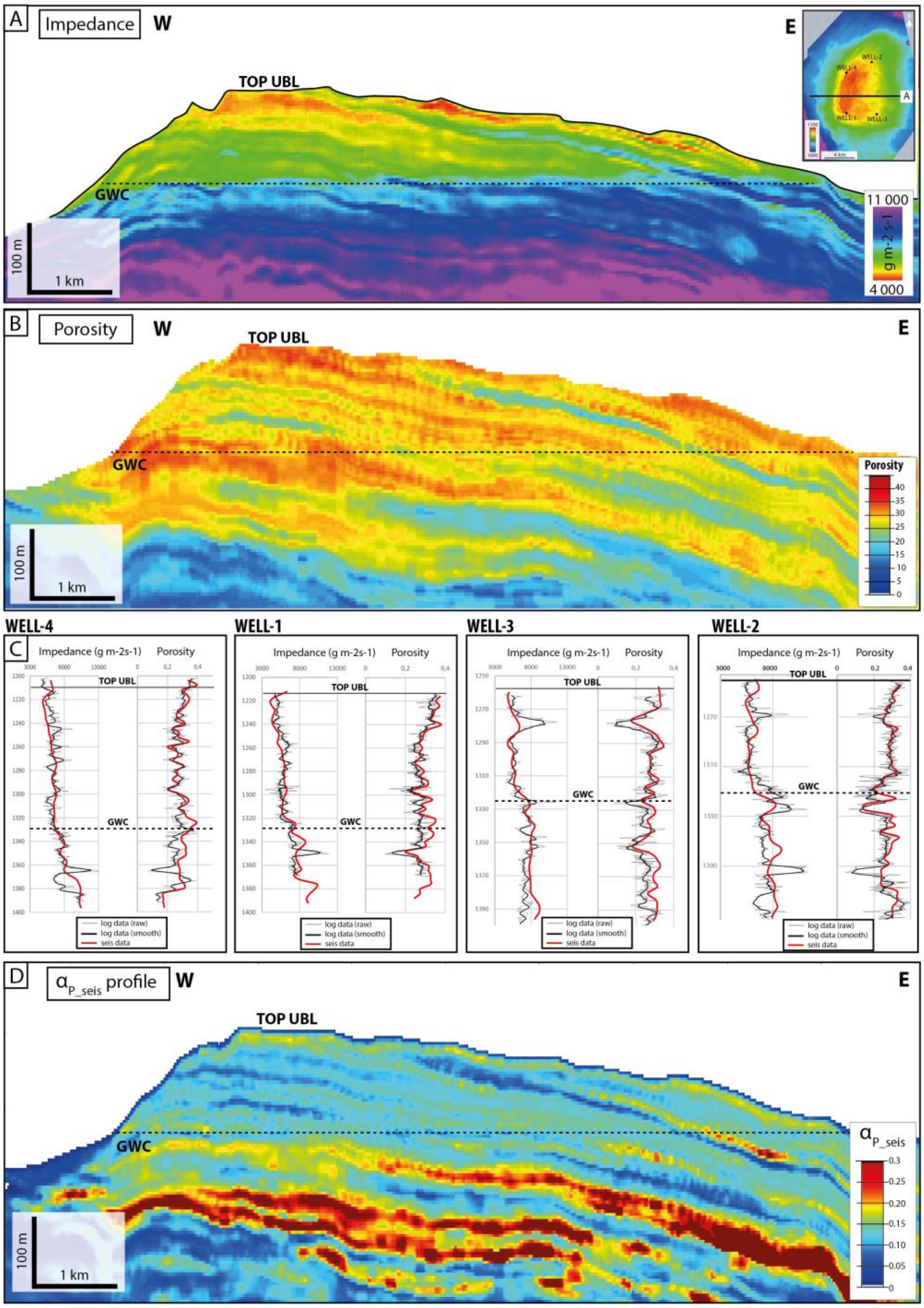

Figure 5-10 : Geophysical Pore Type Inversion of 3D seismic data: (A) section of inverted acoustic impedance coming from poststack seismic data (input). (B) Section of estimated porosity from static reservoir model (input). (C) QA of seismic data: simple averaging well logs of porosity and impedance of the four wells (black lines) are compared to porosity and impedance from seismic data at well localization (red lines). (D) Section of Geophysical Pore Type (a_{P_seis}).

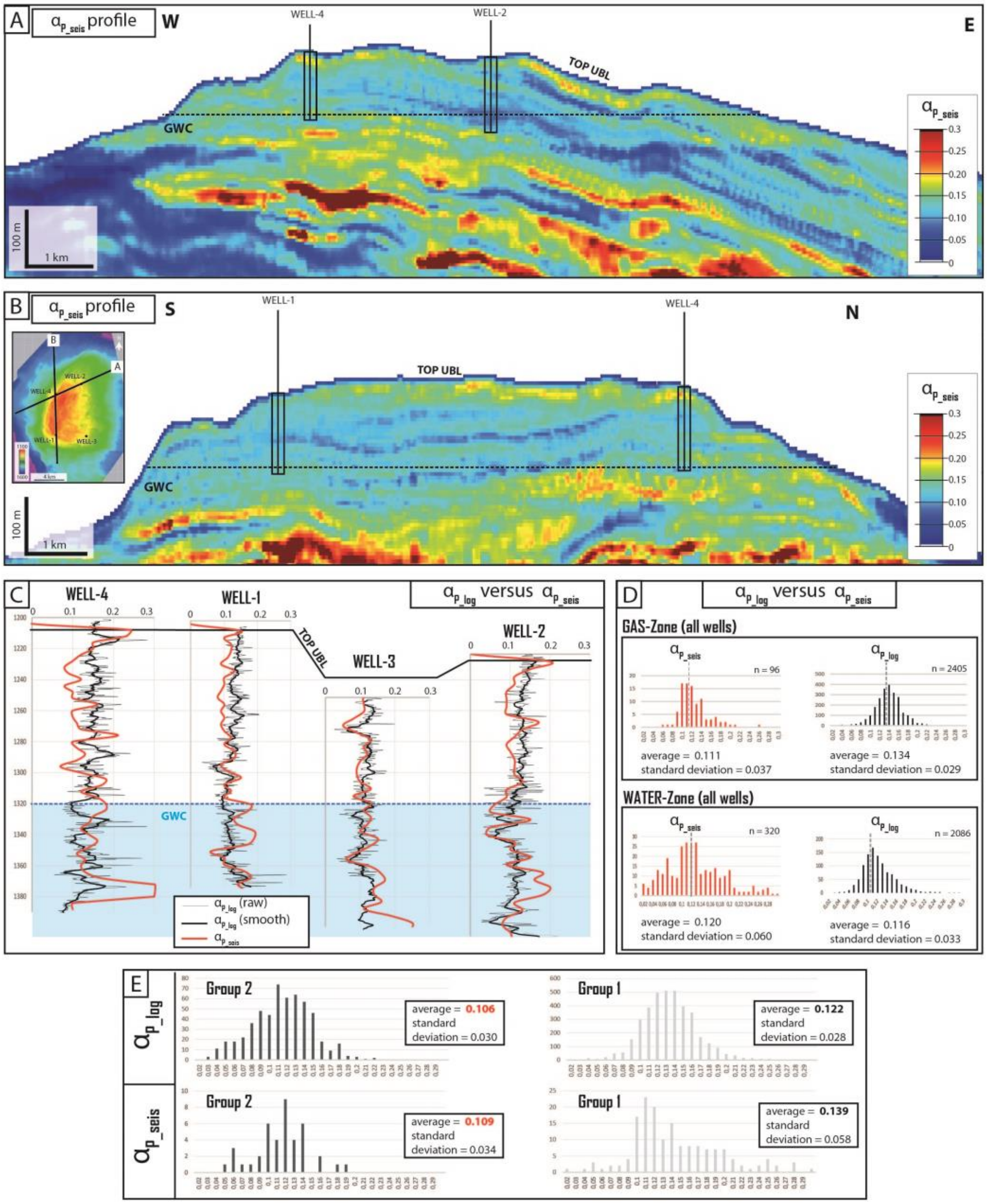

Figure 5-11 : Geophysical Pore Type Inversion of 3D seismic data: (A) E/W and (B) N/S sections of geophysical pore type (α_{P_seis}) from seismic data crossing wells. (C) Quality analysis of the inversion results: α_{P_log} (black lines) in comparison to a_{P_seis} at well localization (red lines). (D) Histograms of α_{P_seis} and α_{P_log} for the four wells in water and gas zone and as function of petroacoustic groups.

lateral variations of α_{P_seis} are consistent with the variations of α_{P_logs} computed from well logs. Few laterally extended (> 1km) heterogeneities have been detected within the reservoirs and refers to thin (<20 m) stratiform and laterally continuous intervals with low α_{P_seis} values ranging from 0.05 to 0.10 (dark blue color on Figs 5-10D, 5-11A).

In contrast, in the water zone (=below the GWC), significant discrepancies between α_{P_log} and α_{P_seis} curves occurred. For example, continuous and relatively thick (up to 50 m) intervals with very high α_{P_seis} values have been identified (α_{P_seis} up to 0.3, red color area on Fig. 5-10). Some of these intervals display a lateral decrease in α_{P_seis} across the gas-water contact (Fig. 5-11D, 5-11E).

5.5 Discussion

5.5.1 Diagenetic significance of α_P

The comparison between diagenetic zonation identified from cores coupled to the α_{P_log} variations makes it possible to assess the diagenetic and the pore type control on the geophysical pore type inversion. The range of α_{P_log} and porosity values for samples with macroporosity (Fig. 5-9B) largely overlaps that of pure microporous samples. Since the proportion of microporosity is always dominant in the limestones of Yadana (in average 75% of the whole pore volume), it is likely that the acoustic properties of macroporous limestones are largely controlled by the microporous host and therefore by micrite microfabrics. Such a control by micrite microfabric on acoustic properties is demonstrated by the α_{P_log} distribution for the distinct diagenetic facies (Fig. 5-9C). Diagenetic facies with the highest modal value of α_{P_log} (0.13-0.16) are characterized by loosely packed M1 micrite microfabric (G-DF1, G-DF2 and G-DF3), whereas coral floatstones and breccias (G-DF4) with dominant densely packed M2 micrite or carbonates from the water leg with M3 microfabrics (W-DF1, W-DF2) display significantly lower α_{P_log} modal values (0.06-0.10). The apparent paradox of the stiff nature of pore networks in loosely packed micrites has been interpreted to result from the occurrence of micro-vugs -(Fig. 5-7) in such microfabrics and from the coalescence of micrite particles at their contact (Fournier et al., 2018). Such an acoustic behavior is common in highly microporous carbonates (Fournier et al., 2014, 2011; Hairabian et al., 2014). In Yadana microporous carbonates, high geophysical pore type is also likely related to the common occurrence of moldic and vuggy pores which are commonly considered as stiff pores (e.g Anselmetti & Eberli 1999; Eberli *et al.* 2003; Brigaud *et al.* 2010; Fournier *et al.* 2014)

Within the gas zone, upscaled log-derived α_{P_log} and seismic-derived α_{P_seis} display similar vertical variations (Fig. 5-11C) as well as comparable distribution and modal values (Fig. 5-11D). However, in the water leg, the discrepancies that occur in some intervals between α_{P_log} and α_{P_seis} are likely to be related to an overestimation of porosity in the reservoir model used for α_{P_seis} computations. Indeed, the shift between the well-log porosity and the porosity derived from the reservoir model may reach 10% in some intervals (Fig. 5-10C). Additionally, a ~~wrong~~ poor estimation of the mineralogical content, particularly in un-cored intervals, may also lead to a ~~poor~~ very uncertain inversion of the geophysical pore type from seismic. For example, if the dolomite content is higher than 15%, α_{P_seis} will be significantly overestimated (>10% error), since computations are based on the assumption of a 100% calcite composition.

Finally, the geophysical pore type inversion from seismic appears to be a reliable tool for detecting diagenetic heterogeneities within the gas zone (i.e., the cored intervals), which represents a volume of the carbonate buildup where mineralogical composition is well-known (pure calcite to low-dolomite content), and where spatial variations of porosity are well constrained.

5.5.2 Spatial distribution of major diagenetic heterogeneities using (α_P)

According to reconstructions of the diagenetic evolution of the Yadana reservoir (Teillet et al.,2019): 1) the densely packed micrite formed very early during early marine eogenesis; 2) microporosity largely developed in shallow-burial marine environments and has been preserved or possibly enhanced after gas emplacements and 3) moldic and vuggy pores mainly formed during and/or after gas emplacements. In addition, five coral-rich intervals, which are correlatable at the reservoir scale, have been identified within the Yadana gas zone (Fig. 5-4; Teillet et al., 2019).

Based on the geophysical pore type inversion of the 3D seismic data, five distinct main reservoir-scale diagenetic heterogeneities with low α_{P_seis} values have been detected in the gas zone (<0.10; Group 2; dark blue area on Fig. 5-12B). Such lateral kilometer-scale heterogeneities range from 5 to 20 meters in thickness and correspond to coral-rich intervals (floatstone and brecciated) with low proportion of micro--porosity and a densely packed

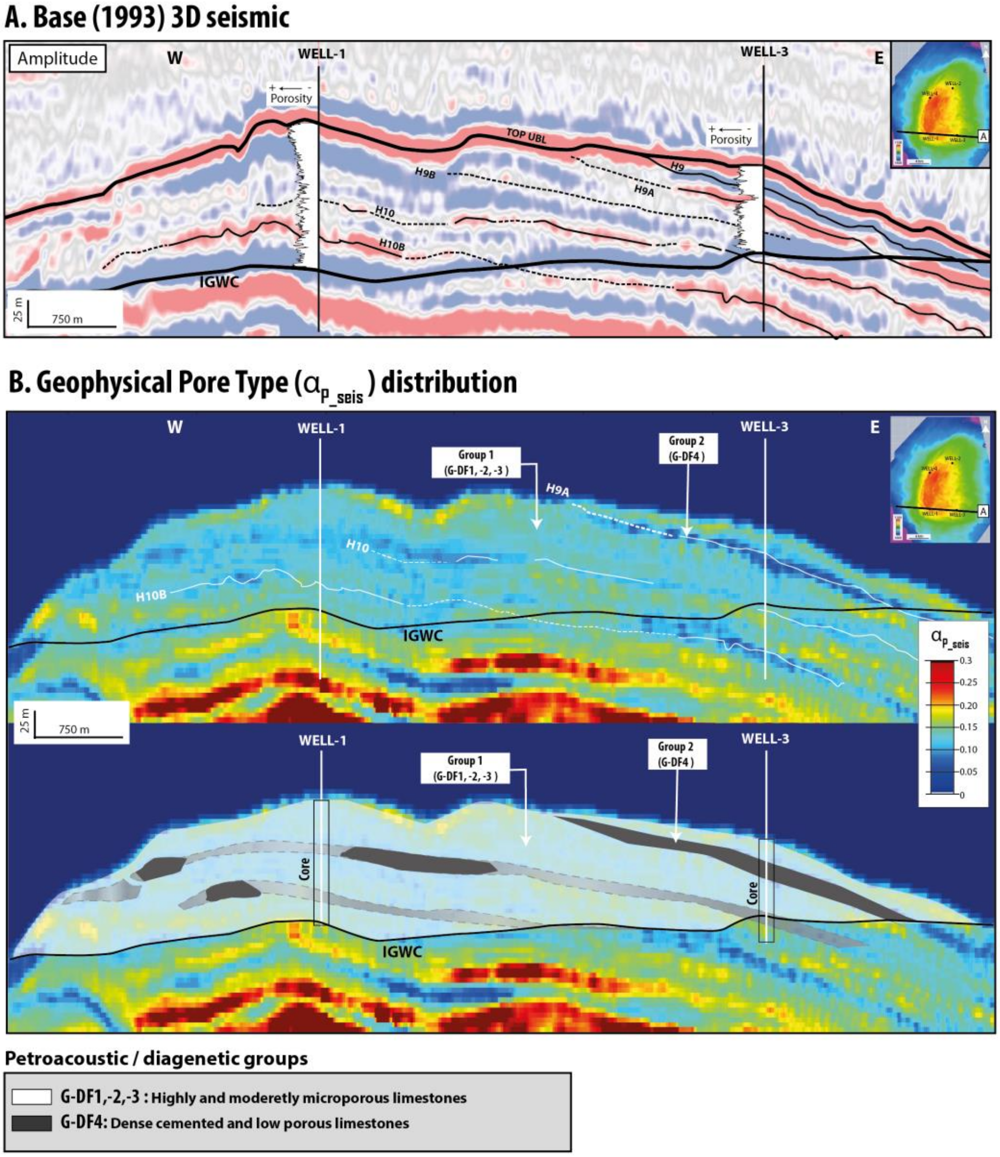

Figure 5-12 : Interpretation of Geophysical Pore Type (α_{P_seis}) distribution from seismic data (A) Section of stacked seismic data crossing WELL-1 and WELL-3. (B) α_{P_seis} distribution from the same section of seismic data than illustrating the main seismic heterogeneities relative to the spatial variation of Geophysical Pore type (α_{P_seis})

matrix micrite microfabrics. These heterogeneities are embedded within vuggy and highly microporous limestones (Group 1; α_{P_seis}>0.10; clear blue area Fig. 5-12B).

The two uppermost low α_{P_seis} coral-rich units are well identified in the east part of the reservoir along the seismic reflector H9A and corresponds to early cemented layers (G-DF4). However, the diagenetic patterns for the three lower coral-rich intervals in the west part of the platform may change laterally and vertically (Teillet et al.2019 b) as a function of their subsequent diagenetic evolution. They have shown to display in cores G-DF1b (later development and preservation of microporosity and moldic/vuggy porosity during burial), G-DF3 (meteoric overprint) or G-DF4 diagenetic facies (early-lithified intervals) (Fig. 5-4). Lateral changes in geophysical pore type in the west part of the reservoir (Fig.12B) are therefore likely to reflect such lateral changes in diagenetic facies. For example, a lateral change from low (<0.10) to higher a_{P_seis} values (0.10-0.20) is interpreted to represent a lateral change from a G-DF4 to a G-DF1b or G-DF3 diagenetic facies, within a coral-rich interval (Fig. 5-12).

In the case of the Yadana gas reservoir, the geophysical pore type inversion is able to detect the major heterogeneities such as the dense coral-floatstone beds early formed. As mentioned by Teillet et al. 2019, theses specific intervals may have a significant impact on flow during gas production. The detected heterogeneities are below the vertical resolution of seismic (around 20 meters in the gas reservoir with a frequency of the 3D seismic data of 45 hertz), since down to 5 meter-thick G-DF4 units have been detected by the inversion method. Below this limit (5 meters ~ $\lambda/12$, λ being the wave length of the seismic signal), diagenetic heterogeneities are unable to be detected, such as the uppermost dense coral body (Fig. 5-4; top of the WELL-3) which is too thin (3 meters) to be properly captured by impedance inversion and as a consequence by geophysical pore type inversion.

5.5.3 Uncertainty analysis for quantification of α_P

Various factors may be sources of uncertainties for α_P inversion: the quality of the seismic and acoustic well-logs data, the quality of the porosity model and the validity of the assumptions regarding mineralogy and fluid content. Sensitivity tests on inversion results are presented in Fig. 5-13 and relates uncertainties on selected parameters such as porosity, water saturation mineralogy and P-wave velocity.

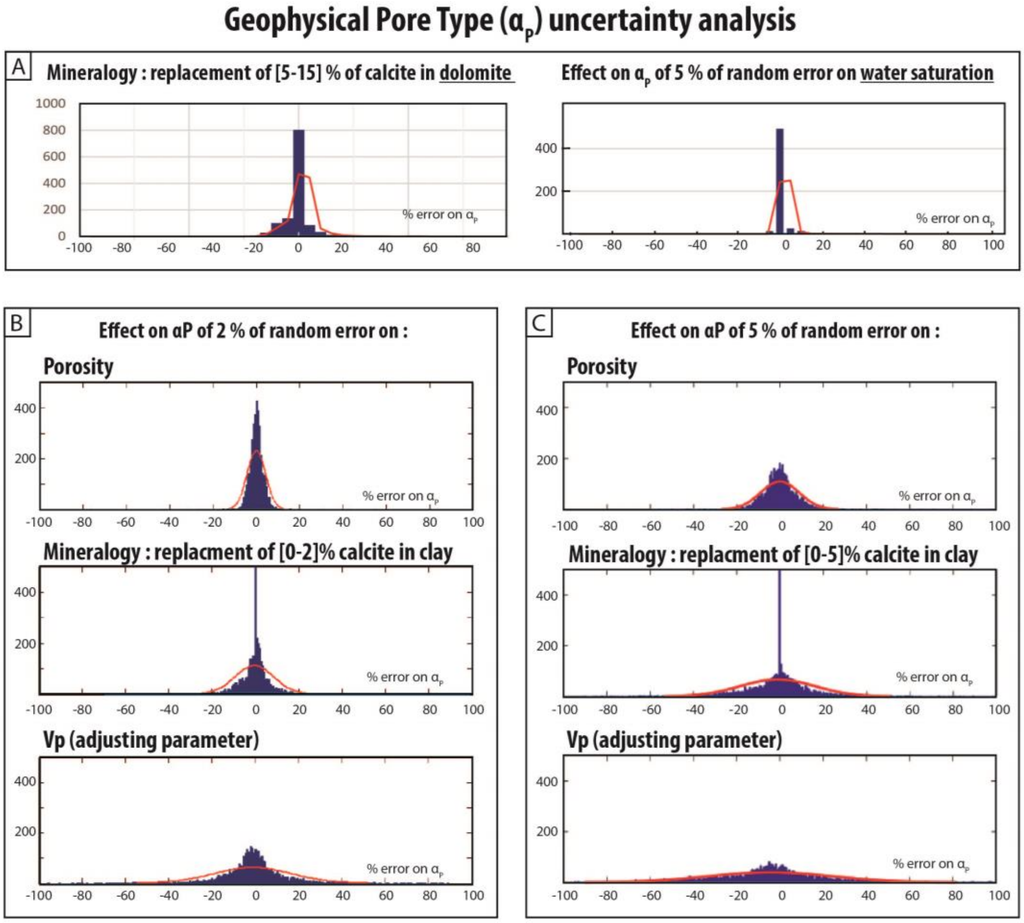

Figure 5-13 : α_{P_log} error distribution if inputs porosity, velocity and mineralogy have 2%, 5% or 15% of random error.

Globally, the Fig. 5-13B shows that a variation of 2% of porosity or P-wave velocity as well as the introduction of 2% to 5% of clay led to an error lower than 8% on the α_P computation (with a 95% confidence level). At well-log scale, porosity estimation (neutron porosity) is usually consistent with plug porosity, the difference being typically lower than 5%. Regarding the mineralogical composition of the rock, as shown previously for dolomite, an introduction/error of 2% and 5% of clay content modifies respectively the value of α_P from 10% to 20% (Fig. 5-13A, B). Nevertheless, the XRD measurements provided by Teillet et al. 2019a, as well as a grain density of 2.708 g.cm^3 (n=39; Table 9) and the very low values of gamma ray logs (10-20 API, Fig. 5-7) clearly indicate that clay content is likely to be always very low within the reservoir of Yadana and suggest that the assumption of a purely calcitic mineralogy is largely valid. Concerning water saturation

(Fig. 5-13D), the inversion results appeared to be very little influenced by water saturation variations and an error of 5% of water saturation has almost no impact on the calculation of α_P.

At the seismic scale, uncertainties are more significant. While similar trends are observed between the inverted seismic impedance and the well logs derived impedance in the gas zone, in the water zone the inverted seismic impedance is commonly overestimated. Unfortunately, without core constraints, it is impossible to interpret such major differences. The quality of the porosity models which are used as inputs for the α_P inversion is likely a major cause of uncertainty. Indeed, in the Fig 5-13, it can be seen that differences in porosity greater than 10% can exist between the porosity of logs and the reservoir model and could have a significant impact on the prediction of the seismic geophysical pore type.

~~5.6~~ Finally, to avoid the use of static and deterministic reservoir models as inputs for the geophysical pore type inversion, keys forward for future work in the case study of Yadana and more generally in the quantitative exploration of carbonate reservoirs should be the use of neural networks (Gharechelou et al., 2015; Zhao et al., 2013), stratigraphic forward models (Lanteaume et al., 2016) or 4D seismic attributes as inputs to improve the porosity prediction and consequently the rock physics based inversions.

~~5.7~~5.6 Conclusion

The present work shows the potentiality of the Geophysical pore type inversion approach to detect laterally extended (100-1000 meters) and sub-seismic to seismic scale (>5 meters thickness) geological heterogeneities. Geophysical pore type α_P may be computed from a 3D seismic impedance cube and a porosity model (static reservoir model), or from a selection of well logs (density, P-wave sonic and porosity). Major results are listed below:

1) Based on a detailed petrographic analysis of cores and thin sections, we establish a correspondence between the geophysical pore type parameter (α_P) derived from a rock physics inversion scheme and the depositional, diagenetic fabrics and pore type associations from the carbonates reservoirs rock of Yadana.
2) Major vertical trends and distributions of well-log-derived α_{P_log} have been shown to be comparable with those of seismic-derived α_{P_seis}, thus showing that the depositional / diagenetic information carried by the geophysical aspect ratio at core/well-log scale (0.10 meter) is preserved at sub-seismic to seismic scale (5-20 meters).

3) The inversion of the geophysical pore type from the Yadana 3D seismic data allowed two main associations of diagenetic geobodies to be discriminated in the reservoir: 1) coral floatstone /breccia units with low microporosity matrix formed by densely-packed micrite, and 2) highly microporous, vuggy floatstones and grainstones/rudstones.
4) The distinct range of geophysical aspect ratio (α_P) between these two diagenetic facies associations is interpreted to result from distinct pore geometries and solid network between a densely packed (α_P <0.10) and a loosely packed micrite microfabric (α_P>0.10).

Finally, one major limitation of the geophysical pore type inversion in Yadana carbonate reservoir appears to be the use, as inputs, of spatial porosity distribution coming from static reservoir models. Further use of neural networks, stratigraphic forward models or 4D seismic attributes is recommended for reducing uncertainties in geophysical aspect ratio inversion.

~~5.8~~5.7 Appendix

The differential effective medium theory models the effective elastic moduli of two-phase composites by adding infinitesimal quantities of inclusions to the host phase (Clearly et al. 1980, Norris 1985, Zimmerman, 1991, Berryman, 1991). In this theory, the effective bulk and shear moduli of the composite K*(y) and µ*(y) respectively, are governed by a coupled system of ordinary differential equations (Mavko et al., 2008):

$$(1-y)\frac{d}{dy}[K^*(y)] = P\ (K2-K^*)(y)$$

$$(1-y)\frac{d}{dy}[\mu^*(y)] = P\ (\mu2 - \mu^*)(y)$$

With initial conditions $K^*(0) = K1 = 71$ GPa and $\mu^*(0) = \mu1 = 30$ GPa, and

K1, µ1	bulk and shear moduli of the initial host material (pure calcite), respectively
K2, µ2	bulk and shear moduli of the inclusion (pure calcite), respectively
y	concentration of the inclusions

The coefficients P and Q depend upon the shape of the inclusion and upon the elastic moduli of the host and inclusion phases. For spherical inclusions P and Q are given by (Berryman, 1995).

$$P = \frac{Kc + \frac{4}{3}\mu c}{Km + \frac{4}{3}\mu c}$$

$$Q = \frac{Kc + \xi c}{Km + \xi c}$$

with (5) $\xi c = \left(\frac{\mu c}{6}\right)\left(\frac{9Kc+8\mu c}{Kc+2\mu c}\right)$

VI. Conclusion

6.1 Conclusions

This thesis implements geological and geophysical approaches to characterize the gas reservoir of Yadana (Early Miocene, offshore Myanmar). The work is based on the analysis and interpretation of a comprehensive subsurface data set (seismic, wells, and core data), and integrates contrasting scales of study, from the thin section to the seismic. From a scientific perspective, this multidisciplinary study has improved the general understanding of carbonate systems of South East Asia by highlighted the paleoenvironmental conditions in the Andaman Sea during the early Miocene. Secondly, this work allowed the reconstruction of the diagenetic history of a Cenozoic isolated carbonate buildup.From an industrial perspective, we demonstrate that a good geological knowledge of carbonate sedimentology is crucial for any stage of a reservoir study (e.g., exploration, reservoir characterization, and production monitoring) to characterize heterogeneities both at micro and macro scales. One advantage of this study is to provide a consistent interpretation of the large amount quantitative data (well-log and seismic data), based on naturalistic approaches coupled with rock physics. We also demonstrate that the integration of seismic data can help to develop geological hypothesis by limiting *a-priori* statements and giving crucial information for well correlation and constraining high resolution property heterogeneities. Finally, this multidisciplinary and integrated work appears essential when faced with the growing quantity of data on mature fields and aim to avoid trouble when making decisions. The conclusions specific to the different parts of the thesis are detailed below.

The Yadana buildup: an incipiently drowned, oligo-mesophotic platform controlled by monsoonal activity and internal waves.

The layer-cake architecture inferred from seismic and well correlations, together with the low lateral changes in lithofacies, suggest deposition on top of a flat-topped and open platform throughout the early Miocene period. Depending on the paleoenvironmental context, three types of carbonate factories operated at the top of the platform: (1) a scleractinian carbonate factory developed under mesophotic conditions during periods of high particulate nutrient supplies; (2) an echinodermal carbonate factory occupied the dysphotic to aphotic area of the shelf, coeval with the scleractinian carbonate factory; and (3) large benthic foraminiferal-coralline algal carbonate factories prevailed under oligo-mesophotic and oligo-mesotrophic conditions.

The three fundamental parameters controlling carbonate production on the Yadana platform were: (1) turbidity, (2) nutrient supplies, and (3) water energy. The dominantly low-energy setting of the oligo-mesophotic deposits suggests that deposition occurred below the fair-weather wave base. Changes from mesophotic to dysphotic-aphotic carbonate factories on the Yadana platform top over time may be related either to changes in water depth or water transparency. The usual fragmentation of branching rhodoliths, and the recurrent occurrence of brecciated intervals within early cemented coral-echinodermal lithofacies, are indicative of frequent and episodic high energy events such as storms, internal waves, and/or cyclones. Changes in monsoonal intensity and terrestrial runoff from the Irrawaddy River are thought to have largely controlled the paleoceanographic history of the Andaman Sea during the early Miocene. Such events were likely responsible for changes in water turbidity and nutrient supplies, as well as for the episodic occurrence of upwelling currents. Internal waves may also be regarded as a potential factor controlling both hydro-dynamism and nutrient supplies. Such paleoceanographic conditions, characterized by variable trophic regimes, promoted the development of an incipiently drowned platform in oligo-mesophotic settings, during the entire early Miocene period.

Diagenetic history and the porosity evolution: early lithification vs. late burial dissolution (gas zone) and cementation (water zone).

The high (28%) average porosity is dominantly related to the significant development of microporosity in the micritized grains and matrix, as well as moldic and vuggy porosity. Microporosity development and the formation of loosely packed, subrounded micrites were likely to have mainly occurred in marine to marine-shallow burial environments, although the hypothesis of a later phase of micrite corrosion cannot be ruled out. Mud supported, coral-rich sediments have undergone significant early marine dissolution of aragonite grains and lithification of the micrite matrix, thus leading to the development of dense layers. Only one potential subaerial exposure surface correlatable with wells were evidenced, and with the exception of this thin (<10 m) interval, the Upper Burman carbonates no show petrographic or geochemical evidence of meteoric overprint.

The stable isotope and petrographic data suggest that the long-term depositional hiatus at the top of the platform (Middle to Late Miocene: ~10 Myr) was related to the platform drowning and non-deposition in a deep marine setting. Partial dolomitization, which affected preferentially the top and flanks of the platform, likely occurred during such a depositional hiatus, in the deep marine environment.

Lastly, the major decrease in porosity (up to 10%) below the gas-water contact resulted from a major phase of porosity evolution during and/or after the gas emplacement. Such a porosity shift is mainly related to 1) increased moldic and vuggy porosity development within the gas zone, 2) microporosity preservation or enhancement in loosely packed, subrounded micrites (M1) within the gas zone, and 3) microporosity reduction by calcite micro-overgrowth within the water zone leading to the development of densely packed, euhedral micrites (M3). The present findings provide identification of diagenetic heterogeneities and therefore new insights into the porosity evolution in Cenozoic carbonate reservoirs from South-East Asian.

Depositional timelines vs. stratigraphy-cross-cutting seismic reflectors.

By modifying drastically porosity and pore networks, the diagenesis largely controls the acoustic architecture and the seismic expression of the reservoir. Porosity is the main controlling factor, the limited proportion of dolomite has a low impact on the elastic properties, and the second order controlling factors are pore types and fluids.

In terms of geological control, acoustic properties are determined by the reservoir zonation into meter to decameter-thick intervals of diagenetic facies. The low impedance limestone units, which represent more than 80% of the gas reservoir interval, appears to be highly microporous, with vuggy pores of foraminifera and coralline algal (=highly microporous background). The total porosity of these limestones had been significantly enhanced in the burial environment, either during or after the gas emplacement. The relatively infrequent, high to moderate impedance units representing only 20% of the reservoir intervals may correspond to 1) thin (<10 m) low porous, laterally continuous intervals of coral floatstones whose matrix was partly cemented during early marine diagenesis, 2) foraminiferal rudstone geobodies of variable thickness (<1 m to>10 m) whose intergranular space was occluded by sparry calcite cements formed in shallow burial environments, and 3) relatively thick (up to 20 m) and laterally continuous coral breccia intervals, whose aragonite was calcified during an intra-formational stage of subaerial exposure. At the seismic scale, the well-to seismic tie suggests that reflectors may form at the boundary between two diagenetic units, or may result from the interference between reflection at the base and top of such intervals. Even though they are essentially diagenetic in origin, most of the main seismic reflectors appear to roughly conform to the depositional architecture. However, a stratigraphy-cross-cutting reflector has been formed at a diagenetic boundary. This reflector coincides with the pre-production (i.e., initial) gas-water contact (IGWC) and remains at the same location after gas production and the rising gas-water contact.

Finally, the combined analysis of the water rises from the monitor seismic data (4D) and the diagenetic significance of seismic reflectors help to the prediction and the mapping of the major heterogeneities which matter for flow during production. By using such an approach, two types of horizontal baffles for flow have been identified throughout the Yadana reservoir: (1) the brecciated and moderately porous units which are related to intra-formational subaerial exposure, and (2) the early lithified and low porous coral-rich intervals.

Geophysical pore type inversion: how far can we go into the quantitative and qualitative interpretation of the 3D seismic data?

Pore types being a major controlling factor for elastic properties and permeability in carbonates, so we have developed a petrophysical inversion method based on pore types. The $_P$ parameter is a proxy resulting from DEM rock physics model (DEM: Differential Effective Medium).

In the carbonate reservoir of Yadana, the α_P parameter (i.e., the geophysical pore type) can effectively quantify the pore type effect on the elastic property. The geophysical pore type inversion resulting from well-log data is calibrated to actual pore types based on core, thin sections, digital image analysis (DIA), and pore throat radius measurements. Based on the predicted spatial distribution of the geophysical pore type (α_P) we identified the likely diagenetic processes and interpreted the possible implications for reservoir characterization. The most represented limestones is the high microporous intervals, which present moderate α_P values. Within the microporous background, low α_P heterogeneities consist of plurimetric, early lithified coral floatstone layers, characterized by low proportion of macroporosity and by a matrix made of a densely packed micrite.

In conclusion, the present geophysical pore type inversion, which integrates both geological and geophysical data sets should be an approach applicable to other carbonate reservoirs which are purely calcitic or with well-constrained mineralogy. The integration of petrographic, sedimentological, and diagenetic inputs appears to be the key for the identification and spatial characterization of the relevant heterogeneities which impact the flow during production. This integration also improves the use of quantitative seismic approaches in reservoir studies, both at the stages of exploration, evaluation and production.

6.2 Perspectives

Testing stratigraphic hypotheses through forward stratigraphic modeling would make it possible to quantify the impact of controlling factors such as nutrients, hydrodynamics, and tectonics on the development of the carbonate platform. Regarding diagenetic and pore type characterization additional analysis from the water zone (on cutting material?) would allow interpreting some intervals with high geophysical pore type. The use of nano-CT-scan imaging would have allowed a detailed quantification of microporosity within the reservoir. This would have led to better quantify the loss of porosity by calcite micro-overgrowth developments in the water leg. There is also widespread uncertainty associated with the geophysical pore-type inversion from seismic data that depends on many factors: the quality of seismic data, number of wells, acoustic impedance cubes, porosity volumes, mineralogy content, and fluid content. Therefore, it would be interesting to calculate statistics on multi-realization inversion models and finally, new inputs for the inversion could include as 4D seismic attributes. Additionally the Geophysical Pore Type inversion method could be significantly improved by the use of neural network methodology where the actual database will provide network training would clearly improve the geophysical pore type inversion and would avoid the use of a deterministic porosity model as input of the inversion.

Finally, this work allowed to establish methodological tracks for the future development of a still nascent discipline: seismic diagenesis. The perspectives of such a discipline are immense, not only for the 3D characterization of the large-scale heterogeneities in carbonate reservoirs, but also, more fundamentally for the understanding of the diagenetic processes themselves. The latter requires the quantification of the volumes of dissolved, precipitated or neomorphosed carbonate at the scale of a reservoir which is surely a future challenge for seismic diagenesis.

Mais sitôt que j'eus achevé tout ce cours d'études, au bout duquel on a coutume d'être reçu au rang de doctes, je changeai entièrement d'opinion. Car je me trouvais embarrassé de tant de doutes et d'erreurs, qu'il me semblait n'avoir fait autre profit, en tâchant de m'instruire, sinon que j'avais découvert de plus en plus mon ignorance.

— René Descartes — Discours de la méthode — 1637

But as soon as I had finished my course of study, at which time it is usual to be admitted to the ranks of the well educated, I completely changed my opinion, for I found myself bogged down in so many doubts and errors, that it seemed to me that having set out to become learned, I had derived no benefit from my studies, other than that of progressively revealing to myself how ignorant I was.

— René Descartes — A discourse on the Method - 1637

VII. References

A. Racey, M.F.R., 2015. Chapter 4 Onshore petroleum geology of Myanmar : Central Burma Depression. Geol. Soc. London, Mem. 21–50. https://doi.org/10.1144/M45.04

Adams, C.G., 1965. The Foraminifera and stratigraphy of the Melinau Limestone, Sarawak, and its importance in Tertiary correlation. Q. J. Geol. Soc. 121, 283–338. https://doi.org/10.1144/gsjgs.121.1.0283

Adey WH, 1979. Crustose coralline algae as microenvironmental indicators in the tertiary. In : Gar J, Boucot (eds) Historiacal biogeographyn plate tectonics and the chnaging environment. Oregon State Univ. Press. Corvallis 459–464.

Akbar, M., Vissprada, B., Ali H. Alghamdi, Allen, D., Herron, M., Carnegie, A., Dutta, D., Olesen, J.-R., Chourasiya, R.D., Logan, D., Stief, D., Netherwood, R., Russell, S.D., Saxena, K., 2000. Carbonate reservoir evaluation has been a high priority for researchers and oil.

Alamaru, A., Loya, Y., Brokovich, E., Yam, R., Shemesh, A., 2009. Carbon and nitrogen utilization in two species of Red Sea corals along a depth gradient: Insights from stable isotope analysis of total organic material and lipids. Geochim. Cosmochim. Acta 73, 5333–5342. https://doi.org/10.1016/j.gca.2009.06.018

Ali, M., 1995. Carbonate cement stratigraphy and timing of diagenesis in a Miocene mixed carbonate-clastic sequence, offshore Sabah, Malaysia: constraints from cathodoluminescence, geochemistry, and isotope studies. Sediment. Geol. 99, 191–214. https://doi.org/10.1016/0037-0738(95)00044-9

Alpers, W., Wang-Chen, H., Hock, L., 1997. Observation of internal waves in the Andaman Sea by ERS SAR. Eur. Sp. Agency, (Special Publ. ESA SP 1287–1291. https://doi.org/10.1109/IGARSS.1997.608926

Anderson Thomas, A.M., 1983. Stable isotopes of oxygen and carbon and their application to sedimentologic and paleoenvironmental problems, in: Stable Isotopes in Sedimentary Geology.

Anselmetti, F.S., Eberli, G.P., 1999. The Velocity-Deviation Log : A Tool to Predict Pore Type and Permeability Trends in Carbonate Drill Holes from Sonic and Porosity or Density Logs 1. AAPG Mem. 3, 450–466. https://doi.org/10.1306/00AA9BCE-1730-

11D7-8645000102C1865D

Anselmetti, F.S., Von Salis, G.A., Cunningham, K.J., Eberli, G.P., 1997. Acoustic properties of Neogene carbonates and siliciclastics from the subsurface of the Florida keys: Implications for seismic reflectivity. Mar. Geol. 144, 9–31. https://doi.org/10.1016/S0025-3227(97)00081-9

Apel, J.R., Holbrook, J.R., Liu, A.K., Tsai, J.J., 1985. The Sulu Sea Internal Soliton Experiment. J. Phys. Oceanogr. https://doi.org/10.1175/1520-0485(1985)015<1625:TSSISE>2.0.CO; 2

Aronson, R.B., 2009. Metaphor, inference, and prediction in paleoecology: climate change and the Antarctic bottom fauna. Paleontol. Soc. Pap. 15, 177–194.

Aronson, R.B., Blake, D.B., Oji, T., 1997. Retrograde community structure in the late Eocene of Antarctica Retrograde community structure in the late Eocene of Antarctica—Geology. Geology 25, 903–906. https://doi.org/10.1130/0091-7613(1997)025<0903

Arosi, H.A., Wilson, M.E.J., 2015. Diagenesis and fracturing of a large-scale, syntectonic carbonate platform. Sediment. Geol. 326, 109–134. https://doi.org/10.1016/j.sedgeo.2015.06.010

Atkinson, M.J., Bilger, R.W., 1992. Effects of water velocity on phosphate uptake in coral reef-flat communities. Limnol. Ocean. 37, 273–279. https://doi.org/10.4319/lo.1992.37.2.0273

Bachtel, S.L., Kissling, R.D., Dunn, P.A., Macdonald, B.A., 2004. Seismic Stratigraphic Evolution of the Miocene—Pliocene Segitig Platform, East Natuna Sea, Indonesia: The Origin, Growth, and Demise of an Isolated Carbonate Platform. AAPG Mem. 309–328.

Baechle, G., Colpaert, a, Eberli, G., Weger, R., 2008. Effects of microporosity on sonic velocity in carbonate rocks. Lead. Edge 27, 1012–1018. https://doi.org/10.1190/1.2967554

Baechle, G.T., Eberli, G.P., 2014. Comparison of rock physics models to predict rock properties in carbonate reservoirs. EAGE/FESM Jt. Reg. Conf. Petrophysics Meets Geosci. From Nano Pores to Mega Struct. 4–8. https://doi.org/10.3997/2214-4609.20132121

Bard, Y., 1974. Nonlinear parameter estimation. https://doi.org/10.1016/S0376-7361(10)05711-0

Bashah, N.S.I., Pierson, B.J., 2012. Quantification of Pore Structure in a Miocene Carbonate Buildup of Central Luconia, Sarawak and Its Relationship to Sonic Velocity. Int. Pet. Technol. Conf.

Bassi, D., 2005. Larger foraminiferal and coralline algal facies in an Upper Eocene storm-influenced, shallow-water carbonate platform (Colli Berici, north-eastern Italy). Palaeogeogr. Palaeoclimatol. Palaeoecol. 226, 17–35. https://doi.org/10.1016/j.palaeo.2005.05.002

Bassi, D., Hottinger, L., Nebelsick, J.H., 2007. Larger foraminifera from the upper Oligocene of the Venetian area, north-east Italy. Palaeontology 50, 845–868. https://doi.org/10.1111/j.1475-4983.2007.00677.x

Bathurst, R.G.. , 1974. Marine diagenesis of shallow water calcium carbonate sediments, in: Annual Revie of Earth And Planetary Sciences. pp. 257–274.

Beavington-Penney, S.J., Nadin, P., Wright, V.P., Clarke, E., McQuilken, J., Bailey, H.W., 2008. Reservoir quality variation on an Eocene carbonate ramp, El Garia Formation, offshore Tunisia: Structural control of burial corrosion and dolomitisation. Sediment. Geol. 209, 42–57. https://doi.org/10.1016/j.sedgeo.2008.06.006

Beavington-Penney, S.J., Racey, A., 2004. Ecology of extant nummulitids and other larger benthic foraminifera: Applications in palaeoenvironmental analysis. Earth-Science Rev. 67, 219–265. https://doi.org/10.1016/j.earscirev.2004.02.005

Behar, F.H., Albrecht, P., 1984. Correlations between carboxylic acids and hydrocarbons in several crude oils. Alteration by biodegradation. Org. Geochem. 6, 597–604. https://doi.org/10.1016/0146-6380(84)90082-2

Berryman, J.G., 1995. Mixture Theories for Rock Properties.

Berryman, J.G., 1992. Single-Scatering approximations for coefficients in Biot's equations of poroelasticity. J. Acoust. Soc. Am.

Betzler, C., Eberli, G.P., Lüdmann, T., Reolid, J., Kroon, D., Reijmer, J.J.G., Swart, P.K., Wright, J., Young, J.R., Alvarez-Zarikian, C., Alonso-García, M., Bialik, O.M., Blättler, C.L., Guo, J.A., Haffen, S., Horozal, S., Inoue, M., Jovane, L., Lanci, L., Laya, J.C., Hui Mee, A.L., Nakakuni, M., Nath, B.N., Niino, K., Petruny, L.M., Pratiwi, S.D., Slagle, A.L., Sloss, C.R., Su, X., Yao, Z., 2018. Refinement of Miocene sea level and monsoon events from the sedimentary archive of the Maldives (Indian Ocean). Prog. Earth Planet. Sci. 5. https://doi.org/10.1186/s40645-018-0165-x

Bjørlykke, K., Mo, A., Palm, E., 1988. Modelling of thermal convection in sedimentary basins and its relevance to diagenetic reactions. Mar. Pet. Geol. 5, 338–351. https://doi.org/10.1016/0264-8172(88)90027-X

Blow, W.., Banner, F.T., 1962. The mid-Tertiary (Upper Eocene to Aquitanian) Globigerinaceae. Cambridge Univ. Press Fundamenta, 61–151.

Bond, C.E., Gibbs, A.D., Shipton, Z.K., Jones, S., 2007. What do you think this is? "Conceptual uncertainty" In geoscience interpretation. GSA Today 17, 4—10. https://doi.org/10.1130/GSAT01711A.1

Borgomano, J., Masse, J.P., Fenerci-Masse, M., Fournier, F., 2013. Petrophysics of lower cretaceous platform carbonate outcrops in provence (SE France): Implications for carbonate reservoir characterization. J. Pet. Geol. 36, 5–41. https://doi.org/10.1111/jpg.12540

Bosence, D.W.J., 1983. Decription and Classification of Rhodoliths (Rhodoids, Rhodolites). Coat. Grains 217—224. https://doi.org/10.1007/978-3-642-68869-0

Bouchette, F., Séguret, M., Moussine-Pouchkine, A., 2001. Coarse carbonate breccias as a result of water-wave cyclic loading (uppermost Jurassic—South-East Basin, France). Sedimentology 48, 767–789. https://doi.org/10.1046/j.1365-3091.2001.00395.x

BouDagher-Fadel, M.K., 2008. Evolution and geological significance of larger benthic foraminifera.

Boudagher-Fadel, M.K., Price, D.G., 2013. The phylogenetic and palaeogeographic evolution of the miogypsinid larger benthic foraminifera. J. Geol. Soc. London. 170, 185–208. https://doi.org/10.1144/jgs2011-149

BouDagher-Fadel, M.K., Wilson, M., 2000. A revision of some larger foraminifera of the Miocene of Southeast Kalimantan. Micropaleontology 46, 153–165.

Bowen, G.J., Wilkinson, B., 2002. Spatial distribution of ▯ 18 O in meteoric precipitation. Geology 30, 315–318. https://doi.org/10.1130/0091-7613(2002)030<0315

Braga, J.C., Aguirre, J., 2004. Coralline algae indicate Pleistocene evolution from deep, open platform to outer barrier reef environments in the northern Great Barrier Reef margin. Coral Reefs 23, 547–558. https://doi.org/10.1007/s00338-004-0414-x

Braga, J.C., Bassi, D., Piller, W., 2010. Palaeoenvironmental significance of Oligocene—Miocene coralline-red algae—a review 165—182. https://doi.org/10.1002/9781118398364.ch10

Brandano, M., Corda, L., 2002. Nutrients, sea level and tectonics: Constrains for the facies architecture of a Miocene carbonate ramp in central Italy. Terra Nov. 14, 257—262. https://doi.org/10.1046/j.1365-3121.2000.00419.x

Brandano, M., Cornacchia, I., Tomassetti, L., 2017. Global versus regional influence on the carbonate factories of Oligo-Miocene carbonate platforms in the Mediterranean area. Mar. Pet. Geol. 87, 188–202. https://doi.org/10.1016/j.marpetgeo.2017.03.001

Brandano, M., Tomassetti, L., Cornacchia, I., 2018. The lower Rupelian cluster reefs of Majella platform, the shallow water record of Eocene to Oligocene transtion. Sediment. Geol. 380. https://doi.org/10.1016/j.sedgeo.2018.11.013

Brie, A., Schlumberger, K.K., Pampuri, F., Marsala, A, F., Meazza, O., 1995. Shear sonic interpretation in gas bearing sands. SPE 30595, 701–710.

Brigaud, B., Vincent, B., Durlet, C., Deconinck, J.-F., Blanc, P., Trouiller, A., 2010. Acoustic Properties of Ancient Shallow-Marine Carbonates: Effects of Depositional Environments and Diagenetic Processes (Middle Jurassic, Paris Basin, France). J. Sediment. Res. 80, 791–807. https://doi.org/10.2110/jsr.2010.071

Budd, D.A., 1997. Cenozoic dolomites of carbonate islands: Their attributes and origin, Earth-Science Reviews. https://doi.org/10.1016/S0012-8252(96)00051-7

Buland, A., Kolbjo/rnsen, O., Hauge, R., Skjæveland, O., Duffaut, K., 2008. Bayesian lithology and fluid prediction from seismic prestack data. Geophysics 73, C13. https://doi.org/10.1190/1.2842150

Burgess, P.M., Winefield, P., Minzoni, M., Winefield, P., International, S., 2013. Methods for identification of isolated carbonate buildups from seismic reflection data. Am. Assoc. Pet. Geol. Bull. 7, 1071—1098. https://doi.org/10.1306/12051212011

Burollet, P.F., Boichard, R., Lambert, B., Villain, J.M., 1986. The Pater Noster Carbonate Platform. Am. Assoc. Pet. Geol. Bull. 1, 155–169.

Buxton, M.W.N., Pedley, H.M., 1989. Short Paper: A standardized model for Tethyan

Tertiary carbonate ramps. J. Geol. Soc. London. 146, 746–748. https://doi.org/10.1144/gsjgs.146.5.0746

Cantrell, D.L., Griffiths, C.M., Hughes, G.W., 2015. New tools and approaches in carbonate reservoir quality prediction : a case history from the Shu ' aiba Formation, Saudi Arabia. Geol. Soc. london 401–424.

Cantrell, D.L., Hagerty, R.M., 1999. Microporosity in Arab Formation Carbonates, Saudi Arabia. GeoArabia 4, 129–154.

Chakraborty, A., Ghosh, A.K., 2016. Ocean upwelling and intense monsoonal activity based on late Miocene diatom assemblages from Neil Island, Andaman and Nicobar Islands, India. Mar. Micropaleontol. 127, 26–41. https://doi.org/10.1016/j.marmicro.2016.07.005

Chakraborty, P.P., Khan, P.K., 2009. Cenozoic geodynamic evolution of the Andaman-Sumatra subduction margin: Current understanding. Isl. Arc 18, 184–200. https://doi.org/10.1111/j.1440-1738.2008.00643.x

Chan, Y.L., Pochon, X., Fisher, M.A., Wagner, D., Concepcion, G.T., Kahng, S.E., Toonen, R.J., Gates, R.D., 2009. Generalist dinoflagellate endosymbionts and host genotype diversity detected from mesophotic (67-100 m depths) coral Leptoseris. BMC Ecol. 9, 1—7. https://doi.org/10.1186/1472-6785-9-21

Chatterjee, A., Shankar, D., McCreary, J.P., Vinayachandran, P.N., Mukherjee, A., 2017. Dynamics of Andaman Sea circulation and its role in connecting the equatorial Indian Ocean to the Bay of Bengal. J. Geophys. Res. Ocean. 122, 3200–3218. https://doi.org/10.1002/2016JC012300

Clift, P.D., Hodges, K. V., Heslop, D., Hannigan, R., Van Long, H., Calves, G., 2008. Correlation of Himalayan exhumation rates and Asian monsoon intensity. Nat. Geosci. 1, 875–880. https://doi.org/10.1038/ngeo351

Clift, P.D., Vanlaningham, S., 2010. A climatic trigger for a major Oligo-Miocene unconformity in the Himalayan foreland basin. Tectonics 29, 1—18. https://doi.org/10.1029/2010TC002711

Coulon, J.— P., Lafet, Y., Deschizeaux, B., Doyen, P.M., Duboz, P., 2006. Stratigraphic elastic inversion for seismic lithology discrimination in a turbiditic reservoir. SEG Annu. Meet. 359–363.

Curray, J.R., 2005. Tectonics and history of the Andaman Sea region. J. Asian Earth Sci. 25, 187–232. https://doi.org/10.1016/j.jseaes.2004.09.001

Davies, R.J., Cartwright J, 2002. A fossilized Opal A to Opal C/T transformation on the northeast Atlantic margin: support for a significantly elevated Palaeogeothermal gradient during the Neogene? Basin Res. 14.

Deville de Periere, M., Durlet, C., Vennin, E., Lambert, L., Bourillot, R., Caline, B., Poli, E., 2011. Morphometry of micrite particles in cretaceous microporous limestones of the middle east: Influence on reservoir properties. Mar. Pet. Geol. 28, 1727–1750. https://doi.org/10.1016/j.marpetgeo.2011.05.002

Dickson, J.A.D., 1966. Carbonate identification and genesis as revealed by staining. J.

Sediment. Petrol. 36, 491–505.

Dickson, J.A.D., Coleman, M.L., 1980. Changes in carbon and oxygen isotope composition during limestone diagenesis. . Sedimentol. 27, 107–118. https://doi.org/10.1111/j.1365-3091.1980.tb01161.x

Dou, Q., Sun, Y., Sullivan, C., 2011. Rock-physics-based carbonate pore type characterization and reservoir permeability heterogeneity evaluation, Upper San Andres reservoir, Permian Basin, west Texas. J. Appl. Geophys. 74, 8–18. https://doi.org/10.1016/j.jappgeo.2011.02.010

Drooger, C.., 1952. Study of American Miogypsinidae. Remarks on cycloclypeus. Proc. Koninklijke Nederla; Amsterdam. University of Utrecht.

Duijndam, A.J.W., 1988. Bayesian estimation in seismic inversion. Part I: principles. Geophys. Prospect. 36, 878–898.

Eberli, G.P., 2002. The chronostratigraphic significance of seismic reflections along the Bahamas Transect. Mar. Geosci. 185, 1–17.

Eberli, G.P., Baechle, G.T., Anselmetti, F.S., Incze, M.L., 2003. Factors controlling elastic properties in carbonate sediments and rocks. Lead. Edge 22, 654–660. https://doi.org/10.1190/1.1599691

Ehrenberg, S.N., Jakobsen, K.G., 2001. Plagioclase dissolution related to biodegradation of oil in Brent Group sandstones (Middle Jurassic) of Gullfaks Field, Northern North Sea. Sedimentology 48, 703–721. https://doi.org/10.1046/j.1365-3091.2001.00387.x

Ehrenberg, S.N., Walderhaug, O., Bjerlykke, K., 2012. Carbonate porosity creation by mesogenetic dissolution: Reality or illusion? Am. Assoc. Pet. Geol. Bull. 96, 217—225. https://doi.org/10.1306/05031110187

Epstein, S., Buchsbaum, R., Lowenstam, H.A., Urey, H.C., 1953. Revised Carbonate-Water Isotopic Temeprature Scale. Geol. Soc. Am. Bull. 64, 1315–1325. https://doi.org/10.1130/0016-7606(1953)64

Epting, M., 1980. Sedimentology of Miocene Carbonate Buildups Central Luconia Offshore Sarawak. Geol. Soc. Malaysia Bull.

Esteban, M., Taberner, C., 2003. Secondary porosity development during late burial in carbonate reservoirs as a result of mixing and/or cooling of brines. J. Geochemical Explor. 78–79, 355–359. https://doi.org/10.1016/S0375-6742(03)00111-0

Feely, R.A., Sabine, C.L., Hernandez-Ayon, J.M., Ianson, D., Hales, B., 2008. Evidence for upwelling of corrosive “acidified” water onto the continental shelf. Science (80—.). 320, 1490—1492. https://doi.org/10.1126/science.1155676

Fournier, F., Borgomano, J., 2009. Critical porosity and elastic properties of microporous mixed carbonate-siliciclastic rocks. Geophysics 74, 93–109.

Fournier, F., Borgomano, J., 2007. Geological significance of seismic reflections and imaging of the reservoir architecture in the Malampaya gas field (Philippines). Am. Assoc. Pet. Geol. Bull. 91, 235–258. https://doi.org/10.1306/10160606043

Fournier, F., Borgomano, J., Montaggioni, L.F., 2005. Development patterns and controlling factors of Tertiary carbonate buildups: Insights from high-resolution 3D seismic and well data in the Malampaya gas field (Offshore Palawan, Philippines). Sediment. Geol. 175, 189—215. https://doi.org/10.1016/j.sedgeo.2005.01.009

Fournier, F., Leonide, P., Biscarrat, K., Gallois, A., Borgomano, J., Foubert, A., 2011. Elastic properties of microporous cemented grainstones. Geophysics 76, E175. https://doi.org/10.1190/geo2011-0047.1

Fournier, F., Léonide, P., Kleipool, L., Toullec, R., Reijmer, J.J.G., Borgomano, J., Klootwijk, T., Van Der Molen, J., 2014. Pore space evolution and elastic properties of platform carbonates (Urgonian limestone, Barremian-Aptian, SE France). Sediment. Geol. 308, 1—17. https://doi.org/10.1016/j.sedgeo.2014.04.008

Fournier, F., Montaggioni, L., Borgomano, J., 2004. Paleoenvironments and high-frequency cyclicity from Cenozoic South-East Asian shallow-water carbonates: A case study from the Oligo-Miocene buildups of Malampaya (Offshore Palawan, Philippines). Mar. Pet. Geol. 21, 1–21. https://doi.org/10.1016/j.marpetgeo.2003.11.012

Fournier, F., Pellerin, M., Villeneuve, Q., Teillet, T., Hong, F., Poli, E., Borgomano, J., Philippe, L., Hairabian, A., 2018. The equivalent pore aspect ratio as a tool for pore type prediction in carbonate reservoirs. Am. Assoc. Pet. Geol. Bull. 7, 1343–1377. https://doi.org/10.1306/10181717058

Freiwald, A., Henrich, R., 1994. Reefal coralline algal buildup within the Arctic Circle: morphology and sedimentary dynamics under extreme environmental seasonality. Sedimentology 41, 963–984. https://doi.org/10.1111/j.1365-3091.1994.tb01435.x

Friedman, G.M., 1998. Rapidity of marine carbonate cementation—implications for carbonate diagenesis and sequence stratigraphy : perspective. Sediment. Geol. 119, 1–4.

Friedman, G.M., 1964. Early diagenesis and lithification in carbonate sediments. J. Sediment. Petrol. 34, 777–813.

Fulthorpe Schlanger., 1989. Paleo-Oceanographic and tectonic settings of early Miocene reefs and associated carbonates of offshore southeast Asia. Am. Assoc. Pet. Geol. Bull.

G, S.M., Barrallon, P.., Villeneuve, Q., Teillet, T., 2016. Lessons Learned From Examples of Reservoir Seismic Characterisation in Pre-salt Context Acoustic Phie, in: Third EAGE/SBGf Workshop.

Gassmann, F., 1951. Uber die elastizitat poroser medien. Vierteljahresschrift der Naturforschenden Gesellschaft Zurich 96, 1–23.

Gharechelou, S., Amini, A., Kadkhodaie-Ilkhchi, A., Moradi, B., 2015. An integrated approach for determination of pore-type distribution in carbonate-siliciclastic Asmari Reservoir, Cheshmeh-Khosh Oilfield, SW Iran. J. Geophys. Eng. 12, 793—809. https://doi.org/10.1088/1742-2132/12/5/793

Gilles A.R. Conesa, Eric Favre, Philippe Münch, Dalmasso, H., Christian Chaix, 2005. Biosedimentaty and paleoenvironmental evolution of the southern Marion platform from the Middle to Late Miocene (Northeast Australia, ODP LEG 194, sites 1196 and 1199). Proc. Ocean Drill. Progr. 194.

Grana, D., 2017. Stochastic inversion of seismic data for reservoir characterization : a rapidly developing emerging technology, in: SEG International Exposition and 87th Annual Meeting. pp. 5278–5283.

Grana, D., Della Rossa, E., 2010. Probabilistic petrophysical-properties estimation integrating statistical rock physics with seismic inversion. Geophysics 75, O21. https://doi.org/10.1190/1.3386676

Grana, D., Mukerji, T., 2015. Bayesian inversion of time-lapse seismic data for the estimation of static reservoir properties and dynamic property changes. Geophys. Prospect. 63, 637–655. https://doi.org/10.1111/1365-2478.12203

Guo, J., Li, H., Zhang, Y., LI, J., Ma, X., Liu, Xi., 2017. Inverting carbonate reservoir porosity affected by pore aspect ratio. progephys.cn.

Haines, T.J., Neilson, J.E., Healy, D., Michie, E.A.H., Aplin, A.C., 2015. The impact of carbonate texture on the quantification of total porosity by image analysis. Comput. Geosci. 85, 112–125. https://doi.org/10.1016/j.cageo.2015.08.016

Hairabian, A., Fournier, F., Borgomano, J., Nardon, S., 2014. Depositional facies, pore types and elastic properties of deep-water gravity flow carbonates. J. Pet. Geol. 37, 231–249. https://doi.org/10.1111/jpg.12581

Halfar, J., Centro, L.G., Ciencias, I. De, Paz, L., 2004. Nutrient and temperature controls on modern carbonate production : An example from the Gulf of California, Mexico. Geol. Soc. Am. 213–216. https://doi.org/10.1130/G20298.1

Halfar, J., Mutti, M., 2005. Global dominance of coralline red-algal facies: A response to Miocene oceanographic events. Geology 33, 481–484. https://doi.org/10.1130/G21462.1

Hall, R., 2012. Late Jurassic-Cenozoic reconstructions of the Indonesian region and the Indian Ocean. Tectonophysics 570–571, 1–41. https://doi.org/10.1016/j.tecto.2012.04.021

Hall, R., 2002. Cenozoic geological and plate tectonic evolution of SE Asia and the SW Pacific: Computer-based reconstructions, model and animations. J. Asian Earth Sci. 20, 353–431. https://doi.org/10.1016/S1367-9120(01)00069-4

Hall, R., 1997. Cenozoic plate tectonic reconstructions of SE Asia. Geol. Soc. London, Spec. Publ. 126, 11–23. https://doi.org/10.1144/GSL.SP.1997.126.01.03

Hallock, P., Glenn, E.C., 1986. Larger Foraminifera: A Tool for Paleoenvironmental Analysis of Cenozoic Carbonate Depositional Facies. Palaios 1, 55–64. https://doi.org/10.2307/3514459

Hallock, P., Pomar, L., 2012. Cenozoic Evolution of Carbonate Shelf and Ramp Habitats: Insights from Paleoceanography 50663.

Hallock, P., Schlager, W., 1986. Nutrient Excess and the Demise of Coral Reefs and Carbonate Platforms. Palaios 1, 389. https://doi.org/10.2307/3514476

Hammond, R.D., Gaither, J.R., 1983. Anomalous seismic character—Bering Sea Shelf. Geophysics 48, 590–605.

Hearn, C., Atkinson, M., Falter, J., 2001. A physical derivation of nutrient-uptake rates in coral reefs: Effects of roughness and waves. Coral Reefs 20, 347–356.

https://doi.org/10.1007/s00338-001-0185-6

Heubeck, C., Story, K., Peng, P., Sullivan, C., Duff, S., 2004. An Integrated Reservoir Study of the Liuhua 11-1 Field Using a High-resolution Three-Dimensional Seismic Data Set 149–168.

Hilbertz, W., Goreau, T., 2002. Saya de Malha expedition report 1–107.

Hill, C.A., 1990. Sulfuric acid speleogenesis of Carlsbad Cavern and its relationship to hydrocarbons, Delaware Basin, New Mexico and Texas. Am. Assoc. Pet. Geol. Bull.

Hill, R., 1952. The Elastic Behaviour of a Crystalline Aggregate 2.

Hine, a. C., 2001. Advances in carbonate sequence stratigraphy: Application to reservoirs, outcrops, and models. Eos, Trans. Am. Geophys. Union 82, 18–18. https://doi.org/10.1029/01EO00014

Hyder, P., Jeans, D.R.G., Cauquil, E., Nerzic, R., 2005. Observations and predictability of internal solitons in the northern Andaman Sea. Appl. Ocean Res. 27, 1–11. https://doi.org/10.1016/j.apor.2005.07.001

Irwin, H., Curtis, C., Coleman, M., 1977. Isotopic evidence for source of diagenetic carbonates formed during burial of organic-rich sediments. Nature 269, 209–213. https://doi.org/10.1038/269209a0

James, N.P., 1997. The cool-water carbonate depositional realm. Sediment. Geol. 56, 1–20.

Jantzen, C., Schmidt, G.M., Wild, C., Roder, C., Khokiattiwong, S., Richter, C., 2013. Benthic reef primary production in response to large amplitude internal waves at the Similan Islands (Andaman Sea, Thailand). PLoS One 8, 1—16. https://doi.org/10.1371/journal.pone.0081834

Kahng, S.E., Garcia-Sais, J.R., Spalding, H.L., Brokovich, E., Wagner, D., Weil, E., Hinderstein, L., Toonen, R.J., 2010. Community ecology of mesophotic coral reef ecosystems. Coral Reefs 29, 255—275. https://doi.org/10.1007/s00338-010-0593-6

Karimpouli, S., Hassani, H., Nabi-Bidhendi, M., Khoshdel, H., Malehmir, A., 2013. Application of probabilistic facies prediction and estimation of rock physics parameters in a carbonate reservoir from Iran. J. Geophys. Eng. 10, 1–14. https://doi.org/10.1088/1742-2132/10/1/015008

Karimpouli, S., Tahmasebi, P., Saenger, E.H., 2018. Estimating 3D elastic moduli of rock from 2D thin-section images using differential effective medium theory. Geophysics 83, MR211—MR219. https://doi.org/10.1190/geo2017-0504.1

Kenter, J.A.M., Braaksma, H., Verwer, K., van Lanen, X.M.T., 2007. Acoustic behavior of sedimentary rocks: Geologic properties versus Poisson's ratios. Lead. Edge 26, 436–444. https://doi.org/10.1190/1.2723206

Lambert, L., Durlet, C., Loreau, J.P., Marnier, G., 2006. Burial dissolution of micrite in Middle East carbonate reservoirs (Jurassic-Cretaceous): Keys for recognition and timing. Mar. Pet. Geol. 23, 79—92. https://doi.org/10.1016/j.marpetgeo.2005.04.003

Lanteaume, C., Fournier, F., Pellerin, M., Borgomano, J., 2016. Testing geologic assumptions and scenarios in carbonate exploration : Insights from integrated stratigraphic, diagenetic, and seismic forward modeling. Lead. Edge 672–680.

https://doi.org/10.1190/tle37090672.1

Laskar, A.H., Raghav, S., Yadava, M.G., Jani, R.A., Narayana, A.C., Ramesh, R., 2011. Potential of Stable Carbon and Oxygen Isotope Variations of Speleothems from Andaman Islands, India, for Paleomonsoon Reconstruction. J. Geol. Res. 2011, 1–7. https://doi.org/10.1155/2011/272971

Lee, T.Y., Lawver, L.A., 1995. Cenozoic plate reconstruction of Southeast Asia. Tectonophysics 251, 85–138. https://doi.org/10.1016/0040-1951(95)00023-2

Léonide, P., Fournier, F., Reijmer, J.J.G., Vonhof, H., Borgomano, J., Dijk, J., Rosenthal, M., van Goethem, M., Cochard, J., Meulenaars, K., 2014. Diagenetic patterns and pore space distribution along a platform to outer-shelf transect (Urgonian limestone, Barremian—Aptian, SE France). Sediment. Geol. 306, 1–23. https://doi.org/10.1016/j.sedgeo.2014.03.001

Lesser, M.P., Slattery, M., Leichter, J.J., 2009. Ecology of mesophotic coral reefs. J. Exp. Mar. Bio. Ecol. 375, 1–8. https://doi.org/10.1016/j.jembe.2009.05.009

Licht, A., Reisberg, L., France-Lanord, C., Naing Soe, A., Jaeger, J.J., 2016. Cenozoic evolution of the central Myanmar drainage system: Insights from sediment provenance in the Minbu Sub-Basin. Basin Res. 28, 237–251. https://doi.org/10.1111/bre.12108

Liu, Y., Wang, Y., 2017. Seismic characterization of a carbonate reservoir in Tarim Basin Case History Seismic characterization of a carbonate reservoir in Tarim Basin. Geophysics 82. https://doi.org/10.1190/geo2016-0517.1

Lüdmann, T., Betzler, C., Eberli, G.P., Reolid, J., Reijmer, J.J.G., Sloss, C.R., Bialik, O.M., Alvarez-Zarikian, C.A., Alonso-García, M., Blättler, C.L., Guo, J.A., Haffen, S., Horozal, S., Inoue, M., Jovane, L., Kroon, D., Lanci, L., Laya, J.C., Mee, A.L.H., Nakakuni, M., Nath, B.N., Niino, K., Petruny, L.M., Pratiwi, S.D., Slagle, A.L., Su, X., Swart, P.K., Wright, J.D., Yao, Z., Young, J.R., 2018. Corrigendum to “Carbonate delta drift: A new sediment drift type” [Mar. Geol. 401 (2018) 98–111] (Marine Geology (2018) 401 (98–111), (S0025322717302761) (10.1016/j.margeo.2018.04.011)). Mar. Geol. 406, 214–215. https://doi.org/10.1016/j.margeo.2018.10.005

Machel, H.G., 2001. Bacterial and thermochemical sulfate reduction in diagenetic settings—old and new insights. Sediment. Geol. 140, 143–175. https://doi.org/10.1016/S0037-0738(00)00176-7

Madden, R.H.C., Wilson, M.E.J., 2013. Diagenesis of a SE Asian Cenozoic carbonate platform margin and its adjacent basinal deposits. Sediment. Geol. 286–287, 20–38. https://doi.org/10.1016/j.sedgeo.2012.11.006

Mass, T., Einbinder, S., Brokovich, E., Shashar, N., Vago, R., Erez, J., Dubinsky, Z., 2007. Photoacclimation of Stylophora pistillata to light extremes: Metabolism and calcification. Mar. Ecol. Prog. Ser. 334, 93–102. https://doi.org/10.3354/meps334093

Mateu-Vicens, G., Pomar, L., Ferràndez-Canadell, C., 2012. Nummulitic banks in the upper Lutetian “Buil level”, Ainsa Basin, South Central Pyrenean Zone: The impact of internal waves. Sedimentology 59, 527–552. https://doi.org/10.1111/j.1365-

3091.2011.01263.x

Matthews, R.K., Allan, J.R., 1982. Isotope signature associated with early meteoric diagenesis. Sedimentology 29, 797–817.

Maurizot, P., Cabioch, G., Fournier, F., Leonide, P., Sebih, S., Rouillard, P., Montaggioni, L., Collot, J., Martin-Garin, B., Chaproniere, G., Braga, J.C., Sevin, B., 2016. Post-obduction carbonate system development in New Caledonia (Népoui, Lower Miocene). Sediment. Geol. 331, 42–62. https://doi.org/10.1016/j.sedgeo.2015.11.003

Mavko, G., Mukerji, T., Dvorkin, J., 2009. The Rock Physics Handbook, Second Edition, World Wide Web Internet And Web Information Systems. https://doi.org/http://dx.doi.org/10.1017/CBO9780511626753

Maw Win, 2011. Exploration scenario in Myanmar Petrolim.

Mazzullo, S.J., Harris, P.M., 1991. An overview of dissolution porosity development in the deep-burial environment, with examples from carbonate reservoirs in the Permian Basin. Permian Basin Play. —Tomorrow's Technol. Today 91–89, 125–138. https://doi.org/DOI:10.1306/05031110187

McKinney, F.K., Hageman, S.J., 2007. Crossing the Ecological Devide: Paleozoic to Modern Marine Ecosystems in the Adriatic Sea. Sediment. Rec. 5. https://doi.org/10.1130/G22707.1

Mendel, J.M., 1983. Optimal Seismic Deconvolution, Academeic. ed.

Miller, K.G., Kominz, M.A., Browning, J. V., Wright, J.D., Mountain, G.S., Katz, M.E., Sugarman, P.J., Cramer, B.S., Christie-Blick, N., Pekar, S.F., 2005. The phanerozoic record of global sea-level change. Science (80—.). 310, 1293–1298. https://doi.org/10.1126/science.1116412

Min Aung, 2014. The attractive hydrocarbon potential sturctures and stratigraphic traps in the Arakan coastal area (onshore, offshore), in: 3rd Myanmar Oil and Gas Summit, Yangon.

Moldovanyi, E.P., Wall, F.M., Yan, Z.J., 1995. Regional exposure events and platform evolution of Zhujiang Formation carbonates, Pearl River mouth basin: evidence from primary and diagenetic seismic facies. Unconformities porosity carbonate Strat. 125–140.

Morad, D., Paganoni, M., Al Harthi, A., Morad, S., Ceriani, A., Mansurbeg, H., Al Suwaidi, A., Al-Aasm, I.S., Ehrenberg, S.N., 2016. Origin and evolution of microporosity in packstones and grainstones in a Lower Cretaceous carbonate reservoir, United Arab Emirates. Geol. Soc. London, Spec. Publ. 435. https://doi.org/10.1144/SP435.20

Morad, S., Ketzer, J.M., DeRos, F., 2000. Spatial and temporal distribution of diagenetic alterations in siliciclastic rocks: implication for mass transfer in sedimentary basins. Sedimentology 47, 95–120. https://doi.org/10.1046/j.1365-3091.2000.00007.x

Morley, C.K., 2013. Discussion of tectonic models for Cenozoic strike-slip fault-affected continental margins of mainland SE Asia. J. Asian Earth Sci. 76, 137–151. https://doi.org/10.1016/j.jseaes.2012.10.019

Morley, C.K., 2012. Late Cretaceous-Early Palaeogene tectonic development of SE Asia.

Earth-Science Rev. 115, 37–75. https://doi.org/10.1016/j.earscirev.2012.08.002

Morsilli, M., Bosellini, F.R., Pomar, L., Hallock, P., Aurell, M., Papazzoni, C.A., 2012. Mesophotic coral buildups in a pro-delta setting (Late Eocene, southern Pyrenees, Spain): A mixed carbonate-siliciclastic system. Sedimentology 59, 766–794. https://doi.org/10.1111/j.1365-3091.2011.01275.x

Morsilli, M., Pomar, L., 2012. Internal waves vs. surface storm waves: A review on the origin of hummocky cross-stratification. Terra Nov. 24, 273–282. https://doi.org/10.1111/j.1365-3121.2012.01070.x

Mullins, H.T., Wise, S.W., Land, L.S., Siegel, D.I., Masters, P.M., Edward, J., Price, K.R., 1985. Geology Authigenic dolomite in Bahamian peri-platform slope sediment 292–295. https://doi.org/10.1130/0091-7613(1985)13<292

Muscatine, L., Falkowski, P.G., Dubinsky, Z., Cook, P.A., McCloskey, L.R., 1989. The Effect of External Nutrient Resources on the Population Dynamics of Zooxanthellae in a Reef Coral. Proc. R. Soc. B Biol. Sci. 236, 311–324. https://doi.org/10.1098/rspb.1989.0025

Noad, J., 2001. The Gomantong Limestone of eastern Borneo: A sedimentological comparison with the near-contemporaneous Luconia Province. Palaeogeogr. Palaeoclimatol. Palaeoecol. 175, 273–302. https://doi.org/10.1016/S0031-0182(01)00376-5

Norris, A.N., 1985. A differential scheme for the effective moduli of composites. Mech. Mater. 4, 1–16. https://doi.org/10.1016/0167-6636(85)90002-X

Nouzé, H., Cosquer, E., Collot, J., Foucher, J.-P., Klingelhoefer, F., Lafoy, Y., Géli, L., 2009. Geophysical characterization of bottom simulating reflectors in the Fairway Basin (off New Caledonia, Southwest Pacific), based on high resolution seismic profiles and heat flow data. Mar. Geol. 266, 80–90. https://doi.org/10.1016/J.MARGEO.2009.07.014

Osborne, A.R., Burch, T.L., 1980. Internal Solitons in the Andaman Sea. Science (80—.). 208, 451–460. https://doi.org/10.1126/science.208.4443.451

Park, R.K., A?, M., C., T.P., 1995. Porosity evolution in the Batu Raja carbonates of the Sunda Basin Windows of opportunity, in: Indonesian Petroleum Association, 24th Annual Convention. pp. 63–184.

Paumard, V., Zuckmeyer, E., Boichard, R., Jorry, S.J., Bourget, J., Borgomano, J., Maurin, T., Ferry, J.N., 2017. Evolution of Late Oligocene—Early Miocene attached and isolated carbonate platforms in a volcanic ridge context (Maldives type), Yadana field, offshore Myanmar. Mar. Pet. Geol. 81, 361–387. https://doi.org/10.1016/j.marpetgeo.2016.12.012

Periere, M.D. De, 2011. Origine sédimento-diagénétique de réservoirs carbonatés microporeux :

Periere, M.D. de, Foote, A., Bertouche, M., Shah, R., al-Darmaki, F., Ishaq, W. bin, 2017. Link Between Microporous Limestones and Elastic Properties in Tight Carbonates. A Case Study from the Lower Arab Formation Upper Jurassic, Onshore United Arab

Emirates. Abu Dhabi Int. Pet. Exhib. Conf. https://doi.org/10.2118/188944-MS

Pingitore, N.E., 1976. Vadose and Phreatic Diagenesis: Processes, Products and their Recognition in Corals. J. Sediment. Res. Vol. 46, 985–1006. https://doi.org/10.1306/212F70B8-2B24-11D7-8648000102C1865D

Pomar, 2015. Follow the food; the waxing & waning of coral buildups during the Cenozoic. Ias Reg. Meet. 2015.

Pomar, L., 2001. Types of carbonate platforms: A genetic approach. Basin Res. 13, 313–334. https://doi.org/10.1046/j.0950-091X.2001.00152.x

Pomar, L., Baceta, J.I., Hallock, P., Mateu-Vicens, G., Basso, D., 2017. Reef building and carbonate production modes in the west-central Tethys during the Cenozoic. Mar. Pet. Geol. 83, 261–304. https://doi.org/10.1016/j.marpetgeo.2017.03.015

Pomar, L., Hallock, P., 2008. Carbonate factories: A conundrum in sedimentary geology. Earth-Science Rev. 87, 134–169. https://doi.org/10.1016/j.earscirev.2007.12.002

Pomar, L., Mateu-Vicens, G., Morsilli, M., Brandano, M., 2014. Carbonate ramp evolution during the Late Oligocene (Chattian), Salento Peninsula, southern Italy. Palaeogeogr. Palaeoclimatol. Palaeoecol. 404, 109–132. https://doi.org/10.1016/j.palaeo.2014.03.023

Pyle, R.L., Boland, R., Bolick, H., Bowen, B.W., Bradley, C.J., Kane, C., Kosaki, R.K., Langston, R., Longenecker, K., Montgomery, A., Parrish, F.A., Popp, B.N., Rooney, J., Smith, C.M., Wagner, D., Spalding, H.L., 2016. A comprehensive investigation of mesophotic coral ecosystems in the Hawaiian Archipelago. PeerJ 4, e2475. https://doi.org/10.7717/peerj.2475

Rabier, C., Anguy, Y., Cabioch, G., Genthon, P., 2008. Characterization of various stages of calcitization in Porites sp corals from uplifted reefs—Case studies from New Caledonia, Vanuatu, and Futuna (South-West Pacific). Sediment. Geol. 211, 73–86. https://doi.org/10.1016/j.sedgeo.2008.08.005

Racey, A., 2015. Petroleum geology of the Moattama Region, Myanmar.

Racey, M.F., Ridd, 2015. Chapter 7 Petroleum geology of the Moattama Region, Myanmar. Geol. Soc. London, Mem. 63–81. https://doi.org/10.1144/M45.07

Rahmani, A., Vaziri-Moghaddam, H., Taheri, A., Ghabeishavi, A., 2009. A model for the paleoenvironmental distribution of larger foraminifera of Oligocene-Miocene carbonate rocks at Khaviz Anticline, Zagros Basin, SW Iran. Hist. Biol. 21, 215–227. https://doi.org/10.1080/08912960903461296

Rama Raju, D. V, Gouveia, A.D., Murty, C.S., 1981. Some Physical Characteristics of Andaman Sea Waters during Winter. I i Indian J. Mar. Sci. 10, 211–218.

Ramaswamy, V., Rao, P.S., Rao, K.H., Thwin, S., Rao, N.S., Raiker, V., 2004. Tidal influence on suspended sediment distribution and dispersal in the northern Andaman Sea and Gulf of Martaban. Mar. Geol. 208, 33–42. https://doi.org/10.1016/j.margeo.2004.04.019

Rankey, E.C., Mitchell, J.., 2003. That's why it's called interpretation : Impact of horizon uncertainty on seismic attribute analysis. Interpret. Corner.

Rankey, E.C., Schlaich, M., Mokhtar, S., Ghon, G., Haroon, S., Poppelreiter, M., 2019. Seismic architecture of a miocene isolated carbonate platform and associated off-platform strata (Central Luconia province, offshore Malaysia). Mar. Pet. Geol. https://doi.org/10.1016/j.marpetgeo.2019.01.009

Rao, P.S., Ramaswamy, V., Thwin, S., 2005. Sediment texture, distribution and transport on the Ayeyarwady continental shelf, Andaman Sea. Mar. Geol. 216, 239–247. https://doi.org/10.1016/j.margeo.2005.02.016

Read, J.F., 1985. Carbonate Platforms Facies Model. Am. Assoc. Pet. Geol. Bull.

Reaves, C.M., 1986. ORGANIC MATIER METABOLIZABILITY AND CALCIUM CARBONATE DISSOLUTION IN NEARSHORE MARINE MUDSl 1986, 486–494.

Renema, W., Troelstra, S.R., 2001. Larger foraminifera distribution on a mesotrophic carbonate shelf in SW Sulawesi (Indonesia). Palaeogeogr. Palaeoclimatol. Palaeoecol. 175, 125–146. https://doi.org/10.1016/S0031-0182(01)00389-3

Ribes, M., Coma, R., Atkinson, M.J., Kinzie, R.A., 2003. Particle removal by coral reef communities: Picoplankton is a major source of nitrogen. Mar. Ecol. Prog. Ser. 257, 13–23. https://doi.org/10.3354/meps257013

Roberts, H.., Phipps, C.V., 1988. Proposed oceanographic controls on modern Indonesian reefs : A turn-off/turn-on mechanism in a monsoonal setting. Proc. 6th Int. Coral Reef Symp. South Sulawesi, Aust. 3.

Roehl, P., Choquette, P.W., 1985. Carbonate petroleum reservoirs.

Rosler, A., Pretkovi, V., Novak, V., Renema, W., Braga, J.C., 2015. Coralline Algae From the Miocene Mahakam Delta (East Kalimantan, Southeast Asia). Palaios 30, 83–93. https://doi.org/10.2110/palo.2013.055

Saller, A., 1993. Sequence Stratigraphy of Aggrading and Backstepping Carboante Shelves, Oligocene, Central Kalimantan, Indonesia.

Saller, A.H., 1984. Petrologic and geochemical constraints on the origin of subsurface dolomite, Enewetak Atoll: an example of dolomitization by normal seawater (Eocene, Sr-isotopes). Geology 12, 217–220. https://doi.org/10.1130/0091-7613(1984)12<217:PAGCOT>2.0.CO

Saller, A.H., Moore, C.H., 1989. Meteoric diagenesis, marine diagenesis, and microporosity in Pleistocene and Oligocene limestones, Enewetak Atoll, Marshall Islands. Sediment. Geol. 63, 253–272. https://doi.org/10.1016/0037-0738(89)90135-8

Saller, A.H., Vijaya, S., 2002. Depositional and diagenetic history of the Kerendan carbonate platform, Oligocene, Central Kalimantan, Indonesia. J. Pet. Geol. 25, 123–150. https://doi.org/10.1111/j.1747-5457.2002.tb00001.x

Sanders, D., 2003. Syndepositional dissolution of calcium carbonate in neritic carbonate environments: Geological recognition, processes, potential significance, Journal of African Earth Sciences. https://doi.org/10.1016/S0899-5362(03)00027-7

Saqab, M.M., Bourget, J., 2016. Seismic geomorphology and evolution of early???mid Miocene isolated carbonate buildups in the Timor Sea, North West Shelf of Australia. Mar. Geol. 379, 224–245. https://doi.org/10.1016/j.margeo.2016.06.007

Sattler, U., Zampetti, V., Schlager, W., Immenhauser, A., 2004. Late leaching under deep burial conditions: A case study from the Miocene Zhujiang Carbonate Reservoir, South China Sea. Mar. Pet. Geol. 21, 977–992. https://doi.org/10.1016/j.marpetgeo.2004.05.005

Schlager, W., 2003. Benthic carbonate factories of the Phanerozoic. Int. J. Earth Sci. 92, 445–464. https://doi.org/10.1007/s00531-003-0327-x

Schlager, W., 2000. Sedimentation rates and growth potential of tropical, cool-water and mud-mound carbonate factories,. Geol. Soc. Spec. Publ. 178, 217–227.

Seguret, M., Moussine-Pouchkine, A., Raja Gabaglia, G., Bouchette, F., 2001. Storm deposits and storm-generated coarse carbonate breccias on a pelagic outer shelf (South-East Basin, France). Sedimentology 48, 231–254. https://doi.org/10.1046/j.1365-3091.2001.00358.x

Sheriff, R.E., 1977. Limitations on resolution of seismic reflections and geologic detail derivable from them: Section 1. Fundamentals of stratigraphic interpretation of seismic data. AAPG Mem. Seism. Stratigr. to Hydrocarb. Explor. 26, 3–14.

Simm, R., Bacon, M., 2014. Seismic Amplitude. Seism. Amplitude. https://doi.org/10.1017/cbo9780511984501

Smit, F.W.H., van Buchem, F.S.P., Holst, J.C., Lüthje, M., Anderskouv, K., Thibault, N., Buijs, G.J.A., Welch, M.J., Stemmerik, L., 2018. Seismic geomorphology and origin of diagenetic geobodies in the Upper Cretaceous Chalk of the North Sea Basin (Danish Central Graben). Basin Res. 30, 895–925. https://doi.org/10.1111/bre.12285

Sun, Q., Esteban, M., 1994. Paleoclimatic Controls on Sedimentation, Diagenesis, and Reservoir Quality: Lessons from Miocene Carbonates. Am. Assoc. Pet. Geol. Bull. 78, 519–543.

Sun, Y.F., K, B., S, V., Eberli, G.P., T, B.G., R.J, W., L, M.J., Gartner, G.B., P.D, W., 2006. Effects of pore structure on 4D seismic signals in carbonates reservoirs, in: SEG New Orleans 2006 Annual Meeting. pp. 3260–3264.

Suzuki, Y., Iryu, Y., Inagaki, S., Yamada, T., Aizawa, S., Budd, D.A., 2006. Origin of atoll dolomites distinguished by geochemistry and crystal chemistry: Kita-daito-jima, northern Philippine Sea. Sediment. Geol. 183, 181–202. https://doi.org/10.1016/j.sedgeo.2005.09.016

Swart, P.K., 2015. The geochemistry of carbonate diagenesis: The past, present and future. Sedimentology 62, 1233—1304. https://doi.org/10.1111/sed.12205

Takayanagi, H., Iryu, Y., Oda, M., Sato, T., Chiyonobu, S., Nishimura, A., Nakazawa, T., Ishikawa, T., Nagaishi, K., 2012. Temporal changes in biotic and abiotic composition of shallow-water carbonates on submerged seamounts in the northwestern Pacific Ocean and their controlling factors. Geodiversitas 34, 189–217. https://doi.org/10.5252/g2012n1a11

Takayanagi, H., Iryu, Y., Yamada, T., Oda, M., Yamamoto, K., Sato, T., Chiyonobu, S., Nishimura, A., Nakazawa, T., Shiokawa, S., 2007. Carbonate deposits on submerged seamounts in the northwestern Pacific Ocean. Isl. Arc 16, 394–419.

https://doi.org/10.1111/j.1440-1738.2007.00595.x

Tan Sin Hok, 1936. Zur Kenntniss der Miogypsiniden. Ingenieur Nederland. Mijnb. Geol. 4, 45–61.

Tarantola, A., 2005. Inverse Problem Theory.

Teillet, T., Fournier, F., Gisquet, F., Montaggioni, L.F., Borgomano, J., Villeneuve, Q., Hong, F., 2019a. Diagenetic history and porosity evolution of an Early Miocene carbonate buildup (Upper Burman Limestone), Yadana gas field, offshore Myanmar. Mar. Pet. Geol. 109, 589–606. https://doi.org/10.1016/j.marpetgeo.2019.06.044

Teillet, T., Fournier, F., Montaggioni, L.F., BouDagher-Fadel, M.K., Borgomano, J., Braga, J.C., Villeneuve, Q., Hong, F., 2019b. Development patterns of an oligo-mesophotic isolated carbonate buildup (Upper Burman Limestone, Lower Miocene, Yadana field, offshore Myanmar). Sediment. Geol. 111, 440–460. https://doi.org/10.1016/j.marpetgeo.2019.08.039

Tomascik, T., Mah, A.J., Nontji, A., Moosa, M.K., 2000. The Ecology of the Indonesian Seas. Part I. The Ecology of Indonesia Series, Volume VII., The Quarterly Review of Biology. https://doi.org/10.1086/393445

Tomassetti, L., Petracchini, L., Brandano, M., Trippetta, F., Tomassi, A., 2018. Modeling lateral facies heterogeneity of an upper Oligocene carbonate ramp (Salento, southern Italy). Mar. Pet. Geol. 96, 254–270. https://doi.org/10.1016/j.marpetgeo.2018.06.004

Tucker, M., Wright, V., 1990. Carbonate sedimentology, Science. https://doi.org/10.1002/9781444314175

Tucker, M.E., 1993. Carbonate Diagenesis and Sequence Stratigraphy. Sedimentol. Rev. 51–72. https://doi.org/10.1002/9781444304534.ch4

Vahrenkamp, V.C., 1998. Miocene carbonates of the Luconia province, offshore Sarawak: implications for regional geology and reservoir properties from Strontium-isotope stratigraphy. Geol. Soc. Malaysia Bull. 42, 1–13.

Vahrenkamp, V.C., David, F., Duijndam, P., Newall, M., Crevello, P., 2004. Growth architecture, faulting, and karstification of a middle Miocene carbonate platform, Luconia Province, offshore Sarawak, Malaysia. Seism. imaging carbonate Reserv. Syst. (AAPG Mem. - 2004, 81329-350) 79, 329–350. https://doi.org/10.1111/mono.12075

Vail, P.R., Todd, R., Sangree, J., 1977. Seismic stratigraphy and global changes of sea level: Part 5—Chronostratigraphic significance of seismic reflections, in. AAPG Mem. 26, 99–116.

Van der vlerk, I.., 1922. No TitleStudiën over nummulinidae en alveolinidae. Haar voorkomen op Soembawa en haar betekenis voor de geologie van oost- Azië en Australië. Wetenschappelijke Mededeelingen van de Dienst van de Mijnbouw. Ned. Oost- Indie.

Veizer, J., 1983. Chemical diagenisis of carbonates: theory and application of trace element technique. Stable Isot. Sediment. Geol. 1–100.

Volery, C., Davaud, E., Foubert, A., Caline, B., 2010. Lacustrine microporous micrites of the Madrid Basin (Late Miocene, Spain) as analogues for shallow-marine carbonates of the Mishrif reservoir formation (Cenomanian to Early Turonian, Middle East). Facies 56, 385–397. https://doi.org/10.1007/s10347-009-0210-8

Wagner, P.D., 1997. 12. Seismic Signatures of Carbonate Diagenesis. Carbonate Seismol. 307–320. https://doi.org/10.1190/1.9781560802099.ch12

Wang, Z., 1997. Seismic properties of carbonate rocks. Carbonate Seismol. 29–52.

Wang, Z., Wang, R., Li, T., Zhao, M., 2017. The combined effects of pore structure and pore fluid on the acoustic properties of cracked and vuggy synthetic rocks. J. Pet. Sci. Eng. 156, 202–211. https://doi.org/10.1016/j.petrol.2017.05.023

Warrlich, G., Bosence, D., Waltham, D., Wood, C., Boylan, A., Badenas, B., 2008. 3D stratigraphic forward modeling for analysis and prediction of carbonate platform stratigraphies in exploration and production. Mar. Pet. Geol. 25, 35–58. https://doi.org/10.1016/j.marpetgeo.2007.04.005

Warrlich, G., Taberner, C., Wenche, A., Stephenson, B., Esteban, M., Boya-Ferrero, M., Dombrowski, A., van Konijnenburg, J.H., 2010. The Impact of Postdepositional Processes on Reservoir Properties: Two Case Studies of Tertiary Carbonate Buildup Gas Fields in Southeast Asia (Malampaya and E11), in: Cenozoic Carbonates Systems of Australasia.

Warrlich, G.M.D., Adams, E.W., Ryba, A., Tam, T., Ting, K.K., Tang, H.K., 2019. What matters for flow and recovery in carbonate gas reservoirs: Insights from the mature Central Luconia Province, offshore Sarawak, Malaysia. Am. Assoc. Pet. Geol. Bull. 103, 691–721. https://doi.org/10.1306/09051817219

Webb, G.E., Nothdurft, L.D., Kamber, B.S., Kloprogge, J.T., Zhao, J.X., 2009. Rare earth element geochemistry of scleractinian coral skeleton during meteoric diagenesis: A sequence through neomorphism of aragonite to calcite. Sedimentology 56, 1433–1463. https://doi.org/10.1111/j.1365-3091.2008.01041.x

Weger, R.J., Eberli, G.P., Baechle, G.T., Massaferro, J.L., Sun, Y.F., 2009. Quantification of pore structure and its effect on sonic velocity and permeability in carbonates. Am. Assoc. Pet. Geol. Bull. 93, 1297–1317. https://doi.org/10.1306/05270909001

Wilson, M., Goldberg, A., 2010. Quantitative Seismic Interpretation for Characterizing Carbonate Diagenesis—an Elk/Antelope Gas Field Study Quantitative Seismic Interpretation for Characterizing Carbonate Diagenesis—an Elk/Antelope Gas Field Study. 2, 1–9. https://doi.org/10.1071/ASEG2010ab128

Wilson, M.E.J., 2008a. Global and regional influences on equatorial shallow-marine carbonates during the Cenozoic. Palaeogeogr. Palaeoclimatol. Palaeoecol. 265, 262–274. https://doi.org/10.1016/j.palaeo.2008.05.012

Wilson, M.E.J., 2008b. Reservoir quality of Cenozoic carbonate buildups and coral reef terraces, in: Proceedings Indonesian Petroleum Association.

Wilson, M.E.J., 2002. Cenozoic carbonates in Southeast Asia: Implications for equatorial carbonate development. Sediment. Geol. 147, 295–428. https://doi.org/10.1016/S0037-0738(01)00228-7

Wilson, M.E.J., Bosence, D.W.J., 1996. The Tertiary evolution of South Sulawesi: a record in redeposited carbonates of the Tonasa Limestone Formation. Geol. Soc. London, Spec. Publ. 106, 365–389. https://doi.org/10.1144/GSL.SP.1996.106.01.24

Wilson, M.E.J., Evans, M.J., 2002. Sedimentology and diagenesis of Tertiary carbonates on the Mangkalihat Peninsula, Borneo: Implications for subsurface reservoir quality. Mar. Pet. Geol. 19, 873–900. https://doi.org/10.1016/S0264-8172(02)00085-5

Wilson, M.E.J., Hall, R., 2010. Tectonic influences on SE Asian carbonate systems and their reservoir development. Cenozoic Carbonate Syst. Australas. SEPM Speci, 13–40.

Wilson, M.E.J., Vecsei, A., 2005. The apparent paradox of abundant foramol facies in low latitudes: Their environmental significance and effect on platform development. Earth-Science Rev. 69, 133–168. https://doi.org/10.1016/j.earscirev.2004.08.003

Xu, S., Payne, M.A., 2009. Modeling elastic properties in carbonates rocks. Lead. Edge 28(1), 66–74. https://doi.org/https://doi.org/10.1190/1.3064148

Zachos, J., Pagani, M., Sloan, L., Thomas, E., Billups, K., 2001. Trends, Rhythms, and Aberrations in Global Climate 65 Ma to Present. Source Sci. New Ser. 292, 686–693. https://doi.org/10.1126/science.1059412

Zampetti, V., Sattler, U., Braaksma, H., 2005. Well log and seismic character of Liuhua 11-1 Field, South China Sea; relationship between diagenesis and seismic reflections. Sediment. Geol. 175, 217—236. https://doi.org/10.1016/j.sedgeo.2004.12.018

Zampetti, V., Schlager, W., van Konijnenburg, J.H., Everts, A.J., 2004. Architecture and growth history of a Miocene carbonate platform from 3D seismic reflection data; Luconia province, offshore Sarawak, Malaysia. Mar. Pet. Geol. 21, 517–534. https://doi.org/10.1016/j.marpetgeo.2004.01.006

Zeng, H., Kerans, C., 2003. Seismic frequency control on carbonate seismic stratigraphy: A case study of the Kingdom Abo sequence, West Texas. Am. Assoc. Pet. Geol. Bull. 87, 273–293. https://doi.org/10.1306/08270201023

Zhao, L., Nasser, M., Han, D.H., 2013. Quantitative geophysical pore-type characterization and its geological implication in carbonate reservoirs. Geophys. Prospect. 61, 827–841. https://doi.org/10.1111/1365-2478.12043

Zimmerman, 1991. Compressibility of sandstones.

Zuckmeyer, E., Boichard, R., Maurin, T., Paumard, V., 2017. The Paleogeography of the Oligo-Miocene Carbonate Platforms of Moattama Basin : New Insights using new 3D Seismic Data The Paleogeography of the Oligo-Miocene Carbonate Platforms of Moattama Basin : New Insights using new 3D Seismic Data. Mar. Pet. Geol. 2015–2016.

VIII. Appendix

1. *Diagenetic and tectonic evolution*

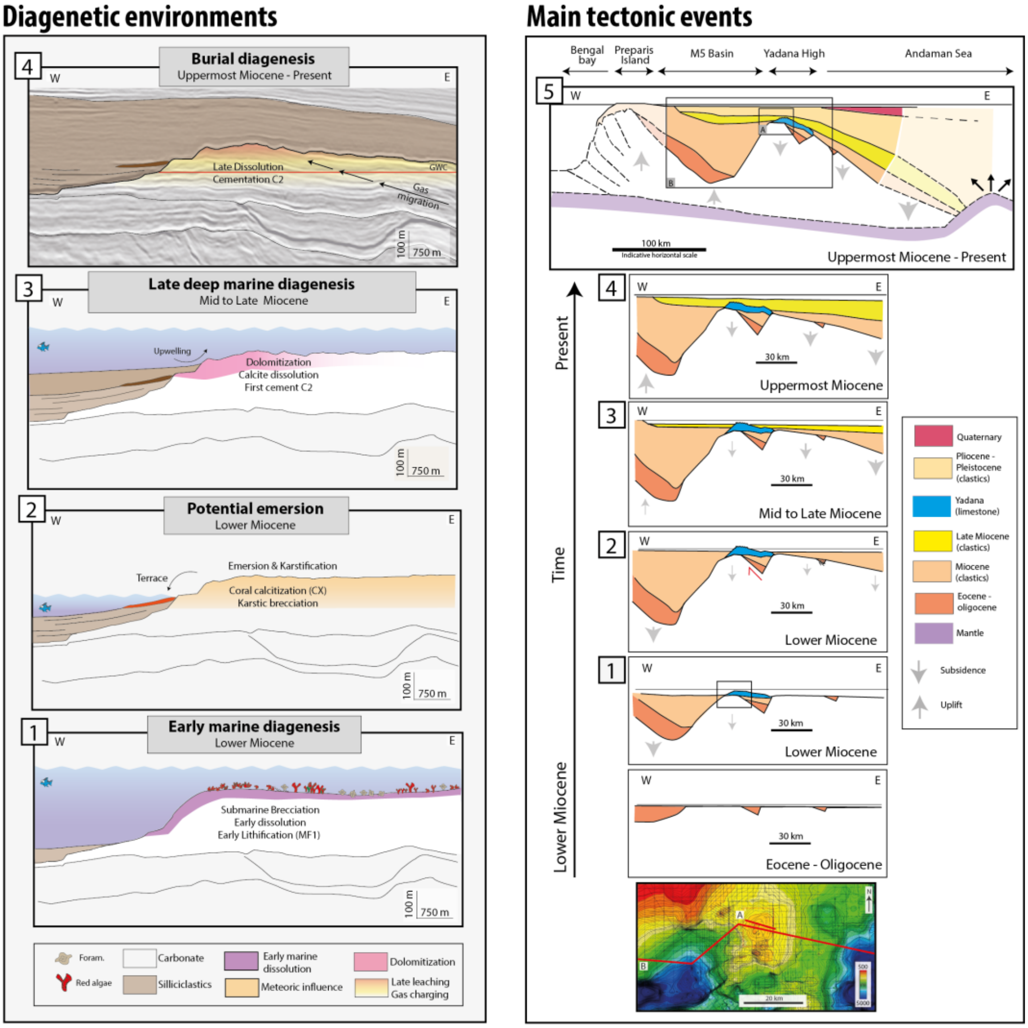

Figure 8-1 : Diagenetic and regional tectonic evolution: (0): Eocene—Oligocene: rifting phase. (1): Late Oligocene—Lower Miocene: Initiation of thermal subsidence, development of the M5 Basin and carbonate deposition on regional high (Yadana High). Period of early marine diagenesis in submarine conditions. (2): Lower Miocene: Potential subaerial emersion and the related diagenesis (karstification) of the carbonate platform could be envisaged regionally by thermal uplift of the M5 Basin and locally constrained with the reactivation of older thrust fault of the Yadana basement. (3): Middle-Late Miocene : Acceleration of subsidence in the Andaman Basin and Yadana High and inversion (uplift) of the M5 Basin eastward related to the India-Asia plate motion eastward the subduction zone (accretion prism). (4): Subsidence increase drastically in the Andaman Basin related to opening of Andaman Sea. Yadana platform has been buried and sealed (begging of burial diagenesis) by overlapping clastic sediments. (5): Present tectonic context.

2. Chemostratigraphic correlations

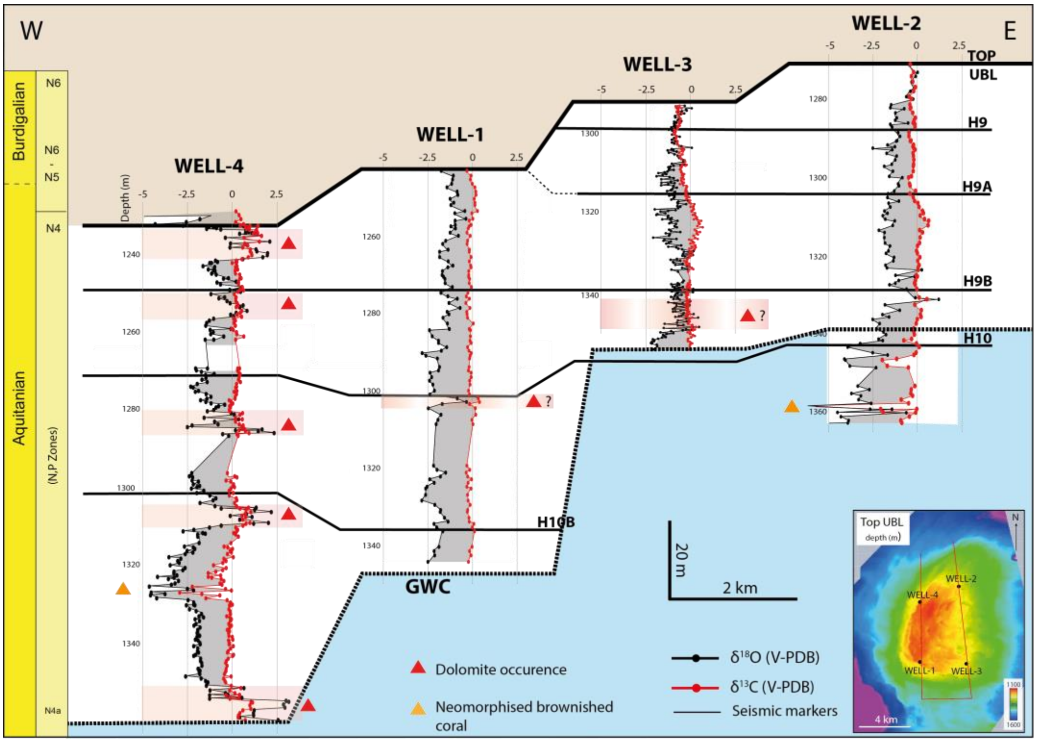

Figure 8-2 : Vertical variations of δ13C and δ18O over the UBL cored interval (bulk-rock measurements) and well correlations based on seismic reflectors and large benthic foraminiferal biostratigraphy (cf. Fig. 2-12). Chemiostratigraphic correlation between wells appears difficult. However, dolomitic intervals are marked by a positive shift of δ13C (WELL-4, red triangle) and potential subaerial emersion with brecciated limestone and neomorphised brownish coral are notified by negative shift of δ13C and δ18O (Orange triangle) in WELL-4 and WELL-2.

3. *Porosity-permeability relationships*

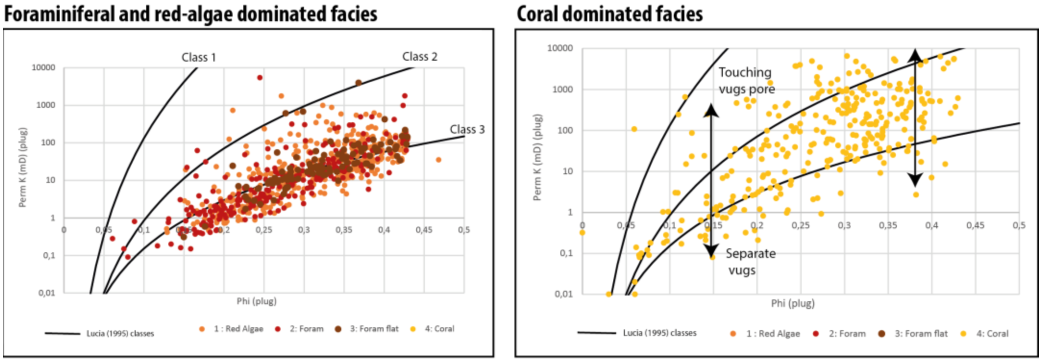
Foraminiferal and red-algae dominated facies

Coral dominated facies

Figure 8-3 : Porosity and permeability relationships depending lithofacies

Porosity and permeability plug data are interpreted regarding the porosity/permeability classes defined by Lucia (1995). Following this classification, the classes 2 and 3 correspond to microporous mud-supported facies while class 1 relates to grain-supported lowly microporous limestones. In the data set of Yadana (Fig 8.3), the foramineral floatstone (LF2.2) as well as dolomitic muddy facies, red algae rudstone (LF1) and the foraminiferal rudstone (LF2.1) perfectly fit to the class 3 of Lucia. This reveals the importance of the microporosity development to control reservoir properties of carbonate rocks (e.g., Urgonian limestone (Borgomano et al., 2013; Deville de Periere et al., 2011).

Controversially to red algae and foramineral facies PHI_plug/K data of coral-rich facies have a wide range of porosity value (from 5% to 42%) and permeability (from 0.01 to 10000 mD) overlapping the classes 1, 2 and 3 of Lucia. This reveals the complex diagenesis of coral-rich limestone consisting of: (1) early dissolution of aragonitic coral enhancing porosity through the production of large molds of coral fragments initial not connected (selective dissolution). (2) early cementation of matrix providing dense cemented matrix reducing porosity and permeability values and (3) potential subaerial emersion, inducing dissolution (touching vugs), karstic brecciation which enhances the porosity and the permeability.

4. *Overburden effect on porosity*

Different methods can be used to determinate the porosity rocks. In many cases, porosity is still measured on core (plugs) and logging provides continuous in situ measurement of bedrock properties. In oil and gas industry, the neutron log is the most convenient log used to measure the porosity. However, well-log porosity in gas reservoir is difficult to estimate due to the nature of fluids. In the case of Yadana, well-log porosity is calculated using an empirical formula (from internal report):

(1) $Phi_{well-log} = 0.03 * DNS - 0.6 * RHOB + 1.95 * 0.6 + 0.45$

With DNS corresponds to density neutron separation computed from logs and RHOB is well-logs density. In this section overburden effect on porosity and differences between plugs porosity (PHI_plug) and well-log (PHI_well-log) porosity are discussed:

At depths ranging from 1240 mCD to 1350 mCD the reservoir pressure are 2510 to 2550 psi (17 Mpa) for a temperature of 60°C (27°C/100 m). The high rate of plugs sampling (1/30 cm) gives the opportunity to directly compare PHI_plug to PHI_well-log and allow checking porosity estimation at different scales. Mean of the porosity PHI_plug (avg. 27.8%) is quite similar to PHI_well-log (avg. 27%). However the variance is slightly wider (var.PHI_plug = 57; var.PHI_well-log= 26). The highest porosity values (>40%) are located at the top of the reservoir (TOP UBL, 1232 mCD in WELL-4), then porosity decrease with depth from 40% at 1230 mCD to 25%, 70 meters below at 1300 mCD. The overburden effect on porosity is studied during compressibility tests. The Fig. 7.4 show the range of porosity reduction related to the increase of stresses. The compressibility factor is not directly proportional to porosity and seems to be related to pore type variations. For example, the compressibility factor of cemented foraminiferal rudstone with moldic porosity is 98.6% (from 22% to 21.7% of porosity at 1450 psi) while the foraminiferal rudstone dominated by microporosity has a compressibility factor of 87.6% (27.9% to 24.4% of porosity in 1450 psi). To convert core porosity at atmospheric condition to in-situ conditions (2500psi), we use the following equation:

(2) $PHI_{plug\,(reservoir)} = 0.92 * PHI_{plug(surface)}$

Considering the low variation of pressure within the reservoir (2500 to 2550 psi), only the pressure cannot be responsible for the rapid vertical decrease of porosity. So, additionally

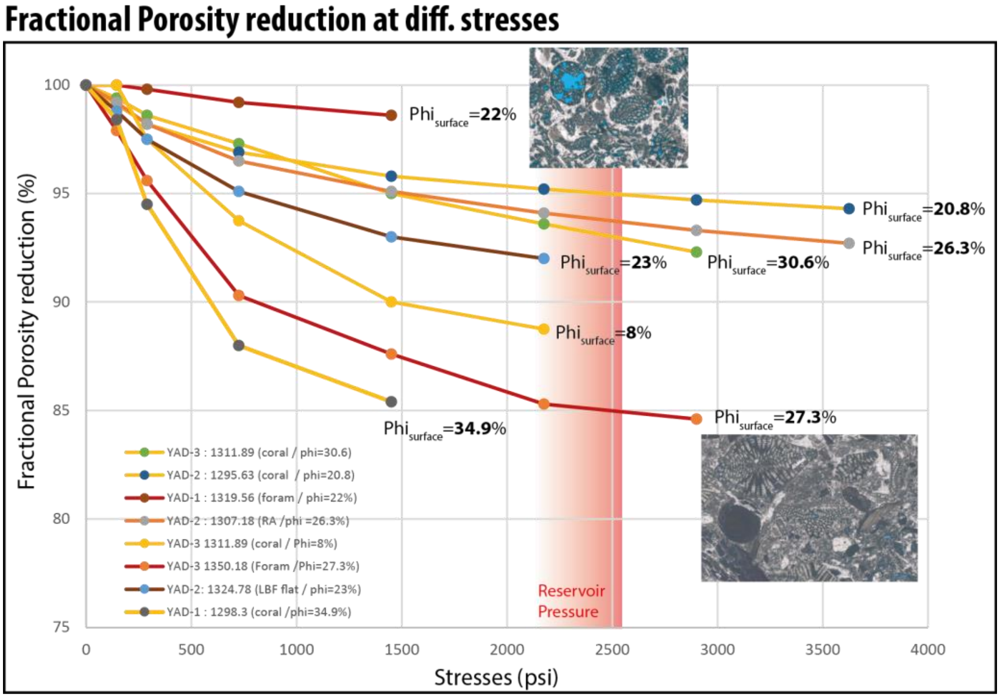

Figure 8-4 : Compressibility tests of selected samples highlighting fractional reduction of porosity versus stresses. The reservoir pressure at 1250 mcD is around 2500 psi (17 MPa).

to the overburden effect, the vertical evolution of porosity could by related to (1) the increase of the compaction (compressibility factor) with depth in this strongly porous limestone and/or (2) related to the differential intensity of the late diagenesis between the top reservoir (highest leaching, low cementation) and the base of the reservoir near the GWC (low leaching, cementation)

In addition, the logs ΔPoro corresponding to the difference of porosity: $\Delta Poro = Phi_{plug} - Phi_{well-log}$ shows important variations between the two methods of porosity measurements. On all wells, independently to the lithofacies, only 30% of PHI_well-log values fit well with PHI_plug values (according to a threshold of ΔPoro ±3%). The logs of $\Delta Poro$ clearly show the difficulty to estimate porosity from well-log data and show that the estimation error is systematic (Fig. 8.5, 8.6). This phenomenon should be related to (1) measurement bias of plugs porosity or (2) poor estimation (empirical formula) of PHI_well-log from neutron and density logs. So, to better estimate the porosity from well-log data, a correction of PHI_well-log for the WELL-2 is proposed based on the analysis of plugs (Fig. 8.7).

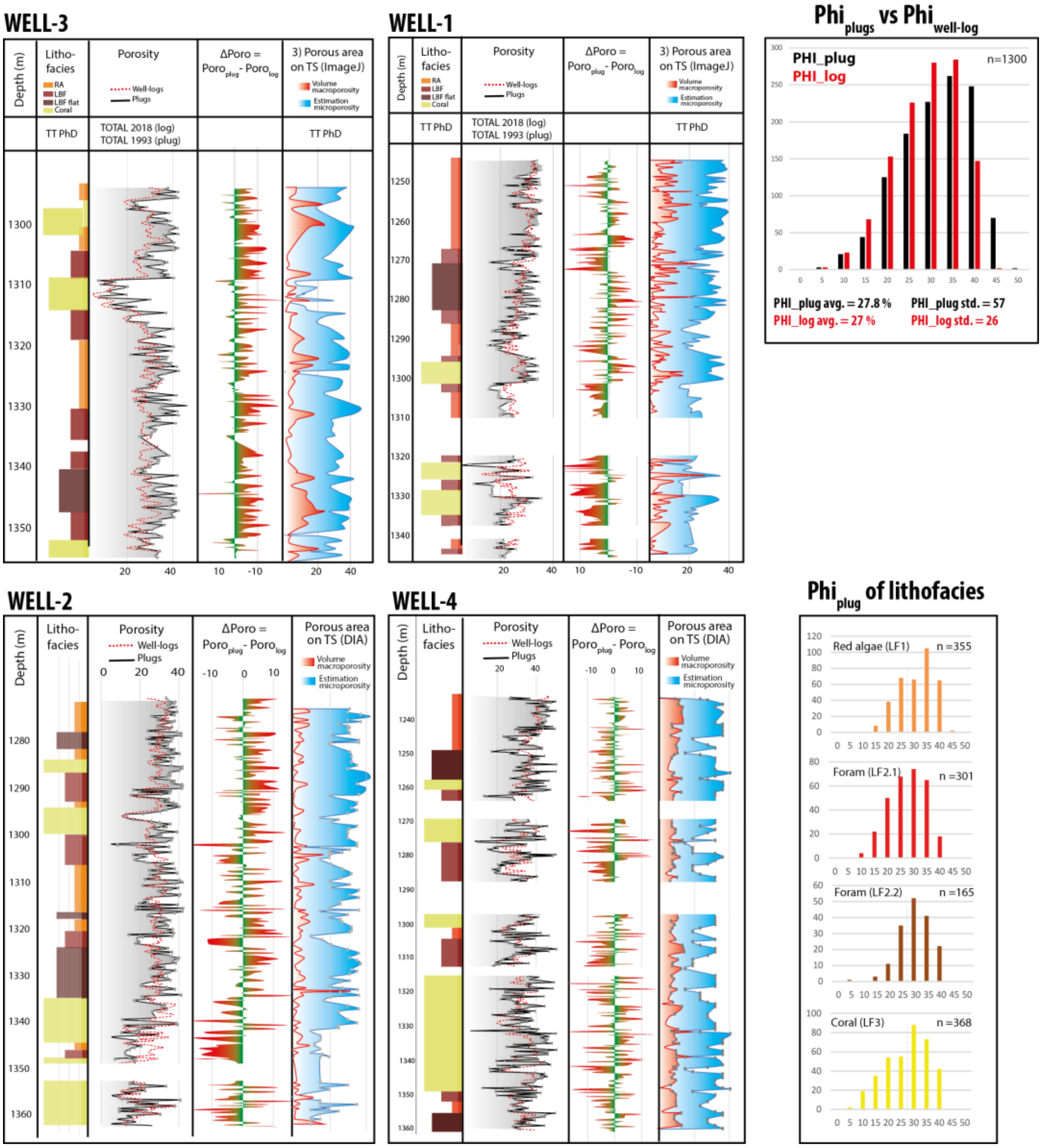

Figure 8-5 : Difference between Phi_plug and Phi_well-log (ΔPoro) for the four cored wells.

Gas correction to calculate PHI_log (neutron porosity; NEUT)

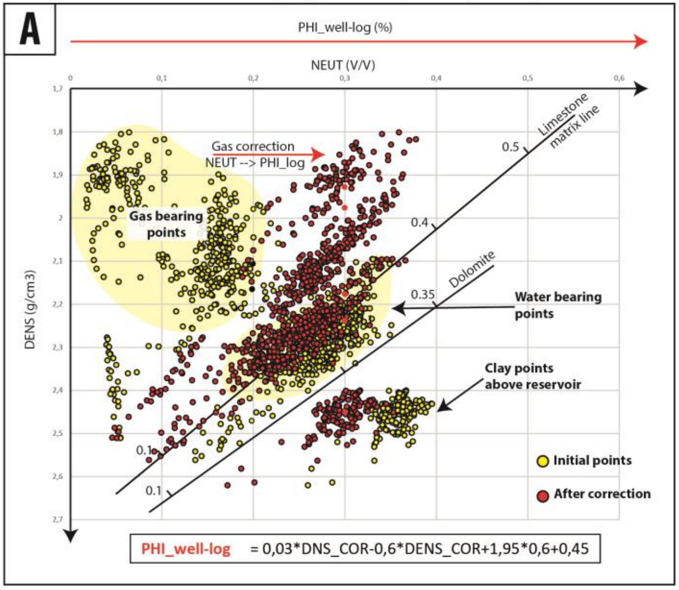

Porosity difference : PHI_plug versus PHI_well-logs

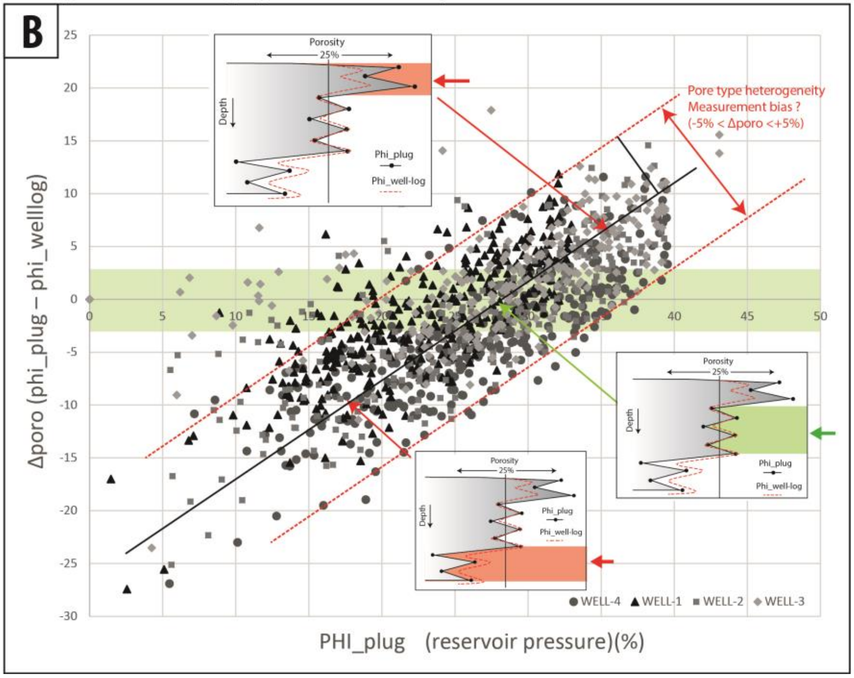

Figure 8-6 : (A) Gas correction to calculate PHI_log in gas reservoir. (B) Crossplot of ΔPoro (Phi_plug - Phi_well-log) versus Phi_plug. The points within the green zone correspond to the depth where the plug porosity (PHI_plug) is equal to the log porosity (PHI_well-log). Over the green area, the PHI_log underestimate PHI_plug. Below the green area, PHI_log overestimate PHI_plug.

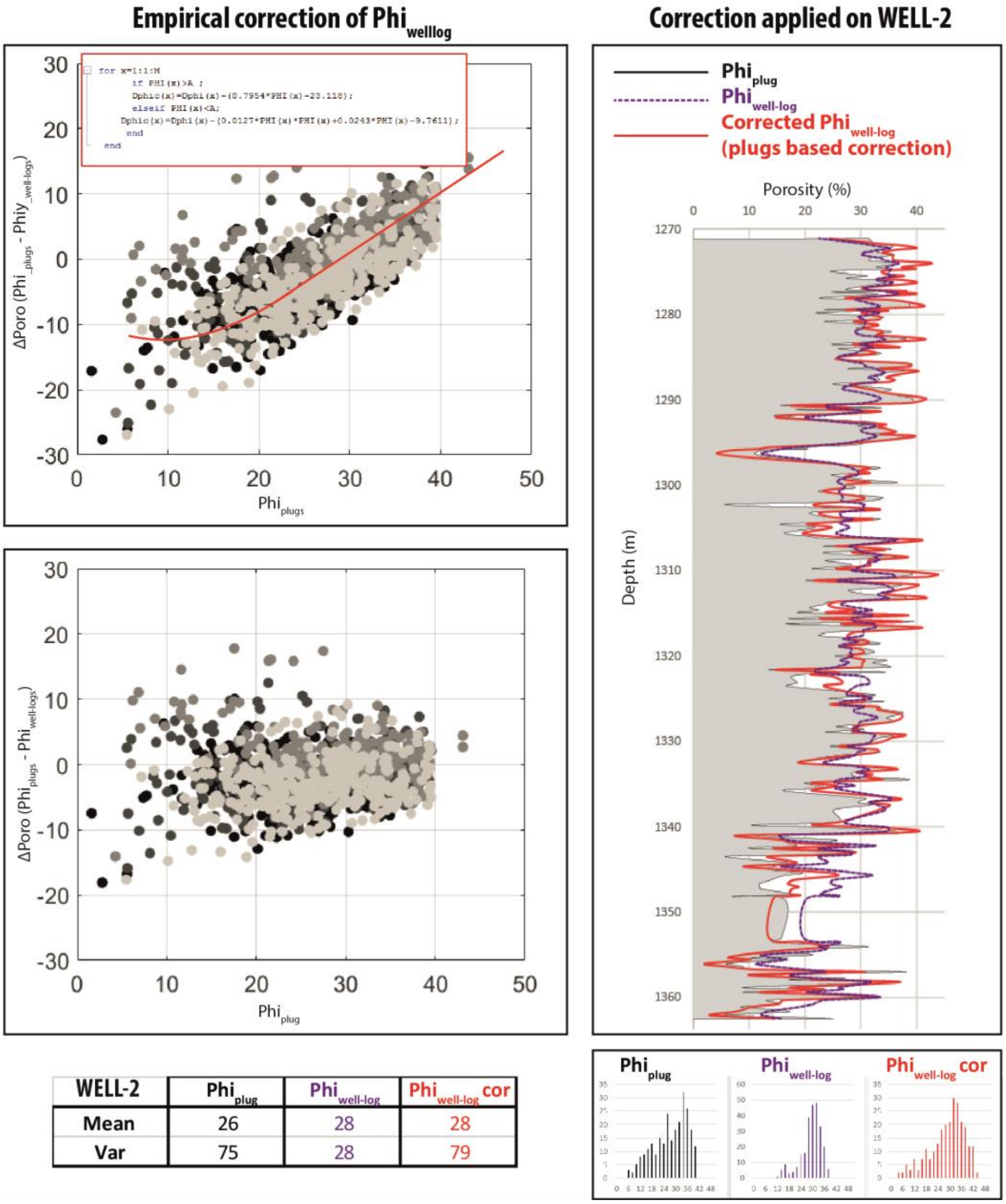

```
for x=1:1:M
      if PHI(x)>A ;
      Dphic(x)=Dphi(x)-(0.7954*PHI(x)-23.118);
      elseif PHI(x)<A;
    Dphic(x)=Dphi(x)-(0.0127*PHI(x)*PHI(x)+0.0243*PHI(x)-9.7611);
     end
 end
```

WELL-2	Phi$_{plug}$	Phi$_{well-log}$	Phi$_{well-log}$ cor
Mean	26	28	28
Var	75	28	79

Figure 8-7: Empirical correction of neutron porosity (PHI_log) based on the analysis of plug porosity. See the corrected Phi$_{welllog}$ (red dash) of the WELL-2 well fitting to the plugs porosity (PHI_plug).

5. *Seismic profiles and maps*

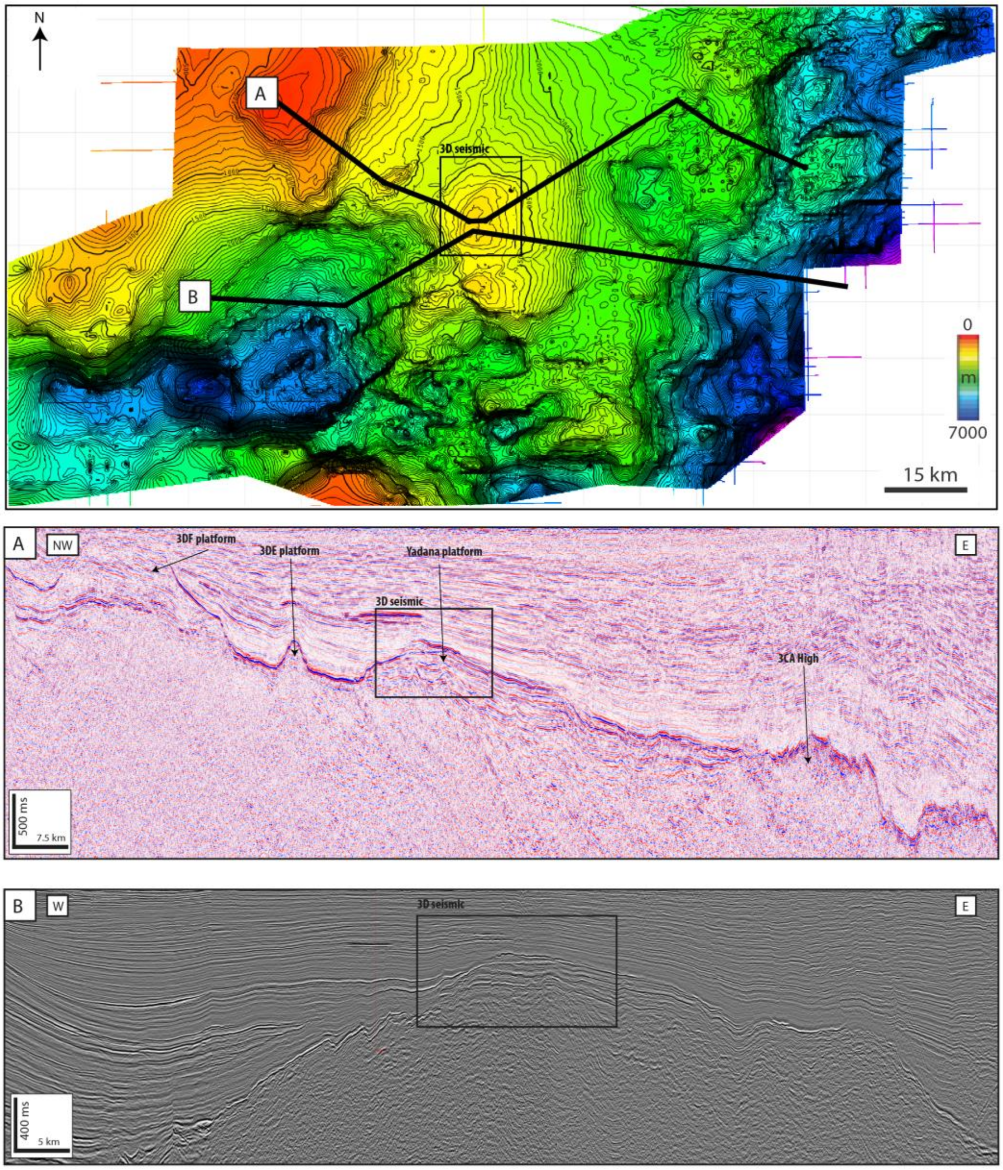

Figure 8-8 : Morphological and geophysical frame of the M5 and M6 Basins and the Yadana High (A) Depth map of TOP UBL surface interpreted from 2D seismic data showing the Yadana High, the M5 (East) and the Moattama (West) Basins. The black square represents the 3D seismic survey of the Yadana field and the red line refers to the seismic profile (Fig. 2B and C). (B) Regional NW/SE seismic profile crossing the Yadana High, the 3DE and the 3DF carbonate platform and the 3CA High (cf. Paumard et al. 2017). (C) Regional E/W seismic profile through the Yadana High.

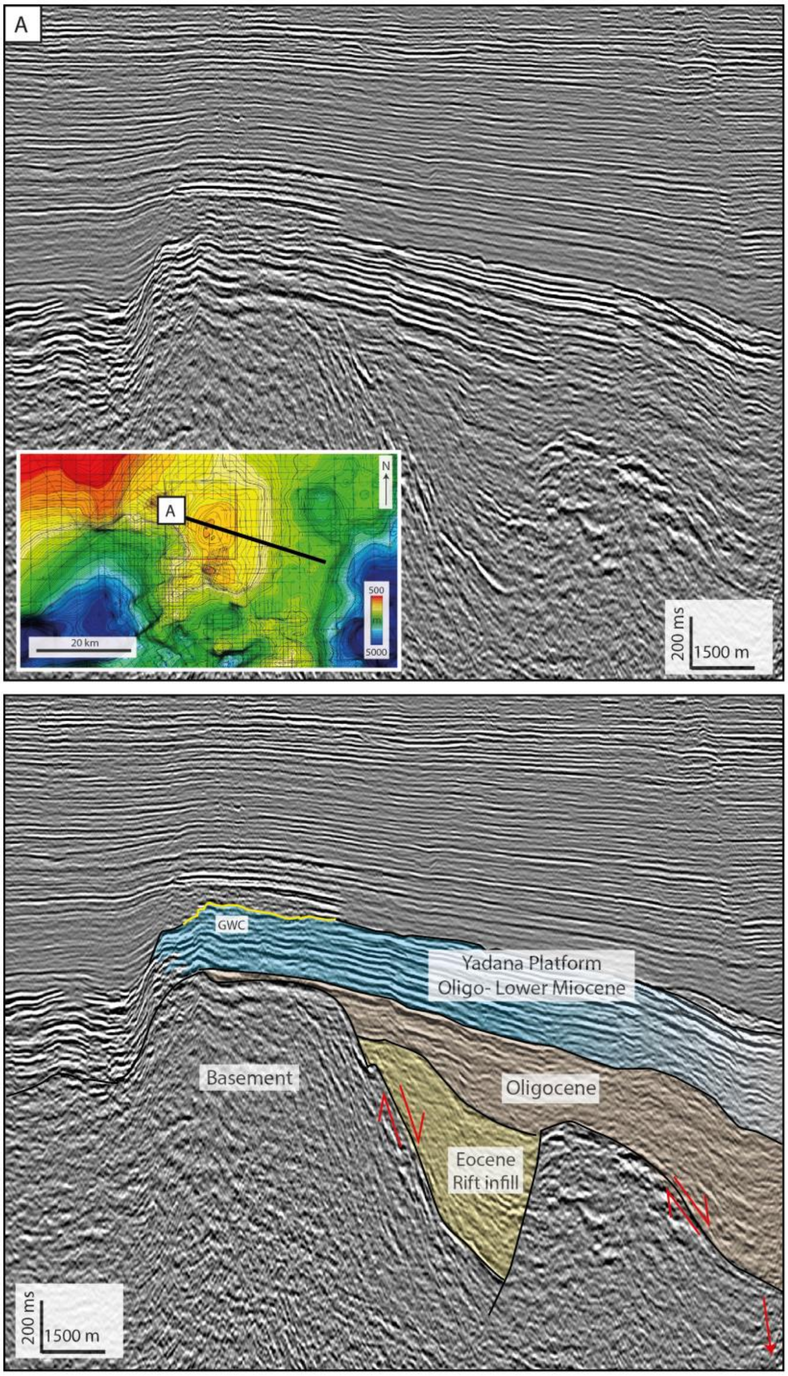

Figure 8-9 : Un-interpreted and interpreted 2D seismic profile crossing the Yadana High and showing the morphology and the faulting within the Eocene basement of the carbonate platform.

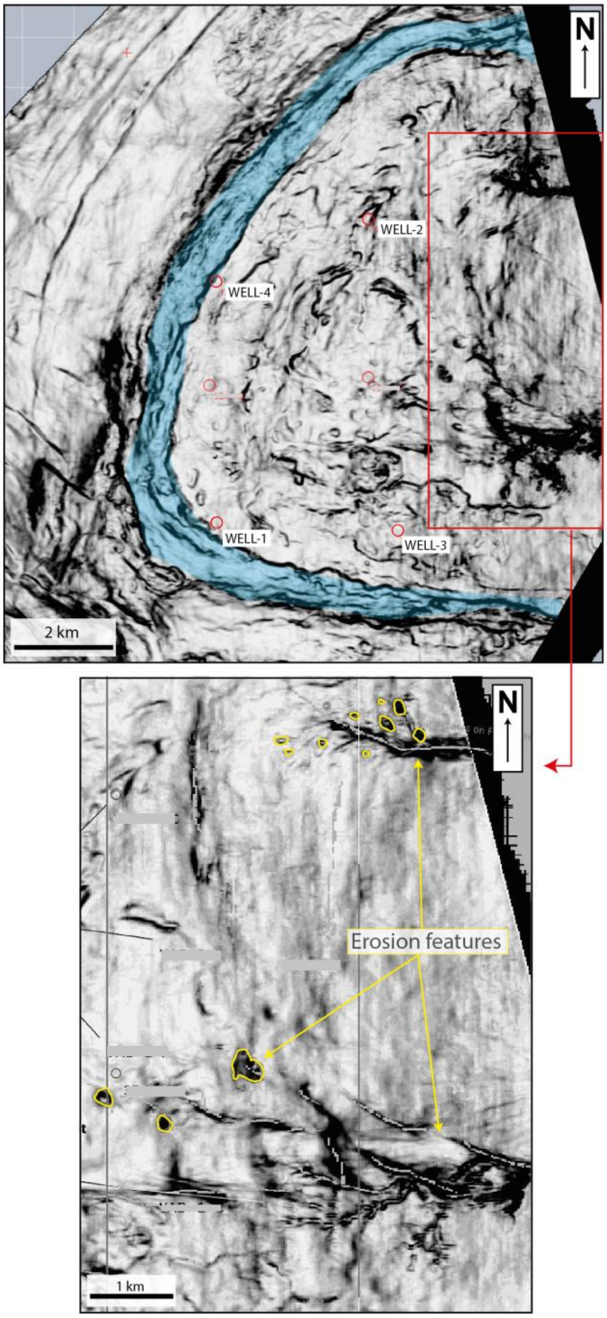

Figure 8-10 : Coherency attributes map showing morphologies of the TOP UBL. See terraces bordering the carbonate buildup in blue color (wave-cut developed during the intra-UBL exposure event, paleo-cliffs; blued highlighted zone) as well as the uneven and rough topography of TOP UBL surface with small-sized.

The Yadana gas Field is located in the Andaman Sea, offshore Myanmar and producing gas since 1998. The reservoir is an isolated carbonate buildup, Miocene in age, sealed below 1200 m of siliciclastic sediments. Predicting the ultimate hydrocarbon resources and the water flows during the production has become a major challenge for such mature gas field.

The PhD work involves the implementation of a methodology allowing the construction of a detailed reservoir architecture that accounts various types of heterogeneities. The work is multiscale and multidisciplinary, covering disciplines such as **sedimentology**, **stratigraphy**, **diagenesis**, **geochemistry**, **rock physics**, **geophysics** and based on a large and comprehensive dataset including, cores, well-logs, petrophysical measurements, production and 3D/4D seismic data.

Providing a robust geological framework for the **reservoir characterization** of the Yadana Field, the thesis gives further insights into the understanding of geological and environmental factors controlling Cenozoic isolated carbonate systems in South East Asia. This work highlights once again the interdependence existing between geology and seismic imaging and demonstrates that an integrated geological/geophysical characterization of carbonate reservoirs remains crucial for both the exploration, the evaluation and the production of hydrocarbon resources.

Thomas Teillet
PhD student in Aix-Marseille University,
CEREGE, France, specialized geology of
carbonate systems & reservoirs.